Dynamics of Interactions of Confined Microcavity Polaritons

THÈSE N^{O} 4726 (2010)

PRÉSENTÉE LE 18 JUIN 2010

À LA FACULTÉ SCIENCES DE BASE

LABORATOIRE D'OPTOÉLECTRONIQUE QUANTIQUE

PROGRAMME DOCTORAL EN PHYSIQUE

ÉCOLE POLYTECHNIQUE FÉDÉRALE DE LAUSANNE

POUR L'OBTENTION DU GRADE DE DOCTEUR ÈS SCIENCES

PAR

Taofiq PARAÏSO

acceptée sur proposition du jury:

Prof. O. Schneider, président du jury
Prof. B. Deveaud-Plédran, directeur de thèse
Prof. J. Bloch, rapporteur
Prof. I. Carusotto, rapporteur
Prof. A. Imamoglu, rapporteur

ÉCOLE POLYTECHNIQUE
FÉDÉRALE DE LAUSANNE

Suisse
2010

Résumé

Ce travail de thèse de doctorat a été effectué entre avril 2006 et avril 2010 dans le Laboratoire d'Optoélectronique Quantique, sous la direction du professeur Benoît Deveaud-Plédran. De façon générale, nous étudions l'effet du confinement latéral sur la dynamique des polaritons dans une microcavité semiconductrice. Cette étude se décline suivant deux principaux axes. Nous étudions d'une part, la relaxation des polaritons, et d'autre part, le rôle du spin dans les interactions entre polaritons.

Dans une première partie, nous introduisons les polaritons de microcavité. Nous décrivons leurs propriétés optiques, ainsi que le formalisme du pseudo-spin pour les polaritons. Nous présentons ensuite l'échantillon étudié et la méthode utilisée pour confiner les polaritons à travers leur composante photonique.

La deuxième partie du manuscrit est consacrée à l'étude de la relaxation des polaritons en milieu confiné. Nous montrons qu'en régime linéaire, l'interaction entre les polaritons et phonons acoustiques est favorisée par le confinement. Nous mettons en évidence une thermalisation des polaritons (interdite dans le cas des polaritons planaires) et montrons qu'elle est plus efficace dans les pièges de petit diamètre. Nous proposons pour la première fois un modèle complet de la dynamique de la relaxation des polaritons confinés et soulignons le rôle des états fortement excitoniques. Cette étude pourra servir au développement de futurs échantillons destinés à l'étude de la condensation de Bose-Einstein.

En régime non linéaire, nous démontrons que la relaxation sous l'effet des collisions polariton-polariton a une influence déterminante sur la dynamique spatiale des polaritons. Nous regardons l'évolution temporelle d'une superposition cohérente d'états confinés. À basse densité, nous observons des oscillations dipolaires de constante amplitude. À haute densité, sous l'effet des collisions, nous observons un amortissement continu des oscillations. Nous montrons que cet amortissement résulte de processus paramétriques multiples, dont l'effet est de redistribuer l'énergie en faveur de l'état fondamental du système. Finalement, nous démontrons que l'amortissement collisionnel des oscillations dipolaires est beaucoup plus efficace pour des collisions entre polaritons de mêmes spins qu'entre polaritons de spins opposés.

La troisième partie du manuscrit porte sur l'étude des effets de spin sur les interactions entre polaritons.

Dans un premier temps, nous nous intéressons aux polaritons planaires. Nous observons que le régime de bistabilité optique peut être fortement modifié en fonction

de l'orientation des spins des polaritons. Sous excitation polarisée linéairement, la bistabilité est fortement réduite, voire supprimée. Nous montrons que cela est dû à un appariement des polaritons de spin opposés pour former des biexcitons. Nous démontrons le contrôle des différents régimes d'instabilité optique à travers la polarisation de l'excitation.

Nous regardons ensuite le cas des polaritons confinés. En travaillant avec un unique état confiné, nous obtenons un contrôle optique complet des interactions de spin entre polaritons. Nous démontrons pour la première fois la multistabilité d'un ensemble cohérent de spins dans l'état solide. Ce résultat est une étape importante dans le cadre de la recherche sur la manipulation de spins pour le développement de dispositifs optoélectroniques.

Finalement, nous montrons l'impact que pourrait avoir le spin des polaritons sur le couplage en polaritons de dimensionnalités différentes ainsi que sur le contrôle des régimes de propagation des fluides de polaritons.

Nos expériences sont appuyées par des modèles théoriques. Nous proposons, en perspective, de nouvelles expériences sur la dynamique des polaritons et sur la manipulation cohérente de spins dans les microcavités.

Mots-clefs: polariton; couplage fort; microcavités; boîtes quantiques; photoluminescence; phénomènes ultrarapides; excitons; biexcitons; optique non linéaire; diffusion paramétrique; relaxation; thermalisation; oscillations dipolaires; amortissement collisionnel; bosons en interaction; contrôle cohérent; manipulation de spins; traitement optique de l'information; logique multivaluée; fluides spinoriels;

Abstract

The present Ph.D. thesis consists in a series of experiments carried out in the Laboratory of Quantum Optoelectronics under the direction of professor Benoît Deveaud-Plédran between April 2006 and April 2010. We study the effect of lateral confinement on the dynamics of microcavity polaritons according to two important subjects. On the one hand, we study the polariton relaxation, on the other hand, we study the role of the spin in polariton mutual interactions.

We first introduce microcavity polaritons, their optical properties and present the polariton pseudospin formalism. In our sample, polaritons are trapped through their photonic component in cylindrical extensions of the cavity length called mesas.

Polariton relaxation is studied in the linear and nonlinear regimes. In the linear regime, we demonstrate that polariton interactions with acoustic phonons are enhanced under lateral confinement. Thermalization, which is forbidden in planar microcavities, is facilitated by confinement, and is very efficient in small diameter mesas. We develop for the first time a comprehensive model of polariton relaxation dynamics under confinement, and highlight the role of polariton states with large exciton content. This work will be profitable to the design of future samples dedicated to the study of Bose-Einstein condensation.

In the nonlinear regime, we study the impact of polariton-polariton collisions on the spatial dynamics of microcavity polaritons. In the low-density regime, when the mesa is excited in a coherent superposition of the three lowest energy states, the polariton dynamics is characterized by dipole oscillations. In the high-density regime, we observe a continuous damping of the dipole oscillation. This is due to multiple parametric scattering processes, which redistribute the energy to the benefit of the ground state. Moreover, we demonstrate that the collisional damping is more efficient for collisions between polaritons of the same spin than between polaritons of opposite spins.

We investigate in detail the influence of polariton spin in the interactions between polaritons. We first consider the case of planar polaritons. We observe that optical bistability is strongly reduced, or even suppressed, when the system contains polaritons of opposite spins. This results from a pairing of polaritons of opposite spins to form biexciton states. We demonstrate the polarization control of the different optical instability regimes.

We then study the case of confined polaritons. As the system is cleaner (we work

with a single polariton energy level), we achieve full optical control over the spinor interactions. We demonstrate the first realization of multi-valued switching with a coherent spin ensemble in the solid state. This is a very important step in the research on spin manipulation for the development of spin optoelectronic devices.

Finally, we show the influence of the polariton spin on the coupling between planar and confined polaritons and on the control of the polariton fluid dynamics.

All our experiments are confirmed by theoretical models. We propose perspectives for the next studies on the dynamics of polaritons and on the coherent spin manipulation in microcavities.

Keywords: polaritons; strong-coupling; microcavities; quantum boxes; photoluminescence; ultra-fast spectroscopy; excitons; biexcitons; nonlinear optics; parametric scattering; relaxation; thermalization; dipole oscillations; collisional relaxation; interacting bosons; coherent control; spin manipulation; logic gates; spin-memories; optical processing; multi-valued switching; spinor fluids;

Acknowledgment

This PhD thesis in the Laboratory of Quantum Optoelectronics has been very enriching personally and scientifically. I acquired strong experimental skills and knowledge in quantum optics. I have developed maturity over solid-state physics, ultra-fast spectroscopy, spin physics and the physics of interacting bosons. In addition, I have developed competences in team-working, teaching and project supervising. I wish to deeply acknowledge everybody who participated to this achievement.

First of all, I would like to thank professor Benoît Deveaud-Plédran, who directed this research and who gave me the opportunity to work in his laboratory. Benoît Deveaud-Plédran is an enthusiastic and motivating supervisor, who knows perfectly how to give precious directions and, in the meantime, how to give freedom to his students to let them develop their own scientific intuition and creativity.

I thank professors Jacqueline Bloch, Iacopo Carusotto, Atac Imamoglu and Olivier Schneider for accepting being part of the jury of my thesis oral examination, for their careful reading of the manuscript. Their positive comments and remarks were very helpful for producing a final version of the manuscript.

I would like to thank my colleagues and friends from the LOEQ. Thanks to the remarkable competence of the postdoctoral assistants and of the other PhD students, we regularly had enlightening and motivating interactions.

I thank my colleagues from the theory group of professor V. Savona, with which we closely collaborate. The main theoretical developments of this thesis were done by Davide Sarchi and Michiel Wouters. Thanks to the proximity of our two institutes we have the lucky opportunity to work with constructive mutual feedback and therefore to optimize our productivity.

I also thank the technical staff, whose outstanding efficiency and availability were determining in solving several technical problems encountered in the laboratory. In addition, I would like to thank our secretaries and highlight the crucial role they play in the management of administrative procedures.

Finally, I would like to thank my friends for providing me a lively social environment and, last but not the least, my family, for being by my side in every moments of my life.

Remerciements

Ces quatre années de thèse de doctorat ont été une source d'enrichissement considérable, tant sur le plan scientifique que sur les plans psychologique et humain. Je ne peux que témoigner ma reconnaissance sincère aux personnes qui m'ont accompagné, de près ou de loin, au cours de ce parcours.

Tout d'abord, je remercie les membres de mon jury de thèse, les professeurs Jacqueline Bloch, Iacopo Carusotto, Atac Imamoglu et Olivier Schneider, qui ont accepté d'expertiser mon travail de thèse, pour leurs questions et commentaires constructifs qui m'ont permis de finaliser ce manuscrit.

J'exprime toute ma gratitude à mon directeur de thèse, le professeur Benoît Deveaud-Plédran, pour la confiance et la liberté qu'il accorde à ses doctorants et post-doctorants. Son enthousiasme et son optimisme sont de réelles forces rassurantes et motivantes. Au-delà de ses qualités de superviseur, je voudrais surtout saluer sa philosophie, qui consiste à miser en premier lieu sur l'aspect humain, afin de favoriser une ambiance de travail où la communication, la créativité et la complicité créent une synergie extrêmement productive scientifiquement.

Cela s'illustre par l'ensemble des collaborateurs scientifiques que j'ai pu côtoyer au LOEQ, et avec qui j'ai tissé de véritables liens d'amitié. Je tiens à remercier les post-doctorants, Augustin Baas, Maxime Richard, Barbara Pietka et Yoan Léger, qui m'ont été d'une aide précieuse dans le déroulement de ce travail. Avec chacun un style complètement personnel, ils ont fait preuve d'une compétence exceptionnelle au niveau de l'encadrement des doctorants. En particulier, je remercie Yoan Léger pour son suivi dans mes dernières expériences et pour sa relecture minutieuse du manuscrit avec Maxime Richard. J'adresse un grand merci aux doctorants de l'"ancienne génération", Ounsi El-Daïf, dont j'ai repris la suite du travail de doctorat, Jean Berney, Samuel Sonderegger, et à ceux de la "nouvelle", Pierre Corfdir, Konstantinos Lagoudakis, Gaël Nardin, Verena Kohnle, Roland Cerna, et plus récemment, Francesco Manni et Gabriele Grosso. Les discussions, les réflexions et l'entraide ont toujours été très naturelles entre nous, et cela a été particulièrement bénéfique au développement des compétences de chacun. Je remercie aussi les étudiants en master que j'ai eu la chance de co-encadrer, Sébastien, Karin et Boris, pour leur efficacité et leur motivation. J'exprime également ma reconnaissance à Marcia Portella-Oberli, qui m'a incité à étudier l'effet de la polarisation d'excitation sur les interactions entre polaritons. Merci à l'unité de Romuald Houdré, avec Jana, Hua, Zhaolu, les Nicolas, Peru, à Jean-Daniel Ganière, Marc-André Dupertuis, Denis Martin et Marcel Py de participer à la vie du LOEQ. Et bien sûr, je remercie particulièrement François Morier-Genoud, sans qui nous n'aurions pas d'échantillons, et avec qui j'ai eu la chance de partager de grands moments de discussion.

Une bonne communication entre théoriciens et expérimentateurs est l'idéal de tout chercheur. En cela, je souhaite exprimer ma profonde reconnaissance envers mes collègues de l'ITP, dans le groupe de Vincenzo Savona, notamment à Michiel Wouters et Davide Sarchi, qui sont des théoriciens extraordinaires, avec qui j'ai pu travailler en étroite collaboration, et avec qui j'ai découvert une démarche de travail unique, où la théorie et l'expérience se complètent mutuellement pour produire une dynamique de recherche terriblement efficace.

Je souhaite remercier l'équipe technique, Roger Rochat, Nicolas Leiser, Yoan Trolliet, Damien Trolliet et Maxime Marendaz, pour leur efficacité et leur disponibilité, ce malgré le grand nombre de laboratoires et d'utilisateurs des salles blanches à gérer. Leur grande expérience leur permet de trouver rapidement une solution adaptée à chaque problème rencontré, et leur aide m'a été précieuse tout au long de mon travail de doctorat.

Je remercie Claire-Lyse Rouiller, et lui témoigne toute ma reconnaissance pour sa gestion irréprochable des affaires administratives du LOEQ. Je remercie Anh Eymann, pour sa bonne humeur et son très précieux travail d'administration de l'école doctorale de Physique. Je remercie également Laurence Carlin, Gabriela Fuchs, Aline Gruaz, Sandra Pochon, Ursula Vaucher, Oana Chiper et Anita Berdoz pour leur travail au secrétariat de l'IPEQ et du NCCR, et leur contribution à la vie agréable de l'institut. Enfin, je souhaite adresser une pensée à la famille de Denise Paroz.

De manière générale, je souhaite remercier mes collègues et amis de l'ICMP, de la section de Physique, des universités de Berne et de Genève, et de l'association "Musical", pour les interactions que nous avons eues au cours de ces quatre années.

Je souhaite à présent exprimer ma gratitude à mon entourage, à commencer par Gisèle, qui a su partager ma vie de doctorant, me supporter, m'encourager de manière inconditionnelle, même dans les moments les plus difficiles. Je remercie également tous mes amis que je n'ai pas encore cités, Amélie, Andreas, Arsène, Aurélie, Béa, Carl, Chiara, Clément, Corinne, Davor, Denise, Gwenola, Hasnia, Lafcadio, Laurence, Linda, les Marie, Marjan, Mars, Mireille et Jean-Luc, Naomi, Nikolay, Olaya, Onya, Pascal, Pascale, Sylfa, Sarah, Sandra, Sandro, Sandy, Saverio, Stefan, Ursle, Val, Yas et Yas... et bien sûr, ceux que j'oublie malencontreusement sur le moment !

Enfin, je souhaite remercier ma famille, pour sa présence, sa chaleur et son soutien.

Contents

Introduction

Semiconductor heterostructures are privileged laboratories to explore light-matter interactions in the solid-state. First, thanks to the developments of quantum mechanics, they have been extensively studied over the last century, which led to a comprehensive knowledge of their fundamental properties. Second, thanks to the considerable precision achieved in fabrication, samples are of very high quality and can be designed and controlled with innumerable possibilities. Finally, semiconductors are the central elements of our technology, and they have an exceptional impact on our society. Therefore, in addition to the important conceptual implications that it may have, the study of light-matter interactions in semiconductors is also promising for future technological advances.

Among all light-matter quantum interactions, *strong coupling* (or *normal mode coupling*) is probably the most fascinating one. When a periodic exchange of energy takes place between a photon and a particle, quantum electrodynamics predicts that they would mix together to form two new, half-light, half-matter quasi-particles. In 1958, while revisiting the concept of light absorption in bulk semiconductors, Hopfield demonstrated that strong coupling naturally takes place between free excitons and photons to form mixed exciton-photon states called *polaritons* [Hopfield 58]. The prediction of Hopfield could be verified experimentally in various bulk semiconductor crystals [Guillaume 70, Sell 71, Weisbuch 77b].

In 1992, inspired by the work of Jaynes and Cumming [Jaynes 62] and by pioneering cavity electrodynamics experiments [Raizen 89] Weisbuch et al. reported the observation of polaritons in a solid-state semiconductor microcavity with an embedded quantum well [Weisbuch 92]. This demonstration of the strong coupling between an electromagnetic field confined in a cavity and quantum well excitons gave new orientations to the research in semiconductor microcavities. Thanks to the unique properties of microcavity polaritons, together with the ease of manufacture and optical characterization, semiconductor microcavities rapidly became ideal candidates for both fundamental and applied research.

Under a critical density, polaritons behave as bosons and present macroscopic coherence properties. Their very small effective mass allows for the observation of quantum effect at higher temperature than the one explored in cold atoms physics. Moreover, polaritons have large de Broglie wavelengths, which makes their trapping and manipulation possible in micrometer-sized structures. Their photonic nature obviously facilitates optical characterization, but also favors the mapping of the knowledge of quantum optics to these new light-matter quasiparticles.

Many efforts were made to observe bosonic behaviors, through stimulated scattering [Savvidis 00a, Erland 01, Kundermann 03], optical parametric amplification

[Messin 01, Saba 01] up to the recent demonstrations of Bose-Einstein condensation [Kasprzak 06, Balili 07, Deng 07], polariton lasing and superfluidity in different microcavity systems [Bajoni 08b, Christmann 08, Amo 09b, Amo 09c].

In the present thesis, we study the effect of lateral confinement on dynamics of microcavity polariton interactions. We demonstrate that confinement provides a better control of polariton interactions and we demonstrate the potential of such structures to develop advanced spin dependent optoelectronic devices.

Part I is an introduction to microcavity polaritons and lateral confinement.

In Chapter 1, we recall some basics of the physics of semiconductors and describe light-matter interactions in the specific case of microcavities. We introduce microcavity polaritons and their physical properties. In particular, we introduce the notion of polariton spin, which will have a central position in the description of polariton interactions.

Then, in Chapter 2, we describe the sample and the method we used to achieve lateral confinement. Trapping polaritons is most commonly achieved by acting on the excitonic nature of polaritons, in micropillars structures [Gérard 98, Bloch 98a, Dasbach 01] or by applying mechanical stresses on the microcavity [Balili 06]. We developed new structures (called *polariton mesas*) to trap polaritons by acting on their photonic nature [Daif 06, Kaitouni 06, El Daif 07]. We present optical characterization measurements and show a major advantage of our technique, which is that it allows the coexistence of both planar and confined polaritons in the same microcavity.

Part II is dedicated to the first objective of the present thesis, which is the development of a picture for the mechanisms and the dynamics of the relaxation of microcavity polaritons confined in mesa structures.

Polariton relaxation has been extensively investigated in planar structures (see, for a review [Houdré 05] and [Senellart 03]). A very interesting feature of polariton relaxation is the existence of two regimes, depending on the polariton density. When the polariton density is low, interactions vary linearly with the polariton density. The regime is called the *linear regime*. A *non-linear regime* appears when the polariton density is high enough to allow significant collisions between polaritons. Numerous studies were dedicated to the differences between those two regimes, regarding the efficiency of the relaxation to lowest energy states or the possibility of forming a *thermalized polariton gas* [Stanley 96, Porras 02a, Cao 04]. In the presence of a confining potential, relaxation processes are likely to be strongly modified by the discretization of energy levels or by the lift of the momentum selection rule. However, such studies were still missing in the case of confined polaritons.

We studied polariton relaxation in mesas in the low and high polariton density regimes.

In Chapter 3, we show that, in the low-density regime, there is a strong influence of the size of the mesa in the relaxation process. Thermalization, which is inefficient in planar microcavities, is facilitated in small diameter mesas. We provide a general scheme for the relaxation of confined polaritons.

In Chapter 4, we study the non-linear dynamics of polariton-polariton interac-

tions. We choose to observe the influence of nonlinearities on the spatial dynamics of polaritons. Polaritons are injected in a special superposition of excited states that exhibits a dipole oscillation dynamics. We evidence that in the high-density regime, the oscillations are damped because of collisional relaxation.

Part III is dedicated to the second objective of this thesis, which is to show the importance of the polariton spin in the dynamics and to show how laterally confined polaritons can be used for device applications (optical processing, bistability, multistability). The idea of polaritonic devices like logic gates, interferometers, i/o couplers, etc., is often put forward but still demands clear ideas of the properties of polaritons that can be used for technological purposes is necessary. In 2007, Gippius et al. proposed to take advantage of the spinor nature of polaritons to observe polarization multistability in microcavities [Gippius 07]. This gave rise to important proposals for the design of spin-based localized memories [Shelykh 08] and optical circuits [Liew 08a].

We show how the spinor nature of polaritons modifies their non-linearities in our sample and study polariton bistability in the cases of planar and confined polaritons.

In Chapter 5, we study the case of planar polaritons. We evidence an unexpected effect, which is the suppression of optical bistability under linearly polarized excitation. We use this effect to demonstrate that optical instabilities can be controlled by the polariton polarization. We claim that this effect originates from a pairing of polaritons of opposite spin into biexciton states and give some experimental indications that support our hypothesis.

In Chapter 6, we study the case of confined polaritons. We demonstrate the first realization of spin multistability in the solid state. We show an exhaustive series of experiments through which we acquired sufficient knowledge on the spinor interactions and the ways of controlling them. Beside multistability, we evidence very rich spin-dependent phenomenology of confined microcavity polaritons. We give perspectives regarding the development of polariton devices, and in particular we demonstrate the possibility of selective multi-valued spin switching.

In Chapter 7, we finally give preliminary indications on how the polariton fluid dynamics is affected by their spinor nature.

Part I

On the Lateral Confinement of Microcavity Polaritons




Chapter 1

Microcavity Polaritons

The existence of normal-mode coupling between light and elementary electronic excitations (excitons) in bulk semiconductors was predicted by Hopfield in 1958. In a paper that would radically change the picture of light-matter interactions in semiconductors, he revisited the mechanisms of light absorption in these materials [Hopfield 58]. He showed that the existing picture of photon absorption by excitons was actually wrong. In Hopfield's theory, because of a periodic energy exchange interaction between photons and excitons due to translation invariance symmetry, the elementary excitations of a bulk semiconductor are mixed exciton-photon states, called polaritons. Light absorption is in fact the result a second order process, in which polaritons are absorbed by impurities. Polariton luminescence was observed experimentally in different materials [Guillaume 70, Sell 71, Weisbuch 77b], and the polariton dispersion was characterized by polariton-phonon inelastic (Brillouin) scattering [Ulbrich 77, Winterling 77b, Sermage 79]. Importantly, it has been shown that, owing to translational symmetry breaking, polaritons are not anymore eigenstates of light-matter interaction in semiconductor quantum wells [Agranovich 66, Tassone 90].

Normal-mode coupling has also been predicted by Jaynes and Cummings, in a study of atoms coupled to a cavity photon [Jaynes 62]. In this case, depending on the interaction strength between the atoms and the electromagnetic field, the systems is either in a *weak-coupling* regime, either in a *strong-coupling* regime. In the former, interactions are small and the electromagnetic field is treated as a perturbation on the atomic system. In the latter, the eigenmodes are mixed atom-photon states. Soon after the observation of this effect with atoms in cavities [Raizen 89], Weisbuch et al. demonstrated the existence of normal-mode splitting in semiconductor quantum wells embedded in microcavity structures [Weisbuch 92]. This observation opened the way to the very rich research field of microcavity polaritons.

In the present chapter, we discuss some aspects of exciton-photon interactions in semiconductor microcavities and describe microcavity polaritons. In Section 1.1, we recall the band structure of semiconductors. In Section 1.2, we introduce excitons in bulk semiconductors and discuss their coupling with light. We then describe excitons confinement in semiconductor quantum wells. In Section 1.3, we describe photon confinement in semiconductor microcavities. In Section 1.4, we present the strong-coupling regime and introduce microcavity exciton polaritons. Finally, in Section 1.5, we introduce the concept of *pseudospin* for microcavity polaritons.

1.1 Band structure in semiconductors

Semiconductors are at the heart of today's technology. Their advantageous electronic properties are widely exploited to design electronic of optoelectronic devices. The main characteristic that makes semiconductors differ from other materials is the existence of a gap in their electronic excitation spectra. To understand this behavior, the recourse to a microscopic description of their electrons behavior is essential. This is best achieved in the framework of the electronic band structure theory, that describes the differences in electron levels filling configurations in the ground and excited states.

1.1.1 Energy bands in solids

In the case of a single atom, quantum mechanics teaches us that an electron has discrete energy levels that correspond to distinct atomic orbitals.

In the case of a chain of a few equally distant atoms, the electron can localize more around one or another atom. For large distances R between the ions, the electron levels are thus N times degenerate. When R decreases, the electron problem is analog to the N coupled quantum wells problem. The degeneracy of each level is lifted, giving rise to *separate energy intervals*, each containing N *distinct energy levels* in which the electron is partially delocalized over the atoms (see Figure 1.1).

In a solid, where the density of atoms is extremely large ($\sim 10^{23}$ cm^3), the number of energy levels within a given interval is so large that they form an energy continuum: the energy intervals are regarded as *energy bands*, of different widths, separated by forbidden energy bands called *bandgaps* [Cohen-Tanoudji 97].

1.1.2 A simple picture

A basic approach to band structures can be derived in the framework of the Born-Oppenheimer approximation [Cohen-Tanoudji 97]. Electrons are moving in the fixed potential formed by the periodic arrangement of ions. In addition, we first consider non interacting electrons. The Schrödinger equation of an electron in a periodic potential reads

$$\left(-\frac{\hbar^2}{2m}\nabla^2 + U(\mathbf{r})\right)\psi(\mathbf{r}) = \epsilon\psi(\mathbf{r}) \tag{1.1}$$

where m is the electron mass, ϵ is an eigenenergy of the Hamiltonian and the periodic potential $U(\mathbf{r}) = U(\mathbf{r}+\mathbf{R})$ has the *translation period* $\mathbf{R}$. The *translational symmetry*, which is the most important symmetry of a crystal, can be described using the translation operator $T_{\mathbf{R}}$ as $T_{\mathbf{R}}f(\mathbf{r}) = f(\mathbf{r}+\mathbf{R})$ for any function f. The Hamiltonian is a translation invariant i.e. a solution of the Hamiltonian remains solution with the same energy after a translation. The eigenfunctions of the Hamiltonian can thus be expressed as combinations of the eigenfunctions of the translation operator $T_{\mathbf{R}}$. That is, one obtains the Bloch theorem, which states that the solutions must have the same periodicity as the potential $U(\mathbf{r})$:

$$\psi_{\mathbf{k}}(\mathbf{r}) = e^{i\mathbf{k}\cdot\mathbf{r}}u_{\mathbf{k}}(r) \tag{1.2}$$

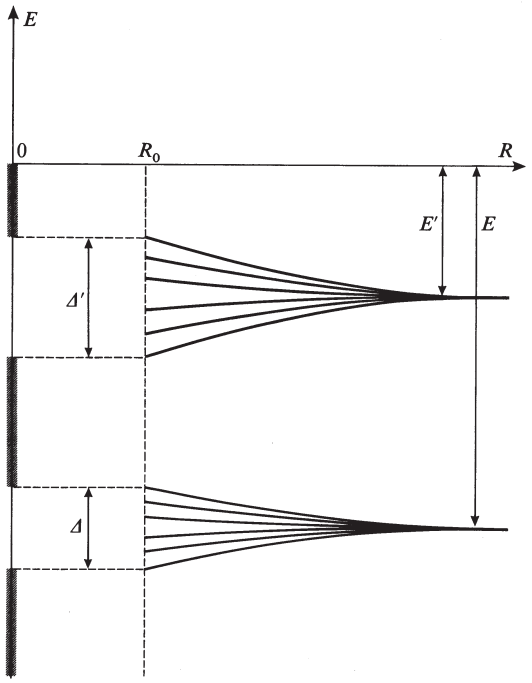

Figure 1.1: **Formation of energy bands.** The energy levels degeneracy of an electron in the potential of N equally distant ions depends on the distance R between them. For large R, the electron can form an atom with any of the N ions. The energy levels E and E' are thus N times degenerate. If R is small, the electron can tunnel from an ion to another so the degeneracy is lifted. Each initial atomic energy level gives rise to an energy interval with N distinct energy levels. If N is very large, we obtain an energy continuum within each interval. The levels E and E' become energy bands of widths Δ and Δ', separated by a bandgap. *From [Cohen-Tanoudji 97]*

.

where $\mathbf{k}$ is the electron wavevector and $u_{\mathbf{k}}(\mathbf{r}+\mathbf{R}) = u_{\mathbf{k}}(r)$ is a periodic function with the same period as the potential U.

Considering a primitive vector $\mathbf{G}$ of the reciprocal lattice ($\mathbf{G}\cdot\mathbf{R} = 1$). Because of *translational symmetry* of the crystal ($\psi_{\mathbf{k}}(\mathbf{r}+\mathbf{R}) = e^{i\mathbf{k}\cdot\mathbf{R}}\psi_{\mathbf{k}}(r)$), two given wavevectors $\mathbf{k}$ and $\mathbf{k}+\mathbf{G}$ correspond to the same Bloch function. One can then restrict to the *first Brillouin zone* of the lattice, delimited by the wavevectors smaller than the primitive reciprocal lattice vectors (if $|\mathbf{k}'| > |\mathbf{G}|$, then $\mathbf{k}'-\mathbf{G}$ is the equivalent solution with a wavevector in the first Brillouin zone).

The resolution of the Schrödinger equation with the Bloch functions is an eigenvalue problem. By using the Born-von Karman periodic boundary conditions, one obtains energy bands $\epsilon_{n,\mathbf{k}}$ separated by bandgaps [Kittel 04]. The electrons fill the energy band according the the Pauli principle. The highest energy state occupied in the ground state is called the Fermi energy ϵ_F.

1.1.3 Metals, insulators and semiconductors

The classification of conductors and insulator materials is one of the major success of the energy band theory.

In an **insulator**, atoms are bound to each-other by valence bonding. Hence, all the bands formed by the mixing of atomic orbitals are all entirely filled or entirely empty. The highest filled energy band is called the valence band, and the lowest empty energy band is called the conduction band. A large energy gap between these bands prevents the transport of electrons for arbitrarily low excitations (heat, voltage, etc.).

In a **metal**, electron orbitals are delocalized over the ionic nuclei of the crystal. Electrons are shared between all the atoms and the bands are therefore partially filled. The energy of the higher electron state coincides with the Fermi energy and it is possible to create electronic excitations of extremely low energy that can propagate throughout the solid.

Insulators with small band gaps are called **semiconductors**. In these materials, the gap can be easily overcome by thermal agitation, by applying a voltage or by optical excitation. When an electron is sent to the conduction band, the lack of one electron in the valence band is represented by a *hole*. The band structure of semiconductors is generally represented in this formalism: the border of the conduction band is represented using the electron energies and the border of the valence band is represented using the hole energies (see Figure 1.2). We distinguish between *direct* and *indirect* gap semiconductors, depending on if a maximum of the valence band corresponds to a minimum of the conduction band or not.

Remark

The Born approximation holds well for metals, where electron are delocalized and can be described by Bloch functions. In the case of insulators and semiconductors, because the electrons remain partially localized around the atoms, the orbital structure is partially preserved and the description is better done using Wannier functions instead of Bloch functions, given by [Schafer 02]

$$w_n(\mathbf{r}-\mathbf{G}) = \frac{1}{\sqrt{N}} \sum_{\mathbf{k}} e^{-i\mathbf{k}\cdot\mathbf{G}} \psi_{n,\mathbf{k}}(\mathbf{r}) \tag{1.3}$$

where n denotes the different bands. This model is called the tight-binding model of electrons, by opposition to the near free electron model. We will see that both models give rise to different types of electronic excitations [Frenkel 31, Wannier 37], tighlty bound in the case of Frenkel excitons (binding energy $\sim$ 1 eV) and weakly bound in the case of (Mott-)Wannier excitons ($\sim$ 0.1 eV).

For the materials we consider, the Mott-Wannier picture is the appropriate one. Band structures of semiconductors are often calculated within the tight-binding model.

1.1.4 Band structure of semiconductors

Direct, indirect gap semiconductors

Figure 1.2 displays the band structures of different semiconductor materials. In Fig 1.2 a, we show the case of Si, which is an indirect gap semiconductor. In Fig 1.2 b to d, we show three different direct gap semiconductors, GaAs, InAs and AlAs. Out of these materials, it is possible create alloys, for instance $In_xGa_{1-x}As$, and the resulting bandgap will then be directly related to x.

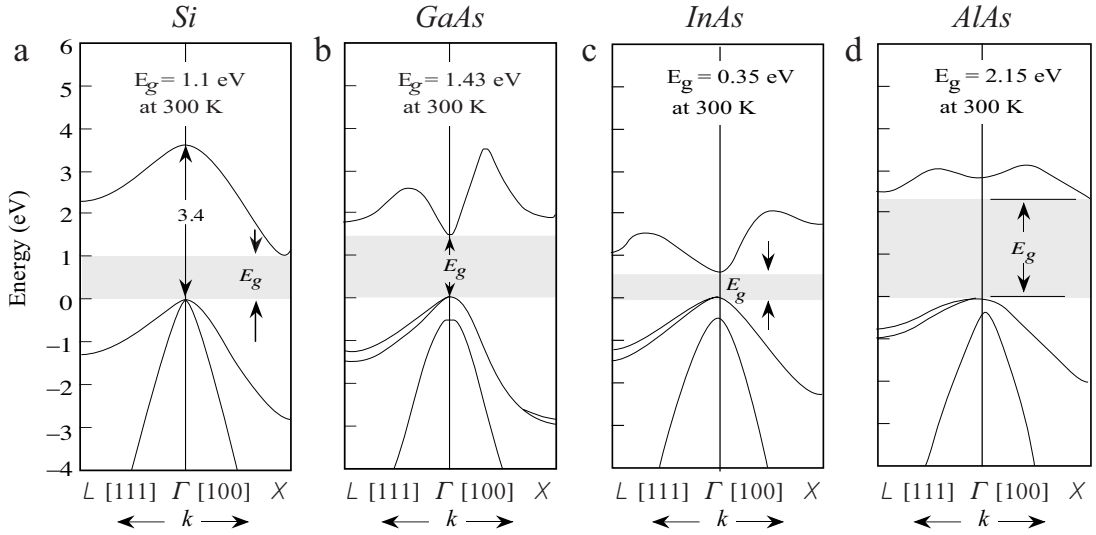

Figure 1.2: **Band structure of semiconductors.** **a** Indirect gap: band structure of Si. **b,c** and **d** Direct gap: band structures of GaAs, InAs and AlAs, respectively. *From [Singh 03].*

Optical excitation

Because of translational symmetry in the crystal, the momentum conservation selection rule applies between a state of the valence band and a state of the conduction band. It is therefore difficult to excite optically states of different wavevectors **k**. For this reason, optical excitations of indirect gap semiconductors are inefficient. Direct gap semiconductors are hence more suitable for optoelectronics applications[1] [Yu 05].

In the following, we only consider the case of direct gap semiconductors. We describe the elementary electronic excitations and their coupling with light.

[1]It is however possible to adjust the band overlap of indirect gap semiconductors by applying a bias voltage. Those materials are very suitable for electronics applications.

1.2 Excitons in semiconductors

We consider the case of direct gap semiconductors. In the vicinity of $\mathbf{k}$=0, the bands are approximated by parabola defined by

$$E(k) = E(k=0) + \frac{\hbar^2 k^2}{2m*_{e,h}} \tag{1.4}$$

where $m^*_{e,h}$ is the effective mass of the electron or the hole, respectively. In general, there exist two bands for the hole (light and heavy holes), with a degeneracy at k=0, but with different effective masses. Their origin is detailed in Section 1.5

If the most obvious excitation of the band structure is the creation of a free electron hole pair, it is however not the elementary electronic excitation. Indeed by taking into account the Coulomb interaction, the motion of the electron and the hole is correlated, resulting in a bound state called *exciton*. As discussed previously, there are two limiting cases. If the electron and the hole are tightly bound, excitons are known as Frenkel excitons [Frenkel 31]. Electron and hole are confined to a single atom in this case. This is usually the case in materials with small dielectric constants, for instance in organic materials. In materials with a strong dielectric constant like semiconductors, the valence electrons screen the Coulomb attraction between the electron and the hole which are thus weakly bound together. These are the Wannier excitons, they are delocalized over the whole crystal [Wannier 37].

Bound electron-hole pairs are thus the elementary electronic excitations in semiconductors. The exciton energy band lays below the bandgap E_{gap}, and is given by

$$E_X(k_X) = E_{\mathrm{gap}} - E_{\mathrm{b}} + \frac{\hbar^2 k_X^2}{2m_X} \tag{1.5}$$

where k_X is the exciton wavevector, m_X its effective mass and E_{b} its binding energy.

The exciton system is described by a Hamiltonian analog to the one of the hydrogen atom. The level structure has the same orbital structure (1s, 2s, 2p, ...). Any hydrogenic system is characterized by a binding energy E^*_I and an effective Bohr radius a^*_0 given by [Savona 99, Cohen-Tanoudji 97]

$$E^*_I = \frac{\mu}{\epsilon^2 m_0} E_I \tag{1.6}$$

$$a^*_0 = \frac{\hbar^2 \epsilon}{\mu e^2} \tag{1.7}$$

where $E_I = m_0\, e^4/2\hbar^2$ is the hydrogen atom ionisation energy (or Rydberg energy), μ the electron-hole reduced mass, ϵ (ϵ_0) the dielectric constant in the medium (vacuum), $e^2 = q^2/4\pi\epsilon_0$ the rescaled electron charge and m_0 the electron mass at rest.

The excitons energy levels $E_{X,n}$ are given by

$$E_{X,n}(k_X) = E_{\mathrm{gap}} - \frac{1}{n^2} E^*_I + \frac{\hbar^2 k_X^2}{2m_X} \tag{1.8}$$

with n=1,2,... an integer.

1.2.1 Light-exciton interactions in bulk semiconductors: polaritons

Light absorption in semiconductors

In the early 1930's, the characterization of semiconductor bandgaps by optical absorption was a well known problem. Theory predicted an absence of light absorption for energies smaller than the gap energy, but experimentally, a series of absorption peaks were observed within the bandgap. These observations probably inspired the works of Frenkel and Wannier, to determine the exact elementary excitations of semiconductors. After the predictions of the existence of excitons, several experiments were devoted to their observation [Apker 50, Apfel 55]. The work of Hopfield was initiated by the need for a clear description of experimental attempts to observe photon absorption by excitons in semiconductors. The existing descriptions of the photon-exciton interaction relied on semiclassical models, which considered photon absorption as a perturbation of excitons. The simplest explanation of absorption was the following: an incoming photon would transform into an exciton, which would re-emit light isotropically.

Hopfield pointed out that, because the ground exciton state is delocalized over all atoms in the crystal, it must satisfy the translation invariance, which implies the conservation of the wavevector. An exciton created by a photon with a given wavevector $\mathbf{k}$ can only emit a photon with an equal wavevector $\mathbf{k}' = \mathbf{k}$. In this description, the energy then oscillates back and forth between the exciton and the photon. The absorption process cannot take place for the exciton. The exciton is in *strong coupling* with the photon.

To treat this problem, Hopfield used the theoretical developments by Fano for the quantum theory of the dielectric constant [Fano 56]. In this approach, the Hamiltonian of the interacting dielectric polarization field and electromagnetic field is written in the second quantification. Photons are the elementary particles of the electromagnetic field, and Hopfield showed that excitons play the role of to the elementary particles of the polarization field[2].

The Hamiltonian has to be diagonalized to find the normal-modes of the system. By this, Hopfield obtained two mixed exciton-photon normal branches, called *polaritons*[3]. In a perfect crystal, polaritons therefore propagate with infinite lifetime: there is no absorption of photons by *free* excitons.

This radically changed the interpretation of experiments. In fact, the absorption observed experimentally was due to the polariton energy losses by scattering with impurities or phonons. If these processes are too important, excitons are scattered to dissipative states before exchanging energy with photons. The absorption experiments actually measured the absorption of exciton states bound to impurities, not of the free excitons [Weisbuch 77a].

[2]Note that Hopfield prealably shows that excitons can be regarded as bosons.
[3]Originally, Hopfield called polaritons the elementary particles of polarization field.

Photoluminescence of polaritons

After the work of Hopfield, several photoluminescence experiments were devoted to the observation of polaritons. The clearest evidences were given by Sell et al. in GaAs [Sell 71], and by Benoît à la Guillaume et al. in CdS. In the latter experiment, the first indications of polariton dispersion could be obtained by angle-resolved photoluminescence under nonresonant excitation [Guillaume 70]. The first resonant polariton photoluminescence experiment was done by Weisbuch et al. [Weisbuch 77a, Weisbuch 77b].

Resonant Brillouin scattering

In 1972, Brenig, Zeyher and Birman showed that, because of polariton inelastic scattering with phonons, a polariton resonantly created with a given $\mathbf{k}$ could emit a phonon and scatter to another polariton branch (resonant Brillouin scattering). Hence, the polariton dispersion can be observed experimentally. The observation of the polariton dispersion by Brillouin scattering was reported by Ulbrich and Weisbuch in GaAs [Ulbrich 77], Winterling and Koteles in CdS [Winterling 77a], and Sermage and Fishman in ZnSe[4] [Sermage 79].

Selection rules in bulk semiconductors.

Optical excitation of excitons in bulk semiconductors must satisfy the following selection rules. Because of translational symmetry in the crystal, the **momentum conservation** selection rule applies. It is not possible to create an exciton of wavevector different from the one of the photon. In addition, the exciton should be regarded as a positronium atom [Yu 05], for which the *ground state* is a $1s$ state. Finally, there is **conservation of the angular momentum**, which is discussed in Section 1.5.

1.2.2 Quantum well excitons

Confinement strongly modifies the energy configuration of excitons [Savona 99]. We will see later that it also has an important impact on the light-matter interactions. Excitons can be confined along one (quantum well), two (quantum wire) or three (quantum dot) dimensions. We discuss the case of quantum well, where excitons are free to move in a plane.

Dingle et al. were the first to report a quantum confinement of excitons in an AlGaAs-GaAs-AlGaAs quantum well [Dingle 74]. They were able to identify up to 4 discrete energy levels for both the heavy-hole and the light-hole excitons. Such confining structures are obtained by inserting a thin layer (typically 10 nm) of a semiconductor between two thicker layers of another semiconductor of larger band gap (see Figure 1.3).

[4] In their work, Sermage and Fishman evidenced polariton branches for both heavy-hole and light-hole excitons.

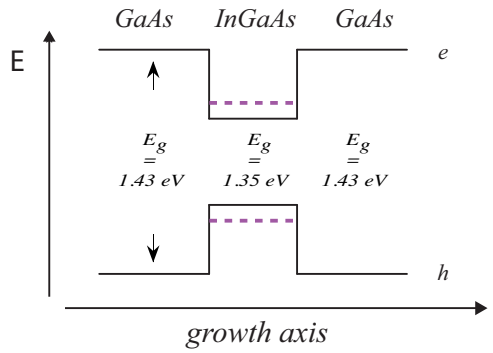

Figure 1.3: **Quantum well.** Schematics of a quantum well. A layer of InGaAs (5%) is inserted between two GaAs layer with larger band gap, resulting in a quantum well for excitons. The dashed purple lines represent the shift of the gap energy because of confinement.

Because of confinement, the gap energy E_{gap} of the quantum well is shifted by $E_0 > 0$. The energies of the quantum well excitons read

$$E_{\text{X,n}}^{\text{2D}} = E_{\text{gap}} + E_0 - \frac{1}{(n+1/2)^2} E_I^* \tag{1.9}$$

and the Bohr radius is $a_0^{*2D} = a_0^*/2$. In an $In_{0.05}Ga_{0.95}As$ quantum well like shown in Fig. 1.3, the exciton binding energy is about 7 meV, which corresponds to a Bohr radius of about 10 nm [Senellart 03].

The most important consequence of confinement is the breaking of translational symmetry in the direction of the confinement [Agranovich 66, Tassone 90]. In a planar (2D) quantum well, excitons with a given in-plane wavevector $\mathbf{k}_\parallel$ are coupled to the *continuum* of photons having the same in-plane wavevector. Contrary to the case of bulk excitons, it is now possible to calculate a radiative lifetime for the free exciton within the Fermi golden rule [Andreani 91]. For this, we introduce a quantity called the oscillator strength f_{osc}, proportional to the probability for an electron in the valence band to create an exciton by absorbing a photon. It is related to the exciton lifetime τ_X by

$$\frac{1}{\tau_X} = \frac{2e^2}{m_0} \frac{f_{\text{osc}}}{S} \tag{1.10}$$

where S is the surface of the crystal.

Selection rules in a semiconductor quantum well

Because of confinement, the momentum selection rule holds only for the in-plane wavevector $\mathbf{k}_\parallel$. Contrarily to the bulk case, a exciton level is now coupled to a continuum of electromagnetic modes. The exciton energy $E_X(\mathbf{k}_\parallel)$ is related to the photon energy $E_\gamma(\mathbf{k}_\parallel)$ by the Fermi golden rule

$$E_X(\mathbf{k}_\parallel) = E_{\text{gap}} + E_0 - E_{\text{b}}^{2D} + \frac{\hbar^2 \mathbf{k}_\parallel^2}{2m_X} = E_\gamma(\mathbf{k}_\parallel) = \hbar \frac{c}{n} \sqrt{\mathbf{k}_\parallel^2 + k_z^2} \tag{1.11}$$

where k_z is the photon wavevector component along the growth axis, c the speed of light and n the refraction index of the quantum well. This relation shows the existence of a maximal in-plane wavevector $\mathbf{k}_{\mathrm{rad}}$, for which $k_z = 0$. It is therefore not possible to excite optically excitons of $\mathbf{k}_{\parallel}$ that exceed $\mathbf{k}_{\mathrm{rad}}$. This defines the *light cone* for exciton-photon interactions. The selection rules on the angular momentum still hold in quantum well and are detailed in Section 1.5. The first exciton level is of s-type, and, because of confinement, its energy separation with the other states is increased. For details on the calculation of exciton energies, the reader can refer to [Senellart 03].

1.3 Semiconductor microcavities

1.3.1 Principle

We now describe light confinement in semiconductor heterostructures. The principle of the light confining structure is the Fabry-Pérot cavity [Saleh 91]. It is achieved in the solid-state by growing interferential mirrors called distributed Bragg reflectors (DBR). By piling pair layers of semiconductors with different refraction indices n_1 and n_2 and different thicknesses L_1 and L_2, we force multiple reflections of the incident electromagnetic field. A proper adjustment of the index contrast and layer thicknesses can lead to interferences that are constructive in reflection and destructive in transmission.

1.3.2 Distributed bragg reflectors

The idea is to grow layers such that $L_1n_1=L_2n_2=\lambda_0$. A transfer matrix calculation of the reflectivity of a DBR structure containing 22 pairs of GaAs/AlAs layers is shown in Figure 1.4. The top panel displays the refractive index profile and the bottom panel displays the reflectivity spectrum. The presence of an energy range (stop band) for which light is totally reflected (reflectivity>99.99 %) is characteristic of DBRs. The width of the stop band is proportional to the ratio between the refraction indices. The central energy corresponds to the reference wavelength λ_0.

1.3.3 Semiconductor microcavity

To obtain a Fabry-Pérot structure, we grow two DBRs separated by a spacer layer of optical length $l = m\frac{\lambda_c}{2}$, where λ_c is the resonance wavelength of the confined electromagnetic mode. Figure 1.5 displays the transfer matrix calculation of a λ_c-cavity structure comparable to the one used for our microcavity sample. The structure contains a 22-pair and a 21-pair DBR. If λ_c belongs to the stop band, a dip appears at an energy E_c in the reflectivity spectrum. An electromagnetic mode is allowed inside the cavity. This mode has a given linewidth γ_c, which characterizes the photon lifetime inside the cavity and determines the quality factor

$$Q = \frac{E_c}{\gamma_c}$$

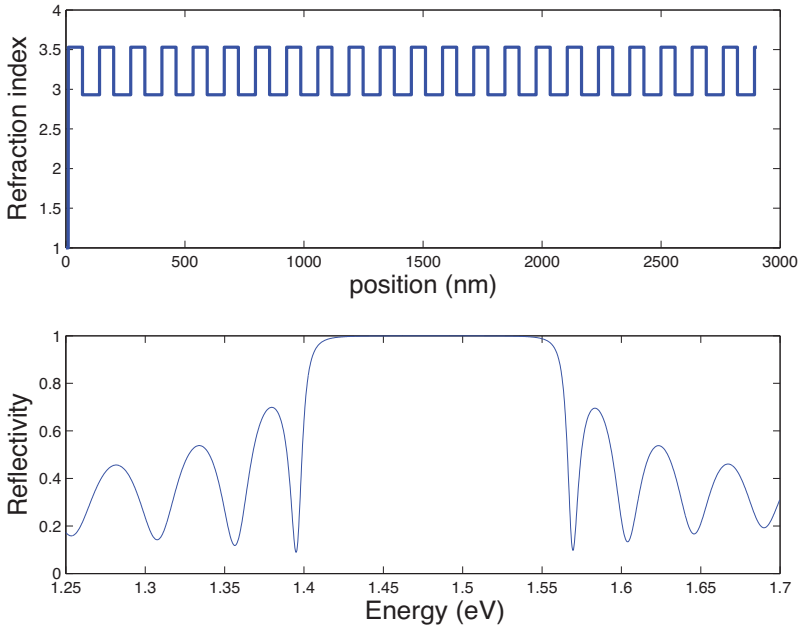

Figure 1.4: **Distributed Bragg reflector structure.** Transfer matrix calculation of the reflectivity of a GaAs/AlAs DBR structure. The simulation considers 22 pairs layers with the following parameters: $n_{AlAs} = 2.92$, $n_{GaAs} = 3.53$, $L_{GaAs} = 59.4$ nm and $L_{AlAs} = 71.6$ nm. The stop band is 100 nm wide and centered at $\lambda_0 = 835$ nm. *From [El Daif 07]*

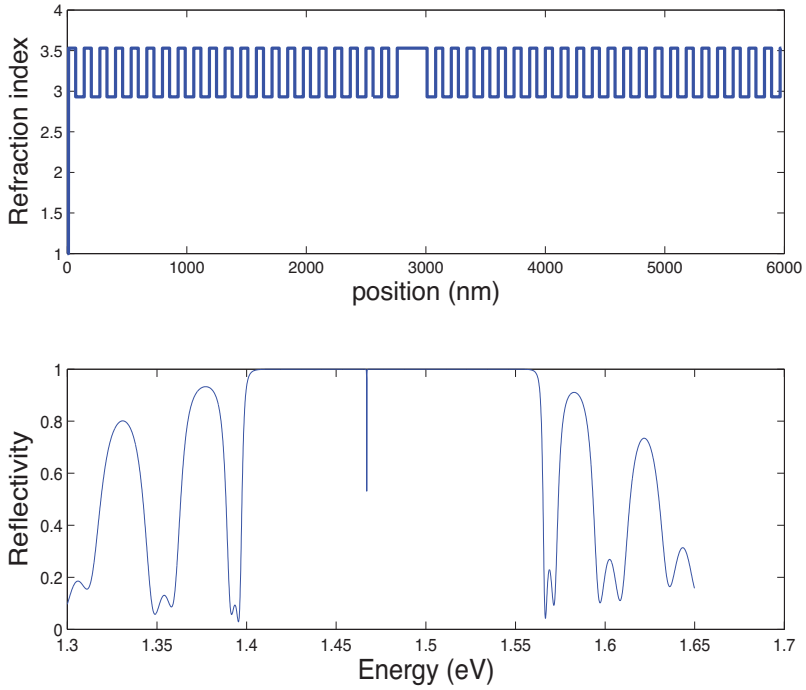

Figure 1.5: **Semiconductor Fabry-Pérot structure.** Transfer matrix calculation of the reflectivity of an GaAs/AlAs λ-cavity structure. *From [El Daif 07]*

In the case of a λ-cavity, the intensity of the field in this mode is maximal in the middle of the spacer. The secondary modes located around the stop band are called leaky modes (or Bragg modes). Their spectral width is much larger than the main cavity mode and their intensity maximum is in the substrate. They therefore contribute to important losses in case of nonresonant excitation.

1.4 Microcavity polaritons

We now come to the proper semiconductor microcavity structure. Consider a semiconductor quantum well inserted in the middle of the cavity spacer described above. Provided that the cavity-exciton detuning $\delta = E_C - E_X$ remains smaller or of the order the exciton-photon interaction energy $\hbar\Omega_R$, photons can interact with excitons. We describe two interaction regimes. In the *weak coupling* regime excitons can be created by light absorption and recombine radiatively. In the *strong coupling* regime, excitons or photons are not eigenmodes of the microcavity anymore. Instead, two polariton modes appear as half-light, half-matter quasiparticles.

1.4.1 Strong-coupling model for a microcavity

The study of light-matter interactions with atoms in a cavity lead Jaynes and Cummings to predict the existence of normal-mode splitting between the cavity mode and the atoms, in the case of strong interactions between them [Jaynes 62]. As Hopfield did, but in a different picture, Jaynes and Cummings compared semiclassical and quantum mechanics approches to study the coupling between atoms and a cavity mode [Jaynes 62]. They showed the existence of two interaction regimes. A weak-coupling regime, that could be treated by a perturbation theory with application of the Fermi golden rule. A strong-coupling regime, with the appearance of normal modes as atom-field quasiparticles. This work gave birth to the cavity electrodynamics research field.

The first clear evidence of normal-mode splitting was given at the end of the 1980's by Raizen, in the group of J. Kimble [Raizen 89]. In their experiment, they could plot a clear anticrossing behavior of the mode frequencies as a function of the cavity detuning. As we will see, this behavior is characteristic of normal-mode splitting.

A hamiltonian analog to the Jaynes-Cumming Hamiltonian can be written to describe exciton-photon interaction in a microcavity. Excitons are regarded as bosons and we assume a density low enough to avoid any contribution from their fermionic nature [Senellart 03]. We define $b^\dagger_{\mathbf{k}}$ ($b_{\mathbf{k}}$) the creation (annihilation) operator of an exciton with in-plane wavevector $\mathbf{k}_\parallel = \mathbf{k}$. We also define $a^\dagger_{\mathbf{k}}$ ($a_{\mathbf{k}}$) as the creation (annihilation) operator of a photon with in-plane wavevector $\mathbf{k}$. The interaction Hamiltonian is given by

$$H = \sum_{\mathbf{k}} E_X(\mathbf{k}) b^\dagger_{\mathbf{k}} b_{\mathbf{k}} + E_C(\mathbf{k}) a^\dagger_{\mathbf{k}} a_{\mathbf{k}} + \frac{\Omega_R}{2}(b^\dagger_{\mathbf{k}} a_{\mathbf{k}} + a^\dagger_{\mathbf{k}} b_{\mathbf{k}}) \tag{1.12}$$

where Ω_R is the light-matter coupling energy[5]. It is related to the exciton oscillator strength f_{osc} by [Senellart 03]

$$\Omega_R = \sqrt{\frac{f_{osc}}{S}} \tag{1.13}$$

where S is the normalization surface, usually the spatial extension of the exciton density.
When diagonalizing this Hamiltonian, one finds the eigenenergies

$$E_{LP}(\mathbf{k}) = E_X + \frac{1}{2}(\delta_\mathbf{k} - \sqrt{\delta_\mathbf{k}^2 + \Omega_R^2}) \tag{1.14}$$

$$E_{UP}(\mathbf{k}) = E_X + \frac{1}{2}(\delta_\mathbf{k} + \sqrt{\delta_\mathbf{k}^2 + \Omega_R^2}) \tag{1.15}$$

where $\delta_\mathbf{k} = E_C(\mathbf{k}) - E_X(\mathbf{k})$ is the cavity-exciton detuning. LP and UP denote the two energy branches called lower and upper polariton, respectively. The associated annihilation operators are $p_\mathbf{k}$ for a lower polariton and $q_\mathbf{k}$ for an upper polariton of in-plane wavevector $\mathbf{k}$. The diagonal Hamiltonian reads

$$H = \sum_\mathbf{k} E_{LP}(\mathbf{k}) p_\mathbf{k}^\dagger p_\mathbf{k} + E_{UP}(\mathbf{k}) q_\mathbf{k}^\dagger q_\mathbf{k} \tag{1.16}$$

in the polariton basis $\{p_\mathbf{k}, q_\mathbf{k}\}$ is defined by

$$\begin{pmatrix} p_\mathbf{k} \\ q_\mathbf{k} \end{pmatrix} = \begin{pmatrix} X_\mathbf{k} & -C_\mathbf{k} \\ C_\mathbf{k} & X_\mathbf{k} \end{pmatrix} \cdot \begin{pmatrix} b_\mathbf{k} \\ a_\mathbf{k} \end{pmatrix} \tag{1.17}$$

where $X_\mathbf{k}$ and $C_\mathbf{k}$ are the excitonic and photonic Hopfield factors defined by

$$X_\mathbf{k}^2 = \frac{\delta_\mathbf{k} + \sqrt{\delta_\mathbf{k}^2 + \Omega_R^2}}{2\sqrt{\delta_\mathbf{k}^2 + \Omega_R^2}} \tag{1.18}$$

$$C_\mathbf{k}^2 = -\frac{\delta_\mathbf{k} - \sqrt{\delta_\mathbf{k}^2 + \Omega_R^2}}{2\sqrt{\delta_\mathbf{k}^2 + \Omega_R^2}} \tag{1.19}$$

with the unitary condition $X_\mathbf{k}^2 + C_\mathbf{k}^2 = 1$. Therefore, the quantity $X_\mathbf{k}^2$ reflects the *excitonic content* of the polariton in the mode $\mathbf{k}$ and $C_\mathbf{k}^2$ reflects its *photonic content*.

1.4.2 Anticrossing

The simplest signature of the strong-coupling regime is certainly the anticrossing behavior observed while varying the detuning $\delta_\mathbf{k}$. Figure 1.6 displays the energies of the coupled and uncoupled modes for $\mathbf{k} = 0$ as a function of the detuning.

The anticrossing behavior is also visible in the polariton dispersions. In Figure 1.7, we see plot dispersions at negative, zero and positive detuning. We see that, at negative detuning, the polariton dispersions do not cross, although the cavity dispersion intersects the exciton dispersion. The dominant nature (light or matter) of

[5]Or vacuum Rabi splitting

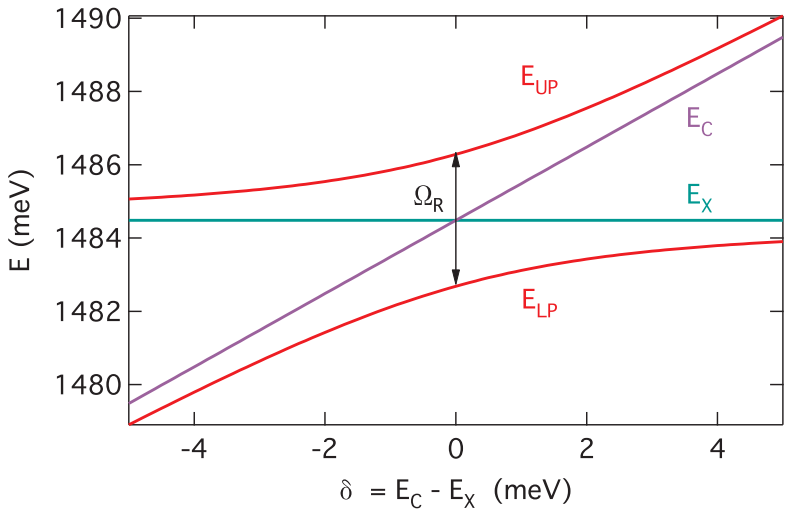

Figure 1.6: **Anticrossing.** The energies of the upper (E_{UP}) and lower (E_{LP}) polaritons are calculated using Eqs. (1.14) and (1.15) for a constant exciton energy $E_X = 1484.5$ meV and a varying cavity energy E_C, with a Rabi splitting $\Omega_R = 3.5$ meV. The anticrossing behavior is characteristic of the strong-coupling regime.

a polariton branch can be qualitatively evaluated by comparing its distance to the uncoupled mode branches. For instance, at negative detuning (Fig. 1.7 a), the lower polariton states around $\mathbf{k} = 0$ are *closer* to the bare cavity dispersion than to the exciton dispersion. These polaritons have a dominant photonic content $C^2 > X^2$. The contrary picture holds at positive detuning (Fig. 1.7 c). At zero detuning $\delta_{\mathbf{k}} = 0$ (Fig. 1.7 b), $\mathbf{k} = 0$ polaritons are exactly half-light, half-matter.

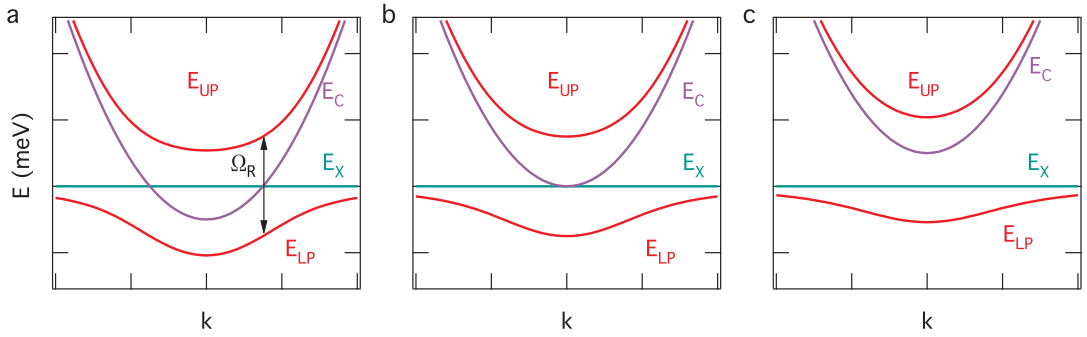

Figure 1.7: **Polariton dispersions.** Exemples at **a** negative, **b** zero and **c** positive detuning. The polariton dispersion can be approximated by a parabola in the vicinity of $\mathbf{k} = \mathbf{0}$. At larger wavevectors, because of the anticrossing, the dispersion of the lower polariton presents an inflection angle.

1.4.3 Strong-coupling condition

Both excitons and photons have finite lifetimes: excitons are in a $1s$ state and recombine at the rate γ_X, photons escape through the cavity mirrors at the rate γ_C. These quantities are introduced in the Hamiltonian as imaginary components of the respective exciton and photon energies, writing

$$E_X{}' = E_X - i\gamma_X$$

and

$$E_C{}' = E_C - i\gamma_C$$

Inserted in Eqs. (1.14) and (1.15), this results into an effective correction of the coupling strength Ω_R introduced in Eq. (1.16) [Richard 04]. At $\mathbf{k} = 0$ and zero detuning, Ω_R becomes

$$\Omega_R{}' = \sqrt{\Omega_R^2 - (\gamma_C - \gamma_X)^2} \tag{1.20}$$

yielding the following condition for the strong-coupling regime

$$\Omega_R > \gamma_X, \gamma_C \tag{1.21}$$

This relation can be intuitively understood as follows. Brought close to resonance, excitons and photons exchange energy at a rate related to Ω_R. During their lifetime, excitons and photons should experience several energy exchanges for strong coupling to occur. The exchange rate is therefore larger than both decay rates in this regime. The strong-coupling condition can be formulated as $\Omega_R' > \gamma_{LP}, \gamma_{UP}$, showing that experimentally, the linewidth of the polariton resonances should remain smaller than their energy separation at zero detuning to observe strong coupling.

1.4.4 Polariton momentum

Because of the selection rule on the in-plane momentum, the polariton momentum is equal to the photon momentum outside the microcavity. A specific polariton state on the dispersion can be excited using a non-zero incident angle for the electromagnetic field. The following relations link the incident angle (θ_x, θ_y) of a laser beam of wavelength λ_L to the polariton in-plane momentum $\mathbf{k} = (k_x, k_y)$:

$$\begin{aligned} k_L \sin\theta_x &= k_x \\ k_L \sin\theta_y &= k_y \\ k_L = \frac{2\pi}{\lambda_L} &= \frac{E_L}{\hbar c} \end{aligned} \tag{1.22}$$

A photon detected at a given angle and a given energy contains all the energy and momentum information[6] about the polariton from which it has been emitted.

[6] In fact *all* the information: position, phase, spin ...

1.5 Polariton spin

The polariton spin is the result of the angular momentum conservation. To understand this, it is important to recall the chemical description of atomic bonds in these materials. For complementary information, the reader can refer to [Karr 01, Hermann 85].

1.5.1 Hybridization in covalent bonding

In most semiconductors, the external electron levels are s- or p-type orbitals. For instance, we give the outermost orbitals of different types of semiconductors. The electrons participating to the covalent bonds are easily identified by the octet rule:

IV Semiconductors
C 1s2 2s2 2p2
Si [Ne] 3s2 3p2
Ge [Ar] 3d10 4s2 4p2

II Semiconductors
Zn [Ar] 3d10 4s2
Cd [Kr] 4d10 5s2

VI Semiconductors
O 1s2 2s2 2p4
Te [Kr] 4d10 5s2 5p4

III Semiconductors
Al [Ne] 3s2 3p1
Ga [Ar] 3d10 4s2 4p1
In [Kr] 4d10 5s2 5p1

V Semiconductors
N 1s2 2s2 2p3
P [Ne] 3s2 3p3
As [Ar] 3d10 4s2 4p3

The covalent bonds (cf. Section 1.1.4) result in a mixing of s- and p-type orbitals, resulting in hybrid orbitals sp^3 that assemble in a tetrahedral structure of orbital momentum. In the above cases (and in general), the lowest energy empty band i.e. the conduction band corresponds to an s orbital.

An optical excitation would then generate an electron in an s orbital, leaving a hole in a p orbital of the valence band.

1.5.2 Total angular momentum of excitons

The total angular momentum J is given by the sum of the orbital momentum J_O and the spin S. For an electron in the conduction band, the s orbital corresponds to an orbital momentum $J^s_O = 0$, and the spin S$= 1/2$. The *total angular momentum* is thus $J^s = 1/2$. For a hole in a p orbital, $J^s_O = 1$, S$= 1/2$ and $J^p = 1/2$ or $3/2$. Because of spin-orbit interaction, the $J^p = 1/2$ band (split-off band) has a higher energy than the $J^p = 3/2$ band and does not participate to the exciton formation.

On the other hand, the projections of J along the growth axis z give $J^s_z = \pm 1/2$ for the electrons and $J^p_z = \pm 3/2, \pm 1/2$ for the holes (heavy and light, respectively). There are two branches for the holes, with different dispersions, hence different

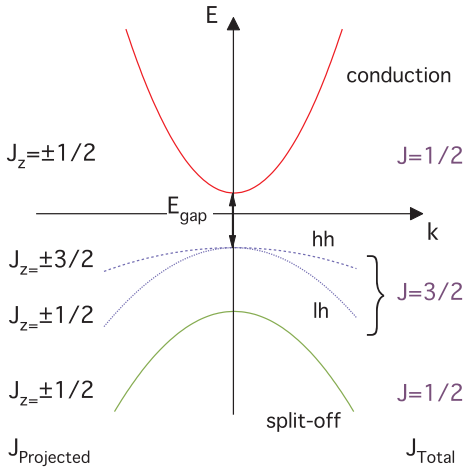

Figure 1.8: **Angular momentum.** The different bands correspond to well-defined values of the total angular momentum J. The corresponding projections J_z on the growth axis are responsible for the two-fold structure (hh,lh) of the J=3/2 hole band.

effective masses. Light holes and heavy holes are degenerate at k=0 in bulk semiconductors. In quantum wells, confinement lifts the degeneracy, leaving the heavy hole band at lower energy. Since excitons are electron-hole bound states, the projection of their total angular momentum J^X along the growth axis z takes different values whether the electron is coupled to a heavy hole (hh) or to a light hole (lh). In case of heavy hole exciton, $J_z^{hh} = \pm 2, \pm 1$. In case of light hole excitons, $J_z^{lh} = \pm 1, 0$. In the following, we only consider the heavy hole excitons.

1.5.3 Coupling with light

Dark and bright exciton states

Because of angular momentum conservation (cf. selection rules in Section 1.1.4), the absorption of a single photon creates an electron-hole pair with spins $\pm 1/2$ for the electron and $\mp 3/2$ for the heavy-hole ($\pm 1/2$ in the case of a light-hole), respectively.

$J_z = \pm 2$ excitons cannot be created by absorption of a single photon and cannot emit photons either. They are therefore called "dark states". The states $J_z = \pm 1$ are excited by right of left circularly polarized photon ($\sigma+$, $\sigma-$). In-plane projections of the angular momentum are excited with linearly polarized photons. As they couple to light, $J_z = \pm 1$ states are called "bright" exciton states.

The picture is valid in the strong coupling regime, so there are similar relations between the photon polarization and the polariton angular momentum. A $\sigma+$ photon creates a $|+1\rangle$ polariton and a $\sigma-$ photon creates a $|-1\rangle$ polariton. A linearly polarized photon creates a polariton in the superposition state $\frac{1}{\sqrt{2}}(|+1\rangle + e^{2i\varphi}|-1\rangle)$, which corresponds to a polariton with a spin oriented in the plane of the quantum well.

Polariton pseudospin

Since the $|\pm 2\rangle$ states are not interacting with light, the polariton angular momentum is a 2-level system that can be described as a 1/2 pseudospin. The 2×2 spin-density matrix of a polariton of wavevector $\mathbf{k}$ is given by [Maialle 93, Shelykh 04]

$$\rho_{\mathbf{k}} = N_{\mathbf{k}} \left[\frac{\mathbb{I}}{2} + \mathbf{S}_{\mathbf{k}} \cdot \sigma_{\mathbf{k}} \right] \tag{1.23}$$

where $N_{\mathbf{k}}$ is the number of polaritons of wavevector $\mathbf{k}$, $\mathbb{I}$ is the 2×2 identity matrix, $\mathbf{S}_{\mathbf{k}}$ is the mean pseudospin vector and $\sigma_{\mathbf{k}}$ are the Pauli matrices. The polariton angular momentum states $|+1\rangle$ and $|-1\rangle$ are represented by the pseudospin states $|\uparrow\rangle$ and $|\downarrow\rangle$, respectively. $\mathbf{S}_{\mathbf{k}}$ can be represented in the Bloch sphere and is in one-to-one correspondence with the Stokes vector of the light polarization in the Poincaré sphere.

This point is fundamental: it means that it is possible to create coherently polaritons with a given spin orientation using polarized excitation. In addition, all the information on the polariton spin orientation[7] is contained in the emitted light and is retrieved by using a polarization resolved analysis. In the following, we will use the term polariton spin.

1.5.4 Poincaré sphere and Bloch sphere

The polariton pseudospin is in one-to-one correspondence with the polarization of the emitted photon.

Light polarization vector in the Poincaré sphere

We define the polarization degrees ρ_{C}, ρ_{L} and ρ_{D} of the emitted light in the circular ($\sigma+$,$\sigma-$), linear (H,V) and diagonal (D+,D-) bases, respectively, as

$$\rho_{\mathrm{C}} = \frac{I_{\sigma+} - I_{\sigma-}}{I_{\sigma+} + I_{\sigma-}},\ \rho_{\mathrm{L}} = \frac{I_H - I_V}{I_H + I_V} \text{ and } \rho_{\mathrm{D}} = \frac{I_{D+} - I_{D-}}{I_{D+} + I_{D-}} \tag{1.24}$$

They correspond to the three Stokes parameters that fully characterize the emission light polarization vector $\mathbf{P}$ in the Poincaré sphere (see Figure 1.9). The norm

$$|\mathbf{P}| = \sqrt{\rho_{\mathrm{C}}^2 + \rho_{\mathrm{L}}^2 + \rho_{\mathrm{D}}^2} \leq 1$$

give the overall degree of polarized light. When $|\mathbf{P}| = 0$, the light is unpolarized.

Spin state in the Bloch sphere

In the spin-up $|\uparrow\rangle$ spin-down $|\downarrow\rangle$ basis, a *pure* spin state $|\psi\rangle$ is written as

$$|\psi\rangle = \cos\theta |\uparrow\rangle + e^{i\varphi} \sin\theta |\downarrow\rangle \tag{1.25}$$

The ensemble of possible spin states determines the Bloch sphere. It is related to the Poincaré sphere as follows:

[7] In fact, *all* the information on the polariton energy, momentum, phase and angular momentum

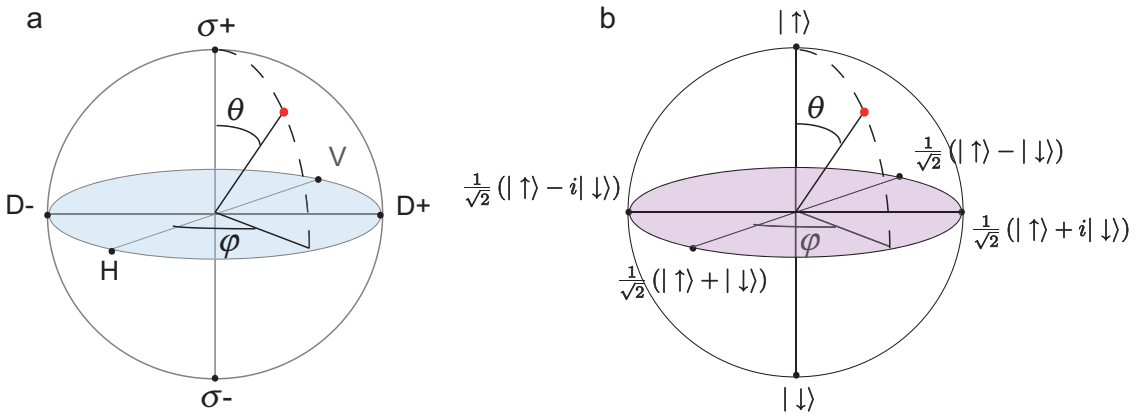

Figure 1.9: **a Poincaré sphere.** The right and left circularly polarized states are located at the north and south poles of the sphere, respectively. Linearly polarized states are on the equator. The other points of the sphere correspond to elliptically polarized states. **b Bloch sphere.** The $|\uparrow\rangle$ and $|\downarrow\rangle$ states are represented at the poles of the sphere. The states of the equator correspond to states with spin oriented in the (x,y) plane.

- The (x, y, z) coordinates of the pseudospin vector $\mathbf{S_k}$ of Eq. (1.23) are

$$\mathbf{S_k} = \begin{pmatrix} \sin 2\theta \cos\varphi \\ \sin 2\theta \sin\varphi \\ \cos 2\theta \end{pmatrix} = \begin{pmatrix} \rho_{\mathrm{L}} \\ \rho_{\mathrm{D}} \\ \rho_{\mathrm{C}} \end{pmatrix} \tag{1.26}$$

- The azimuthal angle φ on the sphere corresponds to the phase difference between spin-up and spin-down polaritons. It depends on the linear and diagonal polarization degrees:

$$\varphi = \arctan \frac{\rho_{\mathrm{D}}}{\rho_{\mathrm{L}}} \tag{1.27}$$

- The inclination angle θ is related to the ellipticity of light and is given by

$$\theta = \arccos \frac{\rho_{\mathrm{C}}}{\sqrt{\rho_{\mathrm{D}}^2 + \rho_{\mathrm{L}}^2}} \tag{1.28}$$

- If the spin state is not a pure state, then the polarization degree $|\mathbf{P}|$ is smaller than 1 and corresponds to the degree of spin coherence.

Chapter 2

Lateral Confinement

Microcavity samples are usually grown by molecular beam epitaxy (MBE) or by metal-organic chemical vapor deposition (MOCVD). With these techniques, materials are deposited atomic layer by atomic layer on a planar substrate. Polaritons are free to move in the plane of the quantum wells, with a well-defined dispersion as shown previously. The confinement of polaritons in reduced dimensionality systems (1D, 0D), causes a modification of polariton properties (dispersion, linewidth) and provide better control of polariton interactions. On the route to Bose-Einstein condensation, trapping appeared as a crucial issue. Several techniques were developed to trap polaritons. For instance, one can act on the excitonic part by etching micropillars from an initially planar structure. It is also possible to act on the photonic part by engineering local variations of the cavity spacer, as we do.

In Section 2.1, we describe our trapping technique and in Section 2.2, we present the optical characterization of confined polaritons.

2.1 The various confining structures

Spatially confined polaritons can be produced in various kinds of structures. Let us briefly review some of them.

2.1.1 Confinement of the excitonic part

Mechanical stress By applying a stress on an exciton quantum well it is possible to create a local redshift of the exciton energy [Negoita 99]. This results in a harmonic potential for excitons. In a microcavity samples, the stress reduces the exciton energy but leaves the photon energy unchanged [Balili 06]. Bose-Einstein condensation has been reported in such traps [Balili 07]. In the case of stress traps, the harmonic potential extends over 100 μm. It permits a smooth localization of 2D polaritons without altering the dispersion.

Quantum dots Strong coupling of single quantum dots embedded in microcavities constitute the smallest confined polariton system, with dots of few tens nanometers diameters [Reithmaier 04]. Coupling quantum dots with cavities was also achieved with photonic crystal cavities [Yoshie 04, Hennessy 07]. These systems are very

suitable for cavity QED and quantum information. Since only one or two polaritons at a time can exist in a dot, phenomena like Bose-Einstein condensation cannot be observed.

2.1.2 Confinement of the photonic part

Micropillars One of the first design of pillar micro-resonators was proposed by Gérard and has been adopted by different groups. In pillar microcavities, the whole microcavity is etched after growth [Gérard 96]. In this case, only confined polariton states exist. Parametric scattering and polariton lasing have been reported in such structures [Bloch 98a, Dasbach 01, Bajoni 08b]. This technique was also used to etch polariton wires [Dasbach 02] and observe exotic parametric processes. The size of micropillars goes from 0.5 to a few hundred micrometers.

Polariton mesas The idea of trapping polaritons through their light nature was developed by T. Guillet, M. Saba and F. Morier-Genoud. It consists in playing with the cavity length i.e. with the energy of the photon. As illustrated in Figure 2.1, a longer cavity length means a smaller photon energy, hence, a smaller polariton energy (see Eq. (1.14) and (1.15)).

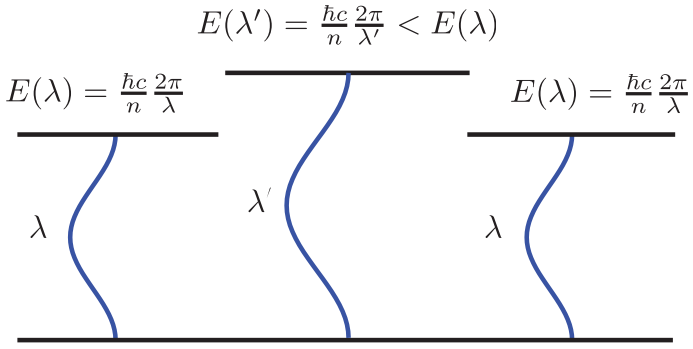

Figure 2.1: **Polariton trapping via the photonic part: principle.** Schematics of a λ-cavity spacer. The spacer (horizontal lines) is larger in the middle of the structure, yielding a larger wavelength $\lambda' > \lambda$, thus a lower energy for the cavity mode. In the strong coupling regime, resulting polaritons are trapped through their photonic part in the central region.

The sample we use for our experiments was engineered by O. El Daif and F. Morier-Genoud [Daif 06]. It is labeled "1485". The sample contains cylindrical mesas of 3, 9 and 20 μm diameter. It also contains other geometrical shapes, like rings, stars and large (300 μm) squares.

The possibilities are in fact unlimited. As presented in El Daif's thesis, the next generation of samples will contain mesas with a much richer variety of shapes and sizes [El Daif 07].

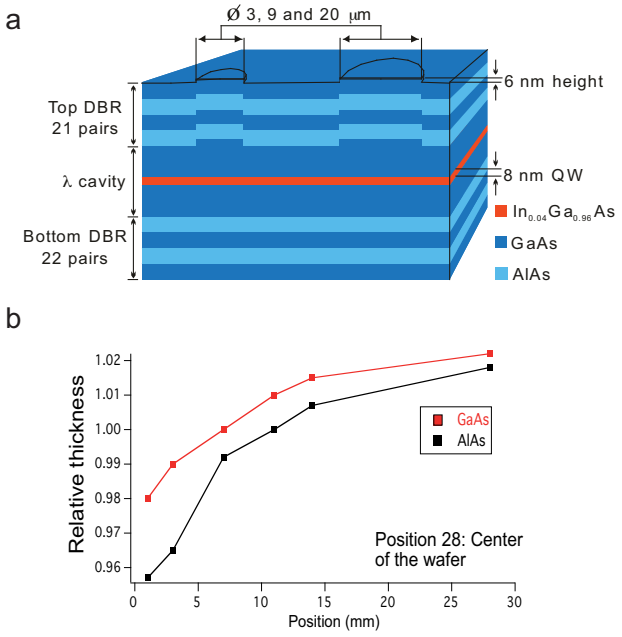

Figure 2.2: **Mesa sample. a** The microcavity consists of two GaAs/AlAs DBRs with an embedded InGaAs quantum well. After the growth of the bottom mirror and the λ-cavity, the sample is taken out of the MBE to fabricate the mesa structures by chemical etching. The sample is then re-introduced in the MBE for growth of the top DBR. Mesa structures of 3, 9 and 19 μm. **b** Characterization of the thickness gradient (wedge) of AlAs and GaAs along the position on the sample. The relative thickness with respect to the one corresponding to a cavity resonance equal to the exciton energy.

2.1.3 Sample fabrication

The "1485" sample is a MBE grown III-V microcavity. The mirrors are made of GaAs/AlAs pair layers and the quantum well is made of $In_{0.04}Ga_{0.96}As$. The whole structure is grown on a GaAs substrate. Because the exciton energy is smaller in $In_{0.05}Ga_{0.95}As$, it is possible to excite the sample through the substrate, as we will show later. The sample is grown in three steps [El Daif 07]:

1 A 22 GaAs/AlAs pairs DBR is first grown on the GaAs substrate. Then the first half (114.5 nm) of the GaAs spacer, the 8 nm InGaAs quantum well and the second half of the spacer are deposited. Then, the cavity extension is grown on top of the spacer. In consists of a complex structure of GaAs layers embedded in AlAs etch stops, dedicated to selective chemical etching.

2 The growth is interrupted in order to fabricate the mesas. The sample is taken out of the MBE, and a photoresist mask of the mesa patterns is deposited by photolithography. The mesa structures are then created by selective chemical etching. The photoresist is then removed and the sample cleaned for regrowth.

3 The crucial step of this procedure is the last one. The sample is re-introduced in the MBE, which contains of a special chamber for in-situ hydrogen plasma

cleaning. The sample surface is then clean enough for the growth of a second DBR.

Mesas of 6 nm height were fabricated using this procedure. The sample is grown with a wedge of 4 %, so that the cavity resonance changes with the position of the sample. Since the exciton energy is only weakly modified by the thickness gradient, it allows to tune the cavity detuning continuously. The cavity resonance shifts of more than 50 meV over the whole sample, while the quantum well exciton energy (1485 meV) changes of less than 3 meV. Mesas of 3, 9 and 20 μm were placed all-along the wedge, resulting in traps of varying relative depths (see Fig. 2.2).

An exciton linewidth of 500 μeV and a cavity mode linewidth of 220 μeV (corresponding to a quality factor of $Q = 7000$) were measured in the planar regions of the sample. In the mesa structures, the cavity mode is about 70 μeV ($Q \simeq 21000$) [El Daif 07].

An atomic force microscope characterization of the sample after regrowth of the top mirror shows that the mesa pattern and height are still visible on top of the entire structure (Fig. 2.3). This shows the very high quality achieved for this sample. The slight ellipticity of the mesa comes from a small asymmetry of the photolithographic mask [Daif 06].

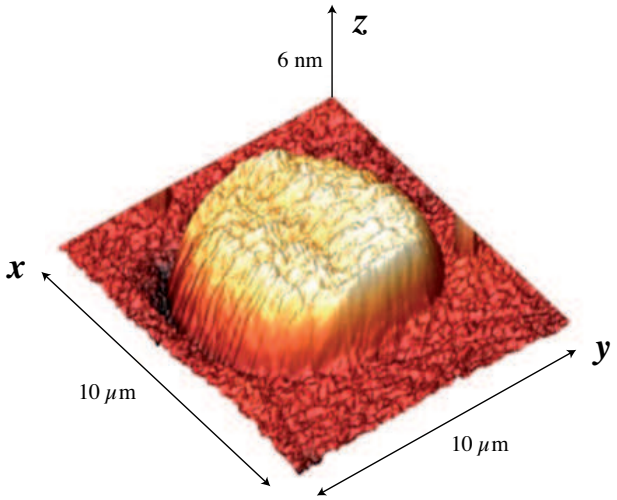

Figure 2.3: **AFM image of a 9 μm mesa.** Top of the sample. The 6 nm step of the etched mesa is still visible after re-growth of the top DBR. The step is sharper along the x-axis than along the y-axis because of the anisotropic mobility of the atoms during the MBE growth. The slight ellipticity originates from the photolithographic mask.

2.2 Spectroscopy

The sample is characterized optically by nonresonant photoluminescence experiments.

2.2.1 Setup

The experimental setup is shown is Figure 2.4. We keep the sample at 4 K in a Helium flow cryostat. We work in the transmission configuration. The continuous wave (cw)-excitation is focused onto a 20 μm spot on the back of the sample (substrate side), using a photo-objective or a lens of 5 cm focal length. The excitation energy is nonresonant with the polariton states. To maximize the coupling to the cavity, the laser is resonant with the first Bragg mode at higher energy than the stop-band (see Section 1.3).

The emission is collected with a large numeric aperture microscope objective in order to collect the entire far-field emission. A low-pass filter is used to select wavelengths longer than 815 nm in order to avoid being disturbed by the laser while doing direct imaging. Spectral information is obtained by sending the emission to an imaging spectrometer. There are two positions for the lens used to focus the light on the slits of the spectrometer depending on if we want to image the near-field or the far-field on the slits. For our experiments, we worked with a 1 m spectrometer, with a 600 grooves per millimeter grating. This granted us with a spectral resolution of $\sim$25 μeV. The output of the spectrometer is sent to a charge coupled device (CCD) to record the spectra.

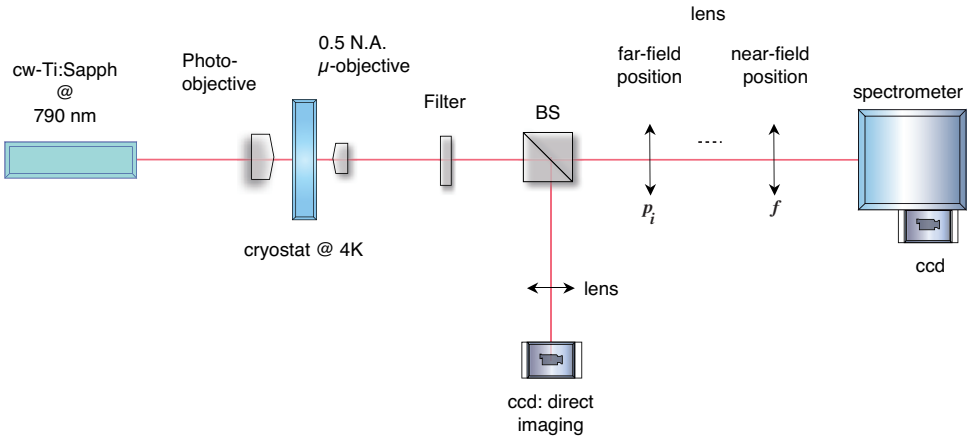

Figure 2.4: **Experimental setup.** The nonresonant laser is focused on the sample kept at 4 K in a helium-flow cryostat. The photoluminescence is sent either on a CCD for direct imaging, either to a monochromator for spectral analysis. In both cases, the position of the imaging lens can be adjusted to measure either the near-field or the far-field emission.

2.2.2 Real space imaging

The lens is placed at the focal distance f of the slits of the spectrometer, in order to image the real space (near-field) and obtain (E, x) spatially resolved spectra.

The spectra acquired close to zero detuning for the three sizes of mesas are displayed in Figure 2.5. The confined upper and lower polaritons (UP0D and LP0D) clearly appear within the dimension of the mesas, at lower energy than the corresponding planar upper and lower polaritons (UP2D and LP2D). The number of

confined states and the spacing between them directly depend on the mesa diameter. The planar polariton density is negligible in the region of the mesa.

2.2.3 Reciprocal space imaging

To obtain the polariton dispersions, one needs to image the momentum space (far-field) on the slits of the spectrometer. The lens position is thus changed to a distance p_i, such that

$$\frac{1}{f} = \frac{1}{p_i} + \frac{1}{d - p_i}$$

where d is the distance between the Fourier plane of the microscope objective and the slits of the spectrometer.

In Figure 2.6, we show polariton dispersions corresponding to the spatially resolved spectra of Fig. 2.5. The angle of emission is directly related to the polariton momentum as shown by Eq. (1.22). The LP2D being at very positive detuning (98 % exciton), its dispersion is flat and approximately at the energy of the exciton. The confined states (40 % exciton for the ground state) are extended along the momentum direction. We will see in the next chapter that this causes a weakening of the momentum selection rule.

Negative detuning

A non-flat dispersion of LP2D can be observed at very negative detuning for the mesa. We show, in Figure 2.7, that in this case, important change are observed in the far-field spectra. We selected a region at slightly positive detuning $\delta = 0.64$ meV for the LP2D, corresponding to an excitonic proportion of 60 % exciton. The LP0D ground state is at $\delta = -6.4$ meV, so an exciton proportion of 5 %. The relative depth of trap seen by lower polaritons is drastically increased: about 2 meV in the previous case against 7 meV here. The number of confined states is therefore larger, as well as the spacing between them. For instance, the energy separation between the ground state and the first excited state is 0.67 meV in Figs. 2.6 and 2.5 and 1.25 meV here.

Finally, it is interesting to notice that there is an energy overlap between the highest excited levels of the mesa and the bottom of the polariton dispersion.

2.3 Quantum or classical?

To which extent can we consider polariton mesas as a quantum system? This is an interesting question, which is often debated. The thermal de Broglie wavelength λ_{dB} of a gas of particles of mass m, is the extent which give the size of a confining system under which the quantum nature of the gas becomes relevant. In particular, the motion of the particles is quantized along the direction of quantum confinement.

The thermal de Broglie wavelength is defined by

$$\lambda_{dB} \sim \frac{h}{\sqrt{m k_B T}} \tag{2.1}$$

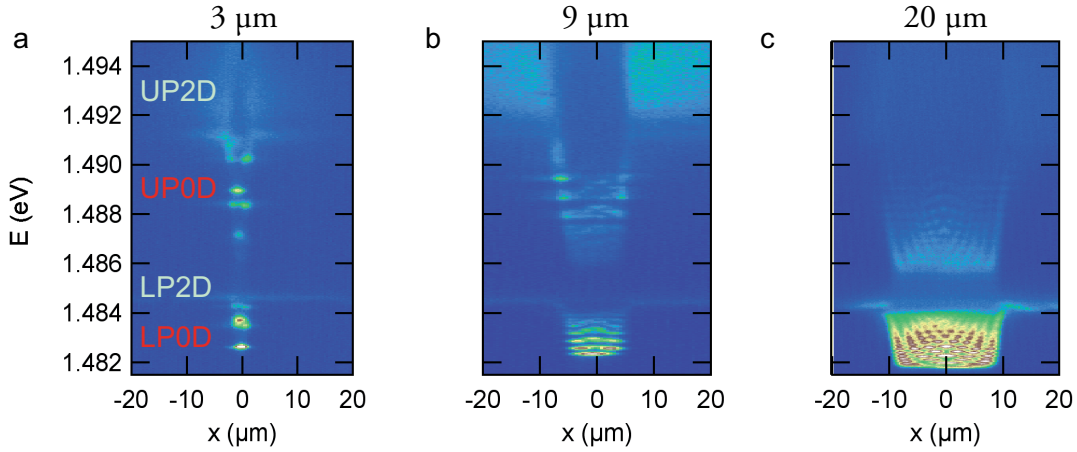

Figure 2.5: **Near field imaging spectroscopy.** Spatially resolved spectra for the three sizes of mesa. The spectra are acquired at zero detuning for the ground confined polariton level. We call LP2D and UP2D the regions of planar lower and upper polaritons, respectively. The confined lower and upper polaritons are labeled LP0D and UP0D, respectively. Within the width of the mesa, the confined states are well visible. **a 3 μm mesa** The discretization is significant. We distinguish only four confined states. There is a separation of about 0.7 meV between the ground state and the first excited state. The same pattern is visible for UP0D and LP0D. In addition, the intensity from 2D polaritons region drops at the position of the mesa. **b 9 μm mesa** There are more confined levels because the trap is larger. The separation between the states is of the order of 100 μeV. **c 20 μm mesa** In the largest mesas, the number of confined states is much more important than in the two others and the states separation is of the order of the spectral resolution. *From [Nardin 10]*

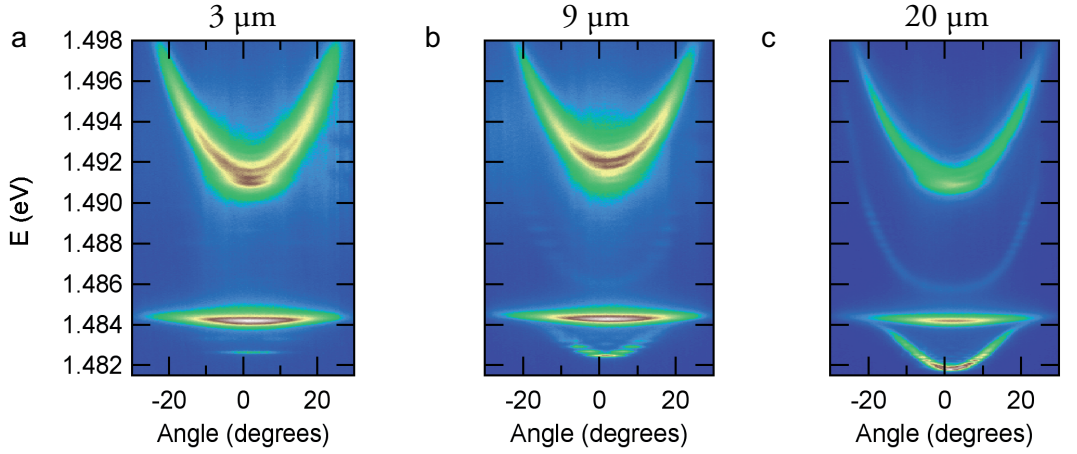

Figure 2.6: **Far field imaging spectroscopy.** Polariton spectra, resolved along one direction of the momentum space, for the same mesas as in Fig. 2.5 **a 3 μm mesa** Because of the strong confinement, the states are extended in the momentum space. Note that the dispersion of LP2D is flat because the detuning of planar polariton is very positive when the mesa is at zero detuning. LP2D is well visible despite its small photon content because we use a spot much larger than the mesa. **b 9 μm mesa** The states are closer to each other, but the dispersion is still discrete. **c 20 μm mesa** The dispersion of confined polaritons is almost continuous. In there mesas, the system is close to a planar cavity. *From [Nardin 10]*

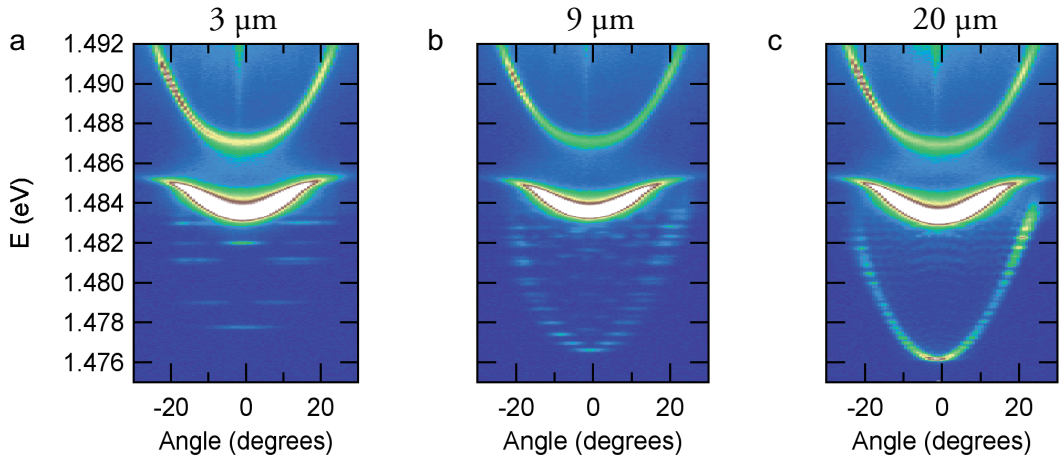

Figure 2.7: **Far field imaging spectroscopy: negative detuning.** Planar polaritons are at slightly positive detuning (1 meV). The confined states are thus at very negative detuning. A clear polariton dispersion is observed for the LP2D. The intensity is saturated to show the confined states. At negative detuning, the relative depth of the well is larger so the spacing between the states is increased. 1.2 meV separate the ground and the first excited state in the 3 μm mesa (**a**). In the 9 and 20 μm mesas (**b** and (**c**)), we see the increasing number of states, as well as their narrowing in the momentum space.

where h is the Planck constant, k_B the Boltzmann constant and T the temperature of the gas. Typical de Broglie wavelengths for polaritons in InGaAs quantum wells is of the order of a few microns at 4 K. Hence, considering confined polaritons as a quantum system would be more justified in 3 μm diameter mesas.

From our spectroscopic measurements (see Figs. 2.6 and 2.7), we see that the momentum quantization is clear in the 3 and 9 μm diameter mesas. In addition, the states are wide in momentum space so that they overlap in a large range of wavevectors. This causes a relaxation of the momentum selection rule.

In the 20 μm diameter mesas, the dispersion is continuous around zero detuning for the mesa. At negative detuning, there is a very small energy spacing between the states, but the dispersion is still nearly continuous. The notion of quantum confinement is more appropriate for 3 and 9 μm diameter mesas. In the next part, we will see that this distinction between 20 μm diameter mesas and smaller mesas has a significant influence on the polariton relaxation dynamics.

2.4 Conclusion

In conclusion, the sample we investigate is a very high quality semiconductor microcavity in which polaritons are trapped in innovative structures. Contrarily to common methods, here, trapping is achieved by acting on the photonic nature of polaritons. The traps consist of local extensions of the cavity length of well-controlled shapes and sizes called mesas. They are fabricated using state-of-the-art techniques.

Characterization by photoluminescence has shown that very efficient polariton trapping of polaritons is achieved in mesa structures. A great advantage of our

sample is the coexistence of planar and confined polaritons. It is therefore possible to study the influence of dimensionality on polaritons and their interactions. El Daif showed that Bose-Einstein condensation do not take place in this sample because it contains only one quantum well [El Daif 07]. Nevertheless, the "1485" sample is particularly suitable for exploring many other aspects of polariton interactions. For instance, the polariton relaxation in a trap, the coupling between polaritons of different dimensionality, polariton nonlinearities, the role of polariton spin or coherent polariton manipulation are all important issues that can be addressed with a unique approach using mesa structures. This is the object of the work developed in the next parts of this thesis.

Part II

On the Relaxation Mechanisms of Confined Microcavity Polaritons

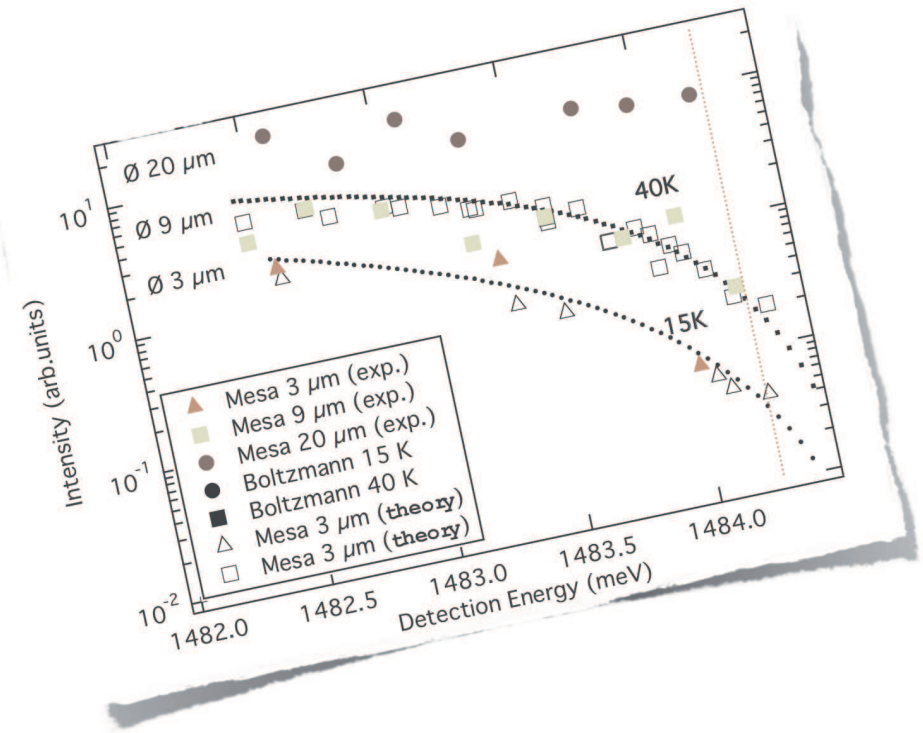

Chapter 3

Thermalization of Confined Polaritons

3.1 Introduction

Owing to their bosonic behavior and their very light effective mass, microcavity polaritons are the ideal tool for investigating quantum phenomena in solid-state systems. Large is the number of studies devoted to the quantum coherence properties of microcavity polaritons, leading to the observation of parametric processes [Savvidis 00a, Messin 01, Saba 01, Kundermann 03, Langbein 04, Bajoni 07b], polariton lasing [Bajoni 08b, Christmann 08, Christopoulos 07] and Bose-Einstein condensation (BEC) [Kasprzak 06, Balili 07, Deng 07].

The great potential of optical measurements makes microcavity polaritons the most promising system to study many fundamental aspects of the BEC physics and superfluidity in the solid state [Griffin 95]. For instance, studies of the fragmentation of a condensate due to disorder [Baas 08], the dynamics of the different order coherence functions [Nardin 09a, del Valle 09, Love 08] and experiments on vortices and superfluidity [Lagoudakis 08, Lagoudakis 09, Amo 09b, Amo 09c, Utsunomiya 08] are the demonstration that fundamental questions explored with cold atoms can also be addressed with polaritons. On top of that, those phenomena can be studied at much higher temperature than in cold atoms experiments, and in a more handleable way. As explained in Chapter 1, all the information on polaritons dispersion, position, phase and time is contained in the emitted photons. Potentially, it could be integrally retrieved by using the appropriate experimental tools.

The future of experiments with polariton will depend on the mastery of polariton physics and on the development of trapping structures. Those experiments will concern two major directions. First, the exploration of quantum mechanics and electrodynamics in the solid state. Second, the application of polariton physics to the engineering of miniaturized optoelectronic devices. To meet these challenges, beside the improvement of the samples quality, it is crucial to understand fully the basics of polariton physics namely the relaxation and the propagation.

An extensive amount of studies already describe polariton relaxation in planar microcavities. However, a proper study of polariton relaxation in a trap was still missing. For now, only a few and very recent works investigate differences

between planar and confined polariton relaxation [Paraïso 09, Balili 09, Nelsen 09, Sanvitto 09]). In trapped structures, polariton relaxation is expected to be modified by the discretization of the dispersion on the one hand, and by the relaxation of the momentum selection rule on the other hand.

In the present chapter, we investigate the relaxation dynamics of confined polaritons in the linear regime, meaning in the absence of two (or more)-polariton scattering processes. The dynamics in the non-linear regime is described in the next chapter. Section 3.2 is an overview of the work that has been done in planar microcavities. We recall the main outcomes of polariton relaxation and describe the relaxation mechanisms. In Section 3.3, we discuss experiments under nonresonant excitation. By means of time resolved photoluminescence experiments, we show what are the limitations of relaxation experiments under off-resonant excitation. In Section 3.4, we describe the experimental techniques used to investigate polariton relaxation and we discuss the results on thermalization of confined polaritons. A theoretical model based on Bogoliubov-de Gennes approximation is developed in Section 3.5. Finally, Section 3.7 compiles theoretical and experimental considerations to establish a picture of the dynamics of confined polaritons relaxation in the linear regime.

3.2 Polariton relaxation: recall and motivations

In planar microcavities, due to the short radiative lifetime of polaritons and the very inefficient mechanisms of energy relaxation and thermalization, the deviations from equilibrium are very important. Indeed, in planar microcavities, thermalization is only possible in the regime of high polariton densities, where the polariton-polariton scattering becomes efficient enough [Kasprzak 06, Balili 07, Deng 07]. In the low-density regime, where the only mechanism of thermalization is the energy exchange between polaritons and phonons or free charges, polaritons do not thermalize. In this density regime, the relaxation can be enhanced only by raising the temperature or by injecting free carriers in the system [Stanley 97, Perrin 05, Tassone 97].

Recently, it has been suggested that the presence of spatial confinement could have an impact on the thermalization process [Sarchi 07]. In addition, pioneering experimental observations in micropillars suggest that spontaneous quantum degeneracy of microcavity polaritons seems to be reached at lower excitation densities than in planar microcavities [Bajoni 07a]. In order to clarify these points, a detailed investigation of the efficiency of relaxation and thermalization of polaritons in spatially confined structures is required.

Before describing our experiment with confined polaritons, we recall the main issues about polariton relaxation in planar microcavities.

3.2.1 From the free carriers reservoir to the polariton branch

Creating polaritons with a laser source can be done either by exciting polaritons states resonantly, either nonresonantly. In the latter case, the laser energy is far above the polaritons energy, and preferably in the first transmission mode of the

distributed Bragg reflectors. Consequently, the quantum well electrons are excited far above the exciton resonance and a plasma of free electrons and holes is created.

In Fig. 3.1, we show the commonly accepted relaxation scheme. At early times, the free carriers relax to the exciton dispersion by emitting optical phonons. This process confers very large wavevectors on excitons, which are thus unable to couple to light. Excitons then loose energy by multiple scattering with acoustic phonons. A thermalized exciton reservoir is then created in the vicinity of the light cone ($k_{\rm rad} \simeq 10^5$ cm^{-1}), where polaritons are formed [Porras 02a, Savona 07].

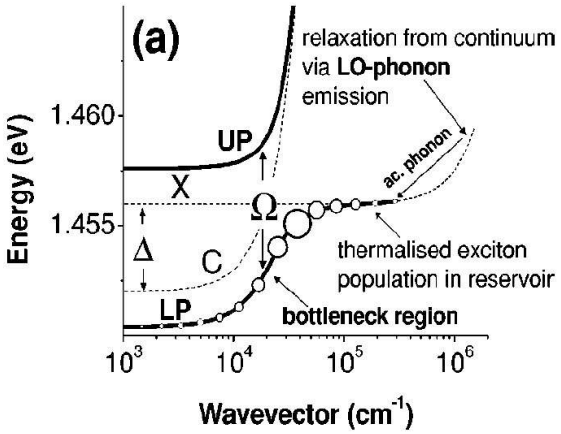

Figure 3.1: **Schematic of polariton formation**. nonresonantly excited free carriers first scatter with LO phonons to the non radiative region of the exciton dispersion. Then exciton relaxation via acoustic phonons takes place. Polaritons are formed when excitons enter the light cone. Competition between polariton-acoustic phonon scattering and fast polariton radiative recombination prevents the system from reaching thermal equilibrium, producing the so-called relaxation bottleneck region. *From [Butté 02].*

For the following discussion, the most important feature of Fig. 3.1 is the *relaxation bottleneck* region. In this region, polaritons accumulate because their lifetime is too short for them to have time to scatter with acoustic phonons down to the bottom of polariton branch [Tassone 97]. The polariton energy distribution strongly differs from a Boltzmann distribution and it is not possible to define a temperature of the polariton gas. Under nonresonant excitation and at low excitation densities, thermalization is totally inefficient in planar microcavities.

3.2.2 About polariton relaxation

The different polariton relaxation mechanisms

Polariton thermalization occurs when the polariton gas undergoes *enough* scatterings to redistribute thermodynamically its energy over all polaritons. The challenge is to ensure that polaritons scatter *many times* during their lifetime. Several techniques have been employed to suppress the relaxation bottleneck. Among those, let us mention the introduction of an electron gas and the temperature augmentation, which accelerate polariton energy redistribution [Stanley 97, Perrin 05].

Linear regime versus non-linear regime

In the low excitation density regime, the emission intensity varies linearly with the excitation power. We call this regime the linear regime. In this regime the main relaxation mechanisms are the interactions with the lattice and with free carriers. The energy blueshift varies also linearly with the injected population and the linewidth is approximately constant.

At higher excitation density, the system enters the non-linear regime. The dependence of the emitted intensity (and of the blueshift) on the excitation power becomes quadratic because of two polariton processes. In addition there is a broadening of the linewidth. At even higher densities, this dependence may become exponential because of bosonic stimulation processes.

3.2.3 Why do we want to thermalize polaritons?

We saw previously that the polariton relaxation to the bottom of the lower polariton dispersion is inhibited by the competition between scattering times and radiative lifetime. To observe spontaneous formation of macroscopic quantum coherence, the system first needs enough energy to increase the relaxation rates and overcome the bottleneck.

This is usually done by increasing the excitation power to provoke collisions, which scattering times are much shorter that the ones obtained in the linear regime. Then, the system needs to have a high enough polariton density to stimulate the relaxation to the final state [Imamoglu 96b]. In general, this happens in the kinetic regime, meaning that thermal equilibrium is not reached before the bosonic stimulation. The condensed phase is then called a polariton laser or a kinetically driven Bose Einstein condensate depending on if the quantum degenerate phase is at thermal equilibrium or not [Kasprzak 08].

Ideally, the term BEC should be used only if the system is at thermal equilibrium *with the lattice* before the BEC transition. This case has been reported in planar microcavities operating at positive detuning, to increase the polariton lifetime [Kasprzak 08, Deng 06].

Another reason for studying thermalization is to contribute to the theoretical investigations concerning the phase diagram of the polariton gas. In particular a stimulating question is to determine the differences and relations between a superfluid and a BEC [Wouters 10, Sarchi 08a, Marchetti 08, Szymanska 06], which is also a debate in the cold atoms community [Carusotto 10, Cooper 10].

Finally, from an applications point of view, approaching thermal equilibrium already in the linear regime would reduce the excitation power needed to observe the buildup of a macroscopic quantum degenerate state. This effect is already suggested by some studies showing that BEC in traps is achieved at lower excitation power [Bajoni 07a].

3.3 Nonresonant excitation

A first approach to investigate polariton relaxation in a trap is to perform time resolved photoluminescence (TRPL) experiments to access the time evolution of the polariton spectrum.

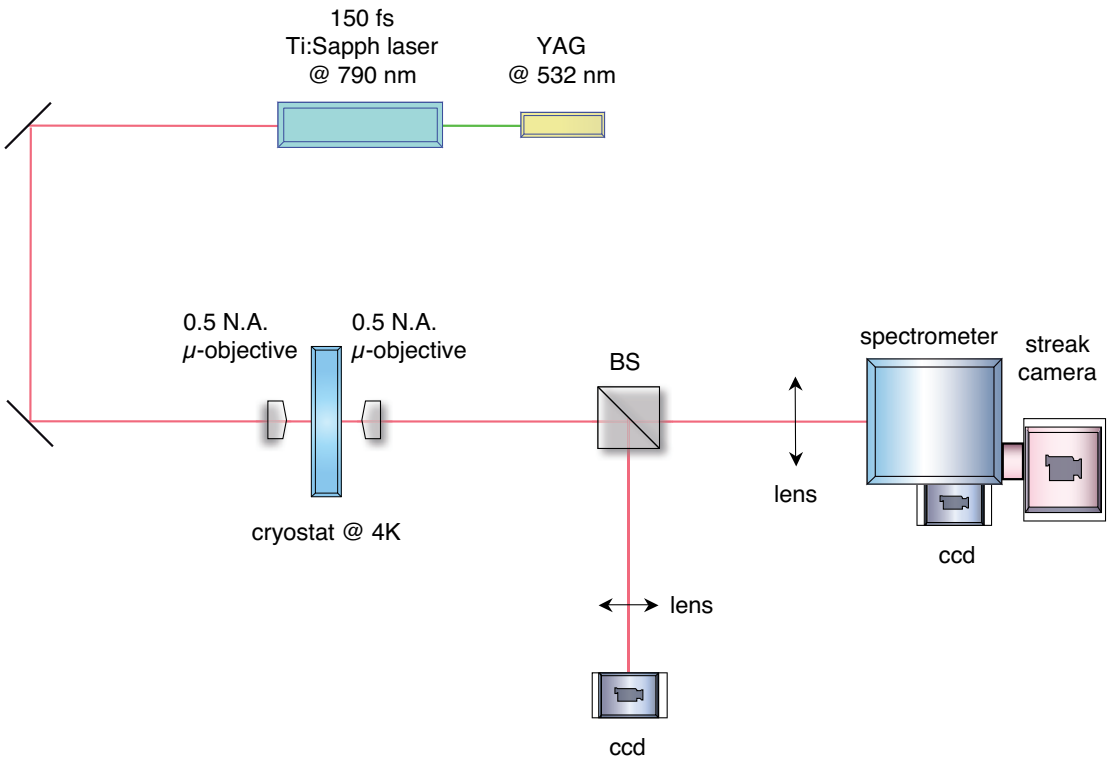

Figure 3.2: **Setup: nonresonant TRPL.** Nonresonant excitation fs pulses are focused on the sample using a micro-objective. The emission is collected on the other side with a similar micro-objective, and sent to a spectrometer. The output of the spectrometer is connected to a streak camera to obtain time resolved spectra of the polariton luminescence.

3.3.1 Experimental setup

In Figure 3.2, we describe the setup we used for the nonresonant TRPL experiments. The sample is excited using a pulsed Ti:Sapphire laser, resonant with the first Bragg mode of the DBRs. The experiment is done in a transmission configuration with two micro-objectives of 0.5 N.A., as for the spectroscopy measurements.

The near-field emission is imaged on the slits of the spectrometer to obtain a spatially resolved spectrum, which is then sent to a streak camera to produce the time resolved spectra. In order to obtain data with a sufficient dynamical range, we needed to run the streak camera in a photon counting mode, with typical acquisition times of 45 to 60 minutes.

3.3.2 Experimental results

Dynamics of quantum well excitons

We performed TRPL experiments on a 9 μm diameter mesa at negative detuning. We obtained time resolved spectra with a 2 ns time window, from which we extracted intensity vs time profiles. The typical results are presented in Fig. 3.3. On the time resolved spectrum, displayed on Fig. 3.3 a, one distinguishes different confined polariton states. Because of the negative detuning, UP0D states have a small photon content, and their emission intensity is weak. On the opposite, LP0D states are well visible. In particular the ground state, the first and second excited state are clearly evidence. Their respective intensity profiles are displayed in Fig. 3.3 b.

At this excitation power (20 μW), the three curves are overlapping. The rise time has been measured to ∼20 ps and the decay time has been evaluated to few nanoseconds. This very slow decay can also be observed in the backtrace at negative time with respect to the laser incoming time $t_L \simeq 300$ ps. It is characteristic of the long dynamics of quantum well excitons, which relax from the large wavevector region of the excitonic dispersion down to the light cone by scattering with acoustic phonons [Deveaud 91] (see Fig. 3.1).

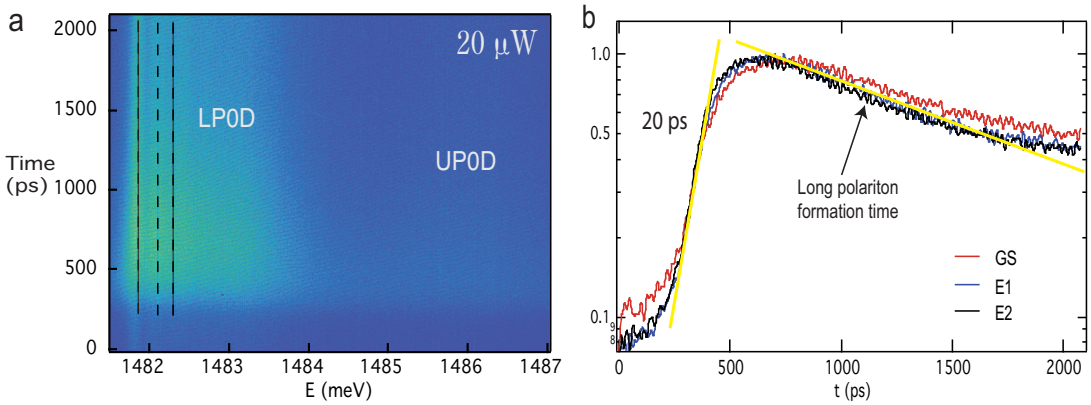

Figure 3.3: **Nonresonant TRPL: 20 μW excitation power.** **a** We distinguish between the confined polariton states and extract the time evolution of the ground (GS), first (E1) and second (E2) excited states. The dashed lines are guide for the eyes. **b** Time profile of the evolution of GS, E1 and E2. The rise time is related to the polariton lifetime. The long decay time is related to the long relaxation time of quantum well excitons down to the region of the light cone.

Power dependence

At higher excitation powers, the system enters the nonlinear regime. Similarly to experiments by Butté et al. [Butté 02], we observe the loss of strong coupling regime and, at higher power, photon lasing. The power dependence study is shown in Fig. 3.4. Fig. 3.4 a, is the linear regime, at 20 μW excitation power.

At 90 and 200 μW, (Fig. 3.4 b and c) we evidence transitions from the weak-coupling to the strong coupling regime. The weak coupling phase is characterized by an intense emission region, wide in energy. This region coincides with the bare cavity modes energies, and shifts toward low energies as time increases, i.e. as free carriers density decreases. In Fig. 3.4 c, it is not possible to identify any polariton state at short time ($\sim$ 500 ps). At longer times ($>$ 1000 ps), the linear behavior is recovered and one can again distinguish between the LP0D states.

At 600 μW (Fig. 3.4 d), the strong coupling completely lost and is not recovered at all. We detect multimode photon laser emission from the different cavity modes.

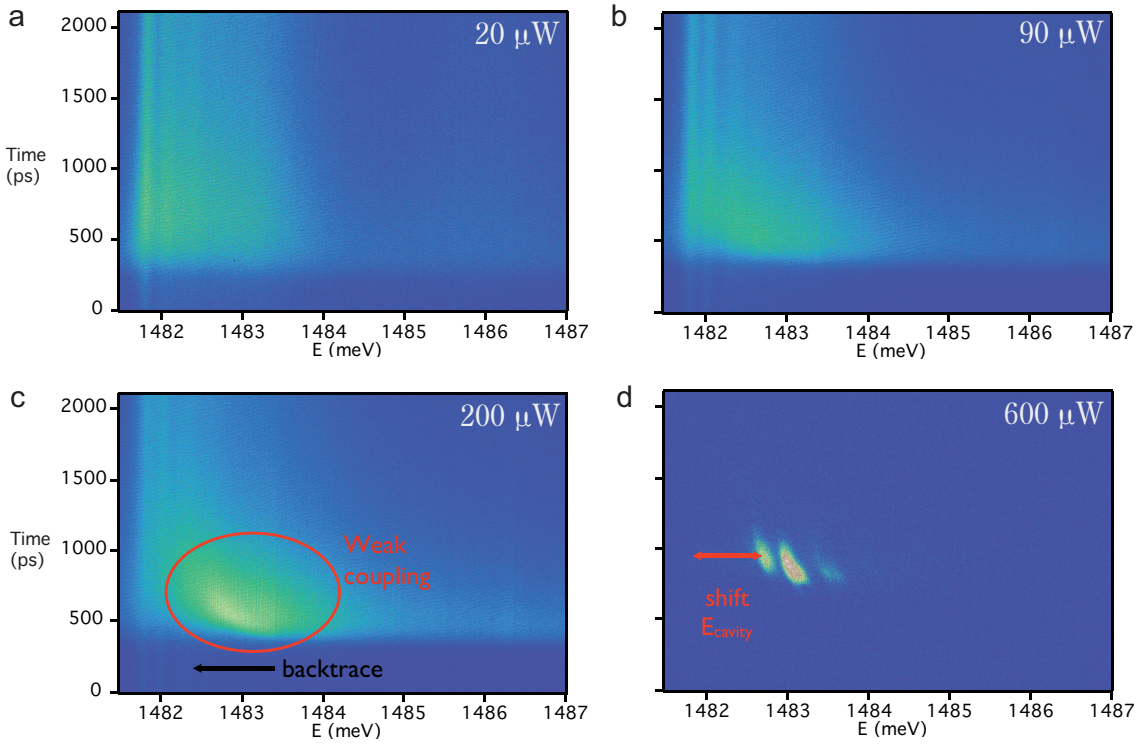

Figure 3.4: **Power dependence.** **a** 20 μW: linear regime. **b** 90 μW: the onset of the non linear regime is visible at short times as a broadening of the confined states. **c** 200 μW: the transition from weak to strong coupling regime is clearly evidenced between 400 and 1000 ps. The linear behavior is recovered at long times. **d** Photon lasing.

3.3.3 Interpretation

Timescales

The conclusions of this study show us the limitations of nonresonant time resolved photoluminescence. Considerations on the rise and decay times reveal that the intensity profiles of Fig. 3.3 b reflect the slow dynamics of the quantum well excitons. Indeed, one can show, using a simple rate equation model, that in such curves the rise time is given by the shortest timescale in the system.

For instance, consider a system $A(t)$ coupled to a reservoir, with a filling channel

and an escape channel, the rate equation reads

$$\dot{A}(t) = \frac{1}{\tau_{\text{in}}} A(t) - \frac{1}{\tau_{\text{out}}} A(t) \tag{3.1}$$

For large differences between the two time scales, the rise time corresponds to the shortest time and the decay time is given by the longest time. This is illustrated in Figure 3.5, by a simple simulation. We show that, for a short escape time $\tau_{\text{out}} =$ 10 ps, the decay time reflects the long filling time, $\tau_{\text{in}} = 500$ or 1000 ps. On the contrary, for a short filling time $\tau_{\text{in}} = 10$ ps, the decay time corresponds to the long escape time $\tau_{\text{in}} = 100$ ps.

In our case, it is well known that the relaxation of quantum wells excitons from the large **k** region down to the light cone (see Fig. 3.1) can exceed several nanoseconds, which is orders of magnitude longer than the polariton lifetime ($\propto$ 10 ps).

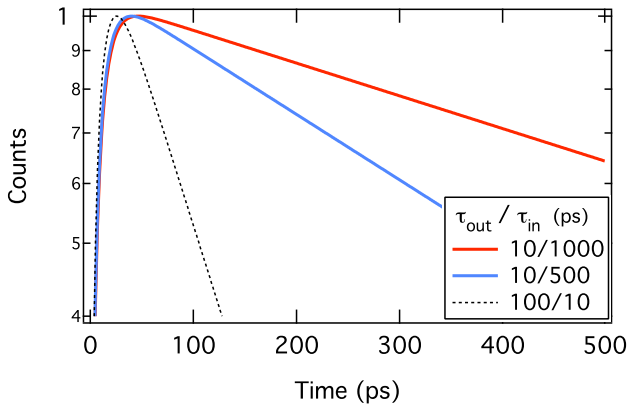

Figure 3.5: **Simple model.** Simulation of a system $A(t)$ coupled to a reservoir using different filling τ_{in} and escape τ_{out} times (see Eq. 3.1). The rise time corresponds to the shortest timescale and the decay time to the longest one.

Nonlinearities: phase space filling versus screening

At high excitation power, the observed nonlinearities are mostly due to the free carriers dynamics. Indeed, the occurrence of weak coupling and photon lasing are indications that the formation of excitons is compromised at very high densities. There are two sources of bleaching of the exciton oscillator strength: the phase space filling nonlinearity and the screening of the excitonic resonance [Senellart 03]. The phase space filling is a saturation effect due to the Pauli exclusion principle [Huang 90]. It happens when the exciton density becomes too strong to neglect their fermionic internal structure. The exciton number reaches 1 exciton per state and further formation of exciton is forbidden. The screening of the Coulomb interaction by free carriers prevents electron and holes from forming a bound state [Khitrova 99, Haug 85, Honold 89]. It is therefore accompanied by a renormalization of the bandgap, i.e. a reduction of the free carrier minimal energy. Under nonresonant pulsed excitation, the screening process is dominant, thus blurring the study of polariton relaxation and favoring photon lasing in semiconductor microcavities.

This phenomenology is related to the *excitonic Mott transition* in the quantum well: at high densities, the quantum well is dominated by the electron-hole plasma phase. Time resolved studies of the excitonic Mott transition by Kappei et al. [Kappei 05] agree in many aspects with our observations of strong to weak coupling regimes transitions. At low excitation power, the excitonic phase is dominant in the quantum well. Hence, strong coupling is observed in the microcavity sample. On the other hand, at high excitation power, the unbound carriers phase is dominant: strong coupling can not be achieved and we observe photon lasing. At intermediate densities, the two phases coexist. Kappei et al. showed that, as in our case, the unbound phase dominates the emission at short times and disappears when time increases. Recently, similar conclusions were reported in microcavities [Balili 09].

Summary of the nonresonant excitation experiment

In conclusion we sum up the nonresonant excitation dynamics as follow:

a) Scattering with optical phonons brings free carriers to the non-radiative region of the exciton dispersion curve, which plays the role of an excitonic reservoir.

b) Multiple scattering with acoustic phonons brings the excitons down to the radiative region, where they strongly couple to light and form polaritons.

c) The time evolution of the full process is governed by the slow relaxation of excitons in the non-radiative region, because the radiative lifetime of polaritons is much shorter than the exciton lifetime.

d) At high excitation power, we observe a time-resolved transition from weak to strong coupling regime. The weak coupling originates from the screening of the electron-hole Coulomb interaction by the free carriers.

Therefore, the relaxation dynamics between confined polariton states can be better characterized by means of *resonant excitation* experiments.

3.4 Resonant excitation

We performed two types of resonant photoluminescence excitation (PLE) experiments. Both consisted in detecting the luminescence spectrum while exciting resonantly the confined states. In one case, the excitation source was a continuous tunable Ti:Sapph laser (cw-PLE) in order to perform precise excitation of single energy states of the system. In the other case, the excitation source was a pulsed Ti:Sapph laser of 500 μeV spectral FWHM (p-PLE). The time duration of the pulse, 8 ps, was shorter than the polariton lifetime. It allowed us to take the relaxation dynamics into account and to study the system by resonant time resolved photoluminescence (Sec. 3.4.4).

To obtain such pulses, the laser was spectrally filtered using a pulse shaper consisting of a grating and a mirror, Fourier conjugated to a lens. On the mirror, an image of the pulse dispersion was formed with total space-wavelength correspondence. The spectral resolution of the dispersed image was of the order of 1.5 nm/mm,

using an 800 grooves per millimeter grating and a 300 mm focal length lens. A mask on the mirror allowed us to select the wavelength with a spectral width of 0.25 μm ($\simeq$ 500 μeV), which is comparable to the spacing between two consecutive confined states.

3.4.1 Pulsed PLE

An image plot of the time-integrated p-PLE is shown in Fig. 3.6. The excitation energies are displayed along the horizontal axis whereas the detected luminescence spectra are displayed vertically.

On the diagonal, the emission energy is equal to the excitation energy. We make four key observations:

i) When exciting the LP0D (from 1482 meV to 1484.5 meV), polaritons redistribute within LP0D states, toward both lower and higher energies. This indicates the presence of efficient interactions with a thermal bath.

ii) When the excitation is resonant with the UP0D (from 1485.5 meV to 1490 meV), the relaxation to LP0D states is very efficient. We do not observe significant polariton redistribution within the UP0D states.

iii) When exciting the UP0D, the relative intensities of the LP0D states suggest that thermalization occurs within the LP0D states.

iv) Contrary to (ii), when the excitation is resonant with the 2D polaritons, the relaxation to LP0D states is inefficient.

We give an interpretation of (i) and (iii) in terms of *thermalization* whereas (ii) and (iv) are discussed with considerations on the polariton *dimensionality*.

3.4.2 Thermalization in mesas.

The p-PLE experiments were carried out in the low-density regime, where polariton-polariton interactions are negligible. Therefore, we attribute the relaxation to polariton-acoustic phonon scattering. Observations (i) and (iii) are clear evidence of efficient thermalization within the LP0D states.

To study in detail the thermalization within LP0D, we focus on the case in which we excite resonantly a UP0D state (1487 meV). In Fig. 3.7, we display the time integrated emission per state, as a function of the energy of the state. This quantity is obtained from the LP0D luminescence spectrum by integrating the luminescence intensity of each peak. It is equal to the population per state weighted by the photonic content of the state.

The data are well fitted by Boltzmann distributions, from which we can extract effective temperatures. The photonic content of the states was taken into account in the Boltzmann distributions by applying an energy dependent correction factor, which explains the non-exponential behavior of the fitting curves.

We obtain effective temperatures of 15 K for the Ø 3 μm mesa and 40 K for the Ø 9 μm mesa. The emission of the Ø 20 μm mesa could not be fitted by a thermal distribution.

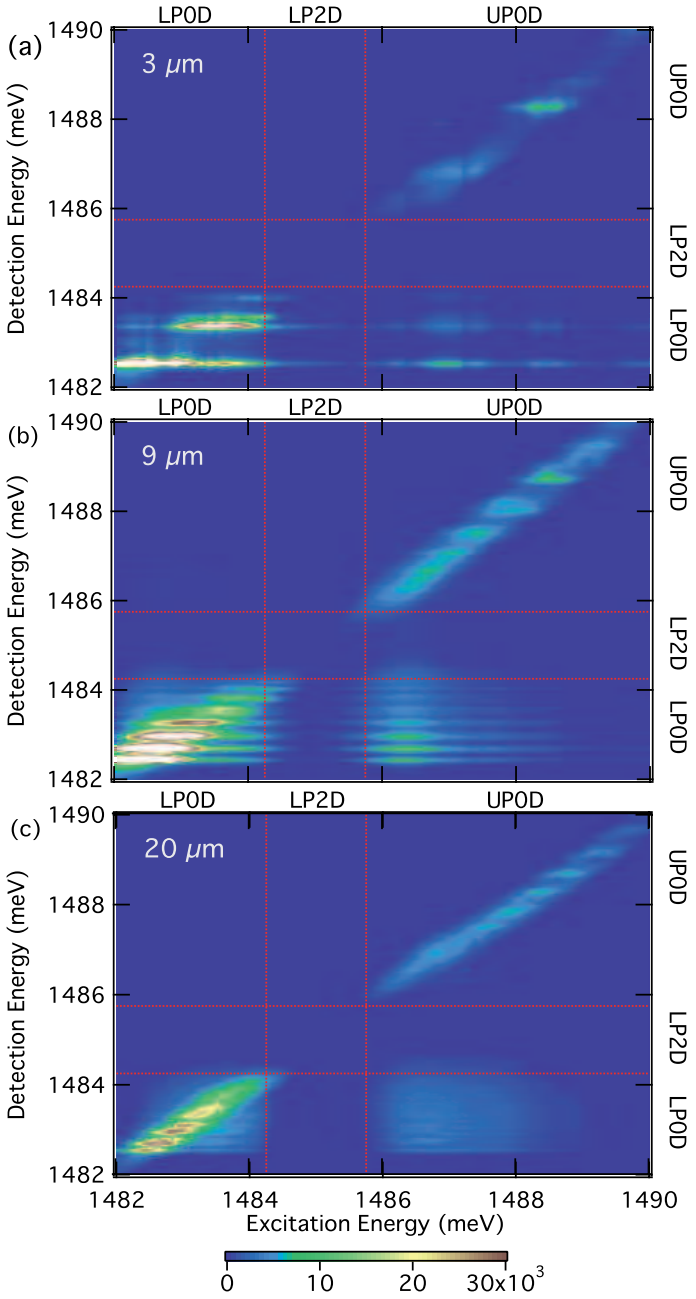

Figure 3.6: **Image plots of p-PLE experiments.** (a) 3 μm, (b) 9 μm and (c) 20 μm diameter mesas. The dotted lines are separations between the LP0D, LP2D and UP0D energy ranges. The relaxation down to the lowest energy state is favored and suggests the presence of a thermalization process. The weak signal between the dotted lines indicates a poor coupling between polaritonic states of different dimensionality. The resolution is 100 μeV on both axes.

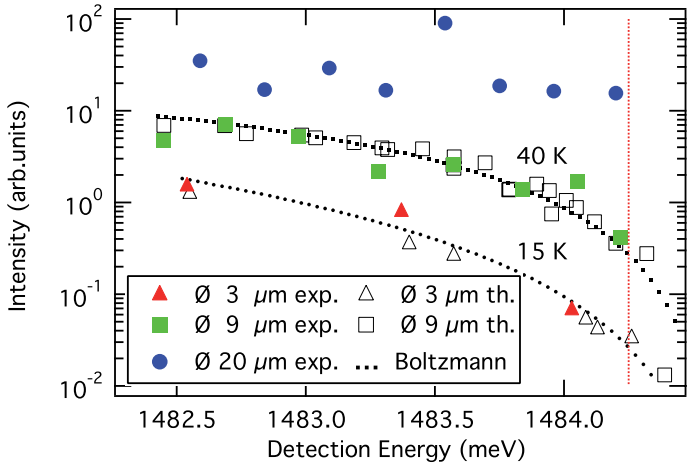

Figure 3.7: **Thermalization of confined polaritons.** Integrated luminescence intensities of the LP0D states for an excitation in the UP0D (1487 meV) for the three sizes of mesas. Experimental data (filled symbols) are compared theoretical prediction (empty symbols). The Boltzmann distributions (dotted lines) are corrected by the photonic weights of the states. The Ø 3 μm and Ø 9 μm mesas emissions present thermalized distribution. The Ø 20 μm mesa emission has a non-thermal distribution. The vertical line is a separation between the LP0D and LP2D energy ranges.

The efficiency of thermalization depends on the difference between the polariton-phonon scattering time τ_{ph} and the polariton radiative lifetime τ_r. There are three possible situations [Deng 06]:

a) $\tau_r \gg \tau_{ph}$: during their lifetime, polaritons scatter many times with phonons. It is possible to define a temperature. This temperature is close to the lattice temperature.

b) $\tau_r \geq \tau_{ph}$: the two time scales are comparable. Polaritons thermalize at a higher temperature than the lattice.

c) $\tau_r \ll \tau_{ph}$: polaritons recombine too fast to undergo enough scatterings with phonons. In this case, polaritons have a non-thermal distribution.

For the Ø 9 μm mesa, the effective temperature of 40 K suggests that thermalization becomes less efficient when the mesa diameter increases. This tendency is confirmed by the non-thermal emission obtained for the Ø 20 μm mesa.

In planar microcavities, Stanley et al. [Stanley 97] observed that, for similar temperatures (4-5K), polaritons did not thermalize. By increasing the lattice temperature up to 30 K, they significantly shortened the polariton-phonon scattering time and could eventually observe a Boltzmann distribution. In our case, the lattice temperature remains unchanged but the confinement in small mesas has a crucial effect: the widening of the wave functions in the momentum space [Kaitouni 06] enhances the polariton-phonon scattering rate and thus favors thermalization in the small mesas. The comparison with theory is developed in Sec. 3.7.

3.4.3 Influence of dimensionality.

Observations (ii) and (iv) strongly suggest that, whereas the relaxation is very efficient within the localized states, it is suppressed between delocalized states and localized states.

However, considering the low probability distribution of the delocalized states above the mesa, it is important to verify that (iv) is not the result of a poor mode matching between the excitation spot and the wave function of the delocalized polariton. We unambiguously confirmed this point with a cw-PLE experiment (Fig. 3.8).

Thanks to the narrow spectral linewidth of the continuous wave excitation, we were able to excite resonantly single polariton states. We could accurately measure, for each of them, the reflected and transmitted intensities in order to extract the absorption. We then normalized the emission of the ground state by the absorption of the pumped state. The measured absorption of the LP2D was 15 percent less than the average absorption of the 0D polaritons.

The results of the cw-PLE experiment on the 9 μm diameter mesa are displayed in Fig. 3.8, together with the p-PLE intensity horizontal profile taken at the ground state energy of Fig. 3.6 (b). For comparison, the figure also features a nonresonant excitation spectrum. One can notice the similar behavior of the p-PLE and the

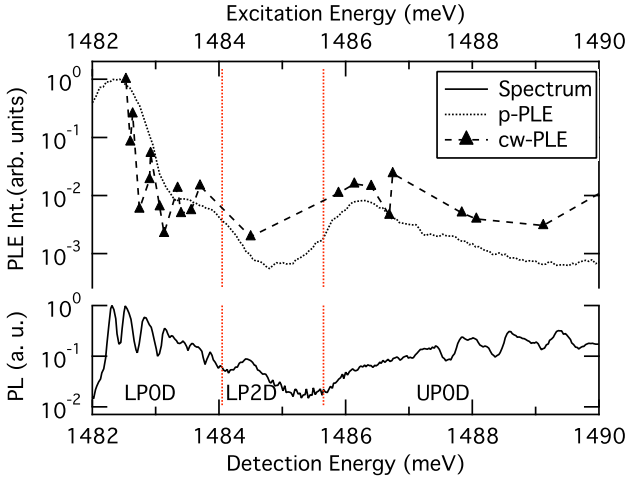

Figure 3.8: **Dimensionality.** Comparison between the PLE spectra obtained with a pulse-shaped pump (dotted line) and with a cw-pump (triangles). The dashed line is a guide for the eye. The nonresonant photoluminescence spectrum (solid line) is plotted as a reference. The dotted lines are separations between the LP0D, LP2D and UP0D energy ranges.

cw-PLE curves despite the fact that the latter is normalized. In both cases, the PLE intensity decreases by one order of magnitude when the excitation is resonant with the LP2D states. This demonstrates that the relaxation between 2D and 0D polaritons is inefficient.

In view of these results, we can infer that, under nonresonant excitation, the 2D states may not be an intermediate channel for the relaxation to the 0D states. One could indeed expect excitons that reach the light cone to first create polaritons in the LP2D branch, and that these polariton would then relax to the LP0D states. In

fact, regarding the inefficient coupling between polaritons of different dimensionality, 0D states are most probably directly populated from the excitonic reservoir.

3.4.4 Dynamics of polariton relaxation

The dynamics of polariton relaxation has been investigated through time resolved photoluminescence (TRPL) experiments under resonant excitation. After exciting a given 0D polariton state, we looked at the time resolved evolution of the emission of the ground state. The luminescence was first sent to the spectrometer and then to a streak camera with 2 ps time resolution. Note that, because of the dispersion on the grating, the experimental time resolution was about 10 ps. We focused our study on the 3 μm and 9 μm diameter mesas, in which polaritons thermalize efficiently with the phonon bath.

In Figs. 3.9 and 3.10, we show the ground state TRPL intensity for the Ø 9 μm and Ø 3 μm mesas, respectively. The luminescence intensity of the ground state increases with a rise time of about 15 ps. This time corresponds to the lifetime of the ground state. On the other hand, the decay times strongly depend on whether the excitation is resonant with a LP0D state or with a UP0D state.

For the Ø 9 μm mesa (Fig. 3.9), when the pump is resonant with a LP0D state, we observe a biexponential decay of the ground state TRPL intensity. When the pump is resonant with a UP0D state, we observe a monoexponential decay. For the Ø 3 μm mesa (Fig. 3.10), the decay is monoexponential in both cases.

The values of the fitted decay times are reported in Table 3.1 for the Ø 9 μm mesa and in Table 3.2 for the Ø 3 μm mesa. We denote τ_S as the short decay time (less than 100 ps) and τ_L as the long decay time (more than 100 ps).

When the excitation energy is resonant with LP0D states, we obtain short decay times for both mesas. The values of τ_S vary between three to five times the lifetime of the ground state. In the case of the Ø 9 μm mesa, we also obtain long decay times, comparable to the decay times obtained while exciting UP0D states. The values of τ_L are one to two orders of magnitude longer than the lifetime of the ground state.

These observations suggest that similar relaxation processes are responsible for the long decay times τ_L observed in both mesas.

Table 3.1: **Decay times in a Ø 9 μm mesa** TRPL intensity of the ground state for different excitation energies. We observe two decay times when exciting LP0D states and only one when exciting UP0D states.

Excitation energy [meV]	τ_S[ps]	τ_L[ps]
1482.96 (LP0D)	45	134
1483.33 (LP0D)	50	137
1483.63 (LP0D)	55	137
1486.51 (UP0D	-	274
1487.27 (UP0D)	-	320
1488.69 (UP0D)	-	907

A possible phenomenological interpretation of these observations is the following:

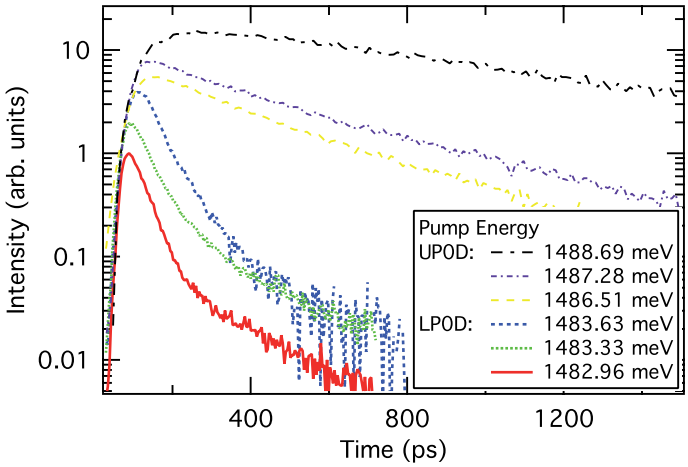

Figure 3.9: **Time-resolved photoluminescence intensity of a 9 μm diameter mesa**. Evolution of the ground state intensity for different excitation energies. When the excitation energy is resonant with LP0D states, we clearly distinguish two relaxation times. When the excitation energy is resonant with UP0D states, there is only one decay time. For the sake of clarity, the curves have been arbitrarily displaced along the vertical axis.

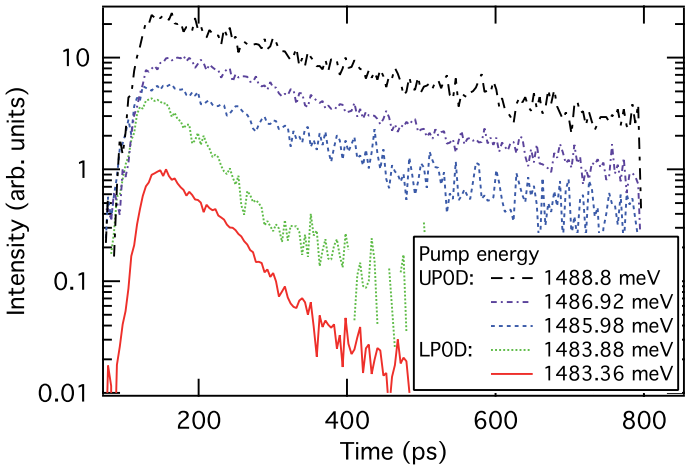

Figure 3.10: **Time-resolved photoluminescence intensity of a 3 μm diameter mesa**. Evolution of the ground state intensity for different excitation energies. Unlike Fig. 3.9, we observe a monoexponential decay at all excitation energies. For the sake of clarity, the curves have been arbitrarily displaced along the vertical axis.

Table 3.2: **Decay times in a Ø 3 μm mesa** TRPL intensity of the ground state for different excitation energies.. We observe only one decay time at each excitation energy.

Excitation energy [meV]	τ_S[ps]	τ_L[ps]
1483.36 (LP0D)	71	-
1483.88 (LP0D)	59	-
1485.98 (UP0D)	-	172
1486.92 (UP0D)	-	183
1488.80 (UP0D)	-	219

a) The relaxation of polaritons created in the UP0D involves polariton states with large excitonic content. Their long radiative lifetime determines the long decay time of the ground state TRPL intensity while exciting UP0D states.

b) Considering the interactions with the phonon bath, polaritons created in a LP0D state have two relaxation paths to the ground state: a direct path, to lower energy states, and an indirect path, corresponding to an initial scattering to states of higher energy followed by relaxation. This latter path possibly gives rise to a second decay time in the ground state luminescence intensity.

c) In the case of the Ø 3 μm mesa, the observation of a monoexponential decay while exciting LP0D states suggests that the indirect relaxation path is less efficient than in the Ø 9 μm mesa. This could be due to the larger energy separation of LP0D states in Ø 3 μm mesas.

The theory exposed in next section provides a comprehensive and quantitative theoretical description of our results.

3.5 Theoretical model

The theoretical analysis is performed in two steps. First, we compute the polariton quasimodes for the present non-uniform case [Savona 07]. Second, we map the polariton-phonon coupling into the basis of the obtained polariton quasimodes. This procedure is justified by the fact that, in spite of the present non-equilibrium regime, the quasiparticle approximation still holds, as discussed below.

3.5.1 Polariton quasimodes

Polariton quasimodes can be computed via Maxwell equations, as in Ref. [Savona 07], or by solving a non-equilibrium Schroedinger-like equation for the exciton-photon problem [Carusotto 05, Sarchi 08b]. The spectrum of excitation, i.e. the frequencies and the lifetimes, obtained within the two approaches is substantially the same, with minor quantitative differences. This quantitative agreement makes the quasiparticle approximation suitable to describe the present non-equilibrium regime.

The exciton and photon Bose fields $\hat{\Psi}_{x,c}(\mathbf{r})$ can then be safely written in terms of the polariton quasimodes as

$$\hat{\Psi}_{x,c}(\mathbf{r}) = \sum_{j,n} \psi_{x,c}^{j,n}(\mathbf{r}) \hat{p}_{j,n} \,, \tag{3.2}$$

where the label j defines the quantum number of the mode, and the label $n = \mathrm{lp,up}$ identifies the lower and the upper polariton branches, while $\hat{p}_{j,n}$ is the polariton annihilation operator obeying Bose statistics. Obviously the sum in Eq. (3.2) refers to both localized (0D) and delocalized (2D) modes. Let us remind here that the exciton and photon wave functions $\psi_{x,c}^{j,n}(\mathbf{r})$ have the same spatial profile, while their amplitudes depend respectively on the excitonic and photonic content of the corresponding polariton mode.

3.5.2 Coupling to acoustic phonons

By means of the decomposition (3.2), the Hamiltonian describing the coupling between the exciton field and the bath of acoustic phonons [Tassone 97] can be written in the basis of polariton quasimodes as

$$\hat{H}_{Xph} = \sum_{j,n,j',n',\mathbf{q}} t^{\mathbf{q}}_{(j,n),(j',n')} (\hat{a}_{\mathbf{q}} + \hat{a}^{\dagger}_{-\mathbf{q}}) \hat{p}^{\dagger}_{j,n} \hat{p}_{j',n'} \,. \tag{3.3}$$

The matrix elements $t^{\mathbf{q}}_{(j,n),(j',n')}$ involve the excitonic wave functions and are given by [Mannarini 06]

$$t^{\mathbf{q}}_{(j,n),(j',n')} = C_{\mathbf{q}} \sqrt{\frac{\hbar\omega^{ph}_{\mathbf{q}}}{A}} \int d\mathbf{r}\, \psi_x^{j,n^*}(\mathbf{r}) e^{-i\mathbf{q}_{\parallel}\cdot\mathbf{r}} \psi_x^{j',n'}(\mathbf{r}) \,, \tag{3.4}$$

where

$$C_{\mathbf{q}} = \frac{\left[D_e K_e(q_z)\chi(\mathbf{q}_{\parallel}\eta_{\mathbf{e}}) + D_h K_h(q_z)\chi(\mathbf{q}_{\parallel}\eta_{\mathbf{h}})\right]}{\sqrt{2u_s^2 \rho_M L_c}} \,, \tag{3.5}$$

A is the phonon quantization area, u_s is the sound velocity, ρ_M is the mass density, L_c is the cavity length, $D_{e,h}$ are the deformation potentials, $\eta_{e,h} = (m_e + m_h)/m_{h,e}$, $\omega^{ph}_{\mathbf{q}} = u_s(q_z^2 + \mathbf{q}_{\parallel}^2)^{1/2}$ is the frequency and $q_{\parallel}$ the in-plane wave vector of the phonon mode $\mathbf{q}$, and, for Gauss confinement and hydrogen-like electron-hole relative motion, $K_{e,h}(q_z) = \exp[-(q_z L_{e,h})^2/2]$ and $\chi(\mathbf{q}_{\parallel}) = [1 + (q_{\parallel}a_0/2)^2]^{3/2}$.

Accounting for the phonon coupling within the Markov approximation, and for the finite lifetime, the rate equations for the populations $N_{j,n} =< \hat{p}^{\dagger}_{j,n}\hat{p}_{j,n} >$ in the different polariton states (j,n) are [Tassone 97, Mannarini 06]

$$\begin{aligned} \dot{N}_{j,n} &= -\Gamma_{j,n} N_{j,n} + \sum_{j',n'} W_{(j',n'),(j,n)} N_{j',n'} \left(N_{j,n} + 1\right) \\ &- W_{(j,n),(j',n')} \left(N_{j',n'} + 1\right) N_{j,n} \end{aligned} \tag{3.6}$$

where the phonon scattering rates are [Tassone 97, Mannarini 06]

$$\begin{aligned} W_{(j,n),(j',n')} &= \sum_{\mathbf{q}} \mid t^{\mathbf{q}}_{(j,n),(j',n')} \mid^2 \left[n_B\left(|\Delta E^{j,n}_{j',n'}|\right) \right. \\ &+ \left. \theta\left(\Delta E^{j,n}_{j',n'}\right) \right] \delta\left(\hbar\omega^{ph}_{\mathbf{q}} - |\Delta E^{j,n}_{j',n'}|\right) \,, \end{aligned} \tag{3.7}$$

$\Delta E^{j,n}_{j',n'} = E_{j,n} - E_{j',n'}$ is the energy difference between the states (j,n) and (j',n'), $n_B(E)$ is the Bose distribution, while $\Gamma_{j,n}$ are the effective polariton lifetimes. These quantities are consistently obtained from the diagonalization of the exciton-photon problem.

Notice that in Eq. (3.7) the sum spans over all the momentum states of phonons, i.e. $q_z = (2\pi/L_c)n_z$ and

$$q_{x,y} = \frac{2\pi}{\sqrt{A}} n_{x,y}\,, \tag{3.8}$$

with $n_{x,y,z} = 0, 1, ...$, and where A is the phonon quantization area also appearing in Eq. (3.4). In the uniform case, for each couple of initial and final states, the only contribution is due to phonon modes having in-plane momentum equal to the momentum difference between the two states [Tassone 97]. Contrarily, in the trapped case, for two polariton states localized in a much smaller area, $A_{mesa} \ll A$ (i.e. wave functions $\psi^{j,n}_x(\mathbf{r})$ are localized within A_{mesa}), it is easy to prove that all the phonon modes with in-plane momentum comprised in the interval $\Delta q_x \times \Delta q_y = 4\pi^2/A_{mesa}$ around $\mathbf{q}$ equally contribute. This means that, for each couple of localized states, the number of phonon modes contributing to the relaxation is proportional to the inverse of A_{mesa}. Then we expect that the relaxation rates scale as $W \sim 1/A_{mesa}$.

On the other hand, the matrix element involving one delocalized and one localized polariton modes is given by Eq. (3.4) where one wavefunction is a plane wave:

$$t^{\mathbf{q}}_{(j,n),2D} \propto \int_{A_{\mathrm{mesa}}} d\mathbf{r}\, u^{j,n*}_x(\mathbf{r}) e^{-i\mathbf{q}_\parallel\cdot\mathbf{r}} \frac{e^{i\mathbf{k_{2D}}\cdot\mathbf{r}}}{\sqrt{A_{\mathrm{2D}}}} \tag{3.9}$$

here, A_{mesa} and A_{2D} are the quantizing surfaces for the mesa state and for the delocalized state, respectively. We consider the fact that A_{2D} is limited by the spatial extension of the excited planar polaritons.

For the ground state, $u^{0,lp}_x \sim 1/\sqrt{A_{\mathrm{mesa}}}$ and the contributing phonon modes have wave vectors $\mathbf{q}_\parallel \sim \mathbf{k_{2D}}$. The corresponding matrix elements are proportional to $\sqrt{A_{\mathrm{mesa}}/A_{\mathrm{2D}}}$.

For the calculations, we use a confining potential in agreement with the AFM images of the mesas [Daif 06], thus accounting for the slightly elliptical shape of the mesas. The decay rates are assumed to be $\gamma_c = 0.05$ meV, in agreement with the reported photon lifetime $\tau_c = 15$ ps, and $\gamma_x = 0.001$ meV. The other parameters are obtained from the experimental characterization of the sample.

The polariton quasimodes computation also accounts for the presence of two-body interactions, whose effect could be in principle very important and amplified by the reduced sizes. We have theoretically verified that, for the pump intensities used in this experiment, the system can be considered in the linear regime, the two-body interactions becoming relevant and eventually dominating only for pump intensities two-three order of magnitude larger.

3.6 Comparison

We now compare the theoretical predictions about polaritons modes and relaxation to the experimental results presented above. The thermalization efficiency and the

influence of dimensionality are discussed. Finally, the time dependent behavior of the relaxation is evaluated.

3.6.1 Polariton spectrum

The calculated luminescence spectrum for the LP0D is plotted in Fig. 3.11, together with an experimental spectrum. One can appreciate the correspondence of the observed and computed energies and linewidths. The theoretical spectrum is weighted by the photonic content of the states but does not take any relaxation mechanism into account. The strong intensity difference between theory and experiment for the excited states is a clear indication of the important role of relaxation mechanisms.

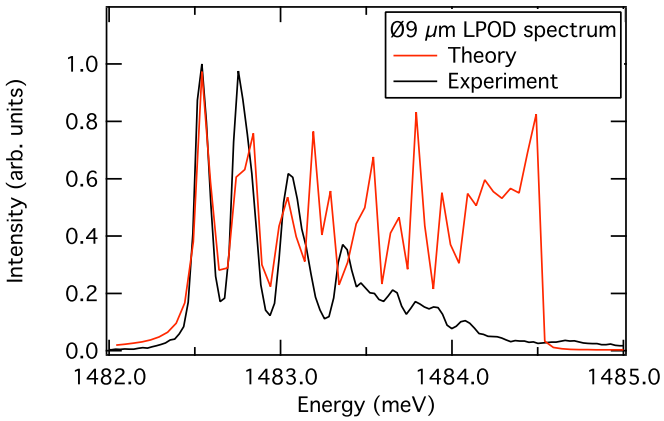

Figure 3.11: **Spectra of the LP0D under nonresonant excitation: theory and experiment.** Note that no relaxation process is taken into account in the plotted theoretical spectrum.

The energies of the polariton states obtained theoretically are in good agreement with the experiment and can therefore be used to simulate the relaxation between different states.

3.6.2 Thermalization

The relaxation is accounted for by applying the rate equations (Eq. (3.6)) to the predicted modes. These rate equations depend on the phonon scattering rates. Note that the scattering rates to states of higher energy decrease exponentially with the energy difference between the initial and final polariton states (see Eq. (3.7)). On the other hand, the scattering rates to lower energy states always have a spontaneous contribution coming from the Heaviside function θ.

In order to reproduce the thermalization experiments presented in Section 3.4.2, we computed the relaxation dynamics after resonant excitation of a UP0D state. The thermalization dependence on the mesa diameter is accurately reproduced, as shown in Fig. 3.7. The predicted effective temperatures are the same as the one obtained experimentally: 15 K and 40 K for the 3 μm and 9 μm diameter mesas, respectively.

As explained in Section 3.5, the scattering rate W between two 0D states is inversely proportional to the area of the mesa $1/A_{mesa}$ (Eqs. (3.4) and (3.7)). This explains the more efficient thermalization in the Ø 3 μm mesas.

The scattering rate between 2D and 0D states is predicted to be proportional to $\sqrt{A_{\mathrm{mesa}}/A_{\mathrm{2D}}}$ (Eq. (3.9)). In our case, this ratio is about 0.1 for $A_{\mathrm{2D}} \simeq$ 1000 μm^2 [Langbein 02]. Therefore, the calculation gives a 0D-0D coupling is nearly one order of magnitude greater than the 2D-0D coupling. This is consistent with the results of Fig. 3.8.

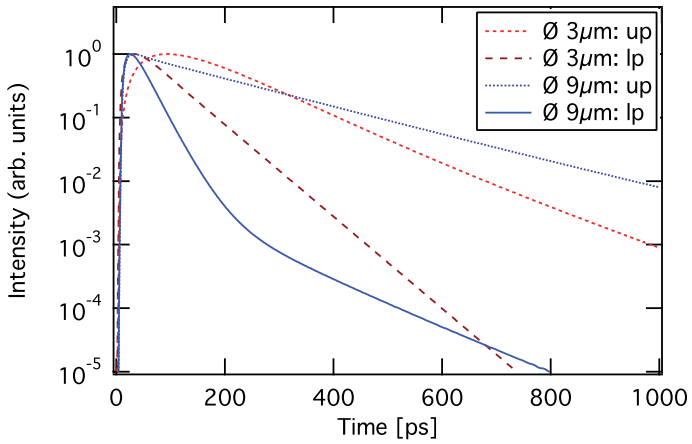

Figure 3.12: **Calculated TRPL.** Time evolution of the ground state intensity in a Ø 3 μm mesa and a Ø 9 μm mesa, when exciting resonantly the LP0D or the UP0D states. The behaviors of Fig. 3.9 and Fig. 3.10 are well reproduced by the theory. Two decay times are predicted in the relaxation of a Ø 9 μm mesa LP0D state.

3.6.3 Dynamics

The last comparison concerns the time resolved photoluminescence experiments. By solving Eq. (3.6), we obtain the time evolution of the population in each polariton state.

The experimental time evolution of the ground state emission intensity is displayed in Figs. 3.9 and 3.10. In Fig. 3.12, we plot the calculated time evolution of the population in the ground state for the two mesa sizes and for excitations in the LP0D and UP0D. The theory reproduces well the experiments. In particular, we obtain two decay times in the case of the Ø 9 μm mesa, when exciting resonantly a LP0D state.

The agreement is also quantitative. Decay rates have been extracted from the decay curves and the theoretical and experimental values are compared in Fig. 3.13. Here, the rates are plotted as a function of the excitation energy. The short decay times give rise to a fast decay regime, with rates between 10^{-2} and 2×10^{-2} ps^{-1}. The long decay times give rise to a slow decay regime, with rates between 2×10^{-3} and 5×10^{-3} ps^{-1}.

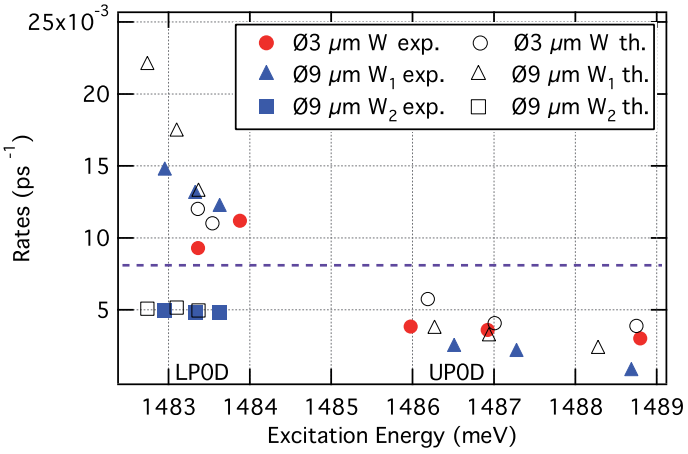

Figure 3.13: **Decay rates.** Measurements in the Ø 3 μm mesa and in the Ø 9 μm mesa (full symbols) and comparison with theory (empty symbols). The data points at lower/higher energy than 1485 meV correspond to excitations resonant with LP0D/UP0D states. The dashed line separates the different decay regimes.

3.7 General scheme

We now discuss how polariton states with large exciton content are responsible for the slow decay regime. As already discussed (cf. section spectroscopy), the states close in energy to the exciton resonance have a large exciton content (LXC), i.e. a small photon content and a long radiative lifetime. They are involved in the relaxation paths from the excited states to the ground state, thus fixing the decay times observed experimentally, for both excitations of UP0D and LP0D states.

Excitation of UP0D states

When exciting UP0D states, both Ø 3 μm and Ø 9 μm mesas present only a slow decay regime. The relaxation of UP0D states to the ground state requires many polariton-phonon scatterings. This results from Eq. (3.7), which asserts that the relaxation is favored between polariton states with small energy difference. Therefore, the relaxation of UP0D states most probably involves large exciton content (LXC) states. These states have a radiative lifetime τ_{LXC} much longer that the one of the ground state τ_{GS}. This is represented in Fig. 3.14 (a).

Due to the very efficient interactions with the phonon bath (cf. Eqs. (3.7) and (3.4)) and to the efficient thermalization observed in Ø 3 μm and Ø 9 μm mesas, we have the relation $\tau_{\mathrm{ph}} \leq \tau_{\mathrm{GS}} < \tau_{\mathrm{LXC}}$. In this case, as sketched in Fig. 3.14 (a), the rise time of the ground state luminescence intensity corresponds to τ_{GS}. Its decay reflects the population decay in the states with large excitonic content, i.e. τ_{LXC}. This leads to the observation of small decay rates in Fig. 3.13. The p-PLE experiment (Fig. 3.6) show that the number of LXC states increases with the diameter of the mesa. We thus expect a slower decay regime in the Ø 9 μm mesa than in the Ø 3 μm mesa. This difference can be appreciated in Fig. 3.13.

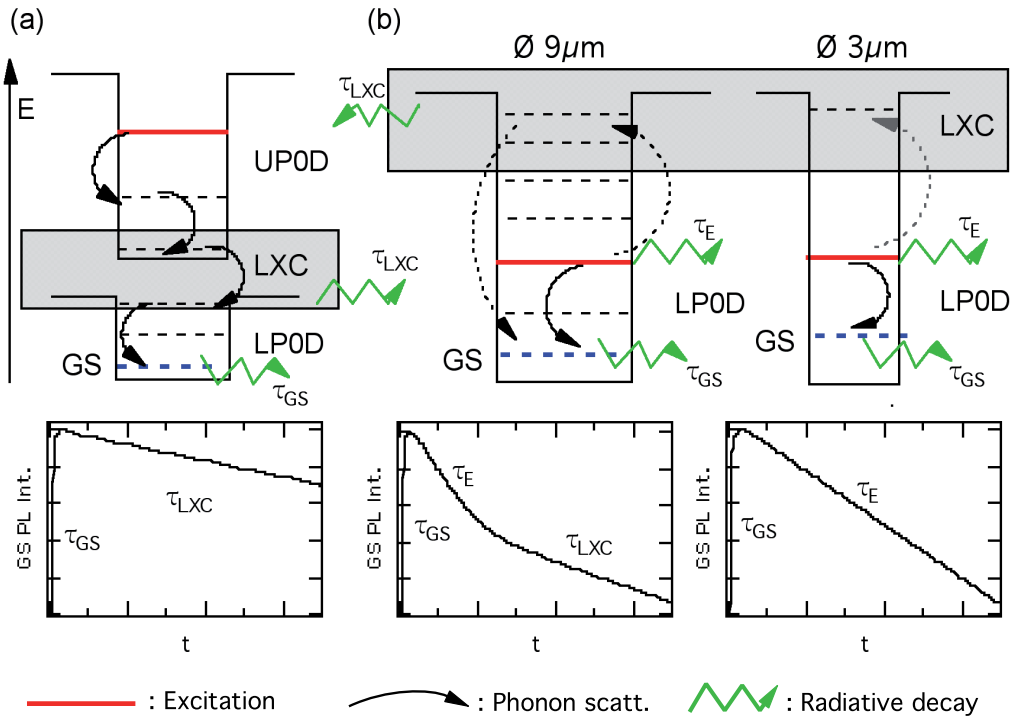

Figure 3.14: **Relaxation scheme.** Role of LXC states in polariton relaxation to the ground state (GS). (a) The excitation is resonant with a UP0D state. The relaxation necessarily involves LXC states. We observe only one decay time in the TRPL intensity of the ground state. (b) The excitation is resonant with a LP0D state. In a Ø 9 μm mesa, two relaxation paths are possible, giving rise to two decay times in the ground state TRPL intensity. In case of a Ø 3 μm mesa, the scattering to states with large exciton content (LXC) is inefficient because of the too large energy separation between the localized states. In the bottom panels, we plot the TRPL intensity of the ground state as predicted by theory.

Excitation of LP0D states

When exciting LP0D states, we observe two decay regimes for the Ø 9 μm mesa and only one for the Ø 3 μm mesa. Due to the very efficient coupling to the phonon bath and to the finite temperature ($T > 0$), the thermalization process of the LP0D states also populates LXC states. Therefore we must consider two possible relaxation paths to the ground state, as represented in Fig. 3.14 (b). The direct relaxation path manifests itself in a fast decay regime, whereas the indirect relaxation path, involving LXC states, manifests itself in a slow decay regime. Again, this contribution is more important for Ø 9 μm mesas than for Ø 3 μm mesas, because of the larger number of LXC states available. Moreover, the energy separations between Ø 9 μm mesa levels are smaller compared to the lattice thermal energy ($k_B T \simeq 0.5$ meV). As a result, we do not observe a slow decay regime in the Ø 3 μm mesa.

3.8 Conclusion

To conclude, let us summarize the physical relevance of this chapter. We showed the limitation of the use of nonresonant excitation to investigate polariton relaxation. Indeed, in this case, the measured dynamics is then governed by the slow excitons relaxation dynamics in the quantum well.

Thermalization

By means of resonant excitation, we obtained the most important result of this chapter, which is the observation of thermalization for microcavity polaritons under lateral confinement, in the low polariton density regime (Sect. 3.4.2). We demonstrate that there is a dependence of the thermalization efficiency on the size of the confinement. For wide traps, we recover the case of planar microcavities, where thermalization is not efficient in the low-density regime.

2D-0D coupling and LXC states

These studies lead us to two other observations. First, the relaxation between 2D and 0D polaritons is not favored in our system. This is critical regarding our possibilities of producing trapped BEC like in Ref. [Balili 07].

Second, by studying the thermalization dynamics, we could put in evidence the contribution of polariton states that have a large excitonic content. Not only this contribution is non negligible, it is also an important issue because of the quasi non-radiative (hence long-lived) nature of those states. Their presence has the effect of a polariton reservoir that slowly relaxes to the low energy state. We will give additional evidence of their role in the next chapter.

Relaxation scheme

We presented a theoretical model of the relaxation of confined microcavity polaritons, focusing on the polariton interactions with acoustic-phonons (Sect. 3.5). The very good quantitative agreement of the theory with all the experimental results presented in the manuscript supports the identification of *polariton-phonon scattering* as the *main relaxation process* in our system. We could then produce a comprehensive scheme of relaxation and thermalization of polaritons under confinement of different sizes and in the linear regime.

The influence of nonlinear effects due to polariton-polariton interactions is studied in the next chapter.

Chapter 4

Collisional Damping of Dipole Oscillations

4.1 Introduction

In the previous chapter, we have shown that, in the linear regime, polariton thermal relaxation is enhanced by lateral confinement. This facilitates the creation of a thermalized gas in the lower polariton dispersion branch, which is necessary to obtain a Bose Einstein Condensate (Sect. 3.2.3). It is important to recall that in the linear regime, the relaxation is mediated by polariton interactions with the lattice and hence does not preserve the coherence in the system. We now propose to investigate the polaritons relaxation dynamics in the nonlinear regime, i.e. in the presence of polariton-polariton interactions.

As we will see (c.f. Section 4.2), nonlinear effects have already been extensively explored in planar cavities and in micropillars, with remarkable outcomes. Our microcavity sample, which is in one sense limited regarding the fact that it contains only one quantum well, is paradoxically an interesting lab for these studies.

Indeed, as shown in Section 3.3.2, the exciton bleaching occurs at too low densities to observe significant polaritonic nonlinearities under nonresonant excitation. For instance one could ask: *in our sample, under resonant excitation, is the dynamics still limited by the saturation density?*

The question is non trivial. Under resonant excitation, the only source of exciton bleaching is the phase space filling. If, in our sample, we can observe significant nonlinearities, it would for instance give additional confirmation that the loss of strong coupling under nonresonant excitation is the consequence of the screening of Coulomb interactions than that of the phase space filling.

The previous work by O. El Daif on the same sample suggested the possibility of observing stimulated relaxation by resonant excitation experiments in a 9 μm diameter mesa [El Daif 08, El Daif 07]. By increasing the excitation power, he could observe a threshold power from which the emission was strongly dominated by the ground state. The emission intensity first increased linearly with the pump power, then quadratically before reaching a saturation regime. The hypothesis of a stimulated parametric process was put forward but he could not observe any idler. The reason is probably that the idler state was of large exciton content, so weakly coupled

to light.

We choose to perform time resolved experiments to observe the effects of nonlinear interactions on the spatial dynamics of a confined polariton gas. We create the polariton gas in a superposition of the three lowest energy states, which results in a large amplitude dipole oscillation state in the real space and momentum space. Because of the high polariton density, this state experiences collisional relaxation. This results in a strong time dependent damping of the dipole oscillations. We investigate this relaxation as a function of the polariton density and polarization. The latter highlights the role of interactions, because the change of polarization directly affects the effective strength of the interactions between polaritons [Shelykh 05].

We start this chapter with a review of nonlinear effects in planar cavities and in micropillars (Section 4.2). We describe the experiment in Section 4.3, and present our results in Sections 4.4 and 4.5. A comparison with theory is given in Section 4.6. Finally, in Section 4.7, we give a general conclusion on our time resolved experiments on polariton relaxation in mesas.

4.2 Review on polariton nonlinearities experiments

4.2.1 Motivation

It is obviously a hard task to detail all the work done about polariton nonlinear relaxation. We propose a chronological review of the major developments in this field. So let's go back to 1992, when Claude Weisbuch and the group of Arakawa published the first observation of strong coupling between light and excitons in microcavities [Weisbuch 92]. The authors directly acknowledged the importance of strong coupling in the solid-state and its potential consequences on the nonlinear effects of excitons (like increasing VCSEL efficiency for electro-optical devices [Keller 93, Miller 84]).

Two years later, Houdré et al. published experimental measurements of the polariton dispersion [Houdré 94] and studies of the saturation of the polariton resonance [Houdré 95]. These works were among the first to treat polaritons as quasiparticles and, from then, the interest on polaritons increased very rapidly. The observation of Bose-Einstein condensation in the middle of 1995 by Cornell and Wieman et al. [Anderson 95] and by the group of Ketterle [Davis 95] strongly motivated the quest for bosonic effects in many systems. In the case of exciton-polaritons, the proposals of Imamoglu of an exciton-polariton laser without inversion consisted in exploiting the bosonic nature of polaritons to generate a stimulation of the polariton-phonon relaxation and obtain a macroscopic coherent exciton-polariton state [Imamoglu 96a, Imamoglu 96b]. In the mean time, the group of Cirac and Zoller also made a proposal for an atom laser by using a Bose-Einstein condensate as a source of coherent atoms [Holland 96].

We will see that the subsequent works with microcavity polaritons were very controversial. A major confusion came from the fact that it is not simple to distinguish experimentally an exciton-polariton laser from a photon laser.

In addition, bosonic stimulation was often regarded as an exceptional mechanism that necessarily leads to a "boser", i.e. a macroscopic coherent state. Furthermore, in the first experiments, polariton nonlinearities were mistaken and directly

attributed to bosonic stimulation.

In fact, bosonic stimulation is a feature of all relaxation processes involving bosons. It simply means that, for bosons, the probability of transition between an initial and a final state depends on the occupation number o the final state. The build-up of a macroscopic occupation number in a state depends on the time scales of the system (relaxation rates, radiative lifetimes). Finally, there are substantial differences whether the systems is strongly out of equilibrium (case of resonant excitation experiments) or close to equilibrium (case of single source, nonresonant excitation experiments). In this latter case, the system undergoes a thermodynamically driven phase transition and might be referred to as a BEC. In the other cases, we will see that there are several appellations.

The issue is nicely formulated in the abstract of Ref. [Holland 96]:

"Superconductivity, superfluidity, Bose-Einstein condensation, and laser amplification are all examples of a general mechanism involving the stimulated transfer of bosons into a specific quantum state. When the occupation number of the state is large, this mechanism may generate a macroscopic coherence for the state amplitude"

The first claims of observing polariton lasing under *nonresonant excitation* faced these difficulties [Pau 96]. The observed phenomenon was actually conventional photon lasing [Kira 97, Cao 97, Fan 97], showing that, under nonresonant excitation, the saturation due to exciton bleaching prevailed on the build-up of polaritons nonlinearities. It is interesting to note that, in the meantime, Tredicucci et al. proposed to take advantage of the saturation to achieve polariton optical bistability [Tredicucci 96]. The prediction of a polariton relaxation bottleneck by Tassone et al. might have been another "bad news" [Tassone 97]. However, between 1997 and 2002, a series of crucial experiments under *resonant excitation* provided deep enlightenment of polaritonic nonlinearities.

4.2.2 Nonlinear emission

The first evidences of polariton nonlinear emission were reported by four-wave mixing experiments in a GaAs cavity [Kuwata-Gonokami 97]. Then Dang et al. [Dang 98] demonstrated nonlinear emission in a CdTe cavity under nonresonant excitation. Following demonstrations of nonlinear emission under nonresonant excitation in GaAs [Senellart 99] and InGaAs [Tartakovskii 99] proved that the relaxation bottleneck could be suppressed by increasing the polariton density. In particular, Senellart showed the existence of two nonlinear thresholds in the emission intensity: the first one corresponding to the suppression of the relaxation bottleneck, the second one corresponding to the photon laser transition.

Nonresonant excitation

The nonlinearities were first attributed to stimulated relaxation processes. This was very controversial [Khitrova 99], especially for nonresonant excitation in GaAs microcavities, since in previous experiments, stimulated behavior occurred only in the weak coupling regime [Cao 97]. Huang, Tassone and Yamamoto, showed that in the

case of Ref. [Senellart 99], the nonlinearities observed under nonresonant excitation were most probably the result of exciton-exciton scattering in the bottleneck region [Huang 00, Tartakovskii 00][1].

Later, other experiments would confirm this point, showing that stimulation appeared only in the weak coupling regime [Bloch 02, Butté 02] in GaAs samples and appealing to more improvement of microcavity samples [Bloch 98b, Jensen 00].

In the case of CdTe microcavities, stimulated behavior under nonresonant excitation was confirmed by the group of Dang via pump-probe experiments with one *nonresonant pump* and one *resonant probe* at k=0 [Boeuf 00, Alexandrou 01].

Resonant excitation

The studies under resonant excitation were also the subjects of active discussions. Polariton-polariton scattering was first investigated in 1997 by a four-wave mixing experiment [Kuwata-Gonokami 97]. Then, using the same method, Baars et al. could confirm an interesting prediction by Ciuti about a threshold dependence for the linewidth homogeneous broadening due to collisions [Ciuti 98, Baars 00].

Savvidis et al. observed stimulated parametric scattering in pump-probe experiment. [Savvidis 00a]. Their idea was to send a pump at different angles and to probe the k=0 state. They observed a resonance at the inflection point of the polariton dispersion. Another experiment, this time with a single cw pump [Stevenson 00], showed the same resonance at the so-called "magic angle".

This work was followed by the experiments of Houdré in the far field emission [Houdré 00], and lead to the theory by Ciuti [Ciuti 00a, Ciuti 00b] on polariton-polariton parametric scattering. In this theory those phenomena are explained as gain due to phase-matched condition more than boser effect. The theory is verified by Messin et al. [Messin 01], who observed the phase dependence of the amplification, signature of a polariton wave mixing process.

Let us clarify these experiments in the following way. Polariton-polariton scattering is by definition a parametric process, which scatters two polaritons towards two different states of the dispersion curve while conserving energy and momentum. For instance, at the magic angle, a peculiar phase matching condition is reached. There exist several possible collisions preserving energy and momentum, giving rise to the famous eight-shaped pattern observed by Langbein [Langbein 04]. Using an additional probe beam, it is possible to enhance a particular parametric process by increasing locally the density; we talk of **parametric amplification**. Parametric scattering can be spontaneously amplified if the pump reaches a critical density; we talk of **parametric luminescence**. At the magic angle, relaxation generally creates a population imbalance to the benefit of a given state (in general at $\mathbf{k} = 0$). Above a critical density in the signal or idler state, the gain diverges and one observes the build-up of a macroscopic coherent state; we talk of **parametric oscillation** [Ciuti 01].

[1] Huang et al. injected two exciton populations with opposite wavevectors and observed stimulated scattering of excitons towards the k=0 state of the polariton branch.

4.2.3 Amplification, condensation

These works, which provided clear understanding of the different polariton nonlinearities, were followed by very successful developments. We highlight the coherent control of parametric scattering [Kundermann 03], the demonstration of a high temperature polariton amplifier [Saba 01], the time resolved observation of spontaneous parametric scattering and amplification in the momentum space after a resonant pulsed excitation [Erland 01, Langbein 04], and the prediction by Porras of Bose Einstein condensation in CdTe microcavities [Porras 02b], which lead to the first unambiguous demonstration of polariton BEC [Richard 05, Kasprzak 06] in CdTe. Regarding confining structures, squared Dasbach et al. reported parametric scattering in a squared micropillar [Dasbach 01]. Recently, the group of J. Bloch demonstrated parametric luminescence as well as polariton lasing in micropillars [Bajoni 07a, Bajoni 08b]. Bose-Einstein condensation was reported in microcavities with a stress trap by the group of D. Snoke [Balili 07].

4.2.4 Other issues

Biexciton The formation of biexciton and their impact on the polariton-polariton interactions are important issues that have been studied by different groups [Saba 00, Combescot 09, Baars 01, Borri 00, Kwong 01]. We will see in the next chapters the strong impact of biexcitons on polariton interactions. In particular, Saba et al. observed biexciton polaritons in four-wave mixing experiments.

Bistability Another issue is the third order nonlinearity, which is responsible for polariton bistability. In parallel to the intense debate on stimulated processes, some experiments investigated polariton bistability and resulting noise reduction [Baas 04a, Karr 04, Cavigli 05]. We report two attempts to link both effects [Gippius 04, Baas 04b]. In the next part of this thesis, we study polariton nonlinearities in the bistability regime and show how it is related to the parametric oscillation regime.

Polarization The polarization dependence of polariton-polariton interaction has been investigated by Martín et al. and Lagoudakis et al. [Martín 02, Lagoudakis 02] and a general theory has been developed by Shelykh, Kavokin and Malpuech [Shelykh 05].

4.3 Experimental procedure

4.3.1 Experimental setup

The goal of this experiment is to study the consequences of polariton nonlinearities on the spatial dynamics of polaritons in a mesa. We want to measure the time resolved evolution of the polariton gas in the momentum space, together with the time resolved evolution of the dispersion. In addition to the peculiar detection scheme, we need selective excitation of the momentum space and control on the excitation polarization.

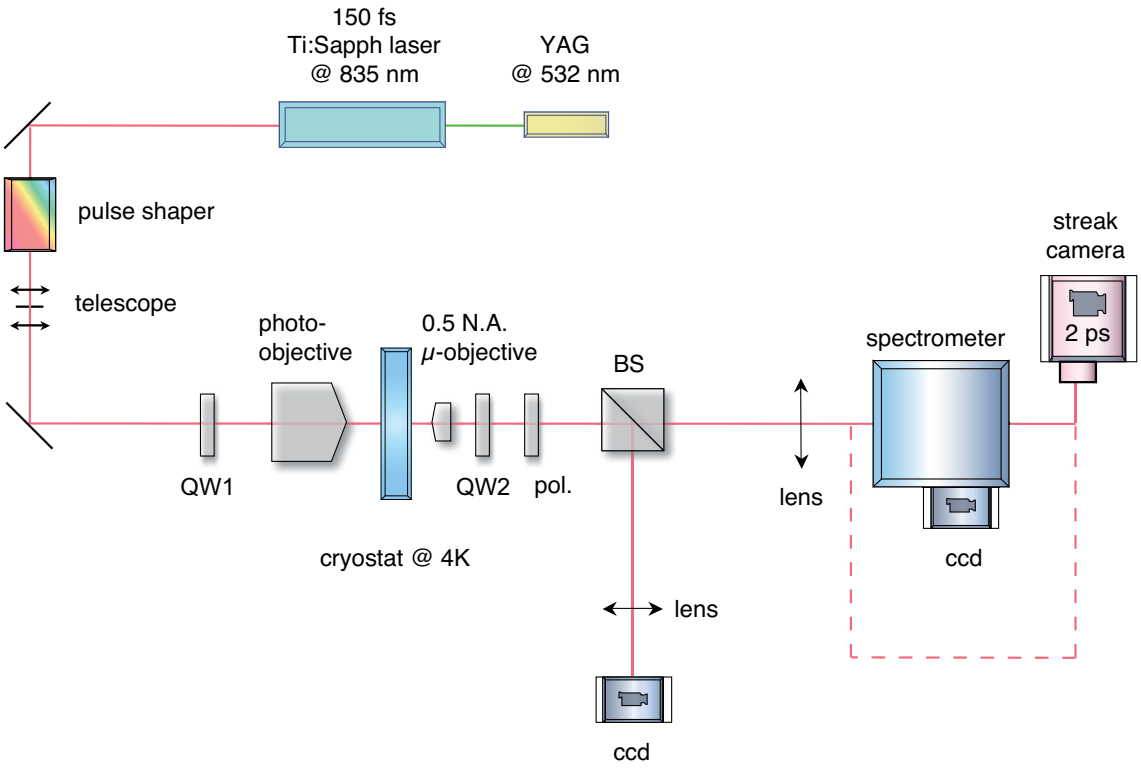

Figure 4.1: **Setup.** The telescope and the pulse shaper are used to control the excitation selectivity in energy and momentum. It is possible to excite one or a few polariton states. The incident laser can be displaced from the optical axis to give an angle to the excitation. The focus is realized with a photo-objective of 50 mm focal length. The emission is collected using a large numeric aperture microscope objective. The emission is then sent to the streak camera either directly via the dashed path, either via the monochromator to obtain time resolved spectra. The imaging lens is mounted on a motorized translation stage to allow wavefront scanning in front of the slits of the spectrometer or of the streak camera. The $\lambda/4$ plate (QW1) is used to switch from circularly to linearly polarized excitation. The detection in the circular polarization basis is done with another $\lambda/4$ plate (QW2) and a polarizer (pol.).

The experimental setup is depicted in Figure 4.1. As for the pulsed PLE experiment, the femtosecond pulses are first sent to a pulse shaper to obtain 10 ps pulses with less than 500 μeV FWHM. The focus on the sample is done with a photo-objective. We can shift the incident beam from the optical axis in order to give a precise angle to the excitation and to thus select its direction in the momentum space. The combination of narrow pulses in energy domain and momentum space makes possible the excitation of single polariton states. Using a telescope, we can adjust the spot size on the sample, so the excitation selectivity in the momentum space: the narrower the excitation spot is in real space, the wider it is in reciprocal space.

Before the photo-objective, a quarter waveplate (QW1) can be inserted in order to change the excitation from linearly to circularly polarized.

On the detection side, the signal is collected with a 0.5 N.A. microscope objec-

tive and sent to the monochromator, which we use in conjunction with the streak camera to produce time resolved spectra. The imaging lens is mounted on a motorized translation stage in order to scan the image wavefront on the slits of the spectrometer. We acquire successive time resolved spectra, each corresponding to a different slice of the momentum space. By this, we are able to reconstruct the time evolution of the spectral distribution along one momentum direction (k_x,E,t).

A path to send the signal directly to the streak camera is also required to measure the polariton dynamics in the momentum space[2]. We thus deviate part of the signal after the imaging lens. We form an intermediate image (equivalent to the one at the monochromator entrance), which is re-imaged on the slits of the streak camera through a bypass path (dashed).

Finally, the co- and counter-circularly polarized signals (referred to as $\sigma+$ and $\sigma-$ signals) are resolved using a second quarter wave plate (QW2) and a polarizer. For a circularly polarized incoming laser, the $\sigma+/\sigma-$ intensity ratio is of more than two orders of magnitude.

4.3.2 Procedure

The in-plane wave vector $k_\parallel$ of microcavity polaritons is directly related to the angle θ of the excitation beam by $k_\parallel = \frac{E_p}{\hbar c}\sin(\theta)$. This relation allows highly selective excitation of individual states, by adjusting both the energy and angle of the excitation beam. To obtain an incidence angle θ, we have to shift the excitation of a distance d from the optical axis such as $d = f\tan(\theta)$, f being the effective focal length of the photo-objective.

We study 9 μm diameter mesas with ground state excitonic Hopfield factors X_{X}^2 ranging from 0.4 to 0.7.

4.3.3 Single state dynamics

One can expect that, if the energy separation between the states is larger enough and if the excitation is very narrow in momentum space, it would be possible to excite a single state and to observe its time evolution.

We tried this experiment with a slightly negatively detuned mesa, using the telescope to obtain large excitation spots. The slightly negative detuning allowed large enough energy difference between the states, and the large spot size (about 50 μm) allowed very narrow excitation in the momentum space. The states were excited at very low power, to avoid any blueshift, which might have introduced a contribution from the other excited states. In Figure 4.2, one can see panels describing the reconstructed time evolution (k_x, k_y, t) for the 5 lower energy states. We adjusted the excitation conditions to maximize the resonance alternatively with the ground state (GS), the two lobes (E1), fours lobes (E2) and six lobes (E3) states and the n=2 state (N2). The laser pulse arrives at $t = 6$ ps and last for about 10 ps. Qualitatively, we can assume that after the maximum is reached, (for $t > 21$ ps),

[2]This could be done by setting the monochromator to zero order as in the TRPL experiments of the previous chapter. However, this solution is not convenient here, since we need to have simultaneously spectral information on the laser and the mesas during our experiments

the states evolve independently from the laser. We notice that the lobes, which result from interference between the $\pm m$ degenerate states are well defined only after 30 ps. Then the intensity decreases without any significant change in the lobe pattern. The differences between the different states decay times are negligible.

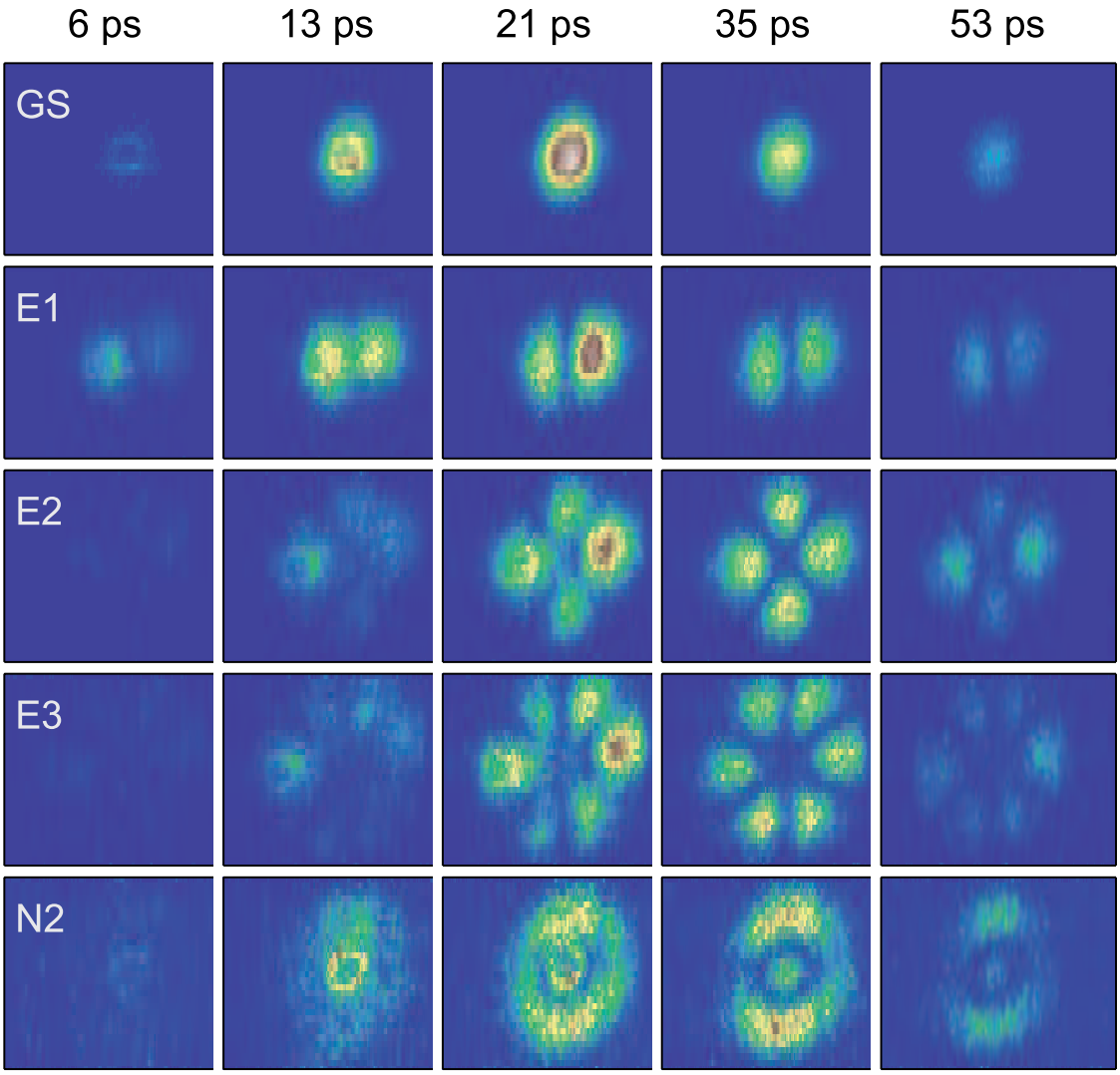

Figure 4.2: **Single state evolution.** We excite resonantly single confined polariton states to see their evolution in time. The confined modes can be labeled with two quantum numbers, $n \geq 1$, the radial number, and m, the angular momentum number. The $\pm m$ states are degenerate so that under nonresonant excitation, they interfere producing lobes in the angular direction. The number of lobes in the radial direction is given by n and the number of lobes in the angular direction is twice the angular momentum number $2|m|$ (see [Cerna 10, Nardin 09b]). The laser arrives at $t = 6$ ps. The lobe pattern formation, coming from interference between opposite angular momentum states, is complete only after 30 ps. The rise and decay times are qualitatively the same for all the states.

4.3.4 Multiple states dynamics: dipole oscillations

To access a dynamics of polaritons in the momentum (hence, the real) space, we need to excite simultaneously several states. In an experiment proposed by R. Cerna, we studied the polariton spatial dynamics in the linear regime as a function of the number of interfering states [Cerna 10]. In the small mesas, only a few states were excited simultaneously and the dynamics was well described in terms of interference. In the 20 μm diameter mesas, a very large number of states were excited and the dynamics was better described in terms of propagating wavepacket, like in planar polariton systems.

In the present experiment, we are interested in the effects of nonlinearities on the polariton dynamics. In order to simplify the experiments, we focus on the *three lowest energy states* GS, E1 and E2. A simple phenomenological model can be used to illustrate the resulting dynamics. The analytical expressions for bound states in a cylindrical potential by Leyronas and Combescot [Leyronas 01] can be applied to mesas[3]. The states are given by Bessel functions and using their energy differences one can simulate their relative phase evolution. In Figure 4.3, we show the time evolution of the resulting interference for the very simple case of GS and E1 only. The probability distributions of two states are plotted in Fig. 4.3 a, together with their relative phase. Note that there is a π phase shift between the two lobes of the first exited state. During the evolution, the two lobes will then be alternatively in and out-of phase with the ground state. We thus expect to observe dipole oscillations in the momentum space. The calculated interference patterns are plotted every 10 ps in Fig. 4.3 b.

Experimental results are discussed in the next section. Section 4.6 describes the theoretical investigations in the framework of a mean field Gross-Pitaevskii equation.

4.3.5 Nonlinearities and dipole oscillations

We now present the experimental results. We excite the 9 μm diameter mesas in a coherent superposition of GS, E1 and E2 to create dipole oscillations. Then we raise the excitation power to increase the initial polariton density and therefore to trigger nonlinear effects.

Changing excitation polarization is a way of controlling polariton interactions. They are expected to be more efficient between co-polarized polaritons. We thus expect to see a difference between experiments under linearly and circularly polarized excitation.

Note that a great advantage of pulsed excitation is that the system evolves spontaneously after the excitation. We present experiments done at negative and positive detuning. A qualitative description of the negative detuning experiment is enough to show the effect of blueshift and indicates a contribution from polariton-polariton collisions. At positive detuning, we evidence the signature of final state stimulation in the spontaneous damping of the dipole oscillations. The role of collisions is highlighted in the latter case.

[3]A more detailed investigation of polariton wavefunctions in mesas has been done by Nardin [unpublished]. Due to mesas ellipticity, the states are better described in terms of Matthieu functions.

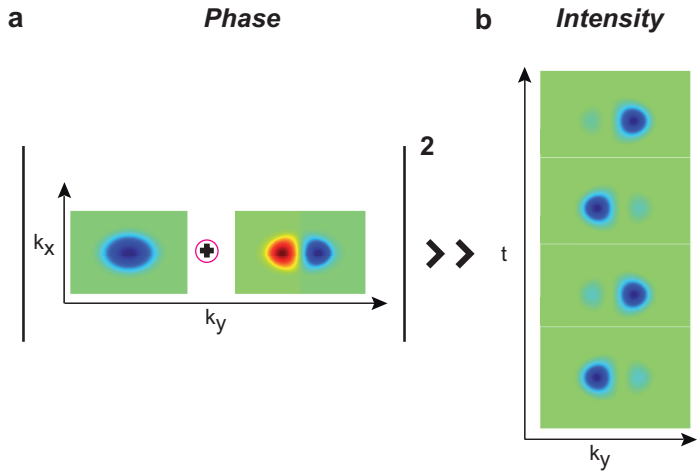

Figure 4.3: **Tutorial.** The dynamics of polaritons in the momentum space results from the evolution of the relative phase (color) between the states excited by the laser. **a** The ground state and the first excited states are represented in momentum space. E1 lobes are in phase opposition. **b** During the evolution, if one lobe interferes constructively with GS, the other interferes destructively, giving rise to a dipole oscillation dynamics.

Terminology

Note that, in the following, we use the following notation to describe our experimental polarization conditions:

$\sigma+$: we use **right-circular excitation** and detect the right-circular signal.

$\sigma-$: we use **right-circular excitation** and detect the left-circular signal.

lin.: we use **linearly polarized excitation** and detect the right-circular signal (except if indicated).

4.4 Negative detuning

4.4.1 Dipole oscillations

In Figure 4.4, we first show dipole oscillations obtained in a 9 μm mesa at slightly negative detuning. The excitation power is 10 μW. The in-plane laser momentum is $k_{\text{laser}} = 0.5\ \mu\text{m}^{-1}$. The first maximum occurs at $t_0 = 18$ ps. At this time, the laser is forcing constructive interferences for the $k_X > 0$ lobe, and consequently destructive interferences for the $k_X < 0$ lobe. 14 ps later, the maximum is localized on the $k_X < 0$ lobe. One can already assume that the system is evolving spontaneously. The following sequence of snapshots taken every 14 ps show clear evidence of dipole oscillations with a period $T = 28\ ps$.

4.4.2 Reduction of the oscillation amplitude

What is happens if we increase the polariton density?

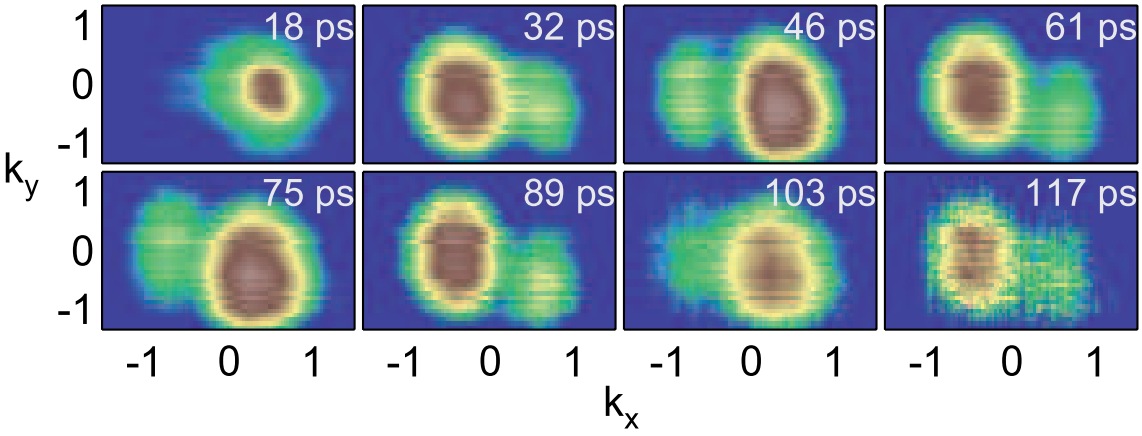

Figure 4.4: **Dipole oscillations (log color scale).** Spontaneous dynamics of a 9 μm diameter mesa at *negative detuning* after pulsed excitation of a coherent superposition of GS,E1 and E2. We observe dipole oscillations of constant amplitude.

We repeated the experiment for excitation powers of 1, 10 at 20 μW. In addition, we used both circularly and linearly polarized excitation. The signal was in all cases detected in the $\{\sigma+,\sigma-\}$ basis. In this basis, the excitation polarization was either $\sigma+$, either $\frac{\sigma+ + \sigma-}{\sqrt{2}}$. To have a better understanding of the experiments, we integrate the (k_x, k_y, t) matrix over the k_y direction. We obtain the 2D images (k_x, t) displayed in Figure 4.5.

The upper panel shows the results in $\sigma+$. The middle panel show the results in $\sigma-$. The third panel also displays the $\sigma+$ results, but with normalized intensity at each time. The data obtained under linearly polarized excitation at 20 μW are shown on the last column.

From the top panel, one can see the important changes in the dynamics when we excitation power increases. At 1 and 10 μW, we can observe oscillations between quite distinct lobes. At 20 μW, the oscillations seem to be more continuous and the lobes are not well resolved. Strikingly, the oscillations at 20 μW under linearly polarized excitation resemble more the 10 μW case under circularly polarized excitation. But even more striking is the fact that an identical behavior is detected in the counter-circular polarization $\sigma-$ (middle panel).

An unambiguous representation of these effects is given in the normalized intensity in the lower panel of Fig 4.5. By tracking the maximum at each time we see that the oscillation amplitude decreases with the excitation power and that the dynamics evolves from a squared oscillation pattern to a more continuous pattern. Under linearly polarized excitation, the reduction of the amplitude is clearly negligible.

4.4.3 Evidence for a polariton blueshift

We plot time evolution of the maxima in Figure 4.6. The reduction of the oscillation amplitude is illustrated in Fig. 4.6 a. The amplitudes obtained at 20 μW are compared in Fig. 4.6 b. The oscillation amplitude is lower under circularly polarized excitation than under linearly polarized excitation. Moreover, we notice that the

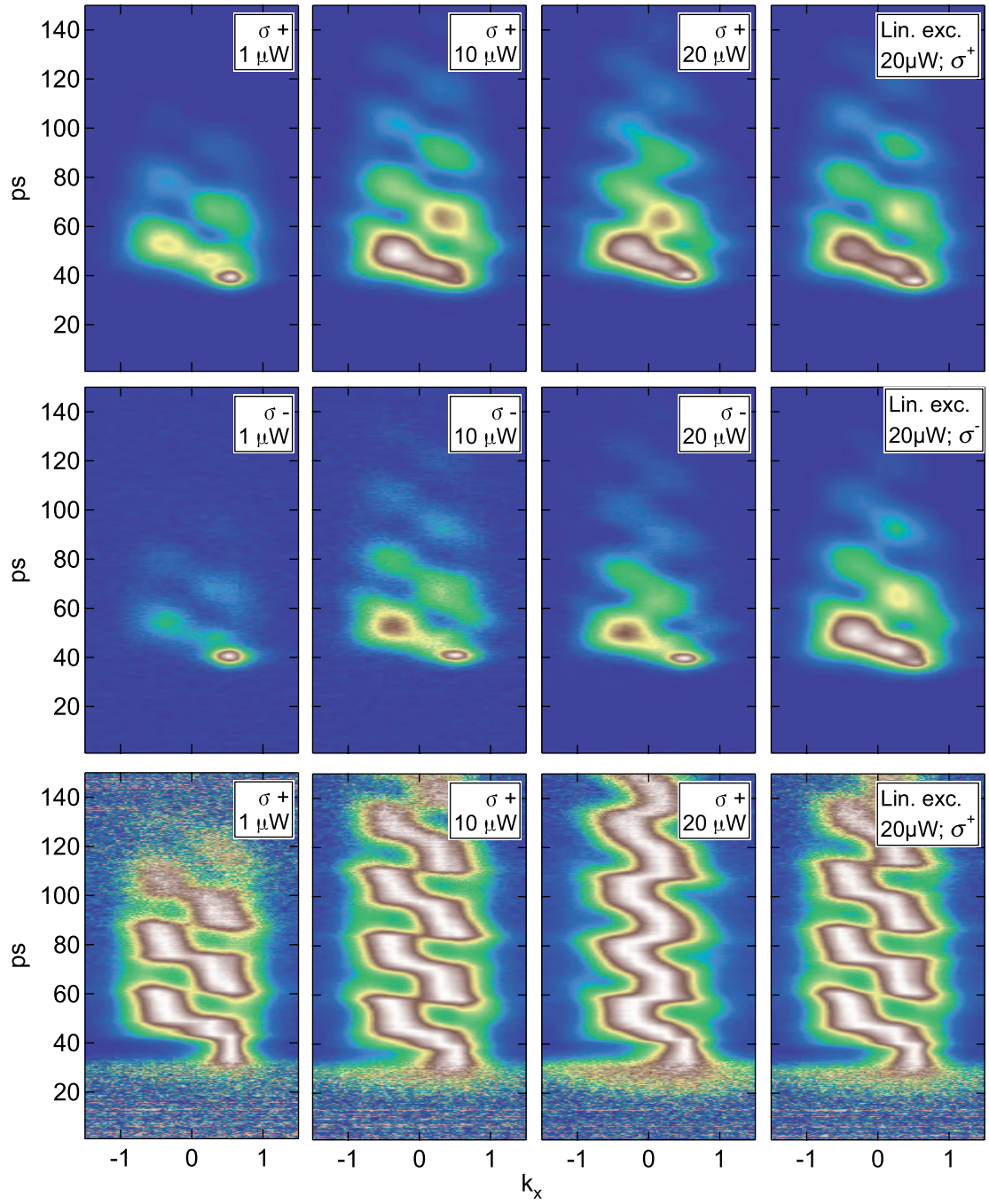

Figure 4.5: **Amplitude vs power.** Oscillation amplitude in function of the pump power and polarization detected in $\sigma+$ (Top) and $\sigma-$ (Middle). The bottom panel show the $\sigma+$ data normalized at each time. The proportion of GS in the superposition fixes the initial amplitude of the dipole oscillation. The greater the GS proportion, the low the amplitude. We see that this proportion increases as the power is raised. We see that, at 20 μW, the oscillation amplitude is larger under linearly polarized excitation. We attribute this effect to a blueshift induced by polariton-polariton collisions.

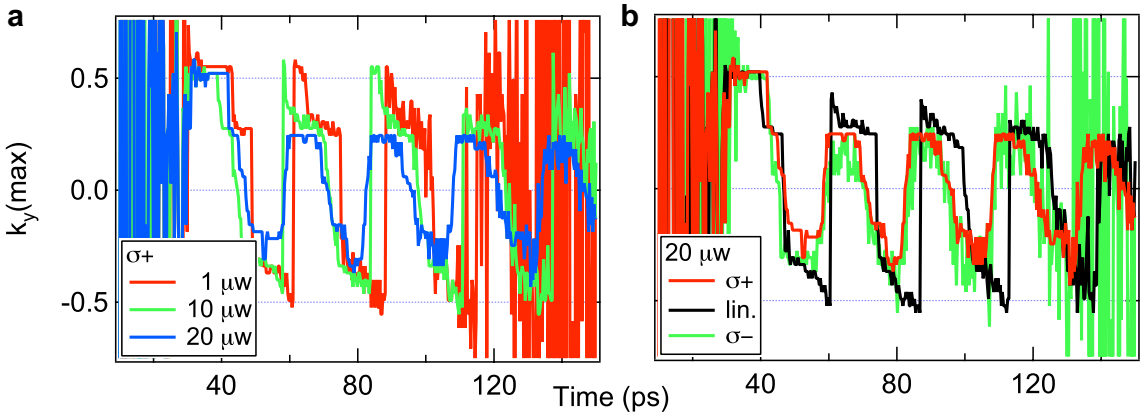

Figure 4.6: **Position of the maximum. a** The amplitude of the dipole oscillations decreases when we increase the excitation power. Because the blueshift is different for all the states, we see a different period for $\sigma+$ than for linearly polarized excitation. $\sigma-$ is evidenced as a probe for $\sigma+$. **b** The effect is less important under linearly polarized excitation at the same power.

period is slightly shorter at high excitation power (Fig. 4.6 a). This point indicates a blueshift of the states. Indeed, as the energy shift is supposed to be different for the different confined states, we expect to measure different periods at low and high polariton density. The fact that the period is shorter suggests that the energy spacing actually increases.

An analysis in the framework of the phenomenological Bessel function model reveals that the oscillation amplitude depends on the proportion of ground state in the coherent superposition. In addition, the squared oscillation pattern is the signature of beats between E1 and E2, while the continuous oscillation pattern is the result of beats between GS and E1. Obviously, since the dynamics is the result of interferences, the two lobes and four lobes states alone can not produce constructive interference at k=0. A continuous pattern can only be observed if there is a significant amount of GS in the superposition.

We are now able to formulate the hypothesis that an increase of the polariton density causes an initial blueshift that bring GS more to resonance with the excitation. The effect is suppressed under linearly polarized excitation, which suggests that collisions play an important role in the blueshift. We confirm this point by looking at the emitted intensity in the different cases.

4.4.4 Polarization and collisions

It is expected that the nonlinear coefficient describing polariton interactions is about one order of magnitude stronger for polaritons of the same polarizations than for polaritons of opposite polarizations. The absence of amplitude reduction under linearly polarized excitation is therefore an indication for the influence of polariton-polariton collisions. However, it could be an artifact due to a weaker injection of the laser in the sample.

In Figure 4.7, we rule this objection out by showing that the signal detected in

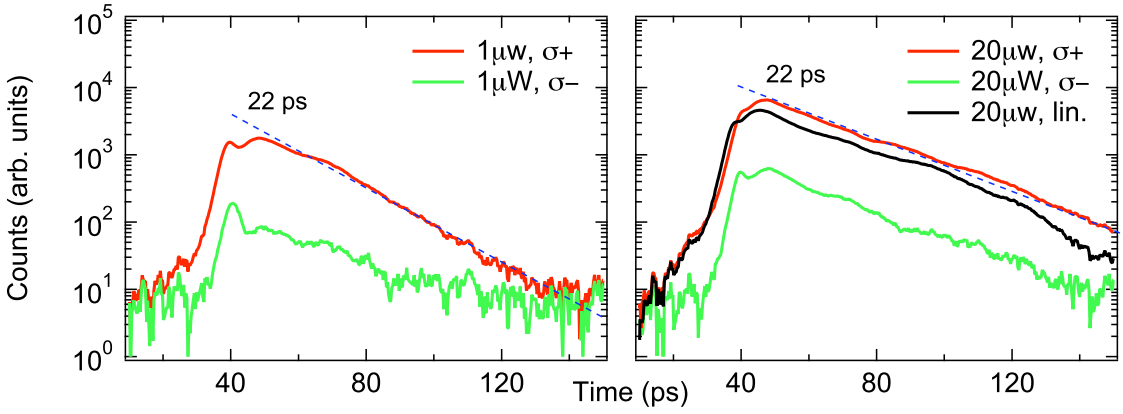

Figure 4.7: **Time profiles. a** The $\sigma-$ signal is one order of magnitude weaker than the $\sigma+$ signal. **b** The intensity detected under linearly polarized excitation show that the injected polariton density is the same than under $\sigma+$ excitation. There is no difference in the decay times at low and high density, which indicates a fast collisional dynamics. Finally a hint of spin flip process is visible in the large proportion of $\sigma-$ and in the small oscillations of the intensity profiles.

$\sigma+$ is of the same order of magnitude whether the excitation polarization is linear or circular (see Fig. 4.7 b). This demonstrates that the blueshift is the result of polariton-polariton collisions. As the laser energy is constant, is also suggests that, *before* the laser disappears, polaritons have time to blueshift significantly and see an increase of the GS population.

By comparing the time profiles at low (Fig. 4.7 a) and high (Fig. 4.7 b) density, we see no difference in the rise and decay times. This confirms that, in this experiment, collisions play a role mostly at the beginning of the dynamics.

Finally, despite the fact that the $\sigma-$ intensity is one order of magnitude lower than the linear signal, we measured a reduction of the amplitude in $\sigma-$ equal to the one in $\sigma+$ (see Fig. 4.6 and Fig. 4.7). We interpret this point as a fast spin flip process due to interactions between polaritons of opposite polarizations, which might explain the slight oscillations in the time profiles (Fig. 4.7 a and b).

4.4.5 Conclusion of the negative detuning experiment

In conclusion, this experiment shows us the very rich physics of the nonlinear polariton dynamics. We excite the mesa in a superposition of its three lower energy states. The resulting dynamics is characterized by dipole oscillations. Upon increasing the excitation power, fast polariton-polariton collisions induce a blueshift that is responsible for an increase of GS population in the dipole state, and thus a reduction of the oscillation amplitude. The role of collisions is highlighted by the fact that the amplitude reduction is negligible under linearly polarized excitation.

4.5 Positive detuning

4.5.1 Damping of oscillations

The dynamics measured at positive detuning is even more interesting. Nonlinear interactions are enhanced because of the higher exciton content of polaritons. At low excitation power, we observe the dipole oscillations described above. At high excitation power, we see a continuous damping of the oscillations. This original dynamics is illustrated in Figure 4.8, where we show snapshots of the time evolution of the polariton density (k_x, k_y, t), for an excitation power of 20 μW. The oscillation amplitude decreases continuously in time and the polariton density eventually stabilizes around $\mathbf{k} = 0$.

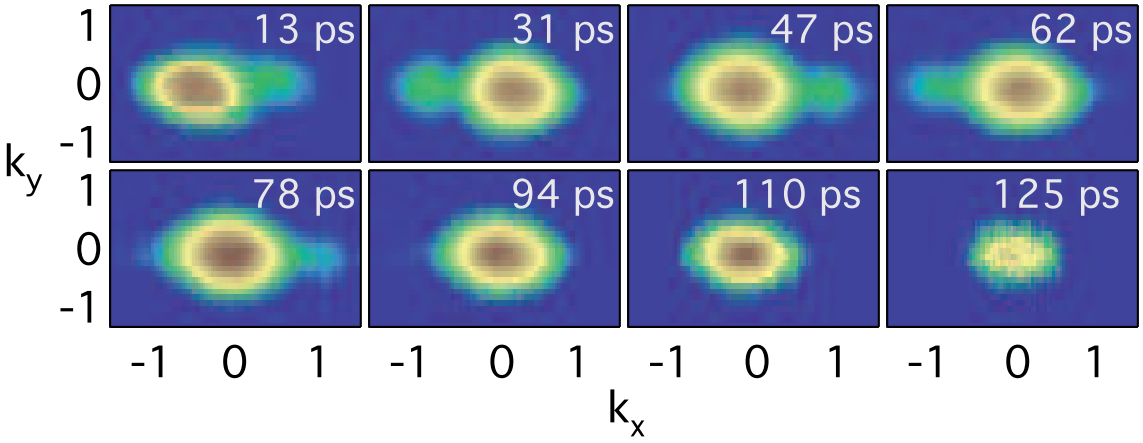

Figure 4.8: **Oscillations Damping (log color scale).** Spontaneous dynamics of a 9 μm diameter mesa at *positive detuning* after pulsed excitation of a coherent superposition of GS,E1 and E2. We see that the amplitude of the oscillations decrease with time. At long times, the polariton density is located around k=0.

4.5.2 Power dependence

As in the experiments at negative detuning, we studied the dynamics of the dipole oscillations as function of the excitation power. The data, integrated along k_y, are displayed in Figure 4.9. The top panel shows the evolution of the intensity detected in $\sigma+$. We proceed as in the previous section and normalize the data at each time to have a better understanding of the evolution (middle panel). At low power (1 μW), we see a squared oscillation pattern of constant amplitude. At 10 μW, the oscillations become more continuous and the amplitude reduces as time increases.

The damping is even more pronounced and faster when the power is increased to 20 μW and 40 μW. In the bottom panel, we show the data for $\sigma-$ and for linearly polarized excitation at 20 μW and 40 μW. The $\sigma-$ signal is damped similarly to the $\sigma+$ signal, as observed in the experiment at negative detuning. Under linearly polarized excitation, the dipole oscillations are damped at 40 μW but not at 20 μW, underlining the underlying polariton-polariton collision processes.

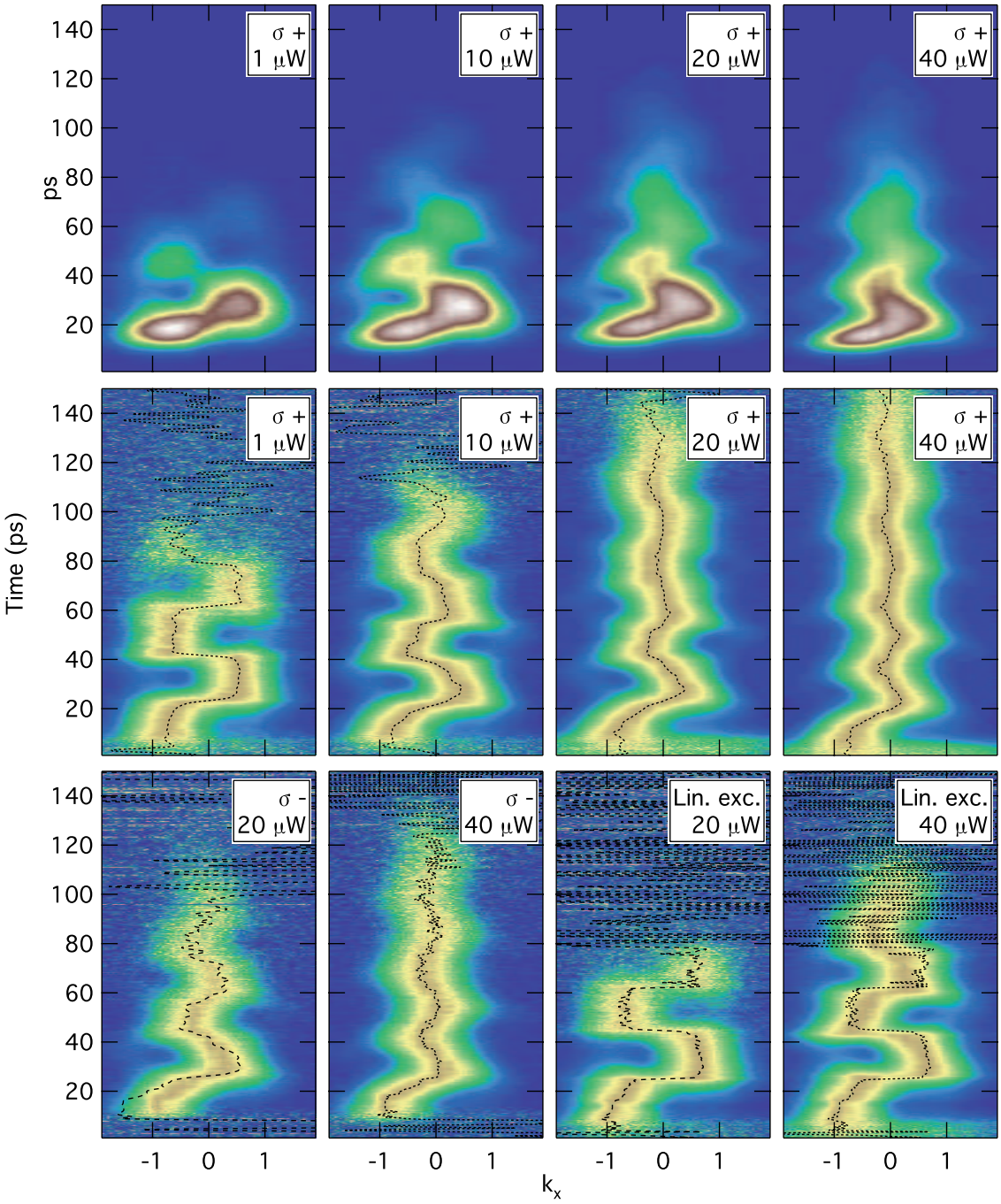

Figure 4.9: **Damping of dipole oscillations.** Top panel: evolution of the intensity detected in $\sigma+$. Middle panel: normalized data for $\sigma+$. At 1 μW, the evolution is characterized by dipole oscillations of constant amplitude. At 10 μW and above, the oscillations are continuously damped. Bottom panel: normalized data for $\sigma-$ intensity and under linearly polarized excitation. At identical powers, the damping is stronger in the $\sigma-$ configuration than under linearly polarized excitation. This experiments highlights the role of collisions in the oscillations damping.

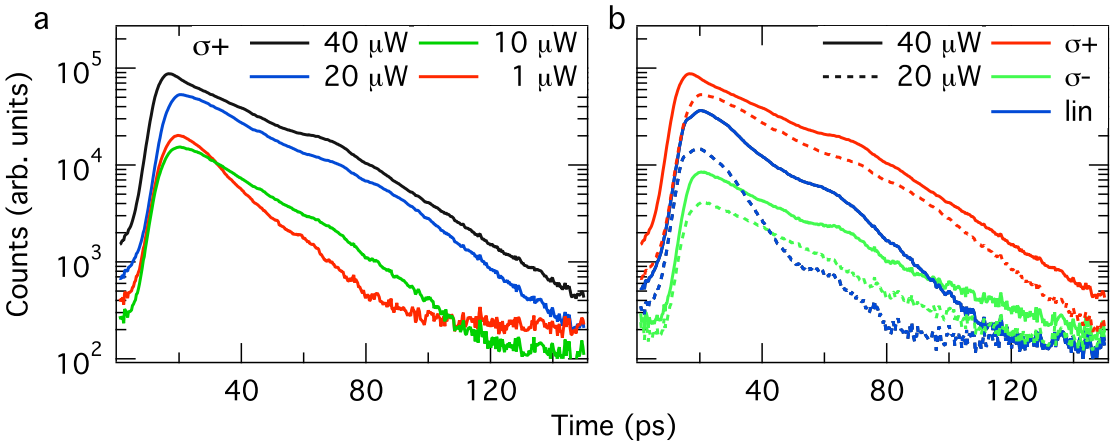

Figure 4.10: **Time profiles. a $\sigma+$ signal at different excitation powers.** One can see that the decay time increases with the pump power, which indicates the presence of high-energy states. **b Comparison of the different signals at high excitation power** The dynamics of the $\sigma-$ signal follows the one of the $\sigma+$ signal despite the one order of magnitude intensity difference. On the other hand, the dynamics under linearly polarized excitation at high excitation power is similar to the one at low power under circularly polarized excitation.

Table 4.1: **Decay times.** Values extracted from the time profiles of Fig. 4.10. The decay times are compared for the $\sigma+$, $\sigma-$ signal in case of $\sigma+$ excitation, and for the signal emitted under linearly polarized excitation (lin.). Times are indicated in picoseconds. The larger decay times measured in $\sigma+$ and $\sigma-$ indicate the presence of high-energy states, populated by multiple scattering processes.

Power (μW)	1	10	20	40
$\sigma+$	14	23	27	31
$\sigma-$	-	-	27	28
Lin. exc.	-	-	11	17

4.5.3 Evidence for an energy redistribution

The power dependent time profiles measured at positive detuning are also very different from what we saw at negative detuning. In Figure 4.10 a, we can see that at positive detuning, the decay time increases with the excitation power. The values are detailed in Table 4.1. In Figure 4.10 b, we compare the behaviors at high excitation power. Under linearly polarized excitation, the dynamics is similar to the low excitation power dynamics in $\sigma+$. Once again, these observations show that polariton-polariton collisions play a crucial role in the relaxation dynamics.

In addition, a polarization flip process is suggested by the $\sigma-$ measurements. The $\sigma-$ signal is nearly one order of magnitude lower than the one under linearly polarized excitation. However, at high excitation power, it has the same dynamics as the $\sigma+$ signal (see also times in Table 4.1). This process must be much faster

than the radiative lifetime so that it influences the dynamics of $\sigma-$ polaritons.

At high excitation power, the large decay times indicate that a significant number of polaritons are scattered to higher energy states. As we saw in the Sect. 3.7, the higher the states energy (in the LP0D), the less they couple to light and the longer their relaxation times.

We deduce that, at positive detuning, because of the stronger nonlinear interactions, polaritons undergo *multiple polariton-polariton scatterings*. This dynamics is responsible for an important energy redistribution over the high-energy confined polariton states. The occupancy of the ground state is favored during these scattering processes because of energy conservation.

4.5.4 Evolution of the different states

The energy redistribution can be studied by a TRPL experiment. The results are given in Figure 4.11. At low excitation power (Fig. 4.11 a and b), there is no significant difference in the dynamics of the different states. We measure decay times of 16 ps. The small oscillations are the signature of parametric scattering.

At high excitation power (Fig. 4.11 c and d), one can see that there is an important population transfer to the ground state, which emission becomes dominant. We measure decay times of about 20 ps for E1 and E2. The dynamics of the ground state is more complicated and we are only able to give an average decay time of 50 ps.

If the polariton lifetime is long enough, thermal equilibrium can be achieved. We propose to analyze the polariton spectrum at long times to see whether or not we obtain a Boltzmann distribution. We proceed as in the previous chapter: the emission of each state is integrated and weighted by the corresponding photonic Hopfield factor C_X^2. The results are displayed in Figure 4.12. The distributions are shown for 110 ps, 130 ps and 150 ps. We do not observe any thermal equilibrium. On the contrary, at long times, the occupancy rather drops at the energy of the first excited state to re-increase at the energies of the second and third excited states. This is a consequence of the fact that the lifetime is longer for the high-energy states. We also see that the blueshift is more important for those states.

4.5.5 Conclusion of the positive detuning experiment

We have investigated the effect of nonlinearities on the dynamics of dipole oscillations in a mesa at positive detuning. When the power is increased, we see a continuous damping of the oscillation amplitude. At long times, the polariton density remains located around $k = 0$.

The investigation of the spectrum time evolution shows an important redistribution of the energy to the benefit of the ground state. In addition the increase of the decay time indicates the presence of states with large exciton content.

The interpretation of these results is the following. Because of the multiple polariton-polariton scattering processes, the high-energy states are more and more populated. Since the scattering process are energy conserving, the ground state is privileged and dominates the emission.

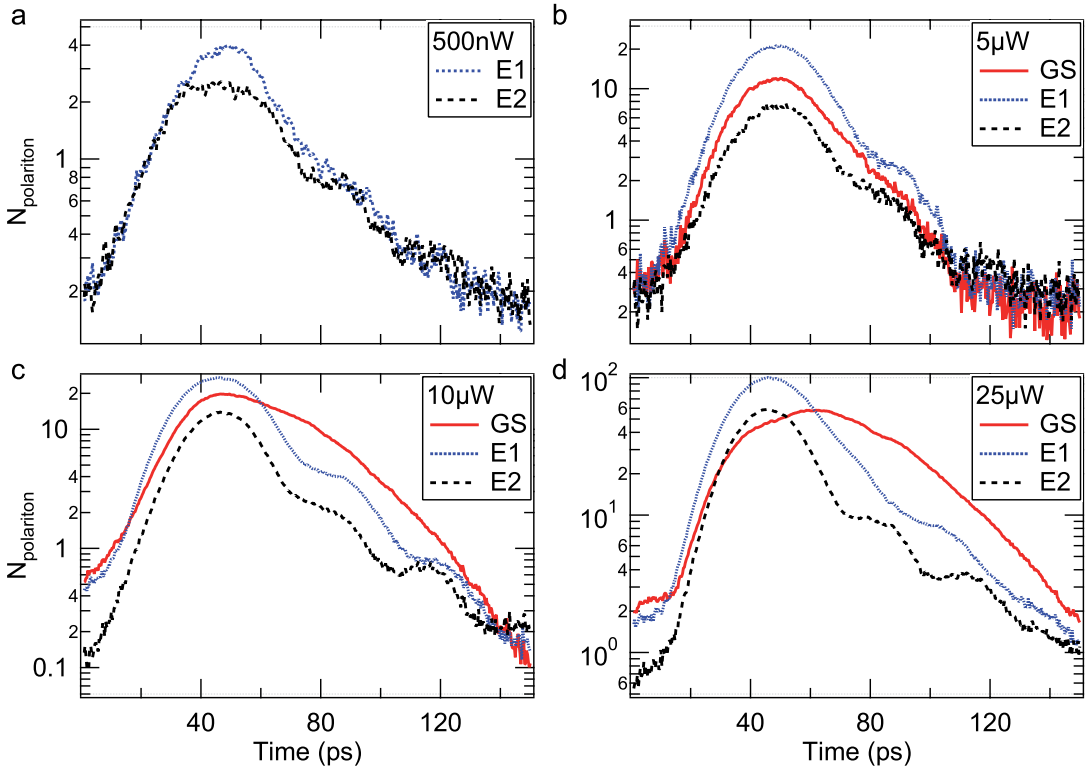

Figure 4.11: **Evolution of the confined states. a and b** Low excitation power. The dynamics is the same for all the states. **c and d** High excitation power. An important energy redistribution favors the occupancy of the ground state.

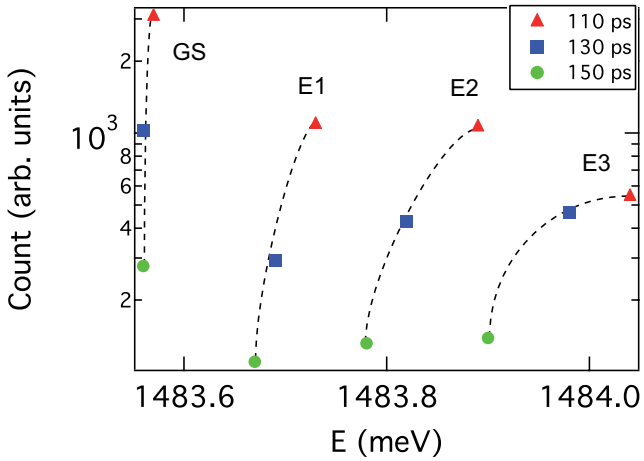

Figure 4.12: **Distribution at long times.** The occupancy of the low energy states is represented at 110 ps (triangles), 130 ps (squares) and 150 ps (circles). The ground state (GS) occupancy is three time larger than the one of the first excited state. The distributions strongly differ from Boltzmann distribution. As a consequence of parametric scattering, the occupancy of the first excited state (E1) is lower than the one of the second (E2) and third (E3) excited states. The states experience different energy shifts because of their different exciton contents.

4.6 Theoretical Model

4.6.1 Model

We now propose a phenomenological approach to describe the damping of the oscillations. The polariton oscillation dynamics can be understood within a classical field (Gross-Pitaevskii) framework, because due to the coherent excitation, the population of the relevant modes is much larger than unity. Despite the polarization flip, there is no significant polarization beats in the experiments[4]. We thus consider only a weak coupling between opposite polarization states and spin degrees of freedom can be neglected in this model. In the next Chapter, we will see that spin interactions can seriously modify the outcomes of the Gross-Pitaevskii equation. Here, we justify our choice by the fact that, in the frame of this model, we do not study the case of elliptically or linearly polarized excitation.

Polaritons are described as two coupled fields constituted by the excitons (ψ_X) and photons (ψ_C)

$$i\frac{d}{dt}\psi_C = [\epsilon_C(-i\nabla) - i\frac{\gamma_C}{2} + V_{\text{ext}}]\psi_C + \omega_R\psi_X + F_L \quad (4.1)$$

$$i\frac{d}{dt}\psi_X = [\epsilon_X - i\frac{\gamma_X}{2} + g|\psi_X|^2]\psi_X + \omega_R\psi_C, \quad (4.2)$$

where the cavity photon dispersion is given by $\epsilon_C(k) = \omega_C\sqrt{1 + k/k_z^2}$, the lifetime of the excitons and photons is denoted by $\gamma_{X,C}$ respectively and exciton-exciton interactions are modeled by a contact interaction with strength g. The external laser field F_L creates the photons that are reversibly converted into excitons through the Rabi coupling term with strength ω_R. The external potential V_{ext} describes the photonic trap that confines the polariton.

4.6.2 Collisional damping

Numerical simulations with the above Gross-Pitaevskii model are reported in Fig. 4.13. We obtain satisfactory qualitative agreement with the experimental observations.

The relaxation process from the first excited to the ground state is complex: the dominant mechanism is a parametric process $2E_1 \rightarrow G+E_2$ and this process is highly nonlinear due to stimulated scattering. The calculated time evolution of the G, E_1 and E_2 states are displayed in Fig. 4.14. The behavior observed experimentally is again well reproduced.

4.7 Conclusion

In conclusion, we have evidenced the impact of polariton nonlinearities on the polariton dynamics in the momentum space. We excited 9 μm diameter mesas in a coherent superposition of the three lowest energy states. In the low-density regime,

[4]Note that polarization beats leading to quasi-periodic reversal of the polarization degree have been accidentally observed in our sample, in mesas located near linear defects.

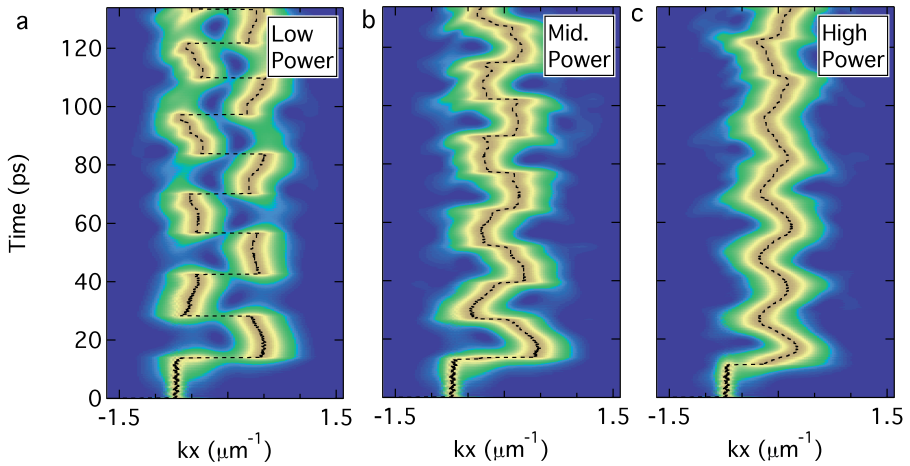

Figure 4.13: **Theoretical evolution of the dipole oscillations. a** Low, **b** intermediate and **c** high power. The behavior observed experimentally (see Fig 4.9) is well reproduced.

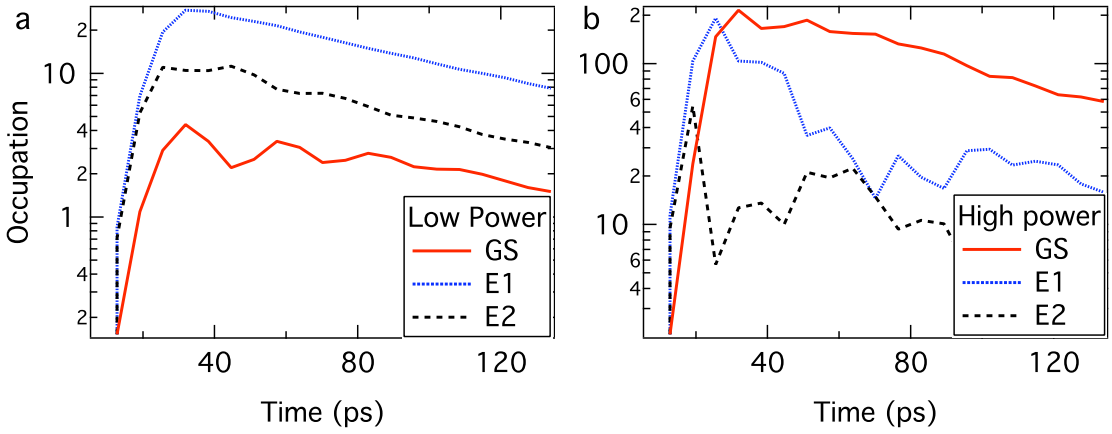

Figure 4.14: **Theoretical time evolution of the GS, E1 and E2 states.** We find qualitative agreement with the experimental data presented in Fig. 4.11. **a** At low excitation power, the states evolve with the same dynamics. **b** At high excitation power, because of multiple parametric processes, the ground state occupation becomes dominant. The small oscillations in the dynamics are also reproduced.

the dynamics of such a superposition is characterized by dipole oscillations of constant amplitude. We studied the modifications of this dynamics in the high-density regime.

At negative detuning, the main consequence of polariton-polariton interactions is a reduction of the oscillation amplitude due to a blueshift of the states.

At positive detuning, where interactions are stronger because of a larger excitonic content, we observe a continuous damping of the oscillation amplitude. By studying the time evolution of the different states, we showed that, at positive detuning, multiple scattering processes are responsible for important the scattering to high-

energy states and to the ground state.

The key role of collisions is highlighted by the fact that under linearly polarized excitation, the oscillation damping occurs at much higher excitation powers than under circularly polarized excitation. Finally, the experiments are well reproduced by numerical simulations based on a Gross-Pitaevskii model.

4.8 Summary

This part of the thesis was dedicated to the confined polariton dynamics in the linear and nonlinear regimes.

Linear regime We studied *polariton-phonon interactions*. We clearly observed that polariton thermalization is enhanced under lateral confinement. In addition, the large exciton content states play a crucial role in the slowing down of the polariton relaxation. We finally were able to give a general scheme for confined polariton relaxation and thermalization depending on the size of the mesa.

Nonlinear regime We studied *polariton-polariton interactions*. We showed the influence of polariton-polariton collisions on the dynamics in the momentum space. We evidenced a continuous damping of dipole oscillations because of multiple parametric scattering. In addition, we showed the crucial impact of the excitation polarization in this process.

Next chapters In the following, we study more in detail the polarization dependence of polariton nonlinear interactions. We have seen that interactions are weaker between polaritons of antiparallel spins, and it would be useful to obtain more information about these interactions. We saw in Chapter 1 that there is a close relation between the emission polarization and the polariton spin. The next part of this thesis is thus dedicated to *polariton spinor interactions*.

Part III

On the Spinor Nature of Polariton Interactions

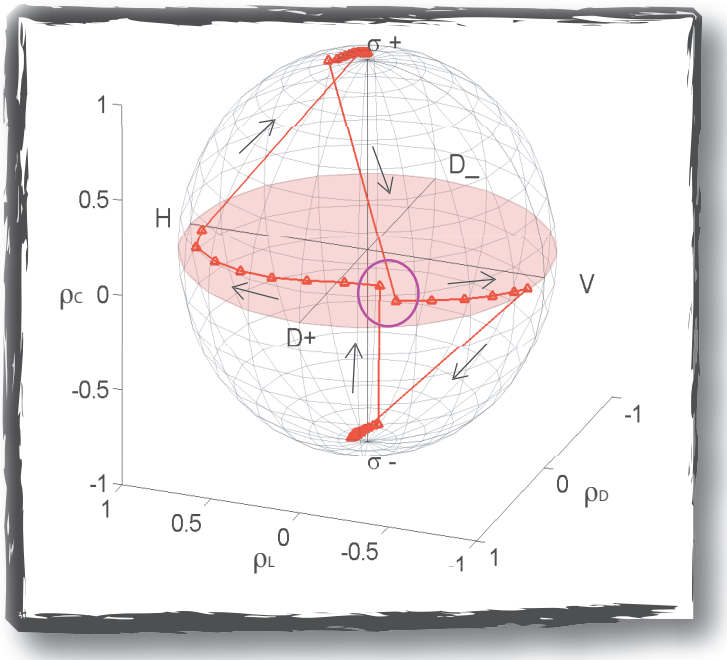

In this last part, we investigate the nature of polariton spinor interactions through two important examples: polariton optical bistability and polariton collective fluid dynamics. As we will see, these are in fact two closely related phenomena that address the polariton-polariton scattering problem in a regime different from the parametric scattering [Baas 04a, Tredicucci 96, Carusotto 04, Ciuti 05]. In Chapter 4, we evidenced the strong influence of the excitation polarization on polariton-polariton scattering. Our goal is now to characterize polariton spinor interactions and to show their crucial influence on the polariton dynamics. By this, we will deepen our understanding of the notion of polariton spin introduced in Chapter 1 (Sect. 1.5).

The interest in polariton spinor interactions arose in the early 2000, with pump-probe experiments on the stimulated spin dynamics of polaritons [Savvidis 00a, Savvidis 00b, Lagoudakis 02, Kavokin 03] and with time resolved photoluminescence experiments [Martín 02, Renucci 05]. Soon, important works were oriented towards the transport of spin-polarized polaritons, with major contributions to the optical spin Hall effect [Kavokin 05, Langbein 07, Leyder 07b, Amo 09a, Liew 09a] and to the design of polarization-controlled optical gate based on interferences in the scattering between two coherent polariton populations created with opposite wavevectors [Romanelli 07, Leyder 07a].

Other important directions of the study of polariton spinor nature concern the characterization of spontaneous polarization building in BEC [Baumberg 08], the generation of polarization vortices [Liew 07, Liew 08b] and the study of half-quantum vortices [Rubo 07, Lagoudakis 09].

Finally, recent theories describing the polariton dynamics and accounting for the polarization degree of freedom have predicted remarkable modifications in the polariton bistable behavior [Gippius 07] and superfluid phase [Solnyshkov 08].

The work of Gippius et al. showed that because of spinor interactions, the polariton bistable behavior is substantially modified, opening the possibility of *polarization-controlled bistability and multistability* [Gippius 07]. It has been followed by interesting proposals for spintronics devices like spin-based memories or logic gates [Liew 08a, Shelykh 08]. In a later work, the same group generalized their approach to study the elementary excitations of a macroscopic state, resonantly created under circularly or linearly polarized pump, showing that the superfluid behavior can be altered in presence of polarization interactions [Solnyshkov 08].

In Chapter 5, we present our work about the effects of spinor interactions on polariton bistability in the case of planar polaritons. Unexpectedly, bistability appears to be suppressed under linearly polarized excitation. We propose a phenomenological model to understand this effect and clarify the experimental conditions to observe it. We discuss the possibilities of observing polarization controlled spin multistability.

In Chapter 6, we study the case of confined polaritons. The advantage of confinement is that experiments can be done with a single confined state, with narrow linewidth and in a weakly disordered environment. In this case, we achieve a better characterization of the interaction strengths. This leads us to observe high-efficiency polarization switching. We demonstrate the multistability of a macroscopic spin ensemble and its coherent control. With a two-beam experiment, with demonstrate the feasibility of triggered switches based on this effect.

In the final Chapter 7, we investigate the superfluid behavior of planar microcavity polaritons. We observe a drop of viscosity and a coupling between planar and confined states. We discuss the effect of spinor interactions on the polariton collective fluid dynamics.

Chapter 5

Polarization control of optical bistability

5.1 Introduction

Optical bistability (OB) denotes the possibility for a system to present two different stable states for a given excitation condition. This effect comes together with a hysteresis behavior. From its very early days, OB has been studied in a great variety of systems with a strong interest for its promising applications to all-optical processing. Many schemes of optical switches and memories have been developed since then [Abraham 82, Miller 84].

In 1995, Tredicucci predicted the possibility of achieving optical bistability with microcavity polaritons [Tredicucci 96]. Experimental demonstrations showed that it can be achieved in different conditions. Polariton bistability exploits either the strong-to-weak coupling transition [Cavigli 05], either the Kerr-like non-linearity resulting from polariton-polariton interactions [Baas 04a]. The advantage of OB in the strong coupling regime is the low power needed to trigger the bistability in comparison to other structures. Recently, bistability has been evidenced in polariton diodes [Bajoni 08a]. This constitutes an important advance in the development of polariton-based devices.

In this chapter, we investigate an aspect of bistability which has been neglected in experiments so far, namely its sensitivity to the excitation polarization. We first work in the planar region of the microcavity. The observed behavior is completely unexpected. While common theories predict an enhancement of OB under linearly polarized excitation, we evidence a strong reduction, or even a total suppression of bistability in some cases. The study of this effect is essential for the understanding of polariton spinor interactions.

In Section 5.2, we present an analytical model that helps understanding the main features of optical bistability. Experiments are detailed and discussed in Sections 5.3 and 5.4. We find that optical bistability is suppressed under linearly polarized excitation, and propose a way to control coherently optical instabilities in our system. In Sections 5.5, we show that our experiments are not reproduced by the previous analytical model. We formulate the hypothesis of a biexcitonic effect and propose a phenomenological model to reproduce our measurements. Our hypothesis is dis-

cussed in Sections 5.6 and 5.7. We give a conclusion of these works in Section 5.8.

5.2 Theoretical picture

In this section, we describe the theoretical approach used by Baas et al., which derive optical bistability from the degenerate parametric scattering equations [Baas 04a]. Their approach led them to the study of optical bistability at the magic angle, where they evidenced analogies with the optical parametric oscillator. The picture is different from the one proposed by Tredicucci, based on the strong to weak coupling transition [Tredicucci 96]. In Baas' experiment, strong coupling is not lost and bistability results from the energy blueshift due to the polariton density.

The microcavity is excited at slightly higher energy than the polariton resonance. At low excitation power, the laser is at slightly higher energy than the polariton state and the transmission is weak. By increasing the excitation power, the polariton density increases and the polariton level blueshifts because of polariton-polariton interactions. Above a critical power, the blueshift is sufficient to make polaritons jump close to resonance and the transmission is high. Then, upon decreasing the excitation power, polaritons remain close to resonance down to an excitation power lower than the one where they jumped up: the transmitted intensity shows hysteresis.

5.2.1 A special interaction regime

We have seen in Chapter 4 that several nonlinear behaviors exist for polaritons. The most investigated is clearly polariton parametric amplification. This process requires both phase matching and energy conservation. If polaritons are created with a wave vector $\mathbf{k}_p$ and an energy $E(\mathbf{k}_p)$, a scattering between two polaritons will give two polaritons (signal and idler) with wave vectors $\mathbf{k}_s$ and $\mathbf{k}_i$ such that $\mathbf{k}_s + \mathbf{k}_i = 2\mathbf{k}_p$ and with energies such that $E(\mathbf{k}_s) + E(\mathbf{k}_i) = 2E(\mathbf{k}_p)$. The inflection point of the polariton dispersion is a peculiar point where a solution exists for all $\mathbf{0} < \mathbf{k}_s < \mathbf{k}_p$. Another special point is the bottom of the dispersion, $\mathbf{k}_p = 0$, where the solution is the trivial $\mathbf{k}_s = \mathbf{k}_i = \mathbf{0}$. This degenerate parametric scattering provides a clear condition for the observation of optical bistability.

5.2.2 Model

Hamiltonian

For the following development, we neglect interactions between upper and lower polaritons and we focus on the lower polariton (LP) branch. The Hamiltonian for polariton-polariton interactions is given by[1]

$$H_{\mathbf{k}} = \sum_{\mathbf{k}} \omega_{LP}(\mathbf{k}) p^{\dagger}_{\mathbf{k}} p_{\mathbf{k}} + \frac{1}{2} \sum_{\mathbf{k},\mathbf{k'},\mathbf{q}} \alpha(\mathbf{k},\mathbf{k'},\mathbf{q}) p^{\dagger}_{\mathbf{k+q}} p^{\dagger}_{\mathbf{k'-q}} p_{\mathbf{k}} p_{\mathbf{k'}} + F_L\, p^{\dagger}_{\mathbf{k}} \qquad (5.1)$$

where $p_{\mathbf{k}}$ is the annihilation operator of a polariton in the mode $\mathbf{k}$, α is the nonlinear constant and $F_L = \sqrt{I^{in}} e^{-i\omega_L t}$ is the pump field of amplitude $\sqrt{I^{in}}$ and frequency

[1] We use $\hbar = 1$

ω_L. In the degenerate case, $p_{\mathbf{k}} = p_{\mathbf{k'}} = p_{\mathbf{0}}$, which we simply note p. We introduce the phenomenological parameter γ to account for the relaxation so that the Hamiltonian becomes

$$H = (\omega_{LP} - i\gamma)p^\dagger p + \alpha p^\dagger p^\dagger pp + F_L\, p^\dagger \tag{5.2}$$

The mean-field evolution of the operator p (Heisenberg picture) is given by

$$\frac{d}{dt}\langle p\rangle = \frac{1}{i}\langle [p, H]\rangle + \langle \frac{\partial p}{\partial t}\rangle \tag{5.3}$$

Using the commutator $[p, p^\dagger] = 1$ and considering solutions of type $p(t) = e^{i\omega_L t}\tilde{p}$, we obtain

$$\frac{d}{dt}\langle p\rangle = -i(\omega_{LP} - i\gamma + \alpha n_p)\langle p\rangle - iF_L + i\omega_L\langle p\rangle \tag{5.4}$$

Bistability condition

The stationary solution verifies $dp/dt = 0$. By multiplying Eq. 5.4 by its complex conjugate, one obtains

$$I^{in} = \left[(\omega_{LP} - \omega_L + \alpha n_p)^2 + \gamma^2\right] n_p \tag{5.5}$$

We obtain a cubic behavior for $I^{in}(n_p)$. Provided that $I^{in}(n_p)$ admits two distinct extrema, the curve $n_p(I^{in})$ presents the S-shaped behavior typical of bistability curves. We therefore look for the solutions of

$$\frac{dI^{in}}{dn_p} = 3\alpha^2 n_p^2 - 4\alpha n_p \Delta + \gamma^2 + \Delta^2 = 0 \tag{5.6}$$

where $\Delta = \omega_L - \omega_{LP}$ is the excitation-polariton detuning. Solutions exist if

$$\alpha^2(\Delta^2 - 3\gamma^2) \geq 0 \tag{5.7}$$

yielding the *bistability condition*

$$\Delta \geq \sqrt{3}\gamma \tag{5.8}$$

5.2.3 Optical bistability

Optical instabilities

The bistability condition (5.8) shows that the observation of bistability depends on the laser detuning and on the polariton linewidth. In Figure 5.1, we represent three possible situations [Gibbs 85]. If $\Delta < \sqrt{3}\gamma$ (Fig. 5.1 a), the excitation is too close to resonance and the polariton state rapidly blueshifts above the laser energy. The polariton blueshift is obviously limited by the coupling of the polariton state to the excitation. The transmitted intensity increases and rapidly saturates. The system works as an **optical limiter (OL)**. In Fig. 5.1 b, $\Delta = \sqrt{3}\gamma$ and the solutions are degenerate. There is a single jump. The system is called an **optical discriminator (OD)**. Fig. 5.1 c corresponds to the **optical bistability (OB)** regime: $\Delta > \sqrt{3}\gamma$, so two distinct jumps occur, one clearly identifies an *upper* and a *lower* bistability thresholds. In the following, we derive analytical expressions for the bistability intensity thresholds and width.

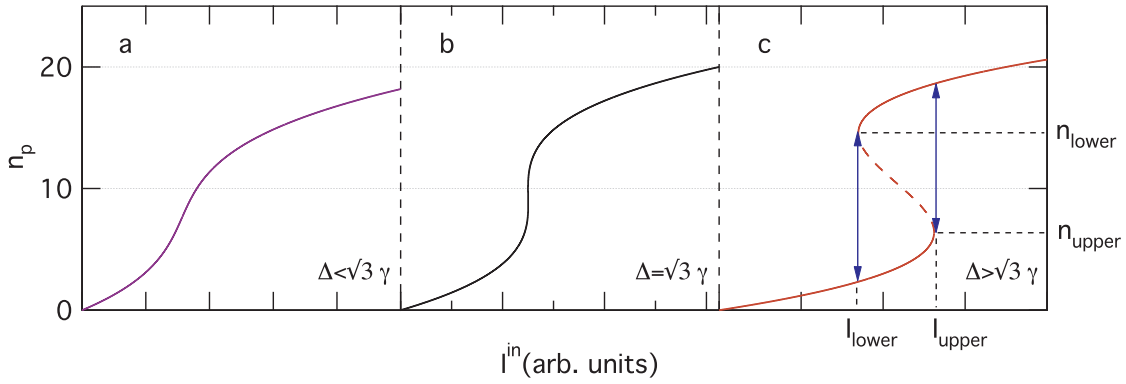

Figure 5.1: **Bistability condition.** Three instability regimes arise from condition (5.8) **a** Optical limiter. **b** Optical discriminator. **c** Optical bistability.

Bistability thresholds and width

The two solutions (5.6) are given by

$$n_{upper} = \frac{2\Delta - \sqrt{\Delta^2 - 3\gamma^2}}{3\alpha} \tag{5.9}$$

$$n_{lower} = \frac{2\Delta + \sqrt{\Delta^2 - 3\gamma^2}}{3\alpha} \tag{5.10}$$

By replacing the solutions in (5.5), we obtain the bistability intensity thresholds

$$I_{upper} = \frac{2\Delta - \kappa}{27\alpha}(6\gamma^2 + 2\Delta^2 + 2\Delta\kappa) \propto \Delta^3 \tag{5.11}$$

$$I_{lower} = \frac{2\Delta + \kappa}{27\alpha}(6\gamma^2 + 2\Delta^2 - 2\Delta\kappa) \propto \Delta \tag{5.12}$$

where $\kappa = \sqrt{\Delta^2 - 3\gamma^2}$. We can now write the bistability width as

$$W = \frac{4\kappa^3}{27\alpha} \tag{5.13}$$

If $\Delta >> \gamma$, then $\kappa \sim \Delta$. In this case, $I_{upper} \propto \Delta^3$, $I_{lower} \propto \Delta$ and $W \propto \Delta^3$. As we will see in the following, the upper threshold is the most influenced by changes in the laser-polariton energy detuning.

5.2.4 Spinor interactions and modification of equations

The model developed above holds for spin-less interacting bosons. In case of a spinor gas, we will see that a model based on coupled Gross-Pitaevskii equations is more appropriate. At the moment, let us neglect interactions between polaritons of opposite spin polarizations. A variation of the excitation polarization degree ρ_p is thus equivalent to a renormalization of the interaction constant α as

$$\alpha' = \alpha(\rho_p^2 + 1)/2 \tag{5.14}$$

5.3 Bistability suppression with planar polaritons

In the present section, we describe the experimental procedure used to investigate spinor effects on optical bistability in our sample. We observe a strong reduction of the bistability width when exciting the sample with a linearly polarized laser. This effect is not predicted by a simple approach based on the spinless model described above.

5.3.1 Experimental setup

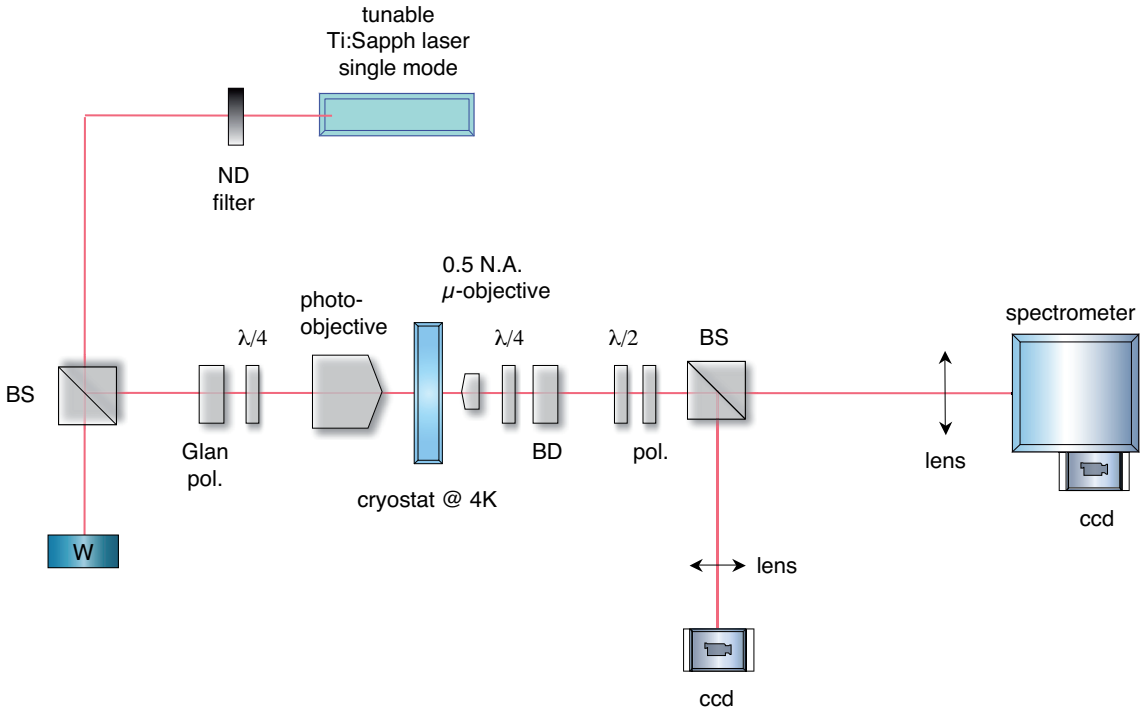

Figure 5.2: **OB Setup.** The cw single mode excitation is prepared using a neutral density (ND filter) and polarization optics. The Glan polarizer (pol.) ensures a linearly polarization and the first quarter-wave ($\lambda/4$) plate is used for precise tuning of the polarization degree. The beam is focused onto the sample at normal incidence. The emission polarization is separated into two channels using a $\lambda/4$ plate in conjunction with a beam displacer (BD). Part of the signal is directly imaged on control CCD while the other part is spectrally resolved.

Setup for polarization resolved excitation and detection

The setup is shown in Figure 5.2. We work in the transmission configuration as described in Chapter 4. The sample is excited at normal incidence using a single-mode continuous wave laser. On the excitation side, the laser can be attenuated with a continuously variable neutral density filter mounted on a motorized translation stage. Half of the beam is sent to a power meter using a non-polarizing beam

splitter. The laser then passes through a Glan polarizer in order to make sure that it is linearly polarized. In our case, the laser is linearly polarized along the horizontal direction (H). The polarizer is followed by a quarter-wave plate mounted on a motorized rotation stage in order to tune the excitation polarization from circular to linear with high precision.

On the detection side, the collected emission is polarization resolved in the circular basis. The emission is sent to a second quarter-wave plate that converts the circularly polarized signal into linearly polarized signal. Then a beam-displacer separates vertically the vertical (V) and horizontal (H) components of the polarized emission. It is known that a spectrometer is polarization selective because of the grating grooves. For instance, if the rules are vertical, a V signal will be underestimated in comparison to a H signal. In order to avoid any artifact from the grating, we use a half-wave plate and a polarizer to convert both H and V signals into signals with the same linear polarization direction.

The polarization resolved emission is then sent to a spectrometer and to a control CCD for direct imaging of the near field.
The neutral density filter, the power meter, the rotation stage and the CCD cameras are monitored by a Labview program. This automation of the experiment is essential to produce accurate graphs and evidence the desired effects.

How to evidence bistability? *à la Baas* experimental procedure

Determinig the conditions to observe bistability is not a trivial task. The values for the excitation detuning and power thresholds strongly depend on the cavity detuning. A very nice procedure is given in the thesis of A. Baas. It consists in identifying optical bistability by scanning the sample position for a given excitation power and frequency. We summarize this procedure as follows:

a) Find a position of the sample at zero or slightly positive detuning (the detuning might be characterized by nonresonant spectroscopy)

b) Set the laser energy about 0.5 meV above the bottom of the lower polariton branch. The laser should be circularly polarized.

c) Set the laser power to about 1-2mW. [2]

d) Scan the sample *slowly* in order to bring the polariton resonance closer to the laser.

e) In the mean time, the emission intensity can be measured with a control CCD. A sudden increase of the intensity should occur, and a hysteresis behavior in the sample position should be observed.

Having identified the appropriate parameters, it is then easy to obtain power dependent bistability curves by only scanning the excitation power back and forth. This is how we proceed for the experiments described in the following.

[2]This power is indicated for our microcavity sample and for a 25 μm diameter excitation spot. The order of magnitude is the important value. It is consistent with the values that can be found in the literature.

5.3.2 Preliminary results

We are interested in the influence of the excitation polarization on the optical bistability of planar polaritons. Figure 5.3 illustrates the bistability curves obtained in the *planar region* of the microcavity. In Fig. 5.3 a, the excitation is nearly circularly polarized. The polarization resolved emission reveals a dominant co-circularly polarized ($\sigma+$) component. A clear bistable behavior is observed, with jumps of two orders of magnitude. This is much more than what was measured in previous works. In Fig. 5.3 b, the excitation is nearly linearly polarized. We observe a *suppression of the bistable behavior*. This observation is very interesting because it shows the possibility of achieving coherent control of optical bistability in semiconductor microcavities.

However, the main aspect of this effect is that it is completely counter-intuitive. Since the blueshift due to polariton-polariton interactions is smaller under linearly polarized excitation, we expect the bistability thresholds to be higher than under circularly polarized excitation. In fact, we expect hysteresis curves to be *wider* under linearly polarized excitation.[3] In next sections, we investigate in more detail this striking behavior and give possible explanations for its origins.

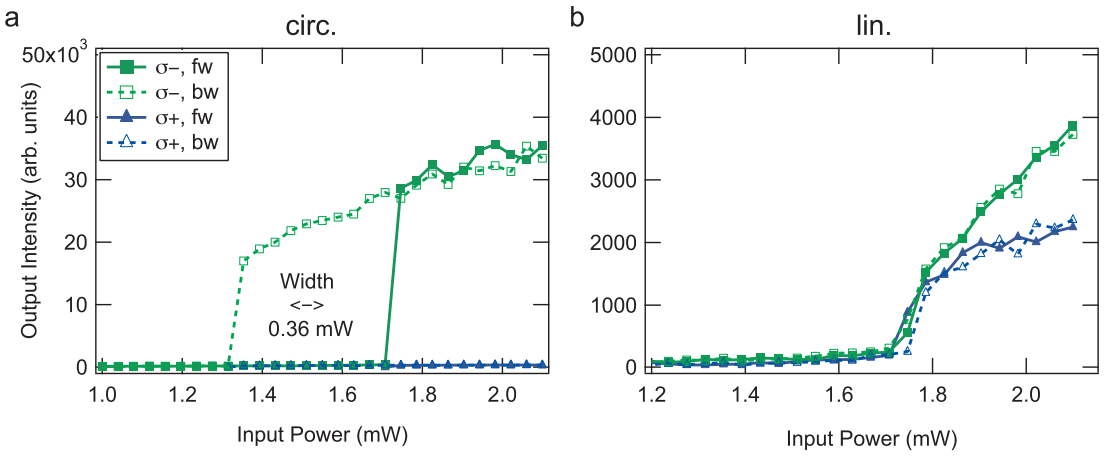

Figure 5.3: **Polarization resolved bistability: circular vs linear excitation.** The bistable behavior of planar polaritons is investigated for two excitation polarization conditions. The plots display the integrated emission intensity. The polariton branch is close to zero detuning. **a** Left-circularly ($\sigma-$) polarized excitation. The co-circular component dominates the emission. We observe a clear bistable behavior, with jumps of two orders of magnitude between the lower and upper branches. **b** Linearly polarized excitation. Optical bistability is suppressed in this case and the system behaves as an optical limiter. Data taken at $\delta \simeq 0$ and $\Delta \simeq 0.5$ meV.

[3]For simplicity, we may use the terms linear, elliptical or circular excitation to refer to linearly, elliptically or circularly polarized excitation, respectively. In the following text, we make no distinction between both expressions.

5.4 Polarization control of optical instabilities

We investigate more in detail the behavior of Fig. 5.3. Indeed, the coherent control of optical instabilities in a spinor system is interesting from many points of view. Regarding all-optical processing application, it could for instance serve for the development of optical switches with tunable sensitivities. It would also allow for the design of spin-optoelectronics devices like polarization modulator and converter operating in the absence of any magnetic field.

5.4.1 Bistability to optical limiter transition

In Figure 5.4, we show polarization resolved bistability curves demonstrating the polarization control of the transition between the different optical instability regimes described in Fig. 5.1. The curves are plotted for different excitation polarizations, going from left circular ($\sigma-$) to right circular ($\sigma+$). The circular polarization degree of the excitation is indicated by ρ_p:

$$\rho_p = \frac{I^{in}_{\sigma+} - I^{in}_{\sigma-}}{I^{in}_{\sigma+} + I^{in}_{\sigma-}} \tag{5.15}$$

We work at positive cavity detuning $\delta \simeq 0.6$ meV, with a laser detuning $\Delta = 0.55$ meV. Optical bistability is observed for nearly circular excitation. The bistability width decreases from 0.34 mW to 0.16 mW when ρ_p increases from -0.99 to -0.64. For $\rho_p = -0.34$ the upper and lower bistability thresholds are equal: the system behaves as an optical discriminator. Under linearly polarized excitation, the system behaves as an optical limiter. A symmetric response is found for positive values of ρ_p.

5.4.2 Polarization conversion

From the polarization resolved bistability data, one can retrieve the polarization degree of the emission ρ_c defined as

$$\rho_c = \frac{I^{out}_{\sigma+} - I^{out}_{\sigma-}}{I^{out}_{\sigma+} + I^{out}_{\sigma-}} \tag{5.16}$$

We display the evolution of ρ_c for the OB-OL transition experiment in Figure 5.5. The polarization degree ρ_c jumps of up to 0.5.

Polarization conversion occurs at the bistability thresholds and presents memory effect in function of the excitation power.

In addition, in the OD regime, the dominant polarization saturates above threshold while the other continues increasing (see Fig. 5.4). Consequently, there is a strong polarization conversion from weakly elliptical to circular at threshold and a continuous modulation above threshold.

Under linear excitation, ρ_c is constant. Note that ρ_c is measured with a systematic shift of $+0.12$. It is attributed to a slight experimental artifact.

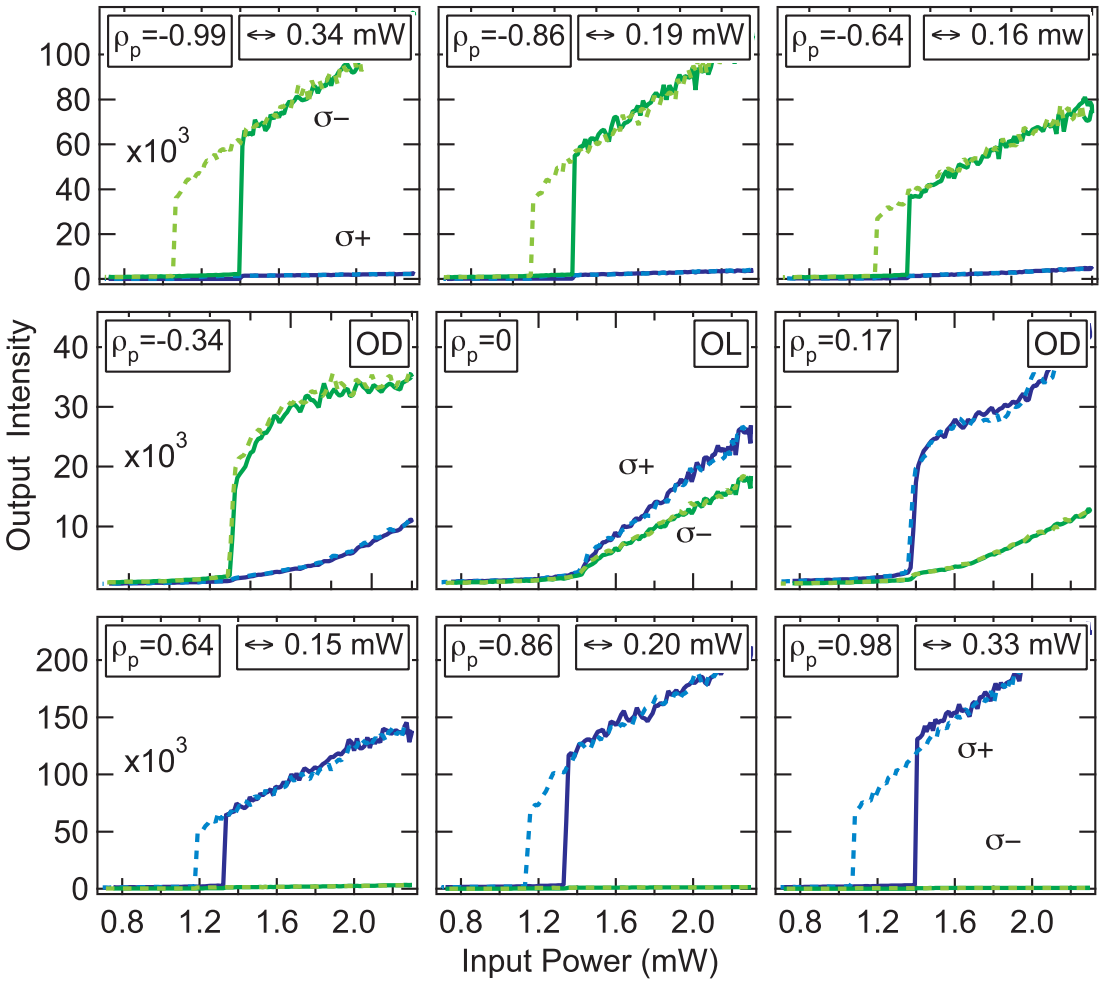

Figure 5.4: **Polarization controlled OB-OL transition: emission intensity.** The excitation power is scanned from 0.6 mW to 2.5 mW (and backward) for 9 different values of the circular polarization degree ρ_p ranging from -1 to +1. OB to OL transitions are observed from $\rho_p = -1$ to $\rho_p = 0$ and from $\rho_p = 0$ to $\rho_p = 1$. The bistable behavior is simply controlled by changing the excitation polarization. Widths ($\leftrightarrow$) are given in mW. Data are taken at $\delta = 0.597$ meV ($X^2 = 0.58$) and $\Delta = 0.55$ meV.

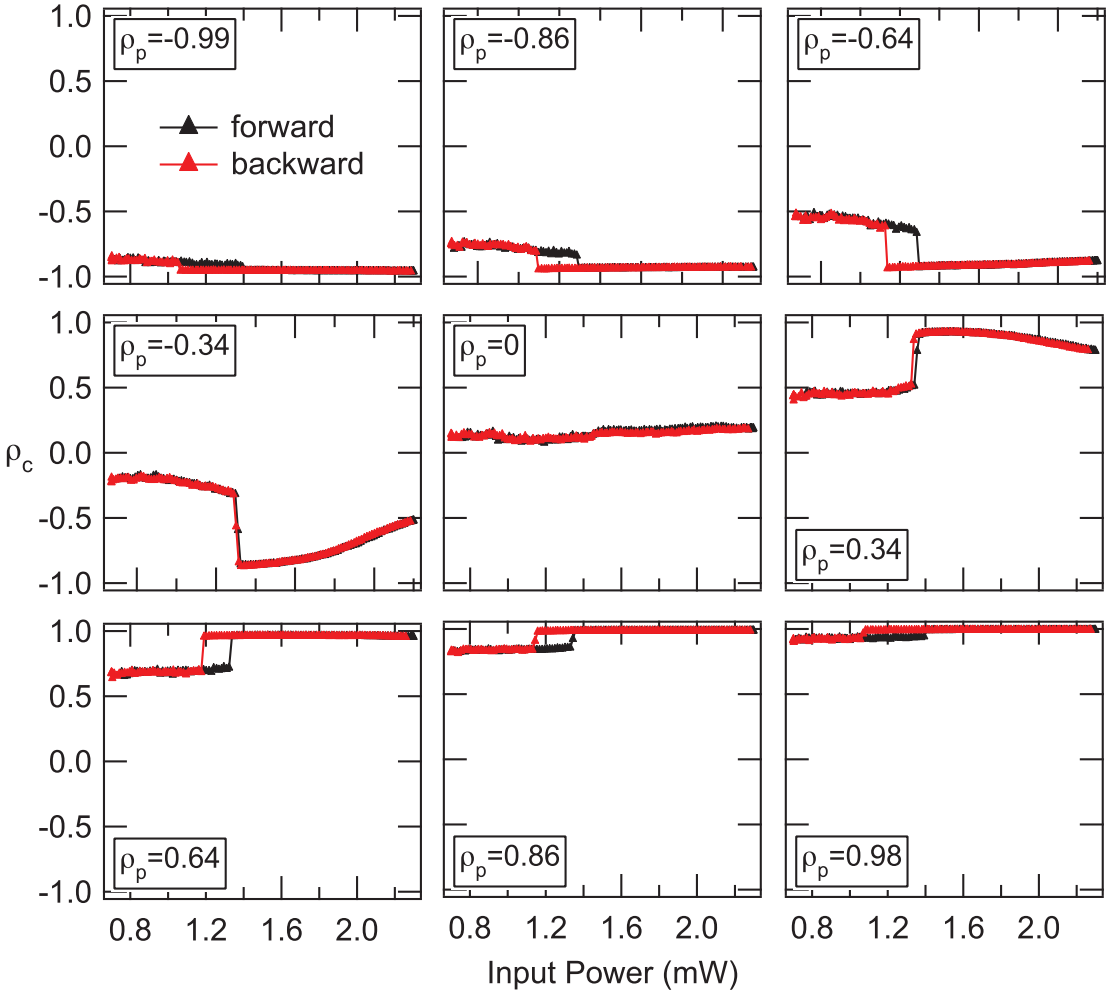

Figure 5.5: **Polarization controlled OB-OL transition: emission polarization degree ρ_c.** The polarization degree is calculated for each plots of Fig.5.4. Because of the bistable behavior of the emission intensity, abrupt jumps are observed in the polarization degree ρ_c at $\rho_p = \pm 0.99$, 0.86 and 0.64. It results in a bistable polarization conversion. Hysteresis disappears at $\rho_p = \pm 0.34$ (OD regime). A power dependent polarization modulation is also observed in this regime. At $\rho_p = 0$ (OL regime), no significant change is observed in ρ_c.

5.5 Model vs experiments

We show here that the experimental results are in opposition with the simple picture for spinor interactions proposed at the end of Section 5.2.4. In this picture, polaritons with opposite spins are assumed to be independent. Consequently, the strength of polariton-polariton interactions is reduced under linear excitation. This approximation is justified by the fact that it is commonly admitted that the interaction strength between polaritons of opposite spin $\alpha_{\uparrow\downarrow}$ is much weaker than the interaction strength between polaritons of same spin $\alpha_{\uparrow\uparrow}$.

5.5.1 Bistability width

The comparison between expectations and experiment is shown in Figure 5.6. We recorded the upper and lower bistability thresholds with respect to the polarization of the excitation. We scanned the $\lambda/4$ plate on the excitation side with steps of 15°. Data are reported in a polar plot. At 0° and 180°, the excitation is $\sigma+$ whereas at 90° and 270° it is $\sigma-$. The excitation is horizontal at 45°, 135°, 225° and 315°.

Figure 5.6 a shows the theoretical prediction. We computed the thresholds and widths according to Eqs. (5.11), (5.12) and (5.13) and using the renormalized expression for the interaction constant given in Eq. (5.14). They are expected to be larger under circularly polarized excitation. The measurements, displayed in Figure 5.6 b, show a very different result. The picture holds for the lower threshold but not for the upper. Therefore, the bistability width is reduced instead of being enhanced.

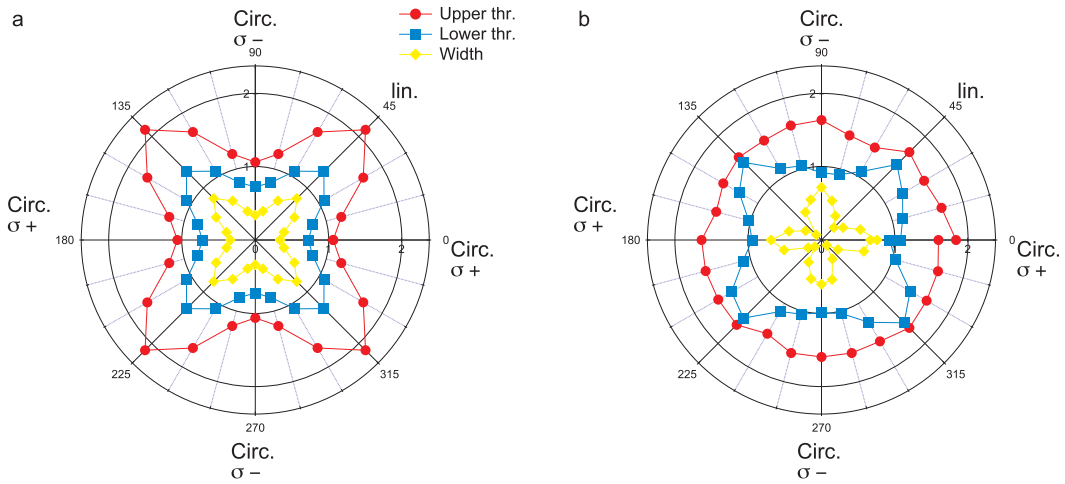

Figure 5.6: **Bistability thresholds vs polarization degree for $\alpha_2 = 0$.** Radius: pump power (mW) Angle: orientation of the $\lambda/4$ wave plate (deg). **a** Theory. For independent opposite spins populations, thresholds are at higher power in case of linearly polarized excitation and the resulting bistability width is larger than under circularly polarized excitation. **b** Experiment. The upper threshold is found to be independent of the polarization degree. Optical bistability is strongly suppressed under linearly polarized excitation. $\delta \simeq +0.16$ meV, $\gamma \simeq 200$ μeV and $\Delta \simeq 0.9$ meV

5.5.2 Thresholds and interactions

The simple treatment of polariton polarization proposed in Section 5.2.4 is therefore not sufficient to describe the observed phenomenology. Interactions between polaritons of opposite spins cannot be neglected. The OB-OL transition shown in Figure 5.4 suggests that the bistable behavior of polaritons with a given spin is compromised by the presence of polaritons with opposite spin. In fact, interactions between polaritons of opposite spins might play a very important role in this process. For the following discussion, we keep in mind the following important observations:

i) optical bistability is suppressed under linearly polarized excitation

ii) in the experiment, the upper threshold does not depend much on the excitation polarization degree

iii) the lower threshold follows the expected behavior and occurs at higher excitation power under linearly polarized excitation

The question is now to identify which process can have such a strong influence on the upper threshold and, in the meantime, leave the lower threshold almost unperturbed.

Hypothesis: biexciton formation

The OB-OL transition suggests that a linearly polarized excitation leads to an effective laser detuning and to an effective polariton linewidth such that $\Delta_{eff} < \sqrt{3}\gamma_{eff}$.

Once again, we stress the fact that the lower threshold follows the expected behavior while the upper threshold does not vary significantly. The suppression of bistability occurs under *linear excitation*, so for a **simultaneous presence of both spin-up and spin-down polaritons**. The effective laser detuning should be such that $\Delta_{eff} < \Delta$: this suggests that the polariton energy is blueshifted under linearly polarized excitation.

In fact, the system behaves as if polaritons of opposite spins paired into nonradiative (so long lived) states that contribute to the dynamics (energy shift, linewidth broadening) without being detected.

We formulate the hypothesis that biexciton states are created under elliptical and linear excitation. Indeed, biexciton states are decoupled to the cavity field and therefore have a long relaxation time. In addition, they contribute to an increase of the exciton density. Consequently, they contribute to the blueshift of both spin-up and spin-down polaritons and to a broadening of the linewidth.

We model phenomenologically the effective laser detuning and polariton linewidth as follows:

$$\Delta_{eff} = \Delta - a(1 - \rho_p^2) \tag{5.17}$$

$$\gamma_{eff} = \gamma + b(1 - \rho_p^2) \tag{5.18}$$

where a and b are two positive parameters.

In Figure 5.7, we show that applying such corrections to our simple model allows efficient fits of the data.

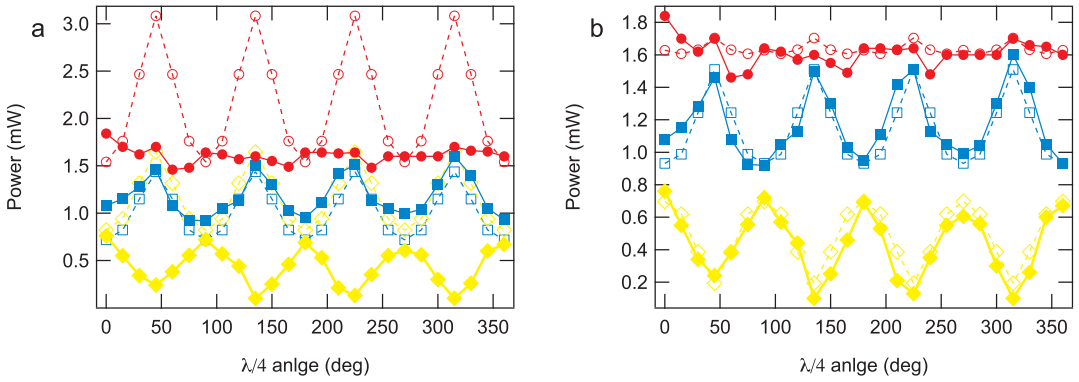

Figure 5.7: **Phenomenological model.** Fit of experiments. Circles: upper thresholds, squares: lower thresholds, losanges: widths. Empty symbols theory. **a** Without effective Δ, γ. The data of Fig. 5.6 a are represented as a function of the angle of the quarter wave plate. The constant upper threshold observed in the experiments is not reproduced by the theory. **b** With effective linewidth and blueshift. The fits are in good agreement with the measurements. Parameter a acts on the upper threshold and parameter b on the lower threshold. *Experiment parameters:* $\delta \simeq 0$, $\Delta = 0.5$ meV and $\gamma \simeq 0.2$ meV. *Realistic fit parameters:* $\delta = 0$, $\Delta = 0.6$ meV, $\gamma = 0.2$ meV, $a = 0.13$ meV, $b = 0.05$ meV and $\alpha = 0.025$.

5.6 Evidence for a contribution of biexcitons

We confirm our hypothesis by verifying two important points.

a) First, if changing from circular to linear excitation indeed modifies Δ and γ so that they do not satisfy the bistability condition anymore, then it should be possible to retrieve a bistable behavior by increasing the initial laser detuning.

b) Second, if this effect is related to the biexciton formation, then it should disappear at negative detuning, where the polariton resonance is farther from the biexciton resonance.

In a series of experiments at different cavity detunings δ, we measure the bistability widths as a function of the laser detuning Δ. The experiment on the laser detuning is presented in Figure 5.8. Each row corresponds to a different cavity detuning. Data are presented as a function of the energy difference between the lower polariton and the exciton resonance δ'. The corresponding exciton content X^2 is also indicated. The left and right columns display the bistability thresholds and widths, respectively. For simplicity, we do not display the numerous bistability curves. We report the changes in the interaction regimes with tags (OL,OD and OB) on the threshold curves.

5.6.1 Influence of the laser detuning

Figs. 5.8 a and b show data taken at $\delta' = -1.01$ meV ($\delta = +2.11$ meV). Under circularly polarized excitation, the system behaves as an optical limiter up to $\Delta = 0.34$ meV where it behaves as an optical discriminator. At $\Delta = 0.43$ meV and

above, we observe a bistable behavior. The thresholds and the width increase with Δ up to $\Delta = 0.55$ meV and then decrease. Under linearly polarized excitation, the system behaves as an optical limiter as observed above. However, for a very large laser detuning $\Delta = 0.74$ meV, we observe an OD behavior. In this case, the width is always zero (the negative value is due to mechanical vibrations or to a small thermal drift).

The effect is even more obvious in Figs. 5.8 c and d, corresponding to $\delta' = -1.24$ meV ($\delta = +1.28$ meV). Under circularly polarized excitation, OD regime starts at $\Delta = 0.32$ meV and OB regime at $\Delta = 0.69$ meV. Under linearly polarized excitation, we observe an OD regime from $\Delta = 0.69$ meV and an OB regime starting at $\Delta = 0.97$ meV.

We evidence bistability under linear excitation for very large values of Δ. The critical laser detunings are larger under linearly polarized excitation, showing that the parameters Δ and γ are actually modified in the presence of both spin-up and spin-down polaritons.

5.6.2 Influence of the cavity detuning

At negative detuning, the bistability suppression effect clearly disappears. Figs. 5.8 e and f are taken at $\delta' = -1.86$ meV ($\delta = -0.19$ meV) and Figs. 5.8 g and h are taken at $\delta' = -2.07$ meV ($\delta = -0.56$ meV). The critical values of Δ are the same under circularly and linearly polarized excitation, and they are much lower than the ones measured at positive detuning.

Furthermore, the upper thresholds are well fitted by a cubic law while the lower thresholds are fitted by linear curves, as expected from Eqs. (5.11) and (5.12). The factor 2 between the linear and circular thresholds and widths is not observed, which is a signature of interactions between polaritons of opposite spin. These interactions decrease with the detuning, as it can be seen by comparing the threshold difference obtained in Fig. 5.8 e and g.

Finally, note that the variation of the threshold curves in Figs. 5.8 a and b and in Fig. 5.8 e for $\Delta > 0.30$ meV is complicated (bumps, saturation...) and not fully understood. This complex behavior is probably related to excitonic effects or many-body collisions and may be the object of further investigations. Fortunately, this does not compromise our conclusions.

5.7 Biexcitons in semiconductor microcavities

We shortly discuss how biexcitons are formed and what is their impact on linewidth, blueshift and spin orientation in the system. Numerous theoretical and experimental studies have been dedicated to the characterization of biexcitons in quantum well and microcavities.

Binding energy

The biexciton is a molecular state composed of two excitons. The energy of a biexciton E^{BX} is given by twice the exciton energy E^X minus the biexciton binding

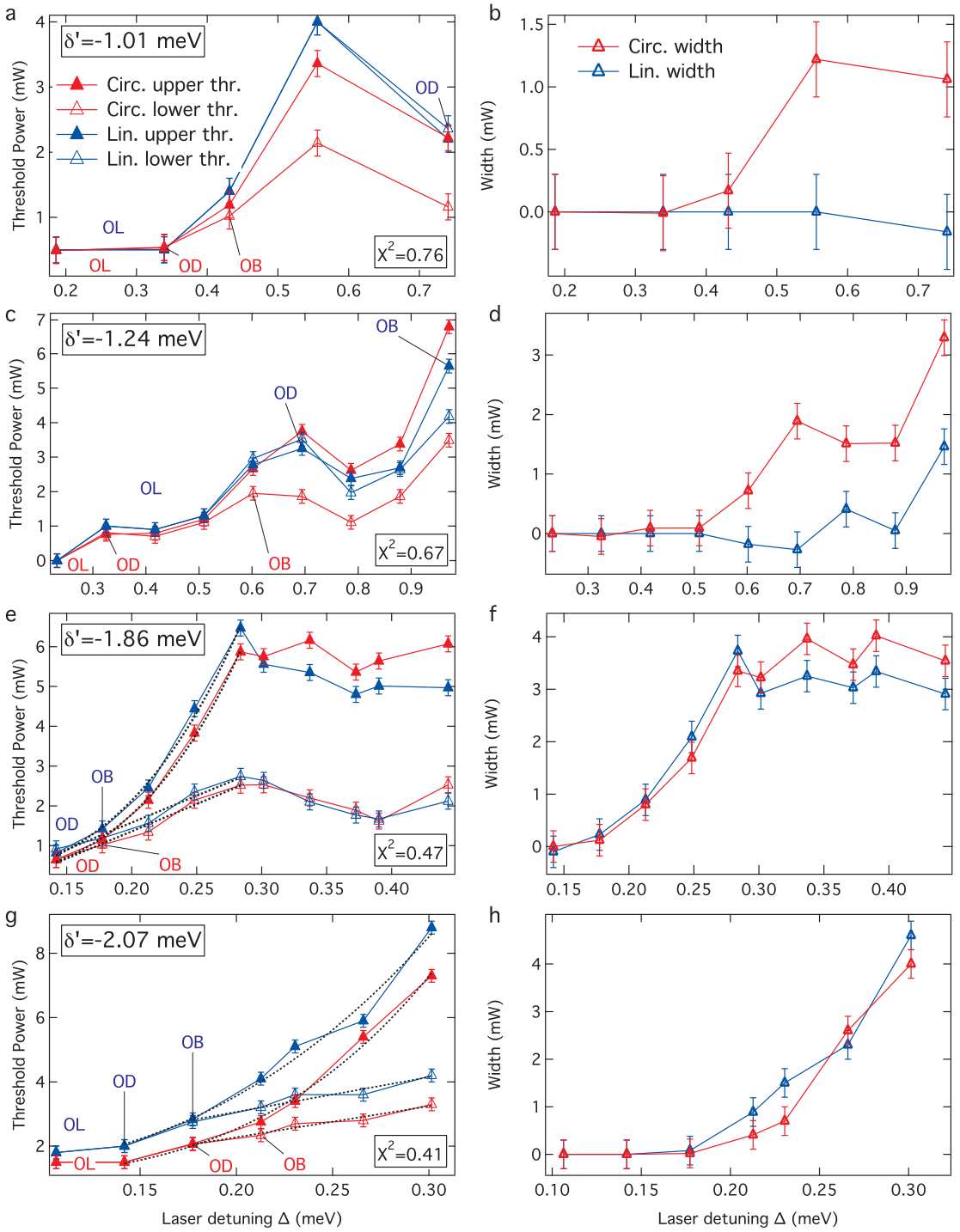

Figure 5.8: **Effect of cavity detuning.** Bistability thresholds (left) and resulting width (right) under circular or linear excitation, at different polariton energies and different laser detunings. **a,b** and **c,d** Bistability is suppressed under linear excitation. The threshold behavior as a function of the laser detuning Δ is very complicated and strongly differs from the theoretical prediction. **e,f** and **g,h** The bistable behavior under linear excitation is retrieved at negative detuning. The threshold dependence on Δ is in agreement with the expectations. The upper (lower) threshold is well fitted using cubic (linear) curves (dotted lines). In **e**, the threshold behavior for $\Delta > 0.3$ meV is unexplained.

energy E_b^{BX}.

$$E^{BX} = 2E^X - E_b^{BX} \tag{5.19}$$

In microcavities with InGaAs quantum wells, E_b^{BX} is of the order of 2 meV [Saba 00, Baars 01, Borri 99]. Therefore, we expect a resonance for biexciton formation our of two polaritons at 1 meV below the exciton energy.

In these experiments on 2D polaritons, we were not able to evidence a clear biexciton resonance. However, our measurements clearly indicate that an important interaction between spin-up and spin-down polaritons takes place up to 1.5 meV below the exciton energy. At very negative detuning the expected bistable behavior is recovered and the correct threshold dependence are found.

Let us highlight two contributions that can be related to our experiment.

Saba's experiment

The first absorption experiments on biexciton were done by Saba et al. with pump-probe measurements in a GaAs microcavity similar to ours. Interestingly, they observed that the formation of $\sigma-$ excitons is inhibited in the presence of a high density of $\sigma+$ excitons. They could measure a *transfer* of the oscillator strength from the exciton to the biexciton, i.e. a decrease of the exciton oscillator strength to the benefit of the biexciton oscillator strength[Saba 00].

This calls to mind our observations in the OB-OL transition experiment. Close to linear excitation, the system is in the OD regime and the dominant population seemed to inhibit the increase of the other (see Fig. 5.4, $\rho_p = \pm 0.34$). Under linear excitation, the system is in the OL regime (see Fig. 5.4, $\rho_p = 0$). The polariton creation is strongly reduced. Finally, the saturation of the dominant population intensity in the OD regime contrasts with the intensity increase in the OB regime.

Theory

A biexciton is a molecular state of two bound excitons. One could argue that, since excitons are electric dipoles, Coulomb interaction between them is small so that biexciton formation should not be an important process. The theory by Combescot et al. describes the mechanisms for the formation of bound state out of two excitons [Combescot 09].

The absorption of a circularly polarized photon in presence of *one* counter-circularly polarized exciton is calculated. The final state is found to be constituted of two excitons of opposite spins that bound with a probability depending on the distance between their center of mass. They obtain a so-called "bare" biexciton oscillator strength, much smaller than exciton oscillator strength (see Chapter 1, Section 1.4), given by

$$f_{osc}^{BX} = \left(\frac{a_{BX}^2}{S}\right) f_{osc}^X$$

where a_{BX} is the biexciton Bohr radius. f_{osc}^{BX} is very small compared to the exciton oscillator strength f_{osc}^X. However, in the presence of an exciton gas, they find that the probability to form biexcitons by absorption increases linearly with the exciton density N_X. This explains why significant biexcitonic effects can be measured experimentally in the high-density regime.

Finally they also indicate that at high densities, many-body effects (higher order collisions, carrier exchange) can be responsible of strong modifications of the biexciton resonance like large energy shifts, modification of the binding energy, broadening. Such effects are probably responsible for the complicated behavior obtained in Fig. 5.8. However, the theoretical treatment of such processes is very complicated and is not in the scope of the present work. Our phenomenological considerations are sufficient to highlight the main issues of spinor effects on optical bistability. In the next chapter, we will introduce the spinor Gross-Pitaevskii equation to model spinor bistability in the case of 0D polaritons.

5.8 Conclusion

In conclusion, we have investigated spinor interactions between planar polaritons in the degenerate parametric scattering regime. In case of circularly polarized excitation, we observe a clear optical bistability for polaritons with the corresponding spin-polarization. By decreasing the excitation circular polarization degree, we increase the proportion of polaritons with opposite spin. We observe a progressive reduction of the bistability width and a transition to optical discrimination and to optical limiting, under linearly polarized excitation.

Detuning dependent experiments indicate that the bistability suppression effect is related to the formation of biexcitons. On the one hand, the effect disappears for very large laser detunings Δ for values δ in the vicinity of the expected biexciton resonance. On the other hand, it also disappears at very negative cavity detunings (i.e. also far from the expected biexciton resonance), where the thresholds follow the expected power dependence.

From an application viewpoint, these experiments demonstrate the coherent control of optical bistability. Transition between OB, OD and OL are simply monitored by changing the polarization degree of the excitation. In addition, the polarization degree of the emission can vary strongly with the excitation power, producing polarization modulation and bistable polarization conversion.

In the next chapter, we investigate spinor interactions with confined polaritons. The weak disorder and the narrow linewidth reduce the biexciton influence and enhance the polarization conversion effects. We successfully demonstrate coherent spin multistability.

Chapter 6

Spin Multistability of Confined Polaritons

Coherent manipulation of spin ensembles in the solid state is a key issue in the development of spintronics. In this respect, polarization multistability is a promising effect. It describes the possibility, for a spinor system in presence of anisotropic interactions, to switch between three different spin states for a given excitation condition. This effect might lead to multi-valued spin switching and to new schemes of spin-based logic gating and memories [Chattopadhyay 09, Lvovsky 09] [1].

In the early 80's Kitano and Ogawa proposed an experiment to observe polarization multistability with atomic vapors of sodium, with Zeeman splitting in the ground state level. It was rapidly followed by several experimental investigations [Cecchi 82, Giusfredi 85, Giacobino 85] in similar systems. However, from the 90's, research in this field dwindled, probably because no equivalent could be achieved in solid-state systems.

The difficulty in observing spin-multistability comes from the fact that it requires both the control of spinor interactions in the system and a strong spin coherence. Recently, the emergence of spintronics stimulated its theoretical investigation in different solid-state systems like magneto-optic cavities [Jonsson 99], ring cavities [Haelterman 94], spatial solitons in fibers [Steiglitz 01], etc.

In 2007, Gippius et al. published a theoretical development pointing out the possibility of observing polarization multistability in semiconductor microcavities [Gippius 07]. In their model, they considered that polaritons of opposite spins are independent, as we first did in Chapter 5, Sections 5.2.4 and 5.5. Hence, they obtained decoupled bistability curves for spin-up and spin-down polaritons and higher thresholds under linearly polarized excitation. By exploiting the latter decoupling, they could determine the appropriate excitation conditions to observe spin multistability. The work of Gippius gave rise to proposals exploiting the huge potential of spin multistability in view of the design of localized memories [Shelykh 08], optical circuits [Liew 08a] and of the optical characterization of optical disorder [Liew 09b].

In this Chapter, we demonstrate spin multistability with confined polaritons. Through a large set of measurements, we could acquire sufficient knowledge about

[1] In a more general way multistability concerns various fields, from brain modeling [Bezrukov 09] to nematic liquid-crystals [Smalyukh 10]

the interactions in our system as well as the ways of controlling them. The spin multistability occurs in a quite different regime than in the original proposal. The main reason is that, in our system, contrarily to the generally admitted picture, polaritons of opposite spins are interacting repulsively and not attractively.

We start the discussion in Section 6.1, with the description of the typical optical instabilities that lead to spin multistability. The sample is excited just above the polariton ground state. Thanks to the narrow linewidth of confined polaritons and to the weak disorder in mesas, the behaviors obtained in Chapter 5, Section 5.4 are modified. For instance, we are able to observe a clear resonance for the biexcitonic effects, and we observe a decoupling of spin-up and spin-down polaritons bistability curves, allowing for multistability. In Section 6.2, we give the theoretical bases to model our experiments. We discuss different issues such as the interaction strengths and the role of nonlinear losses through the formation of biexcitons.

The presence of decoupled bistability curves between spin-up and spin-down polariton gives rise to strong linear to circular polarization conversion. In Section 6.3, we investigate this effect and its dependence on the cavity detuning. Thanks to this study, we could develop a clear experimental procedure to observe spin multistability. Section 6.4 is dedicated to the spin multistability experiments. For a given excitation condition, we demonstrate that the polariton spin switches between three stable states and exhibits macroscopic coherence. Strikingly, we also evidence a regime of macroscopic spin flip-flop, or spin trigger effect.

In addition, we discuss in Section 6.5 a series of measurements investigating the role of the different excitation parameters. We show that the response of the system can be tuned at will.

All these experiments open many pathways to the development of versatile spintronic devices. We review the main perspectives in Section 6.6 and finally conclude in Section 6.7.

6.1 Spinor interactions with confined polaritons

In this section, we describe the main effect responsible for multistability, which the decoupling of bistability curves for spin-up and spin-down polaritons. The theoretical model described in Section 6.2 helped us reproduce the experimental data and estimate the interaction strengths in our system.

6.1.1 Experimental procedure

Setup

The experimental setup is identical to the one described in Chapter 5 (Section 5.3.1) used for studying optical bistability with planar polaritons.

System under investigation

Thanks to the spatial confinement, the experiments are done with a single polariton energy level. We work in 3 μm diameter mesas, where the typical polariton linewidths are of 100 μeV and the spacing between the first excited state and the

ground polariton state is of the order of 1 meV. The microcavity sample is excited with a single-mode continuous wave laser, at normal incidence. The fine tuning of spinor interactions is done by adjusting the excitation parameters: power, polarization and energy detuning Δ with respect to the polariton ground state. We can change both the circular polarization degree of the pump ρ_p and the direction of the linear polarization axis with respect to the crystalline axes. Note that Δ is kept smaller than the energy difference between the first excited state and the ground state.

Real-time monitoring

Observing spin multistability requires the acquisition of a large number of data points, with a high precision. In Section 5.3.1, we highlighted the fact that most of the experimental elements are controlled by a computer. Real-time monitoring and automation of the experiment were crucial to minimize mechanical vibrations, power and thermal fluctuations and to obtain real time information on the polarization resolved signal processing. In addition, the use of a control CCD allowed us to acquire movies of the experiment to visualize the independent evolution of the two polarization resolved channels. Finally, power thresholds are very sensitive to fluctuations and the mesa position in the 20 μm gaussian excitation spot needs to be accurately stabilized. To do so, we inserted piezoelectric actuators in the cryostat translation stages in order to be able to adjust the mesa position within 30 μm with a precision of a few tens of nanometers.

Measurement of spin coherence

We resolved the emission polarization not only in the circular ($\sigma+$,$\sigma-$) basis, but also in the linear (H,V) and diagonal (D+,D-) bases. This gave us the projection of the optical polarization along the three axes of the Poincaré sphere, hence the polariton spin in the Bloch sphere. By this, we could measure the macroscopic spin coherence.

6.1.2 Spinor bistability

The knowledge of spinor interactions in our system was acquired by studying the influence of the excitation power and polarization in various configurations. We scanned the excitation power for different excitation polarizations and resolved the emission in the ($\sigma+$,$\sigma-$) basis. Under circularly polarized excitation, a single polarization component is excited and the emission intensity exhibits conventional bistability. In Fig. 6.1, we show that the behavior is much richer under elliptical or linear polarization.

As discussed in the previous chapter, the reason is that spinor interactions are strongly anisotropic: the interactions strengths between same- (α_1) and opposite- (α_2) spin-polarized polaritons are not equal. In addition, like in the case of planar polaritons, we have strong indications for biexcitonic effects, which we will be able to study very precisely since we work with a single confined state of narrow linewidth (see Section 6.5).

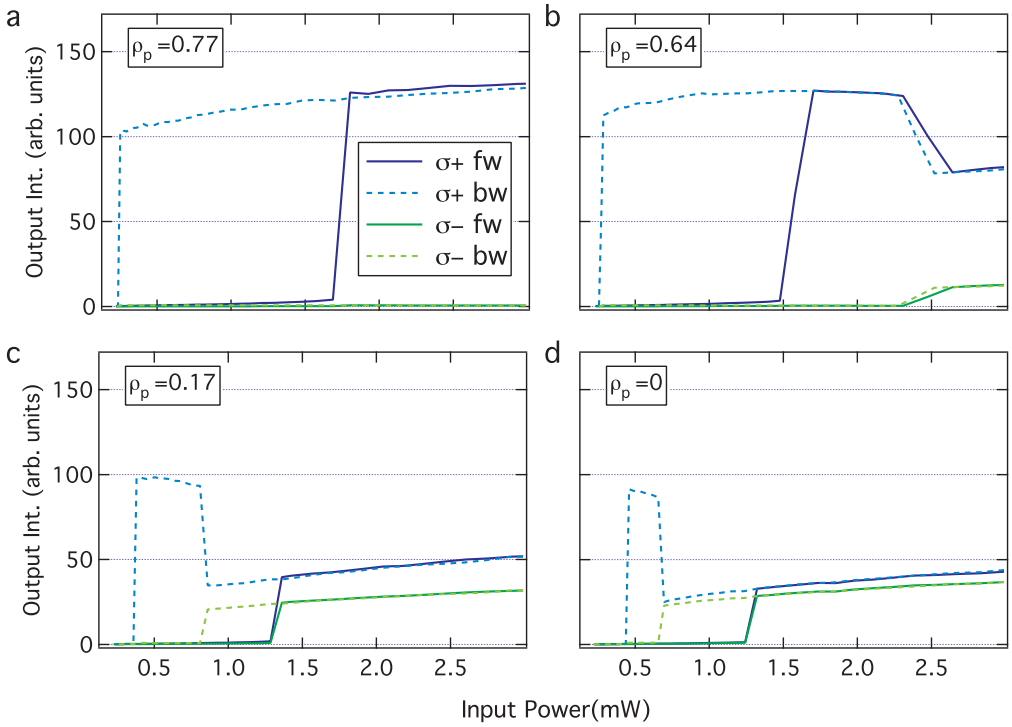

Figure 6.1: **Evidence of spinor interactions through excitation power dependence.** The excitation power was scanned from 0.2 to 3 mW, forward (fw) and backward (bw), for 4 excitation polarization degrees: ρ_p = 0,77, 0,64, 0,17 and 0. **a Conventional bistability.** At high circular polarization degree (ρ_p = 0.77), the system exhibits conventional bistability for only one spin-polarization. **b Evidence for nonlinear losses**. (ρ_p = 0.64) $\sigma+$ polaritons jump to their upper branch at 1.5 mW. The jump of $\sigma-$ polarized polariton to their upper branch causes a very strong decrease of the $\sigma+$ polaritons intensity. This gives rise to the appearance of a *middle intensity* branch. Similarly, when $\sigma-$ polaritons jump to their lower branch, $\sigma+$ polaritons jump back to their upper branch. This shows that important nonlinear losses occur in the presence of polaritons of opposite spins. **c Evidence for a non radiative contribution.** The decrease of the bistability width compared to **a**, as well as the 2.5 intensity ratio between the upper and middle spinor bistability branches are the signature of a non radiative contribution to the dynamics in the presence of polaritons of opposite spins. **c, d Evidence for repulsive interactions.** Simultaneous jumps of $\sigma+$ and $\sigma-$ polaritons are the result of repulsive interactions: the blueshift of the one spin-polarization favors the blueshift of the other spin-polarization. Again, one distinguishes three bistability branches (lower, middle and upper), resulting from important nonlinear losses and from a non radiative contribution to the dynamics. Because of these observations, we formulate the hypothesis that biexciton formation through pairing of spin-up and spin-down polaritons occur under elliptically and linearly polarized excitation. Biexciton states have a long radiative lifetime and contribute to the blueshift of both polarizations. Upper threshold powers are thus lower under linear excitation than under circular excitation. *Parameters:* $\delta' = -1.47\ meV$, Δ =0 .49 meV.

To understand the experimental data plotted in Fig. 6.1, one can first think about two distinct spinor polariton populations, $\sigma+$ and $\sigma-$, independently excited by the laser. The respective *effective excitation powers* felt by $\sigma+$ and $\sigma-$ polaritons are obtained by weighting the nominal excitation power according to the excitation polarization degree ρ_p.

Circularly polarized excitation

For nearly $\sigma+$ excitation, the coherent emission is dominated by $\sigma+$ polaritons (see Fig. 6.1 a). We observe a jump of about two orders of magnitudes in the emission intensity. The measured emission powers are of the order of 10 nW on the lower branch and 1 μW on the upper branch. This latter power corresponds to a number of polaritons of the order of 10^2 in the 10 μm^2 mesa. Hence, the term *macroscopic* is justified in the following discussion.

Elliptically polarized excitation: signature of nonlinear losses

In Fig.6.1 b, ρ_p is decreased to 0.64. The proportion of $\sigma-$ polaritons (18%) becomes sufficient to cause a jump to the upper intensity branch within the range of the power scan. A striking observation is that, at 2.3 mW, the jump in the $\sigma-$ intensity causes a drop in the $\sigma+$ intensity. The scan at higher powers (P>2.3 mW) unveils a middle intensity branch for $\sigma+$ polaritons. When the power is decreased, the reversed process occurs: when $\sigma-$ polaritons jump down, $\sigma+$ polaritons jump back to the upper branch. This shows that the presence of polaritons of opposite spins causes strong nonlinear losses in the spinor populations.

Nearly linearly polarized excitation: signature of a non radiative contribution

For even smaller values of ρ_p, the upper thresholds are equal. The $\sigma-$ hysteresis becomes wider, but the lower threshold for $\sigma-$ stays at higher power than for $\sigma+$ (see Fig. 6.1 c and d). When the $\sigma-$ population jumps down, one observes an increase of the $\sigma+$ population by *more than a factor of 2*. We therefore can distinguish three branches, with notably large intensity differences.

The middle branch is observed when the excitation power is above the upper power thresholds of both $\sigma+$ and $\sigma-$ polaritons. The coexistence of both spinor gases on their upper branch is impeded by a strong nonlinear process. However, when the power is decreased, we observe the jump from the middle branch to the upper branch, with an exceptional gain. Note that the intensity of the upper branch is roughly the same for all excitation polarizations.

These results suggest that, when *both* spin-up and spin-down polaritons are present in the system, a process takes place so that most of them[2] are not coupled to light anymore, while still participating to the dynamics. The formation of a middle bistability branch is the manifestation of such a process. Like in Chapter 5,

[2]About 80 percents under linearly polarized excitation.

we are inclined to think that a pairing of polaritons of opposite spins into non radiative states takes place. Here again, we attribute this effect to the formation of biexcitons.

Note that, as in Chapter 5, the width of the bistability region is smaller under linearly polarized excitation than under circularly polarized excitation.

Thresholds independence

The last comment is about the independence of the lower thresholds around $\rho_p = 0$. It induces drastic changes in the population ratios, hence in the circular polarization degree of the emission. This results into very efficient linear to circular polarization conversion and is crucial for multistability. It will be discussed in Section 6.3.

6.2 Theoretical two-mode model

6.2.1 Model

A theoretical two-mode model qualitatively reproduces the experimentally observed trends and informs us about spinor interactions in the system. The model accounts for polarization anisotropic interactions, polariton linewidth γ and linear polarization splitting ϵ_{lin}. The latter two parameters were directly measured experimentally (see Fig. 6.2). Here, nonlinear losses in the presence of polaritons of opposite spins are included through a nonlinear contribution to the decay rate β. The two coupled Gross-Pitaevskii equations for the field amplitudes read

$$\begin{aligned} i\frac{d}{dt}\psi_{\pm} &= [-\epsilon_g - \frac{i}{2}(\gamma + \beta|\psi_{\mp}|^2) + \alpha_1|\psi_{\pm}|^2 + \alpha_2|\psi_{\mp}|^2]\psi_{\pm} \\ &+ \frac{\epsilon_{\text{lin}}\psi_{\mp}}{2} + F_{\pm}e^{-i\omega_L t} \end{aligned} \tag{6.1}$$

6.2.2 Repulsive interactions

A first issue concerns the sign of the interactions between counter-circularly polarized polaritons α_2. We have experimental evidence for the manifestation of repulsive interactions between polaritons of opposite spins. The most obvious one is the simultaneous jumps at high power observed in Fig. 6.1 d. Indeed, in the bistability regime, the jump to the higher branch occurs once the energy of the state has shifted close enough to resonance. Simultaneous jumps to the higher branch therefore suggest that the high density of one polarization stimulates the blueshift of the other. From Eq. (6.1), the blueshift given by

$$\Delta\epsilon(\psi_{\pm}) = \alpha_1|\psi_{\pm}|^2 + \alpha_2|\psi_{\mp}|^2 \tag{6.2}$$

Therefore, our observations show that $\alpha_2 > 0$. This is in stark contrast with common $\alpha_2 < 0$ value obtained in the Born approximation [Renucci 05]. Theoretical predictions of multistability by Gippius et al. [Gippius 07] were made under this assumption. A refined microscopic calculation however shows that α_2 can be positive when the two-polariton energy is in the vicinity of the biexciton resonance [Kwong 01].

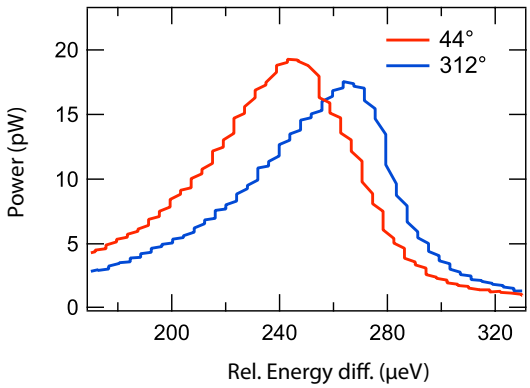

Figure 6.2: **Linear polarization splitting.** We performed high-precision measurements of the polarization resolved transmission spectrum in 3 μm mesas. The excitation linear polarization axis was rotated with respect to our reference horizontal polarization axis, with steps of 4°. For each orientation, we scanned the laser energy over 70 GHz with steps of 0.5 GHz. We obtained a linear polarization splitting of about 20 μeV, with orthogonal axes at ±45° with respect to our reference horizontal polarization axis. These axes correspond to the [001] and [010] crystallographic axes of our microcavity sample.

6.2.3 Nonlinear losses

Second important ingredients of the theory (see Eq. 6.1) are the nonlinear losses in presence of polaritons of opposite spins. An experimental clue of their influence is the narrowing of the hysteresis region when going from circular to linear excitation. Their effect is the most pronounced in Fig. 6.1 b, where the hysteresis loop in $\sigma-$ is much reduced due to the large $\sigma+$ density. Additionally, in Fig. 6.1 c and d, the $\sigma+$ population increases at the lower threshold of $\sigma-$.

The panels of Fig. 6.3 summarize the theoretical investigations on the effects of the different interaction parameters. Fig. 6.3 a shows the theoretical reproduction of the experiments with repulsive interactions $\alpha_2 = 0.4\,\alpha_1$ and nonlinear losses $\beta = 0.3\,\alpha_1$. All the experimental features are qualitatively reproduced by the simulation. At $\rho_p = 0.77$, the emission is dominated by the $\sigma+$ signal. At $\rho_p = 0.64$, an optical discriminator behavior is observed for $\sigma-$ at a higher upper thresholds than $\sigma+$. The increase of the $\sigma-$ intensity corresponds to a decrease of the $\sigma+$ intensity. At $\rho_p = 0.17$, the upper thresholds coincide but the lower thresholds are different. Finally, the $\sigma-$ bistability widens as ρ_p approaches 0.

We stress the fact that our model is not a model of the effects of biexcitons on spinor bistability. We do not account for the non radiative contribution to the dynamics, nor for the many-body effects[3]. Therefore, we may underestimate the intensity losses and the changes in the power thresholds of Fig. 6.1 c and d. Nevertheless, the qualitative agreement is very satisfactory for our needs here. In particular, it is enough to show important differences with the result obtained without nonlinear losses or with attractive interactions. The variation of the parameters from their optimal values significantly alters the reproduction of the experimental results.

[3]This complicated treatment may be the object of a further work.

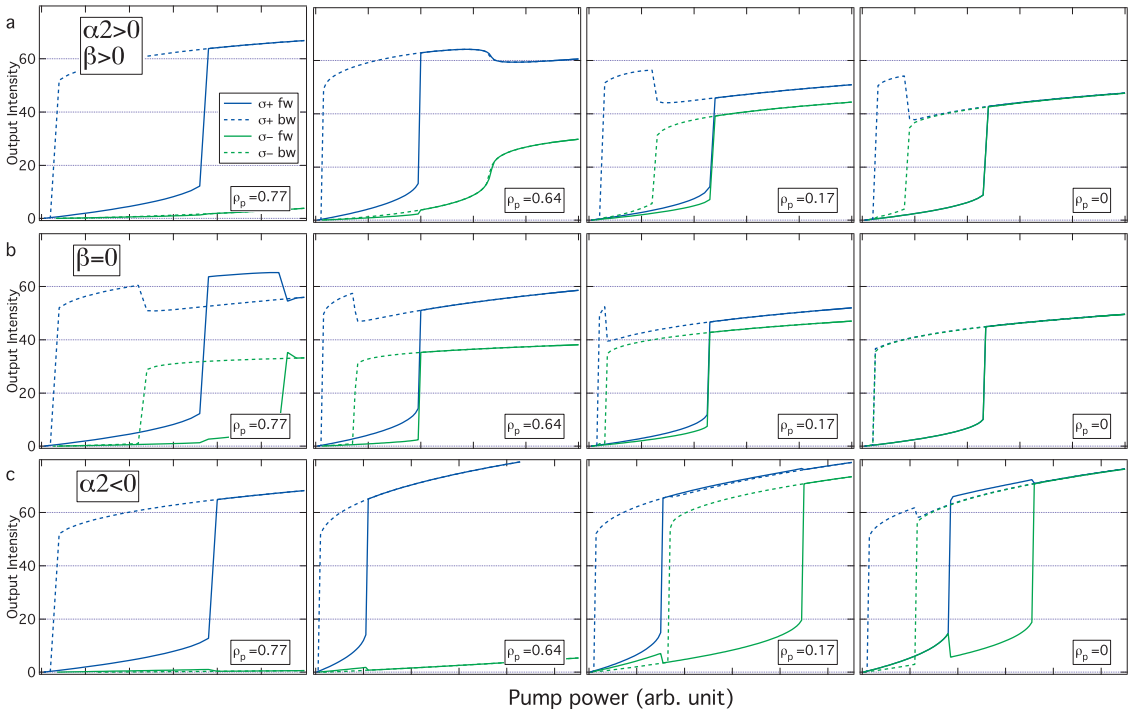

Figure 6.3: **Theoretical modeling.** The experimental behavior observed in Fig. 6.1 is reproduced. We analyze the role of repulsive interactions and the impact of nonlinear losses on the spinor bistability. Each panel contains simulations of a power scan for the 4 excitation polarization degrees used in the experiment. **a** Theory with repulsive spinor interactions $\alpha_2 = 0.4\alpha_1$ and nonlinear losses $\beta = 0.3\alpha_1$. The qualitative behavior of the bistability is well represented. **b** Nonlinear losses are neglected $\beta = 0$. We cannot reproduce the independence of the lower thresholds at $\rho_\mathrm{p} = 0$ nor the separated upper thresholds with the strongly reduced hysteresis width for $\sigma-$ at $\rho_\mathrm{p} = 0.64$. **c** Theory with attractive interactions $\alpha_2 < 0$: the simultaneous jumps to the upper branch cannot be reproduced for $\rho_p = 0.64,\ 0.17,\ 0$.

Figure 6.3 b and c show comparisons with the behavior calculated for $\beta = 0$ and for $\alpha_2 < 0$, respectively. Clearly, theoretical predictions made with the latter two choices of parameters do not agree at all with the experimental observations. When the nonlinear losses are suppressed (panel b), the $\sigma-$ bistability appears at higher values of ρ_p (no inhibition). The effect of repulsive interactions is already visible at $\rho_p = 0.64$, where the upper thresholds already coincide. The threshold independence around $\rho_p = 0$ is suppressed. If, in addition, the interaction between counter-polarized polaritons is made attractive, the upper thresholds are no longer the same.

6.2.4 Threshold independence

Our theoretical simulations have shown that there is a strong interplay between nonlinear losses and repulsive interactions. Repulsive interactions tend to make the thresholds coincide. Nonlinear losses make the lower bistability thresholds under linearly polarized excitation to be different for $\sigma+$ and $\sigma-$. As we will see,

this independence of the lower thresholds close to $\rho_{\mathrm{p}} = 0$ is essential for achieving polarization multistability.

In the prediction by Gippius et al., $\alpha_2 \leq 0$ and $\beta = 0$. With such parameters, the independence concerned the upper threshold as it can be seen in Fig.6.3 c. We comment on this prediction in Section 6.4.4.

In the Section 6.5.1, we show additional experimental confirmation of the role of nonlinear losses. At lower energy δ' of the polariton state, and therefore further away from the biexciton resonance, we find a single lower threshold under linear excitation. An extensive study of the dependence on the detuning allows us to determine a resonance between -0.9 and -1.1 meV, where nonlinear losses are peculiarly important.

6.3 Conversion of the internal spin-polarization

In the present section, we show how multistability arises form the threshold independence around $\rho_p = 0$. We have shown above that the bistability behavior is strongly modified by the interactions between spin-polarized polaritons. From now, we will adopt the pseudospin picture for polaritons and discuss the physics inside the cavity in terms of spin-up and spin-down polariton populations.

6.3.1 Polarization conversion

The main consequence of the threshold independence is the drastic changes in the population ratio, hence, a significant *conversion of the spin-polarization*. In Figure 6.4, we show the polarization conversion resulting from the experiments of Fig 6.1. We calculate the emission polarization degree ρ_c

$$\rho_c = \frac{I_{\sigma+} - I_{\sigma-}}{I_{\sigma+} + I_{\sigma-}}$$

and plot ρ_c versus the excitation power for $\rho_p = 0.64$, 0.17, 0 and -0.10. The threshold independence yields a fully spin-polarized region that we call a *spin conversion plateau*. Fig. 6.4 a corresponds to the case where the upper thresholds are different and the $\sigma-$ bistability is reduced (see Fig. 6.1 b). In the detection, initial elliptical polarization is first converted to fully circular polarization, which corresponds to the situation where spin-up polaritons are at resonance with the laser and spin-down polaritons far from resonance. When spin-down polaritons jump to the upper branch, the emitted light is again elliptically polarized. Fig. 6.4 b,c and d show the cases around $\rho_p = 0$. The main effect is visible on the backward scan, where a linearly polarized excitation results into a fully circularly polarized emission. The near-field polarization resolved emission in the ($\sigma+$,$\sigma-$) basis is shown in Figure 6.5. Depending on the excitation power, the channels can be

a both channels "off" (linear polarization)

b both channels "on" (linear polarization)

c one channel "on", one channel "off" (circular polarization)

for the same value of ρ_p.

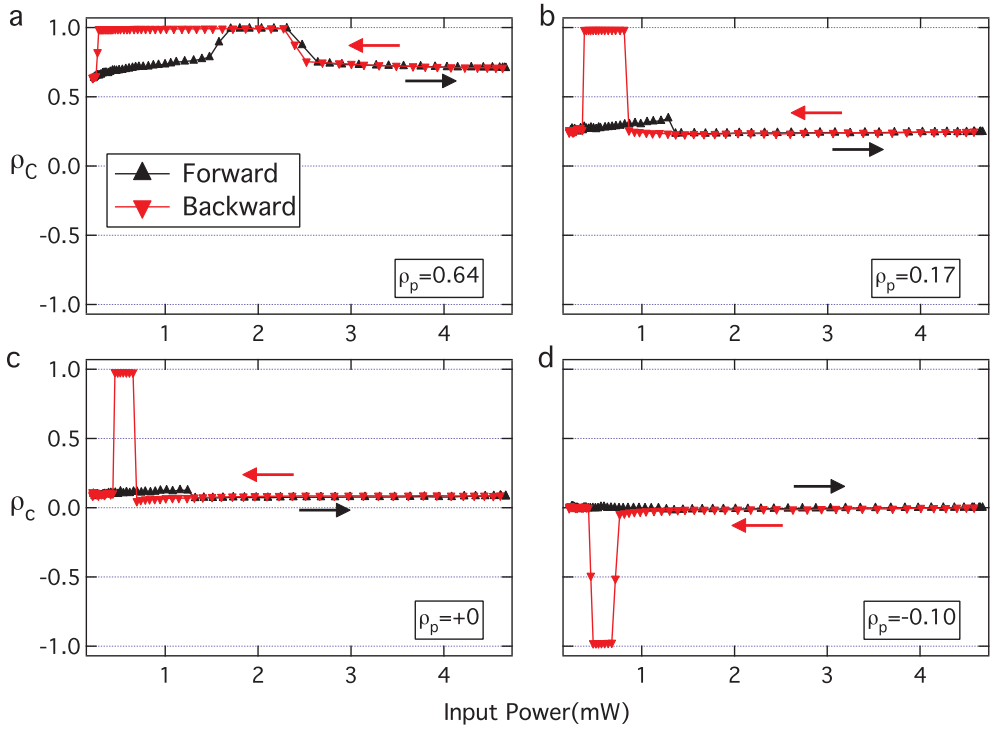

Figure 6.4: **Polarization conversion experiment.** The polarization degree ρ_c is calculated out of the measurements of Fig. 6.1 and plotted versus the excitation power. **a** Data of Fig. 6.1 c. Spin-up polaritons jump to the upper branch at 1.5 mW and the emission becomes fully circularly polarized. At 2.5 mW, spin-down polaritons jump up, which reduces the emission polarization degree to $\rho_c \simeq \rho_p$. On the backward path, spin-down polaritons jump down again at 2.5 mW: their bistability width is reduced by nonlinear losses attributed to biexciton formation. Polarization is again converted to $\rho_c = 1$. Spin-up polaritons jump to their lower branch at 0.3 mW. The threshold independence thus leads to polarization conversion with hysteresis behavior. **b** Data of Fig. 6.1 c. The upper thresholds are coupled because of repulsive interactions. Lower thresholds are at 0.8 mW for spin-down and 0.4 mW for spin-up polaritons. We observe polarization conversion from $\rho_c = 0.23$ to $\rho_c = 0.98$. **c** Data of Fig. 6.1 d. We observe high contrast linear to circular polarization conversion at $\rho_p = 0$. ρ_c jumps from 0.07 to 0.97. The hysteresis is 0.23 mW wide. **d** For slightly negative $\rho_p = -0.10$, ρ_c jumps from -0.04 to -0.97 with a 0.26 mW hysteresis. The polarization conversion of the transmitted light reflects the *macroscopic spin conversion* inside the microcavity. *Parameters:* $\delta' = -1.47$ *meV,* $\Delta = 0.49$ *meV.*

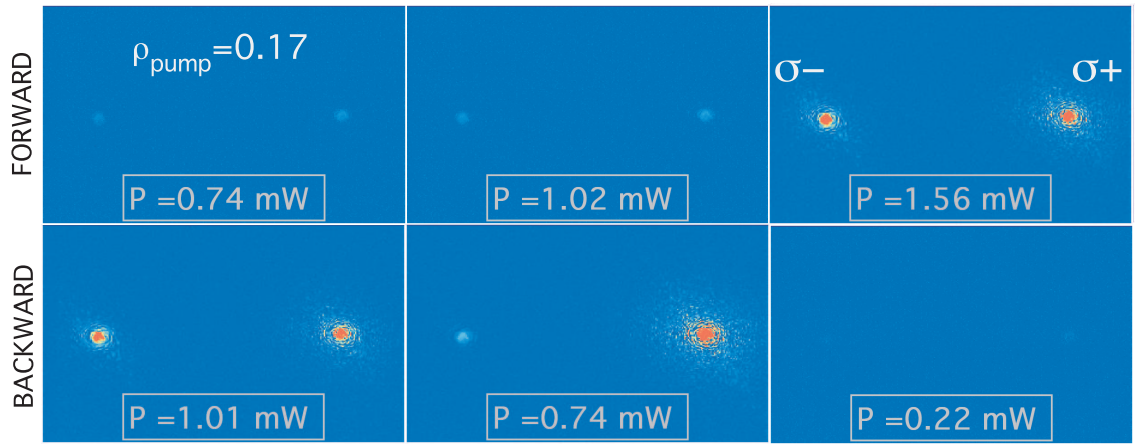

Figure 6.5: **Polarization conversion: CCD snapshots.** Images recorded at different excitation powers during the experiment of Fig. 6.4 c. The emission from the mesa is polarization resolved in the circular polarization basis. Left channel: $\sigma-$, Right channel: $\sigma+$. **Forward scan.** At 0.74 mW and 1.02 mW, both channels are "off". Simultaneous switch "on" occurs at 1.56 mW. **Backward scan.** Hysteresis is visible on the backward scan, where channels are still "on" at 1.01 mW. $\sigma-$ channel switches "off" at 0.74 mW, and one observes a strong increase of the $\sigma+$ channel intensity due to the jump of spin-up polaritons to their higher branch. $\sigma+$ channel switches "off" at 0.22 mW.

6.3.2 Principle of multistability

The inversion of the circular polarization observed between $\rho_p = 0.17$ (Fig. 6.4 b) and $\rho_p = -0.1$ (Fig. 6.4 d) is a crucial point for the appearance of multistability. Consider that the system is on the circular polarization plateau at $\rho_p = 0.17$. Let us now fix the excitation power and slightly scan ρ_p towards -0.17. The question is to figure out *how* the system is going to switch from a $\rho_c = +1$ plateau to a $\rho_c = -1$ plateau.

We may expect a smooth change of the value of the plateau, but the measurement at $\rho_c = 0$ shows that it is not the case. Under linearly polarized excitation, the plateau is not elliptically but still fully circularly polarized. Note that, at $\rho_p = 0$, the sign of the plateau is very sensitive to the excitation conditions (power, mesa position etc.).

Now let us assume that there is polarization hysteresis on the plateau between $\rho_p = +0.17$ and $\rho_p = -0.17$. We may obtain three stable solutions $\rho_c = \pm 1, 0$ in the vicinity of $\rho_p = 0$.

This is illustrated in more details in Figure 6.6.

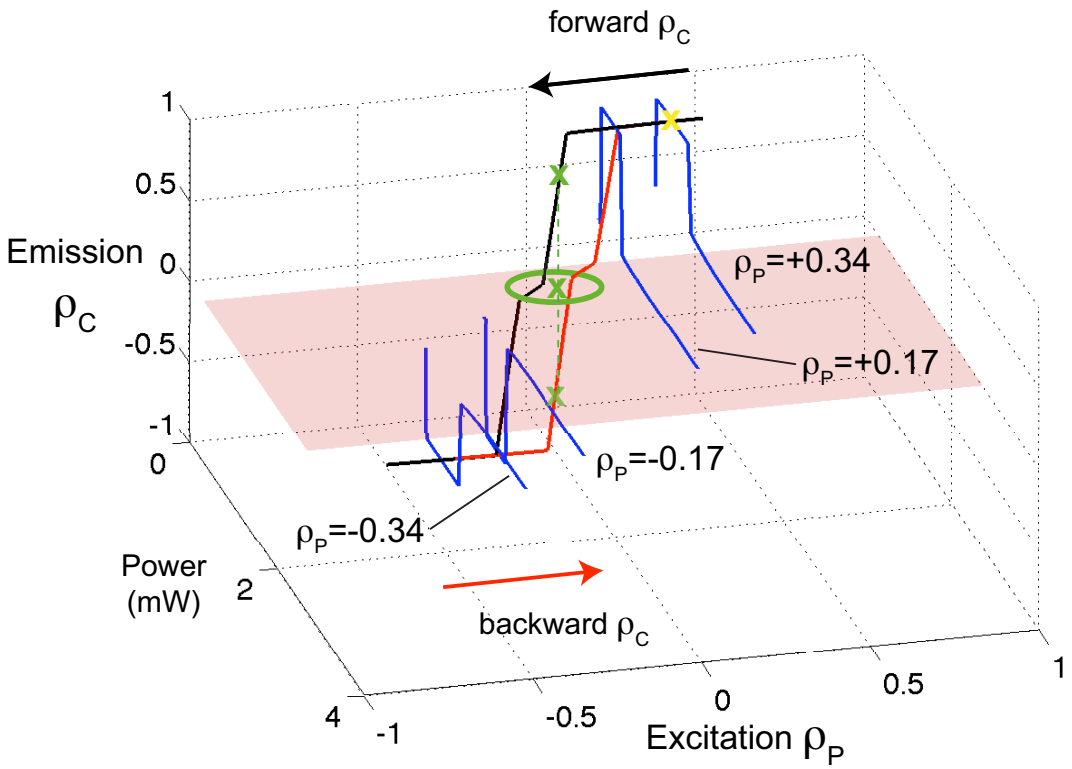

Figure 6.6: **Principle of multistability.** The blue curve represent the spin conversion plateaus obtained in power dependence experiments at different excitation polarization degrees ρ_p =0.34, 0.17, -0.17 and -0.34 (see Fig. 6.4). The sign of the plateau (± 1) depends on the sign of the excitation polarization degree. We represent a case where the polarization conversion is symmetric with respect to the linearly polarized excitation axis and display mirrored curves for nearly linear excitation power. For instance, on the $\rho_p = \pm 0.17$ curve, the polarization is converted to $\rho_c \pm 1$. Consider the system is initially prepared in the yellow cross state (fixed power) in the plateau of the $\rho_p = +0.34$ curve. **Black curve:** *what happens* upon a continuous change of ρ_p from +0.34 to -0.34? In fact, ρ_c will follow the plateaus, and, eventually, polarization hysteresis in the vicinity of $\rho_p = 0$ will causes the right circular polarization $\rho_c = 1$ to be preserved beyond the linearly polarized excitation axis before switching to linear $\rho_c = 0$ and then to left circular $\rho_c = -1$. **Red curve:** on the backward scan of ρ_p (red curve), the opposite polarization $\rho_c = -1$ is preserved by hysteresis, producing a **multistability region** (green circle) around $\rho_p = 0$ where three spin polarization states are admitted (green crosses).

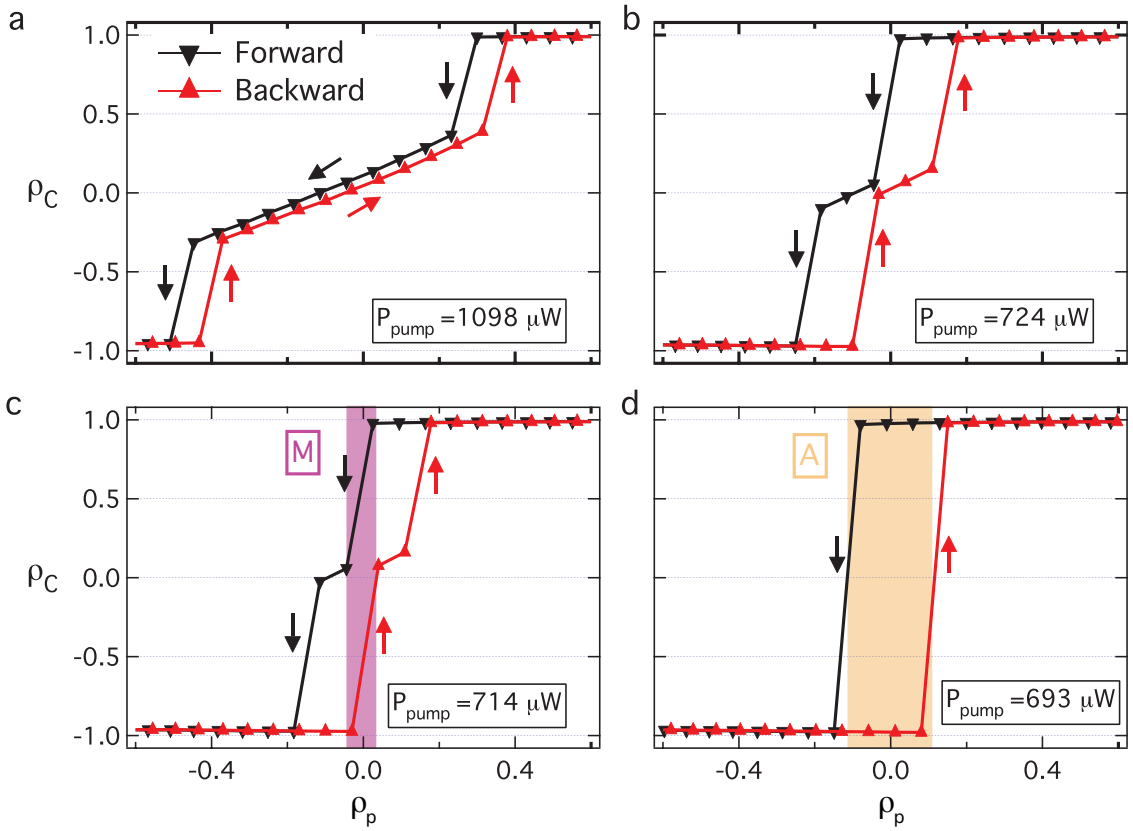

Figure 6.7: **Multistability.** Emission polarization degree ρ_c versus excitation polarization degree ρ_p. At constant excitation power, ρ_p is scanned from +0.5 to -0.5 and backward. **a Polarization hysteresis.** At high excitation power, narrow polarization hysteresis is observed for spin-up and spin-down polaritons. On the forward path (black) a first jump of spin-up polaritons out of their upper branch causes a decrease of ρ_c to a value close to ρ_p. Then a jump of spin-down polaritons to their upper branch brings ρ_c to -1. On the backward path, the process is reversed with a hysteresis behavior **b Effect of excitation power.** A decrease of the excitation power brings the polarization hysteresis cycles close to $\rho_p = 0$. **c Multistability.** Further decrease of the power make the two polarization hystereses merge, as described in Fig. 6.6. Three values of ρ_c are allowed in the multistability region M. **d Spin trigger.** At even lower excitation power, the overlap is complete. At the edge of the A region, a small variation of ρ_p leads to a total spin-up/spin-down conversion. ρ_c jumps from ± 0.97 to ∓ 0.97. *Parameters:* $\delta' = -1.47$ *meV*, $\Delta = 0.49$ *meV*.

6.4 Spin multistability

6.4.1 Polarization multistability

We indeed observed strong hysteresis effects as a function of the excitation polarization degree ρ_p. In Fig. 6.7, we show the measured polarization ρ_c versus ρ_p. We see that, for a given ρ_p even three stable solutions for the ρ_c can be found (see Fig. 6.7 b and c).

As a matter of fact, if both spinor gases are on their lower bistability branch, nonlinearities are negligible and ρ_c varies linearly with ρ_p. Hence, to observe multistability, we first prepare the system by using high excitation power with $\rho_p = 1$ in order to place the $\sigma+$ polaritons on the upper branch. The excitation power is then decreased to the desired value, where, thanks to hysteresis, $\sigma+$ polaritons stay on the upper branch.

For high excitation powers (Fig. 6.7 a), by decreasing ρ_p we first observe a jump from $\rho_c = 1$ to $\rho_c = 0.4$ when the $\sigma-$ population becomes sufficient to jump to the upper branch. The emission polarization degree ρ_c then changes linearly with ρ_p until $\rho_p = -0.5$, where the $\sigma+$ population becomes too low to stay on the upper branch and ρ_c jumps to -1. We will see in Section 6.5.3 that the slope of this middle branch depends on the orientation of the excitation linear polarization axis. Presence of hysteresis for both jumps is an evidence of *polarization bistability* for each population.

When the experiment is repeated at lower excitation power, the two hysteresis loops open and get closer to the center of the plot. In other words, the decrease of excitation density must be compensated by the polarization degree for $\sigma-$ polaritons to jump to the upper branch (Fig. 6.7 b). Note that, in this case, the system already behaves as a very high efficiency circular-to-linear polarization switch.

A further decrease of the excitation power brings polaritons to the power range where there is an independence of the lower thresholds around $\rho_p = 0$ (see Fig. 6.1 d and e). The two polarization hysteresis loops merge, which demonstrates the polarization multistability regime. Under linearly polarized excitation, the polarization of the coherent emission can either be $\sigma+$, $\sigma-$ or linear (see Fig. 6.7 c).

Strikingly, at an even lower excitation power, both $\sigma+$ and $\sigma-$ populations jump together in opposite directions without staying on the middle branch(Fig. 6.7 d and g). The polarization degree switches abruptly from $\rho_c > 0.97$ to $\rho_c < -0.97$. We observe a total spin flip of the $\propto 10^2$ polaritons present in the system for a variation of the excitation polarization of only a few percents ($\Delta\rho_p \simeq 0.05$). The system behaves under these conditions as a *spin trigger*. Snapshots of this experiment are displayed in Figure 6.8

Below this critical excitation power, the jump of $\sigma+$ polaritons to the lower branch occurs first (and causes a simultaneous jump of $\sigma-$ polaritons to the lower branch because of repulsive interactions). In this case, both populations end up on their lower branch. Any *memory* of the high-population regime is *lost*. No jump can be observed by re-increasing the excitation polarization degree without changing the excitation power.

Figure 6.9 a and b show that the theory described above is again in good qualitative agreement with the experimental results. The main difference is the strong con-

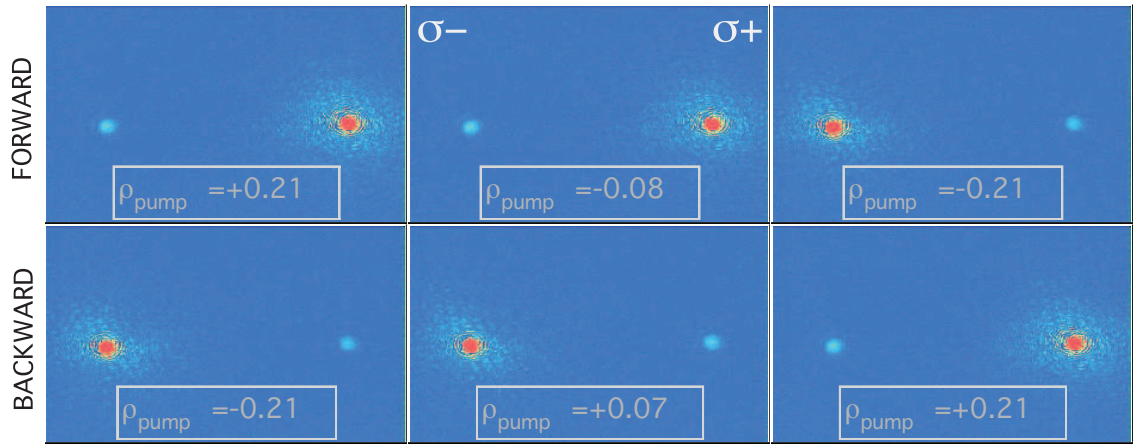

Figure 6.8: **Spin trigger: CCD snapshots.** Images recorded during the spin trigger experiment described in Fig. 6.7 d. Left channel: $\sigma-$, Right channel: $\sigma+$. On the forward scan, the spin-up to spin-down flip is recorded at $\rho_p = -0.2$: the $\sigma+$ channel switches off and the $\sigma-$ channel simultaneously switches on. On the backward scan, the spin-down to spin-up flip is recorded at $\rho_p = +0.2$, showing a 0.4 hysteresis in the spin-flip operation as a function of the excitation polarization degree.

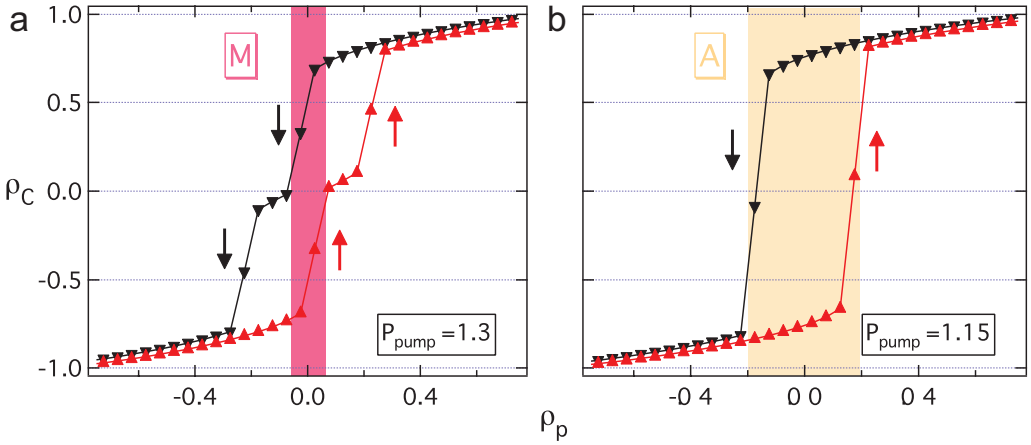

Figure 6.9: **Multistability: theory.** Emission polarization degree ρ_c versus excitation polarization degree ρ_p. Qualitative agreement is found in the reproduction of **a** multistability, **b** spin trigger. The main difference is the strong conservation of the circular polarization degree observed in the experiment (Figs. 6.7 c and d). It is not reproduced because the intensity difference between the middle and upper branches is smaller in the simulation.

servation of the circular polarization degree observed in the experiment (Figs. 6.7 c and d). This comes from the fact that, as explained above, the theory underestimates the intensity difference between the middle and upper branches in the spinor bistability.

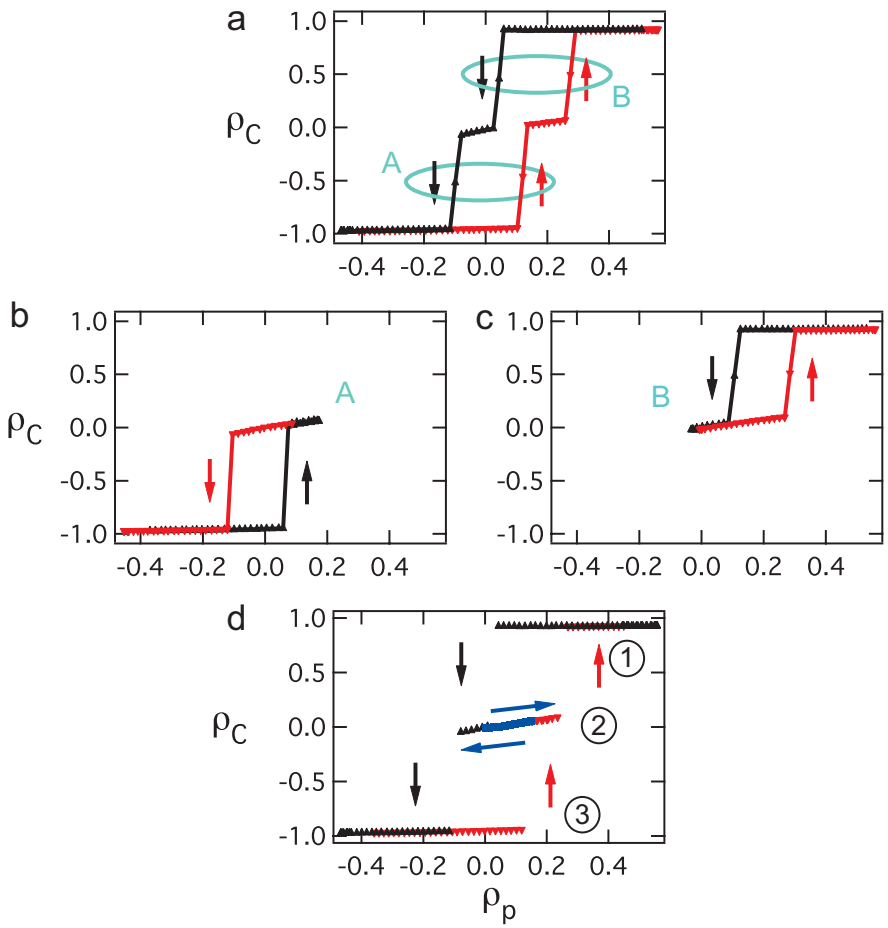

Figure 6.10: **Stability: three spin polarization branches.** The polarization multistability cycle **a** is formed by **b** a $\sigma-$ and **c** a $\sigma+$ polarization hysteresis loops that can be independently measured. **d** During the multistability cycle, the scan of ρ_p is interrupted on the linear polarization branch $\rho_c \simeq 0$. We then play forward and backward with ρ_p to evidence the stability of the linear polarization branch (blue markers and arrows). We thus obtain three branches, labeled 1, 2 and 3, corresponding to three stable spin-polarization states +1, 0 and -1. Multistability appears when the three branches are overlapping in a given range of excitation conditions. *Parameters:* $\delta' = -1.37\ meV$, $\Delta = 0.46\ meV$.

6.4.2 Stability

Three stable polarization states

We verified the stability of the $\rho_c = 0$ solution by scanning the excitation polarization degree back and forth on the middle branch. As explained before, the multistability cycle is composed of two polarization hysteresis cycles that merge in the region of linearly polarized excitation. This is illustrated in Figure 6.10. We interrupted the scan on the middle branch and played back and forth with ρ_p. The gap in the middle branch could then be filled, demonstrating the stability of the $\rho_c = 0$ solution.

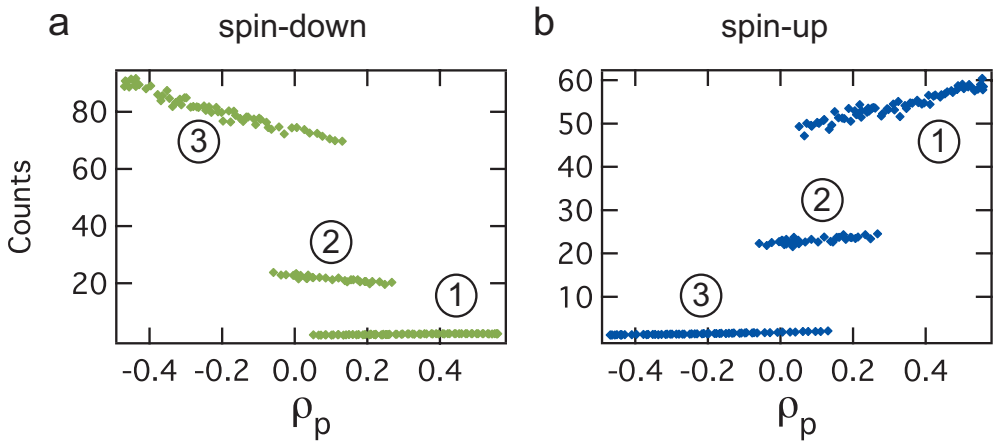

Figure 6.11: **Intensity resolved stability experiment.** Three stable intensity branches (lower, middle and upper) are evidenced for **a** spin-down and **b** spin-up polaritons. The branches are labeled 1, 2 and 3 according to the labeling of the polarization branches in Fig.6.10. They overlap in the multistability regime. Linear polarization occurs when both spin-polarizations are on their respective middle branch. *Parameters:* $\delta' = -1.37\ meV$, $\Delta = 0.46\ meV$.

Three stable intensity branches

Directly correlated to the three polarization branches is the existence of three stable intensity branches for each spin-polarization. In Figure 6.11, we display the polarization resolved intensity of plot 6.10 d. The three branches originate from the biexciton formation, as explained in Section 6.1.2. We label the branches 1, 2 and 3 to show the correspondence with the spin-polarization states. It is interesting to notice that, in fact, the multistability in intensity allows for four stable configurations of the intensity branches:

1. $\sigma+$ in the upper branch and $\sigma-$ in the lower branch $\rightarrow \rho_c = +1$

2. $\sigma+$ in the middle branch and $\sigma-$ in the middle branch $\rightarrow \rho_c = 0$

3. $\sigma+$ in the lower branch and $\sigma-$ in the upper branch $\rightarrow \rho_c = -1$

4. $\sigma+$ in the lower branch and $\sigma-$ in the lower branch $\rightarrow \rho_c = 0$

The last solution corresponds to the loss of bistability for both spin-polarizations. If the system is in this state, there is no way to switch it back to the other states without changing the excitation power. We can say that, in this case, the system is **OFF**. In the three first cases, the system is **ON**. It is possible to switch reversibly between the three spin-polarization states.

Having described the multistability in spin-polarization and intensity, we now come to the demonstration of the macroscopic spin coherence.

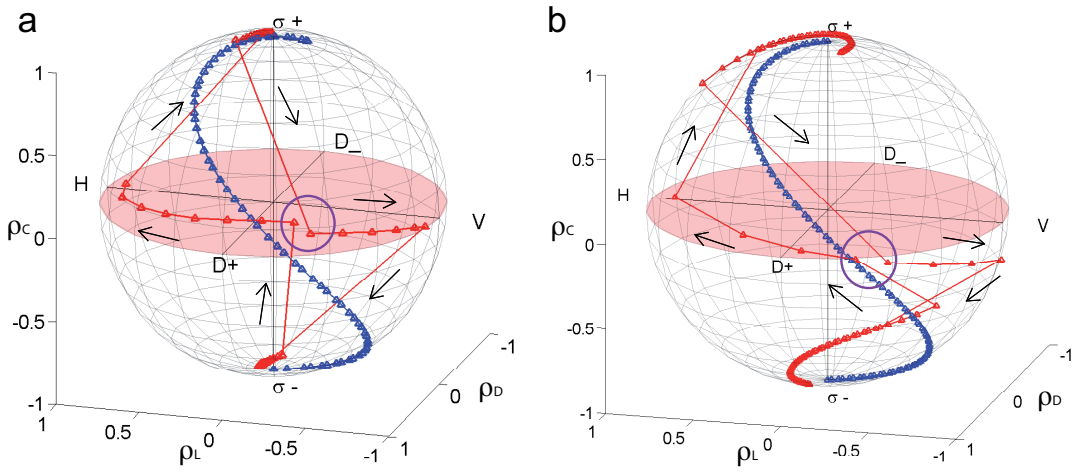

Figure 6.12: **Macroscopic spin coherence.** The four jumps and the gap (circle) in the middle branch trajectory are characteristic of the multistability regime. The spin coherence is maintained during the whole cycle. **a** Experimental data. **b** Theory. The experimental features of polarization multistability are well reproduced: the jumps, the multistability gap, the pseudospin precession as well as the conservation of coherence. The pseudospin trajectory (red triangles) is clearly distinct from the trajectory of the excitation (blue triangles).

6.4.3 Macroscopic spin coherence

In order to characterize the complete polarization state, one needs information on the phase relation between the two spin-polarizations. As explained in Section 1.5 this is done by analyzing the emitted polarization in the Bloch sphere.

Bloch sphere

Thanks to the reproducibility of the multistability cycle, we independently measured the three Stokes parameters to track the pseudospin vector in the Bloch sphere as shown in Figure 6.12.

One easily identifies the features of multistability. In this experiment we started on the $\sigma-$ pole of the sphere, where the pseudospin is pinned before jumping abruptly close to the D+ state. A wide precession towards the H state is then observed before the second jump to the $\sigma+$ pole occurs. On the backward path, the third jump brings the pseudospin farther from the D+ state, producing a gap in the precession trajectory (purple circle in Fig. 6.12). Then the pseudospin precesses towards the V state and finally jumps down to the $\sigma-$ state. No significant loss of coherence is observed during the cycle. As observed in polariton stimulated scattering experiments [Lagoudakis 02], we note that the precession trajectory close to the linear plane does not follow the excitation path. This precession can be explained by the excitation induced splitting between $\sigma+$ and $\sigma-$ polariton states.

Stokes parameters

To illustrate this point, we display the results of the independent measurements of the Stokes parameters in Figure 6.13. It is interesting to notice the existence of three branches also in the linear and diagonal bases. Clearly, on the middle branch, while ρ_p varies along the $\sigma+$ and $\sigma-$ axis, the major changes are observed in the linear (circular and diagonal) polarization degrees.

The conservation of the a pseudospin coherence independent from the excitation during the multistability cycle demonstrates the control of a macroscopic coherent spin ensemble.

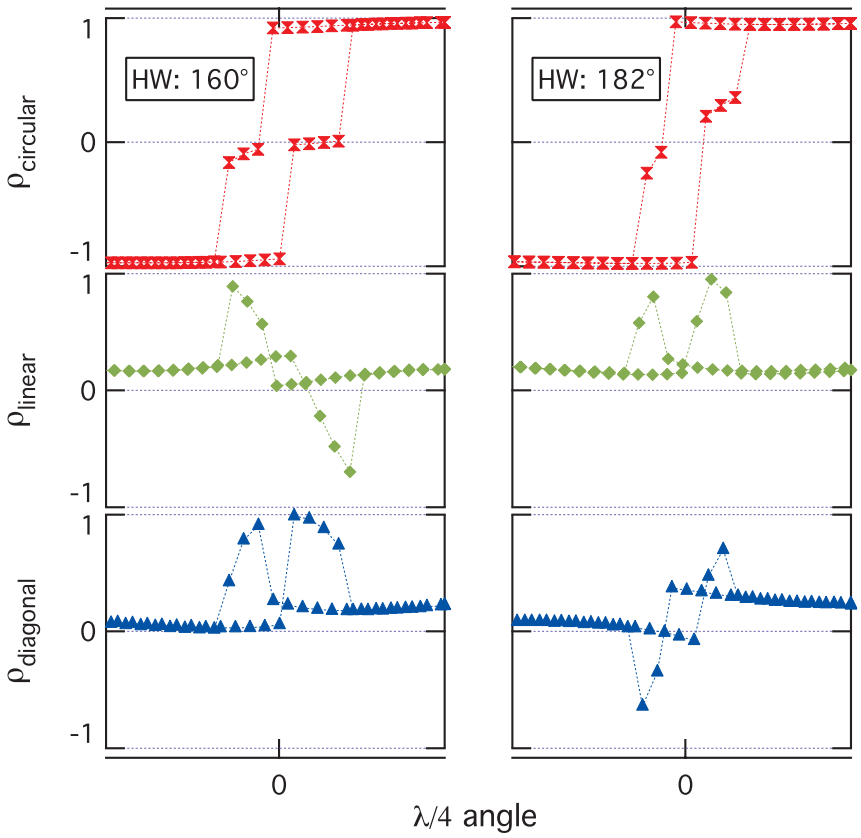

Figure 6.13: **Measurement of the Stokes parameters.** The total spin characterization is done by measuring the emission along the three projections of the Bloch sphere. Three branches are highlighted by the markers while the dotted lines reproduce the multistability cycle in circular, linear and diagonal polarization. **HW160** Orientation of the $\lambda/2$ plate to favor the D+ linear polarization in the multistability region. Note that the D+ and D- directions correspond to the crystallographic axes of the linear polarization splitting. **HW182** The linear axis of the excitation is H. The favored linear polarization in the multistability region is also H. The little shift towards the positive values of linear polarization is attributed to the linear polarization splitting. *Parameters:* $\delta' = -1.77\ meV$, $\Delta = 0.37\ meV$.

6.4.4 Summary

To conclude this section, we summarize our main results.

Polarization conversion

The first observation is that the spinor bistability behavior is very rich. Because of repulsive spinor interactions and biexciton formation, each spin-polarization exhibits three bistability branches. In addition, we could observe independent lower bistability thresholds for spin-up and spin-down polaritons. This independence is responsible for a high contrast linear to circular polarization conversion around linearly polarized excitation $\rho_p = 0$.

Spin multistability

We observed spin-polarization hysteresis as a function of the excitation polarization. When the system is prepared in the high intensity regime, a scan of ρ_p reveals two polarization bistability loops on each side of the $\rho_p = 0$ line. By decreasing the excitation power, the two loops get closer to each other and finally merge, giving rise to a multistability region where three polarization states are available. A special case has been evidenced, where the system is able to switch directly from spin-up to spin-down for minor changes in the excitation polarization degree. We called this regime the spin trigger regime, by analogy with the Schmitt trigger in electronics (see Fig. 6.14).

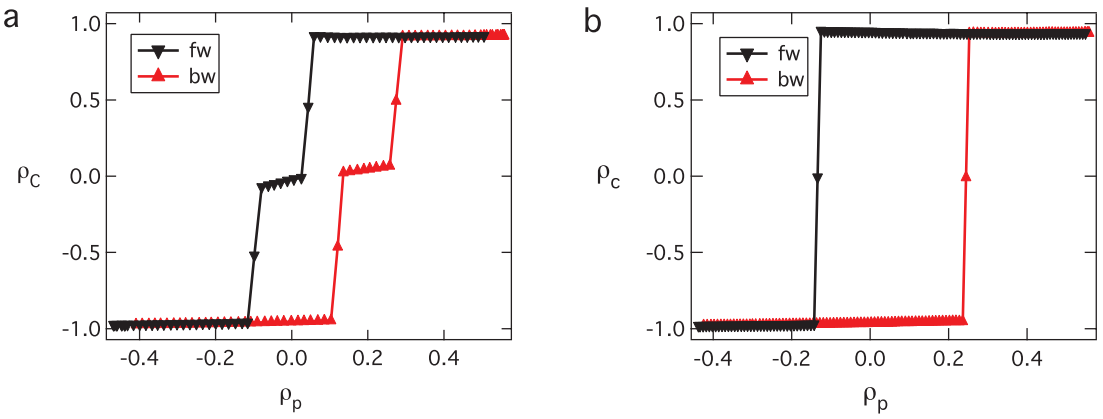

Figure 6.14: **Multistability and spin trigger.** *Parameters:* $\delta' = -1.37$ *meV*, $\Delta = 0.46$ *meV*.

Spin coherence

We characterized the complete polariton spin state by measuring the three Stokes parameters. We could therefore trace the multistability loop in the Bloch sphere and demonstrate the macroscopic spin coherence during the whole cycle. Very distinct trajectories are obtained for the excitation and for the detection polarization vectors.

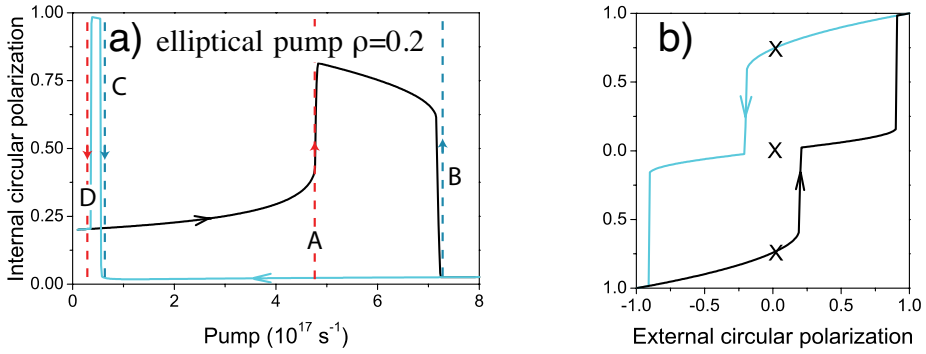

Figure 6.15: **Gippius proposal.** *Image reproduced from [Gippius 07].* The theory considers zero or negative interactions between polaritons of opposite spins. The threshold independence holds for both thresholds (see Fig, 6.3 c). **a** Under weakly elliptical excitation ($\rho = 0.2$), spin-up polaritons jump to the upper branch at A, increasing the internal polarization degree to $\simeq 1$. Spin-down polaritons jump up at B, decreasing the internal polarization degree to close to $\simeq 0$. On the backward path, spin-down polaritons jumps down at C and spin-up polaritons jumps down at D. **b** Multistability is predicted for a constant excitation power between A and B.

The measurement is the demonstration that we are actually manipulating coherently the macroscopic polariton spin ensemble.

Comment on Gippius proposal

The main difference between our results and the original proposal from Gippius et al. comes from the fact that we evidence repulsive spinor interactions. The proposal was made under the assumption that these interactions were attractive or zero. In this case, as shown in the theoretical investigations, the threshold independence holds for both bistability thresholds and is more important for the upper thresholds. A different condition for the multistability power is the found, as shown in Figure 6.15.

Characterization of spinor interactions

The achievement of spin multistability required a control over the spinor interactions and a deep understanding of the different excitation parameters. This knowledge was acquired through a series of experiments in different conditions. In the following section, we overview the role of each optical parameter.

6.5 All-optical control

A series of experiments allowed us to identify the role of each control parameter. We give here a summary of the outcome of these studies. In the following, the energy difference between the polariton ground state and the exciton δ' is indicated preferably to the cavity detuning δ. This allows us to identify critical energies where the nonlinear losses are stronger.

6.5.1 Effect of cavity detuning

In Figs. 6.1 and 6.3, we showed the important role of the nonlinear losses. Those nonlinear losses are attributed to the formation of biexciton (see Section 6.2). We proceed the same way as in Chapter 5 and investigate the role of the cavity detuning on these interactions. Contrary to the 2D polariton case, here, we observe a clear biexciton resonance. We find that nonlinear losses are enhanced in the vicinity of -1.0±0.2 meV below the quantum well exciton, which is the expected biexciton resonance in our sample (see Section 5.7).

Negative δ: away from the biexciton resonance

At very negative detuning, the exciton content is small so the interaction strength is reduced. The threshold powers are larger than at zero detuning. In addition, the ground polariton state is far from the biexciton resonance. The threshold independence is lost for $|\rho_p| < 0.5$. This corresponds to our theoretical predictions for $\beta = 0$ (see Fig. 6.3). The data of this experiment are displayed in Figure 6.16. We distinguish only two bistability branches except for the case $\rho_p = 0.64$, where a small threshold independence is observed.

To understand this, one should recall that the threshold coincidence is the signature of repulsive interactions. Formally, each polarization experiences a different blueshift: $\Delta\epsilon_\uparrow = \alpha_1 n_\uparrow + \alpha_2 n_\downarrow$ versus $\Delta\epsilon_\downarrow = \alpha_1 n_\downarrow + \alpha_2 n_\uparrow$ for spin-up and spin-down polaritons, respectively. This means that the effect of one spin-polarization density on the blueshift of the other is stronger at higher power and for ρ_p close to zero. That is, at $\rho_p = 0.64$ (Fig.6.16 g and h), the lower threshold are still independent. Note that only 18 % of the polaritons are $\sigma-$ polarized in this case. Multistability cannot be observed at such negative detuning.

Polariton state at resonance with the biexciton

In Figure 6.17, we show data taken for a polariton state at 1.2 meV below the exciton resonance, hence in the vicinity of the biexciton resonance.

Suppression of bistability. For small laser detunings, bistability is considerably reduced in the dominant population and suppressed under linearly polarized excitation. In Figs.6.17 a to d, we see that spin-up polaritons exhibit an optical discrimination behavior, while spin-down polaritons are in the optical limiter regime.

When the laser detuning is increased, (see Figs.6.17 e to h), bistability open in one spin-polarization only and remains inhibited in the other.

Polarization modulation. Figures. 6.17 e and f shows the same kind of polarization modulation as observed with planar polaritons (Chapter 5, Section 5.4). The effect is even stronger in the case of confined polaritons. The linear to circular and circular to linear polarization modulation is observed as a function of the excitation power only and under linearly polarized excitation. It is a very interesting effect that could have promising applications.

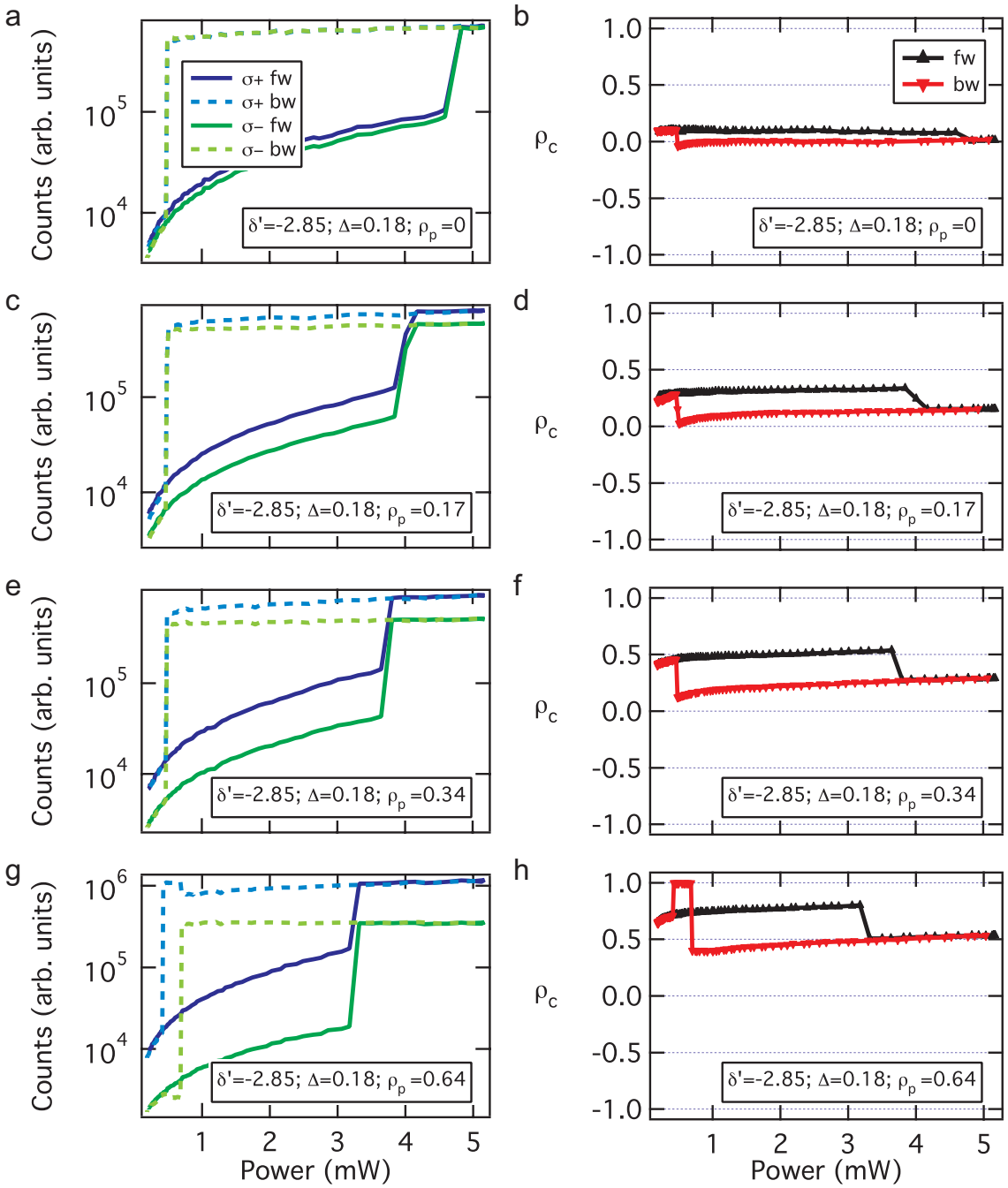

Figure 6.16: **Large negative cavity detuning.** Spinor bistability in function of the excitation circular degree ρ_p. According to our assumptions, at large negative detuning, the polariton state is far from the biexciton resonance. **a - f** Nonlinear losses are negligible. Upper and lower thresholds in $\sigma+$ and $\sigma-$ are equal. **g - h** Threshold independence is only observed for very elliptical excitation . In addition, we notice that the width of the bistability decreases when the excitation approaches the linear polarization. Multistability is not possible at large negative cavity detuning.

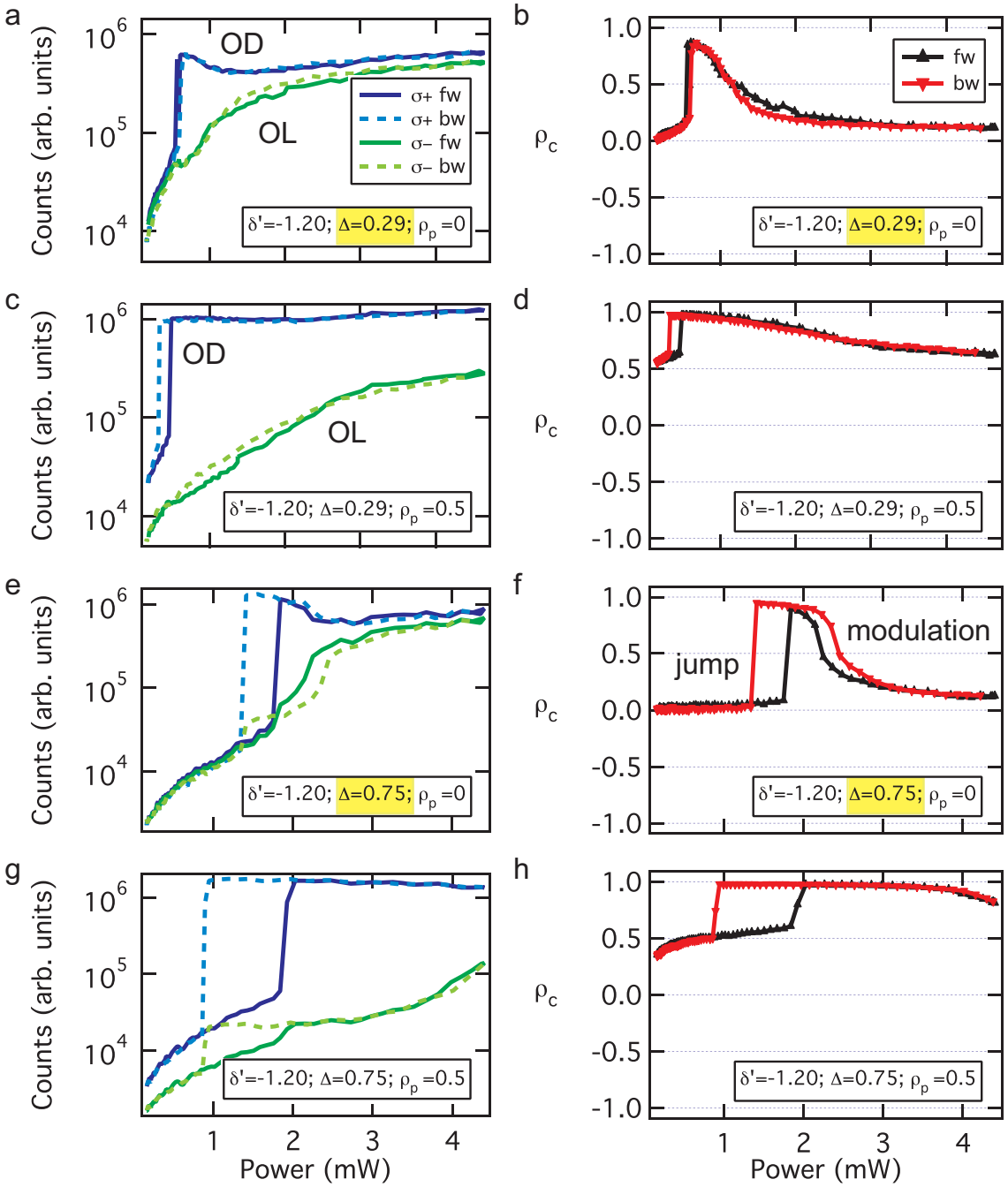

Figure 6.17: **Polariton state at the biexciton resonance.** Two different Δ are studied: 0.29 and 0.75 meV. Nonlinear losses are enhanced by the proximity to the biexciton resonance. **a - d** $\mathbf{\Delta = 0.29}$ meV: spin-up polariton are in the OD regime and spin-down polaritons in the OL regime. We obtain a polarization modulation like in the case of planar polaritons. By increasing the laser detuning to **e - h** $\mathbf{\Delta = 0.75}$ meV: the bistable behavior is recovered for spin-up polaritons. **f** On the forward path, we observe a discontinuous linear to circular polarization conversion and then a circular to linear polarization modulation. A hysteresis in observed on the backward path.

6.5.2 Effect of laser detuning

We showed that nonlinear losses are important when polaritons are near the biexciton resonance. We now discuss the role of the laser detuning Δ. We evidence that the laser detuning is responsible for the robustness of the polarization hystereses leading to multistability. We also show that the conditions for multistability and spin trigger effect (threshold independence, polarization hysteresis) are the best when the laser energy is close to the biexciton resonance.

Hysteresis robustness

We choose a cavity detuning where biexciton effects start to have an influence on the spinor bistability behavior ($\delta' = -1.96$ meV). A threshold independence is observed (see Figure 6.18 a to d). In case of a too small laser detuning $\Delta = 0.27$ meV, it is not possible to merge the polarization hystereses by lowering the excitation power (see Figure 6.18 a to d). Instead, the bistability regime is lost in both spin-polarizations.

By simply increasing the laser detuning to $\Delta = 0.43$ meV, we strengthen the polarization hysteresis and a clear multistability is evidenced (see Figure 6.19). Note that the multistability cycle shown in Fig. 6.19 f is not centered at $\rho_p = 0$ but rather at $\rho_p = 0.2$. We also observed an effect due to the alignment of the excitation linear polarization axis with respect the crystallographic axes of the linear polarization splitting. We confirm this hypothesis later.

Conditions for the spin trigger regime

In the experiment presented in Fig. 6.19, the spin trigger regime could not be observed. In fact, the spin trigger regime requires a more important threshold independence, hence to bring the polaritons a bit closer to the biexciton resonance. In Figure 6.20, we show that the spin trigger regime could be observed for a similar value of Δ (0.39 meV) but for a higher polariton energy ($\delta' = -1.49$ meV instead of -1.96 meV. The three intensity branches are distinct and the polarization conversion plateaus are wide (≥ 0.5 mW). The parameters of this experiment are the same as in the experiment presented in Section 6.4.1.

Large Δ

We finally observed that a too large laser detuning can also prevent multistability to appear (see Figure 6.21). We worked at the same polariton energy as previously $\delta' = -1.49$ meV. We excited the sample at a much larger laser detuning $\Delta = 0.91$ meV instead of 0.39 meV. In this case, the effect of nonlinear losses is also hindered and no threshold independence is observed. This is additional confirmation of our hypothesis of biexciton. We can determine a resonance between -1 meV and -1.2 meV. In the case of planar polariton, we could not evidence such a resonance because of the disorder and of the large polariton linewidths.

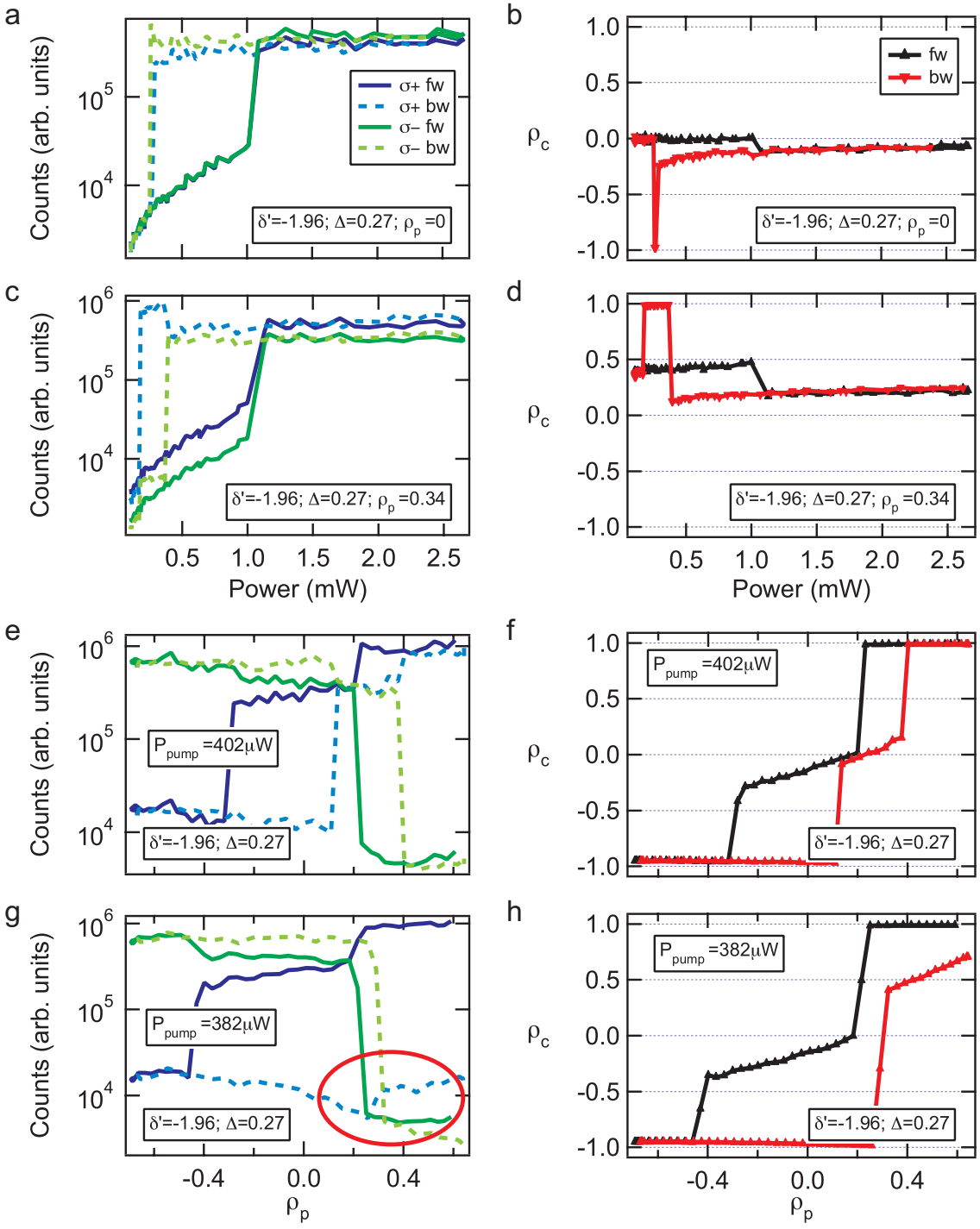

Figure 6.18: **Too small laser detuning. a - d** Spinor bistability measurements. At slightly negative cavity detuning ($\delta = -0.35$ meV) the threshold independence is observed around $\rho_p = 0$. **e - h** Because of a too small laser detuning, the polarization hysteresis is not robust enough and the multistability cannot be observed. **g** Instead, the bistability regime is lost in both spin-polarizations (red circle). **h** The multistability cycle is not "closed". An increase of Δ is necessary.

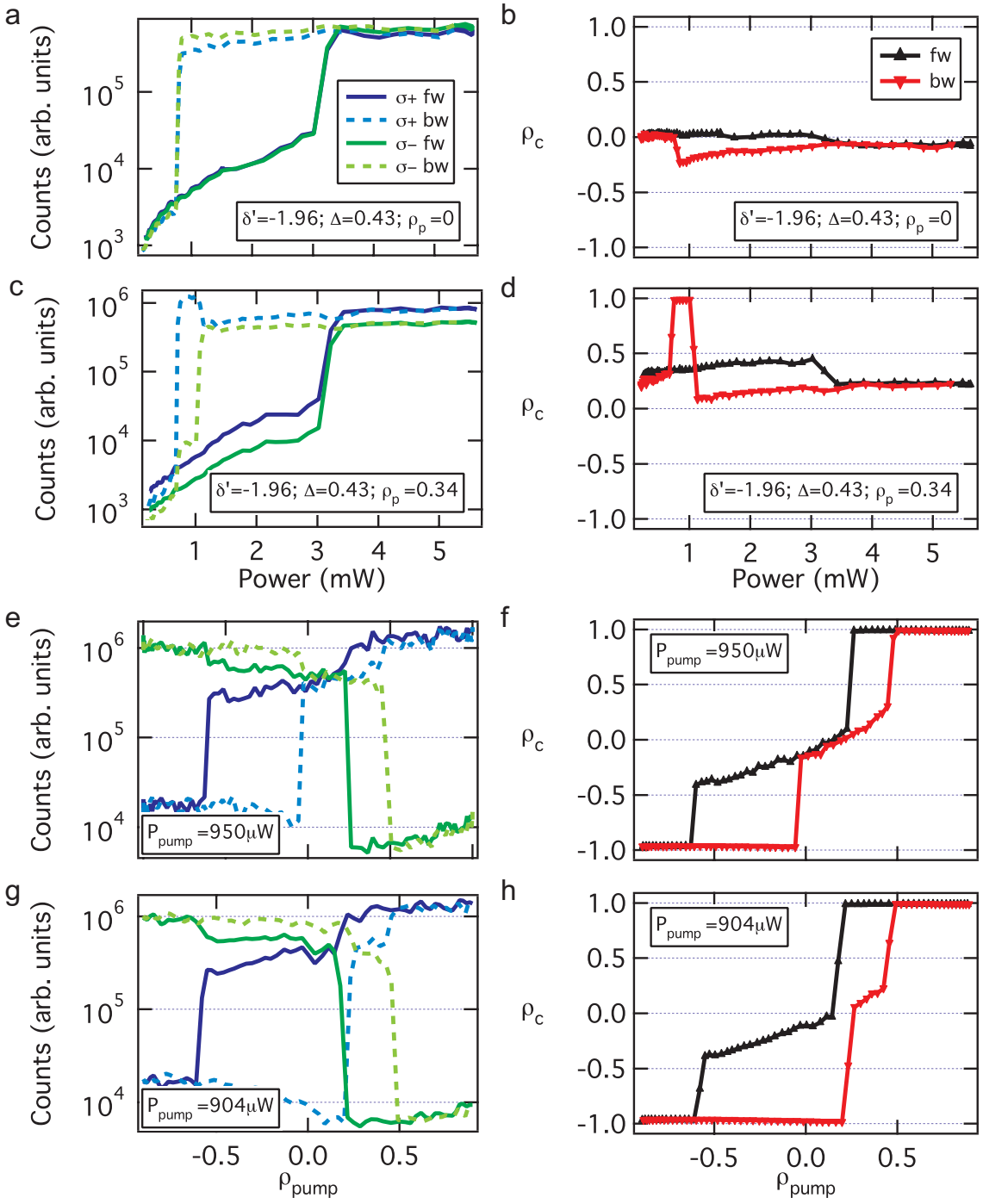

Figure 6.19: **Conditions for spin multistability.** Same cavity detuning as in Fig. 6.18. **a - d** Spinor bistability measurements. Threshold independence is observed at $\rho_p = 0.34$ but not resolved at $\rho_p = 0$. **e - h** Multistability. Because of an asymmetry, multistability occurs at $\rho_p = 0.2$. Polarization hysteresis is more robust than in Fig. 6.18 because of the increase of Δ.

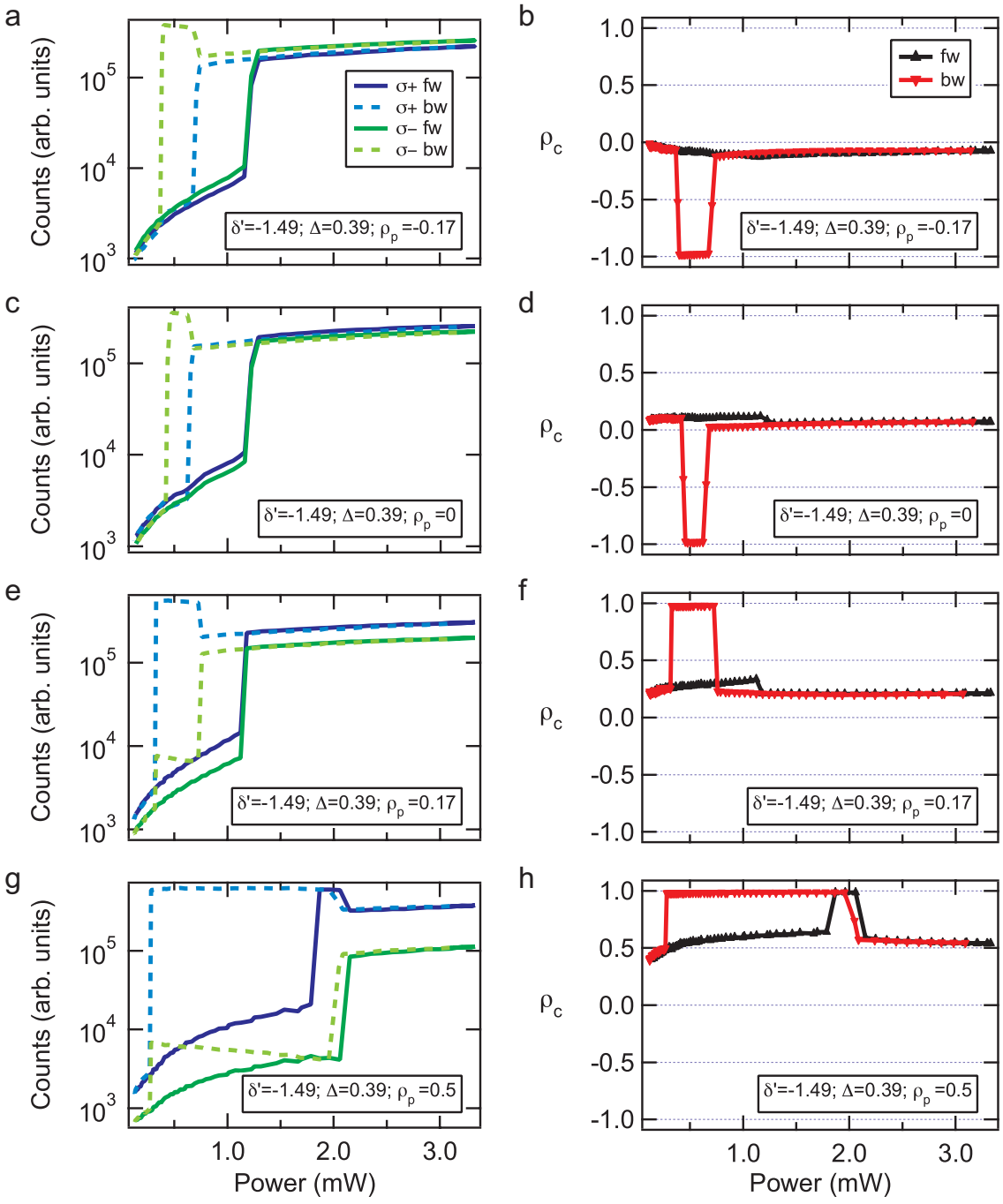

Figure 6.20: **Conditions for spin trigger regime.** Mesa at zero cavity detuning, same Δ as in previous case (Fig. 6.19) . **a - h** Effect of nonlinear losses are more visible, with a significant independence of the lower thresholds around $\rho_p = 0$ (**a, c and e**). High contrast linear to circular polarization conversion is observed (**b, d and f**). Spin multistability and spin trigger regime are observed in this case (see Figure 6.7).

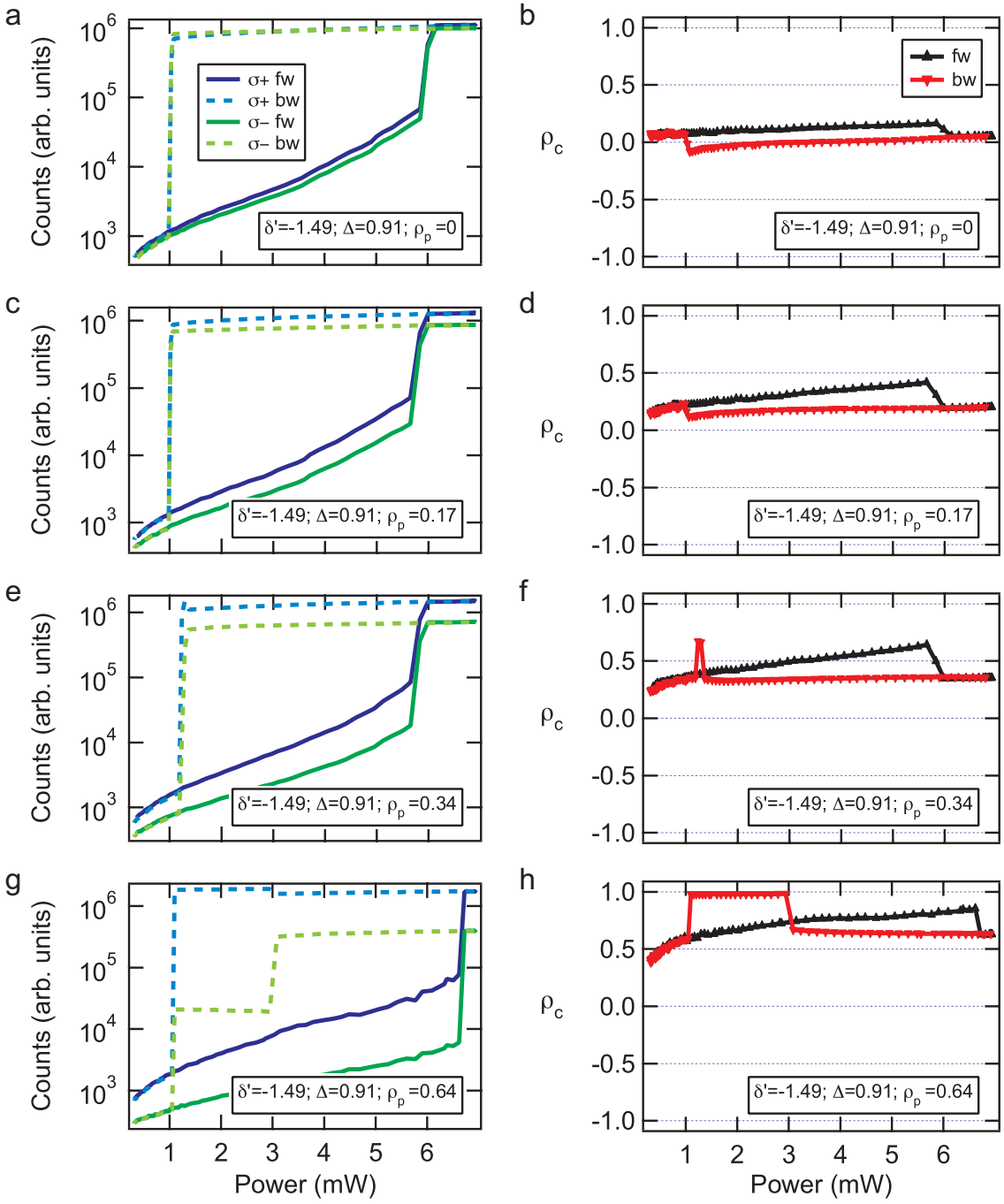

Figure 6.21: **Too large laser detuning.** Mesa at zero cavity detuning. Very large laser detuning . Nonlinear losses are not efficient anymore. Multistability might not be observed in this case. Comparison to Fig. 6.20 shows that the nonlinear losses (through biexciton) resonance is about 1.1 meV lower than the exciton energy, which is consistent with the literature.

Biexciton resonance

The threshold independence is clearly related to the presence of nonlinear losses. In order to confirm experimentally our hypothesis that polariton pairing into biexcitons occur under elliptical excitation, we studied in details the dependence of the nonlinear losses on the laser energy, for a fixed polariton detuning δ'=-1.49 meV. We performed a series of power dependent experiment for different laser detunings and excitation polarization degrees and looked at the evolution of the power difference between the lower thresholds. The results, presented in Fig 6.22, are clearly indicating a resonance for the nonlinear losses at the expected energy of the biexciton resonance.

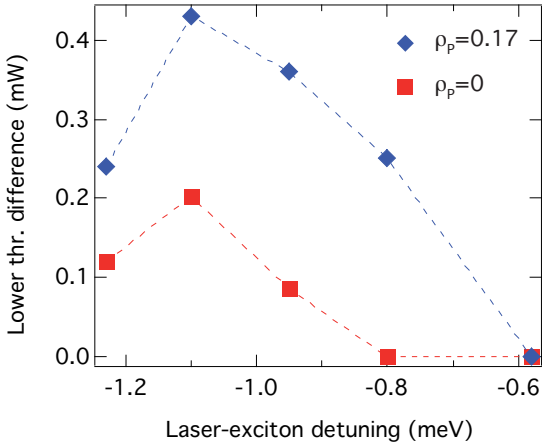

Figure 6.22: **Resonance for nonlinear losses.** We consider a *fixed* polariton energy δ'=-1.49 meV. The laser energy with respect to the exciton Δ' is changed from -1.24 to -0.58 meV. For each value of Δ', a series of spinor bistability experiment is performed. We record the lower threshold difference for linearly polarized excitation $\rho_p = 0$ (red squares) and for elliptically polarized excitation $\rho_p = 0.17$ (blue losanges). We observe a clear enhancement of the nonlinear losses when the laser energy is 1.1 meV lower than the exciton energy, i.e. at the biexciton resonance.

6.5.3 Orientation of the excitation linear polarization

We now confirm the hypothesis of a dependence of the symmetry of the multistability cycle on the orientation of the linear polarization axis. We studied the shape of the multistability cycle in a series of experiments for different angles θ of the linear polarization with respect to the horizontal axis. Depending on the selected angle, we could displace the position of the multistability region and tune the asymmetry in the widths of the polarization hystereses. In Figure 6.23 a, b and c, we show that we could tune the multistability center from -0.3 to +0.3. The polarization hystereses are very large for these orientations of the linear axis. The critical power is found to be much weaker in the symmetric case (Figure 6.23 b). However, by doing the experiment, we found that the multistability behavior is very hard to achieve is this case. The multistability width is very small and bistability is easily lost. This case

corresponds to a linear polarization along the D+ axis, hence along one axis of the linear polarization splitting. The simulations also showed that multistability is more difficult to achieve close to these axes.

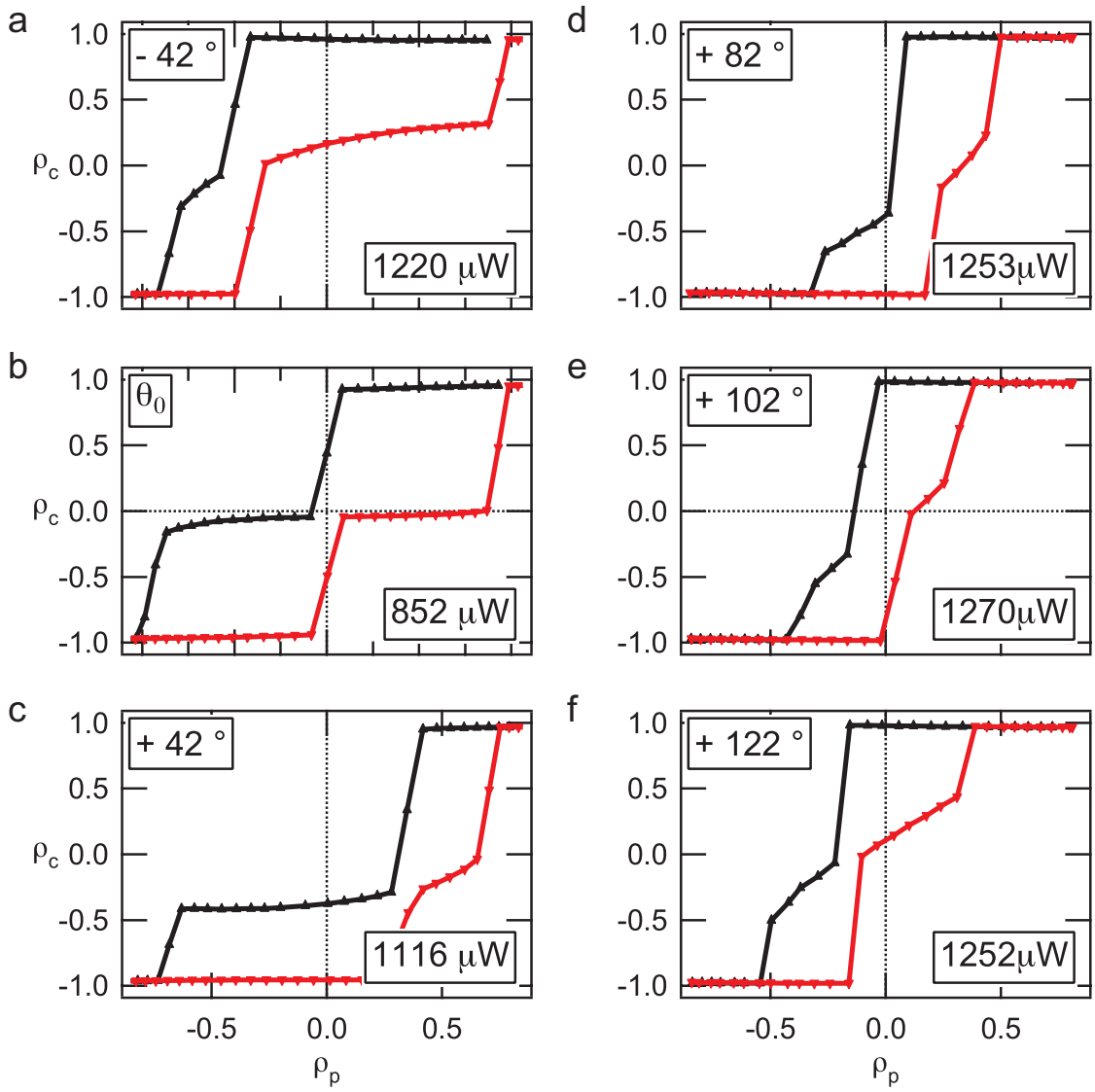

Figure 6.23: **Symmetry.** By rotating the linear polarization axis of the excitation, the multistability cycle can be made strongly asymmetric. The width of the polarization hystereses is also modified. Angles are indicated with respect to the reference orientation θ_0, which corresponds to an orientation along D+, i.e. along one linear polarization splitting axis. **a-c** The middle branch is horizontal. Multistability occurs at **a** $\rho_p = -0.45$, **b** $\rho_p = 0$ and **c** $\rho_p = +0.45$. The power for multistability is much lower in the symmetric case θ_0. **d-f** The middle branch is diagonal. Multistability occurs at **d** $\rho_p = -0.2$, **e** $\rho_p = 0$ and **f** $\rho_p = +0.2$. The power for multistability does not change significantly.

On the other hand, a very robust multistability is obtained for a nearly perpendicular angle. The polarization hystereses are a bit reduced and the multistability gap in the symmetric case is larger (see Figure 6.23 d, e and f). We also notice that

the middle branch is not horizontal but strongly tilted.

To explain this behavior, one can think about the Bloch sphere experiment. A change in the linear polarization axis of the excitation changes the path of the polariton spin vector in the sphere. A different azimuthal angle generates a different phase relation between spin-up and spin-down polaritons. We suspect that, depending on the angle, this phase relation can be more or less favorable to the observation of multistability.

6.5.4 Summary

We realized all-optical control of the spinor interactions in our system. We summarize the role of the different optical parameters as follows:

Cavity detuning δ: tunes exciton content and the strength of the biexciton effect. Multistability disappears at large negative detuning. However, if the biexciton effect is too strong, bistability is suppressed. We observed a circular to linear polarization modulation regime.

Laser detuning Δ: tunes the robustness of the polarization hystereses and can also be used to tune the biexciton formation.

Excitation polarization degree ρ_p: changes the ratio between spin-up and spin-down polaritons

Excitation power P: sets the position on the spin conversion plateaus. It allows to merge the polarization hystereses in order to establish the multistability regime

Orientation of the excitation linear axis θ : tunes the phase relation between spin-up and spin-down polaritons and modifies the symmetry of the multistability cycle.

The design of devices based on multistability would require a full mastering of the optical excitation parameter. A wise combination of their different roles would allow special manipulation of polariton spin ensemble, like for instance, triggering the spin-switching to the desired state, as demonstrated in the following section.

6.6 Perspectives

6.6.1 A spintronic device

This work opens many perspectives. The most direct one will be to characterize the system as a spintronic device. For this, it will be necessary to perform two beam experiments in order to trigger the switching and to characterize the switching time.

Two preliminary two-beam experiments have been carried out. We excited the sample with a pulsed laser in addition to the cw source. The 5 nm (FWHM) broad pulse was centered on the exciton resonance so that the whole polariton spectrum

was resonantly excited. This resulted into a blueshift of the whole polariton spectrum. For both experiments, the pulsed laser was sent with the same polarization as the cw laser.

Suppression of bistability

The first experiment was done under circularly polarized excitation for both sources. We measured the dependence of the bistability threshold powers of the cw laser in function of the power of the background pulsed laser. The results of this experiment are displayed in Figure 6.24. The lower threshold is found to be constant while the upper threshold decreases with the background power.

This experiment may be related to the bistability suppression effect due to biexciton (see Chapter 5 and Section 6.5.1). It shows that, when the polariton states are blueshifted because of a background density, the upper bistability threshold is the most influenced one. The bistable behavior can thus be controlled with an additional source.

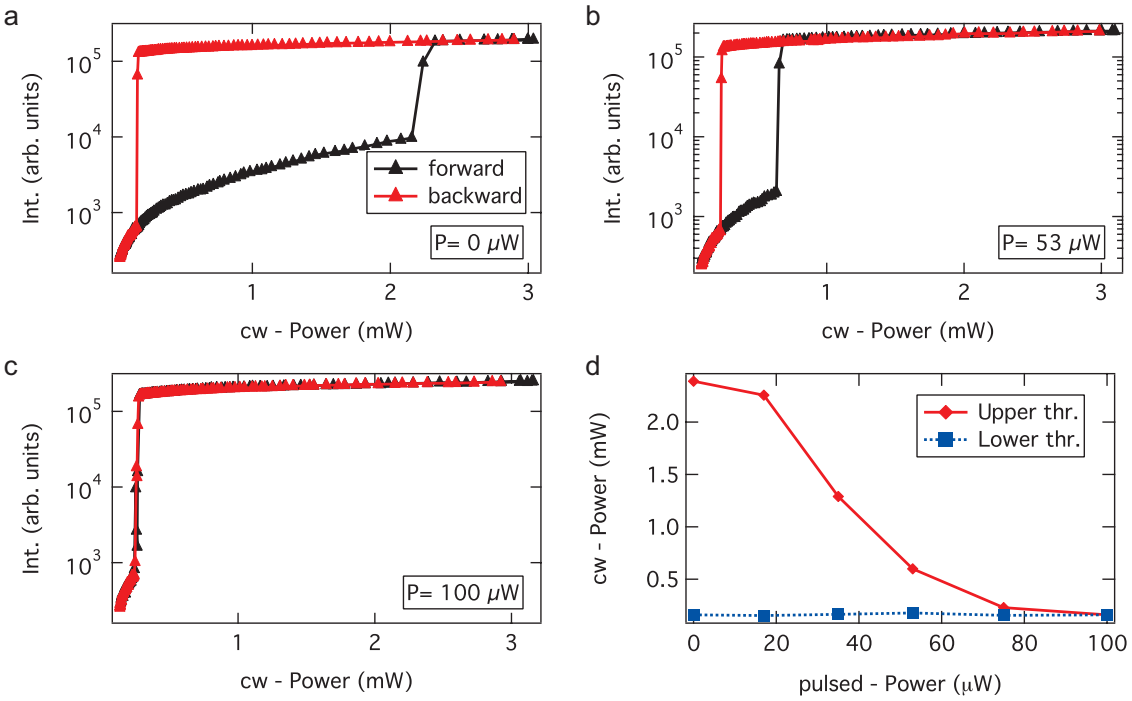

Figure 6.24: **Suppression of bistability** The presence of a background density created by a pulsed excitation mimics the bistability suppression effect due to the biexciton. An increasing power of the pulsed laser leads to an increasing blueshift of the polariton spectrum. The detuning of the cw laser need to be corrected accordingly. The bistability condition should be written as a function of the new effective laser detuning (and polariton linewidth). **a-c** The width of the bistability strongly decreases with the power of the pulsed laser, i.e. with the background density. At 100 μW, the system behaves as an optical discriminator. **d** While the lower threshold is not influenced by the background, the upper threshold drastically decreases with the background power. This reminds the conclusions of the OB-OL transition experiment with planar polaritons.

Triggering multistability

The second preliminary experiment is more device oriented. We took advantage of the power modulation caused by the pulsed laser to trigger a switch in the spin-polarization state. To do so, we first excited the sample with the cw laser alone and prepared the system in the multistability regime. We interrupted the scan of the cw excitation polarization degree on the $\rho_c = -1$ branch, at a value of ρ_p around 0. We then sent the pulsed laser in to modulate the excitation power. Depending on the bias of ρ_p, we could trigger a switch to $\rho_c = 0$ or to $\rho_c = +1$. This experiments demonstrates that spin switching can be triggered selectively with a polarization-biased background control. It opens pathways to the development of logic gates.

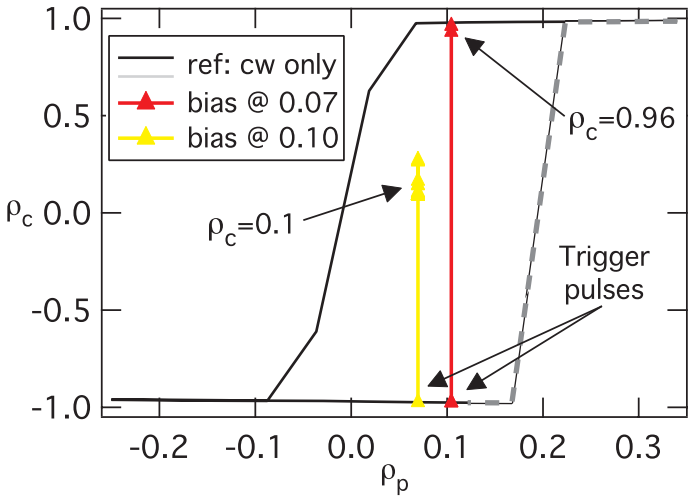

Figure 6.25: **Selective spin switching** The scan of the multistability cycle is interrupted on the $\rho_c = -1$ branch and a secondary excitation is sent to modulate the excitation power. When $\rho_p = 0$, we trigger a polarization switch to $\rho_c \simeq 0$. When $\rho_p = 0.1$ we trigger a switch to $\rho_c = +1$.

Switching time

The characterization of the spin-switching time is an important issue that will be investigated in further experiments. Different time resolved experiments can be designed. We enumerate few of them:

i It is possible to excite the sample near the bistability threshold with the cw laser and to trigger the jump to the upper branch with a secondary excitation. Preliminary tests showed that, depending on the power combination, the system remains or not on the upper branch after the secondary excitation is removed. In the case where it does not, a time resolved experiment would inform us about the switching time. In addition, it would help determine condition under which the system performs either switch or latch operations.

ii The selective spin switching experiment (Fig. 6.25) shows that it should be possible to trigger the switch between three output states -1, 0 and 1 by sending

$\sigma-$, linear or $\sigma+$ pulses on a system prepared with a linearly polarized cw-background[4]. A characterization of the switching time could be done by sending three pulses at different delays. Studies of the dependence of the switch on the pulses power, or of the switch sensitivity on the pulses polarization degree would also be an interesting characterizations of such a multi-valued switch.

6.6.2 Spin squeezing

It is known that, in the bistability regime, squeezing is likely to appear. Karr et al. [Karr 04] demonstrated this effect in the case of planar polaritons. The observed squeezing was quite small (4 percents), and one can expect this effect to be enhanced with confined polaritons as they constitute a much cleaner system. Studying the correlations between spin-up and spin-down polaritons at the edges of the multistability threshold would probably reveal the presence of sizable spin squeezing.

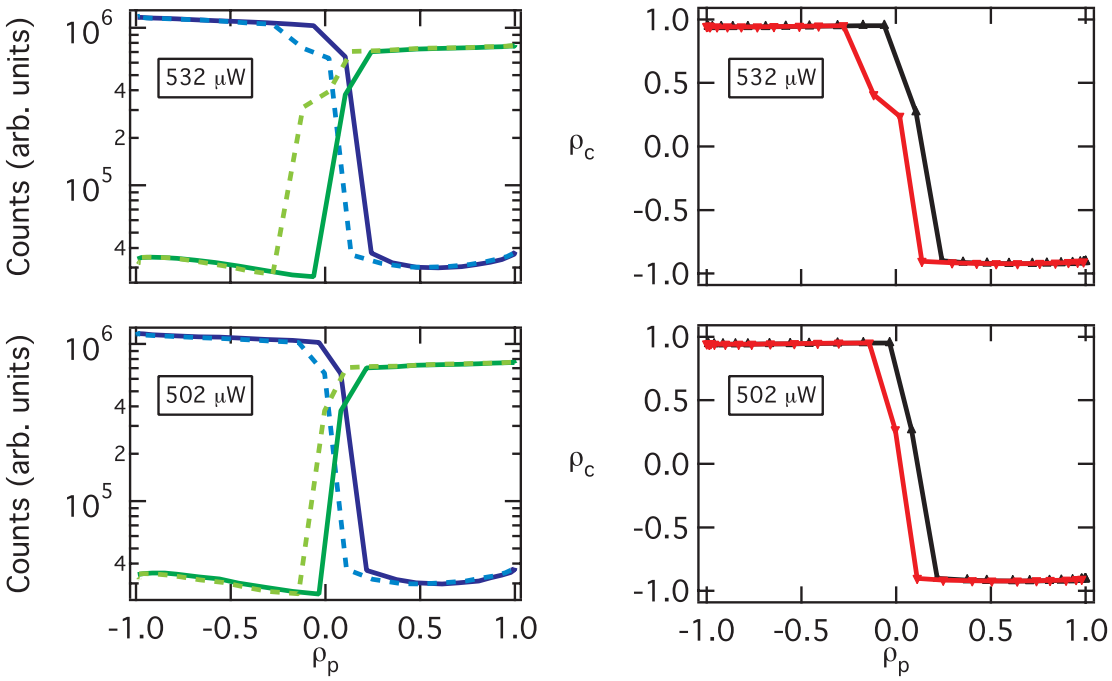

Figure 6.26: **Multistability of excited confined levels: conventional regime** Three branches intensity branches are observed in the intensity plot in the multistability regime. A decrease of the excitation power leads to a spin trigger regime.

6.6.3 Multistability with excited states

We also evidenced multistability with high-energy confined polariton levels. Strikingly, we could observe to multistability regimes, depending on excitation power. In

[4]If the multistability is symmetric, otherwise the background polarization may be slightly elliptical see Fig. 6.23

the first one, shown in Figure 6.26, the behavior is the same as the one observed with the ground state: three intensity branches are present and a transition from multistability to spin triggering regimes is observed by decreasing the excitation power.

In the case of excited states, this gives rise to a second multistability regime, with only two intensity branches. On the middle polarization branch, both spin-polarizations are on their lower intensity branches (see Figure 6.27). This effect is very interesting because it indicates a strong memory effect. It is in contrast with the multistability experiments with the ground state, where we saw that the memory of the high-density regime is completely lost when the two spin-polarizations are on their lower branch.

Here, a possible explanation would be that several energy levels are involved in a multistability cycle so that the if a given states gets out of resonance with the laser, another higher energy state might become resonant.

6.6.4 Transport

Another important observation in the multistability experiment with excited states is that planar polariton states are well populated in the high-density regime. This is illustrated in Figure 6.28, where one distinguishes the confined lower polariton states but also the lower and upper planar polariton dispersions. This experiment suggests a coupling between 0D and 2D states due to parametric scattering processes. In the next chapter, we will see that it can have an influence on the collective spinor-fluid dynamics of planar polaritons.

6.7 Conclusion

In conclusion to this chapter, we have investigated spinor interactions with confined polaritons. The "clean" system that constitute polariton mesas allowed us to acquire a deep knowledge of the influence of the different optical excitation parameters on the excitations. Spinor bistability substantially differs from conventional bistability. In particular we faced an interplay between the repulsive spinor interaction between polaritons of opposite spins and the biexciton formation by pairing of polaritons of opposite spins. The former interaction is responsible for a coupling of the bistability curves while the latter is responsible for a narrowing of the bistability of the minor spin population. This effect can lead to an independence of the lower bistability threshold, that produces drastic variations of the spin-up/spin-down population ratio when the excitation power is changed. We therefore were able to demonstrate high efficiency linear to circular polarization conversion and modulation. In addition, because of the presence of polarization hysteresis, we demonstrated polarization multistability for the first time in the solid state. Thanks to a characterization of the complete polariton spin state, we evidence that the spin coherence is preserved for the $\propto 10^2$ polaritons present in the system. This is the demonstration that, in these experiments, we are coherently manipulating a macroscopic spin ensemble and justifies the use of the term spin-multistability. In addition to this regime, we could evidence a regime of macroscopic spin-flip, where all the spins present in the

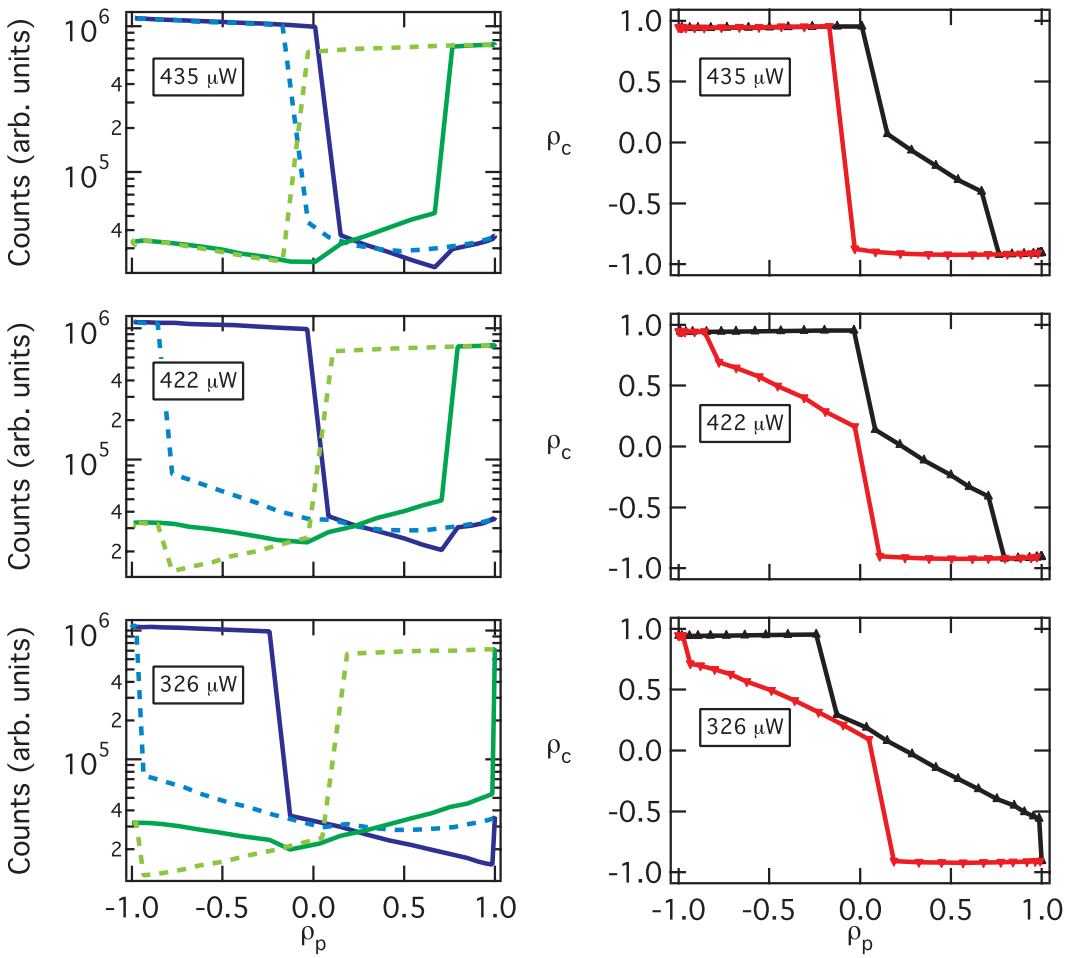

Figure 6.27: **Multistability of excited confined levels: unusual regime.** Lower excitation powers than in Fig. 6.26 are studied. Strikingly, only two intensity branches are observed in the multistability regime. We suppose that several excited states are involved in this effect.

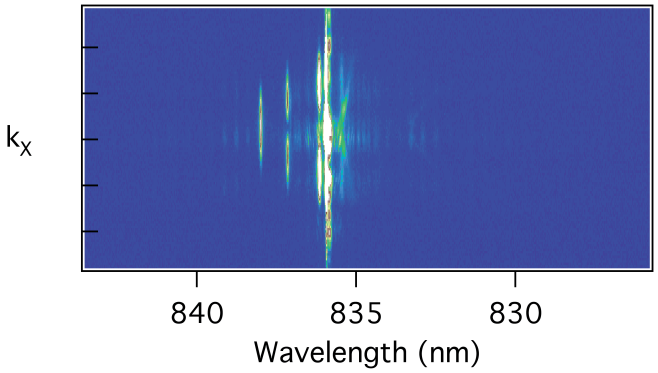

Figure 6.28: **Multistability of excited confined levels: spectral information.** At high excitation power, LP2D and UP2D states are populated because of parametric scattering processes. This indicates a coupling between 2D and 0D in the bistability regime.

system switch from spin-up to spin-down for a very small variation of the excitation polarization degree.

In addition to the understanding of polariton spinor interactions, these experiments open many perspectives to the design of polariton-spintronic devices.

Chapter 7

Spinor Effects in the Polariton Fluid Dynamics

7.1 Theory of polariton superfluidity

The first prediction of microcavity polariton superfluidity was made by Carusotto and Ciuti in 2004. In their approach, developed in Refs. [Carusotto 04] and [Ciuti 05, Ciuti 01], they first consider separately the exciton and photon fields $\Psi_{X,C}(\mathbf{x})$. The elementary excitation spectrum is determined using a linearization theory. In presence of a static defect, different regimes for the collective fluid dynamics can be found. The upper and lower polaritonic excitations can be retrieved by applying the basic transformation Eq. (1.17)

$$\begin{pmatrix} \psi_{LP} \\ \psi_{UP} \end{pmatrix} = \begin{pmatrix} X_{\mathbf{k}} & -C_{\mathbf{k}} \\ C_{\mathbf{k}} & X_{\mathbf{k}} \end{pmatrix} \cdot \begin{pmatrix} \psi_X \\ \psi_C \end{pmatrix} \tag{7.1}$$

where $X_{\mathbf{k}}$ and $C_{\mathbf{k}}$ are the Hopfield factors. In our experiments, the energy blueshifts due to polariton-polariton interactions are smaller than the Rabi splitting. Therefore, upper and lower polaritons are not interacting with each other and can be treated independently. We are then allowed to consider only the lower polariton branch ψ_{LP}. In the following, we give a general summary of this theory and its predictions. We recommend the reader to refer to the original papers for a detailed description of the calculations.

7.1.1 Excitation spectrum

Model

The time evolution of the mean field $\psi_{LP}(\mathbf{x}, t)$ (Schödinger picture) is given by the Gross-Pitaevskii equation

$$i\frac{d}{dt}\psi_{LP} = \left(\omega_{LP} - i\gamma + \alpha|\psi_{LP}|^2\right)\psi_{LP} + F_p\, e^{i(\mathbf{k_p}\cdot\mathbf{x} - w_p t)} \tag{7.2}$$

where the polariton dispersion is approximated by a parabola $\omega_{LP} = \hbar^2 {\mathbf{k_p}}^2/2m_{LP}$. We consider the polariton field in the rotating frame such that

$$\psi_{LP}(\mathbf{x}, t) = \tilde{\psi}_{LP}(\mathbf{x}, t) e^{i(\mathbf{k_p}\cdot\mathbf{x} - w_p t)} \tag{7.3}$$

The Gross-Pitaevskii equation becomes

$$i\frac{d}{dt}\tilde{\psi}_{LP} = \left(\omega_{LP} - \omega_p - i\gamma + \alpha|\tilde{\psi}_{LP}|^2\right)\tilde{\psi}_{LP} + F_p \tag{7.4}$$

Linearization

The elementary excitations are obtained with a procedure analog to the Bogoliubov theory for a weakly interacting Bose gas. The Gross-Pitaevskii equation is linearized around a stationary solution $\tilde{\psi}_0$. We write Eq. (7.4) for $\tilde{\psi}_0 + \delta\psi_{LP}$

$$i\frac{d}{dt}(\tilde{\psi}_0 + \delta\psi_{LP}) = \left(\omega_{LP} - \omega_p - i\gamma + \alpha|\tilde{\psi}_0 + \delta\psi_{LP}|^2\right)(\tilde{\psi}_0 + \delta\psi_{LP}) + F_p \tag{7.5}$$

and develop the expression to the first order

$$i\frac{d}{dt}\delta\psi_{LP} = \left(\omega_{LP} - \omega_p - i\gamma + 2\alpha\tilde{\psi}_0^*\tilde{\psi}_0\right)\delta\psi_{LP} + \alpha\tilde{\psi}_0\tilde{\psi}_0\delta\psi_{LP}^* \tag{7.6}$$

Here again, we can assume that the field $\delta\psi_{LP}$ oscillates at the laser frequency and is in phase with the laser.

Note that the same procedure gives a similar equation for the field $\delta\psi_{LP}^*$. Both equations are coupled to each other. Therefore, the equation can be written in the $(\delta\psi_{LP}, \delta\psi_{LP}^*)$ basis. The evolution of the vector $\delta\vec{\psi}_{LP}$ is then given by

$$i\frac{d}{dt}\delta\vec{\psi}_{LP} = \mathcal{L}\cdot\delta\vec{\psi}_{LP} \tag{7.7}$$

where the matrix $\mathcal{L}$ is

$$\mathcal{L} = \begin{pmatrix} \omega_{LP} - \omega_p + 2\alpha|\tilde{\psi}_0|^2 - i\gamma & \alpha\tilde{\psi}_0{}^2 \\ -\alpha\tilde{\psi}_0{}^{*2} & -\omega_{LP} + \omega_p - 2\alpha|\tilde{\psi}_0|^2 - i\gamma \end{pmatrix} \tag{7.8}$$

The Bogoliubov modes are the eigenvalues of $\mathcal{L}$. They determine two dispersion branches (diagonal terms) with anti-hermitian coupling (opposite signs for the anti-diagonal terms). The two dispersion branches are symmetric with respect to the pump position and are approximated by the following expression [Ciuti 05]

$$\omega_{LP}^{\pm}(\mathbf{k}) \simeq \omega_p + \delta\mathbf{k}\cdot\mathbf{v_p} - i\gamma \pm \sqrt{(2\alpha|\tilde{\psi}_0|^2 + \eta_{\delta\mathbf{k}} - \Delta_p)(\eta_{\delta\mathbf{k}} - \Delta_p)} \tag{7.9}$$

where $\Delta_p = \omega_p - \omega_{LP}(\mathbf{k_p}) - \alpha|\tilde{\psi}_0|^2$ is the effective detuning, $\mathbf{v_p} = \hbar\mathbf{k_p}/m_{LP}$ is the flow velocity, $\delta\mathbf{k} = \mathbf{k} - \mathbf{k_p}$ and $\eta_{\delta\mathbf{k}} = \hbar\delta\mathbf{k}^2/2m_{LP}$.

7.1.2 Scattering against a defect

In presence of a defect, Eq. 7.7 needs to feature a driving force term $\vec{f}$

$$i\frac{d}{dt}\delta\vec{\psi}_{LP} = \mathcal{L}\cdot\delta\vec{\psi}_{LP} + \vec{f} \quad , \qquad \vec{f} = \begin{pmatrix} V_{LP}(\vec{x})\tilde{\psi}_0 \\ -V_{LP}(\vec{x})\tilde{\psi}_0^* \end{pmatrix} \tag{7.10}$$

with $V_{LP}(\vec{x})$, the scattering potential. The excitations satisfy the equation

$$\delta\vec{\psi}_{LP} = \mathcal{L}^{-1}\vec{f} \tag{7.11}$$

This equation presents resonances for

$$\omega^{\pm}(\mathbf{k}) = \omega_p \tag{7.12}$$

This means that when flowing against a defect, polaritons will scatter to the points of the dispersions that have the same energy as the laser. Depending on the excitation conditions, it is possible to suppress the scattering. In this case, the defect does not influence the polariton propagation: polaritons behave as a superfluid. Exact calculations of the Bogoliubov dispersions in the normal and superfluid polariton phases are shown in Figure 7.1, together with the corresponding momentum and real space density patterns.

Non interacting gas

In Fig. 7.1 a, a low density of polaritons is excited resonantly, and with a wavevector $\mathbf{k_p} = 0.34\ \mu\text{m}^{-1}$. The blueshift is very small, so the Bogoliubov dispersions are not interacting. Scattering against the defect produces a resonant Rayleigh scattering (RRS) ring in the momentum space. The real space pattern presents parabolic fringes on top of the defect. The period of these fringes is related to the difference in wavevector $\Delta\mathbf{k}$ between two counter-propagating waves of the Rayleigh ring. In this case, $\Delta\mathbf{k} \simeq 2\mathbf{k_p}$.

Superfluid regime

In Fig. 7.1 b, polaritons are excited with a laser positively detuned and the same wavevector as is the previous case. A high polariton density is created, so that the resulting blueshift is large enough to overcome the laser detuning. The interaction between the Bogoliubov branches is strong and one sees that they are drastically modified. In particular, one notices a linear region of the dispersion. In addition, for a smart choice of $\mathbf{k_p}$, it is possible to obtain special Bogoliubov dispersions for which Eq. (7.12) admits no solution. In this case, scattering against the defect is suppressed. In the presence of a defect, the fluid will flow without being perturbed at all. The far-field collapses at $\mathbf{k_p}$ and no fringes are observed in the near-field.

Landau criterion A criterion analog to the Landau criterion can be written for polariton superfluidity as a function of the sound velocity $c_s = \sqrt{\alpha|\psi|^2/m_{LP}}$ and for $\Delta_p \leq 0$:

$$m_{LP}\frac{\hbar^2{\mathbf{k_p}}^2}{m_{LP}^2} - m_{LP}c_s^2 < |\Delta_p| \tag{7.13}$$

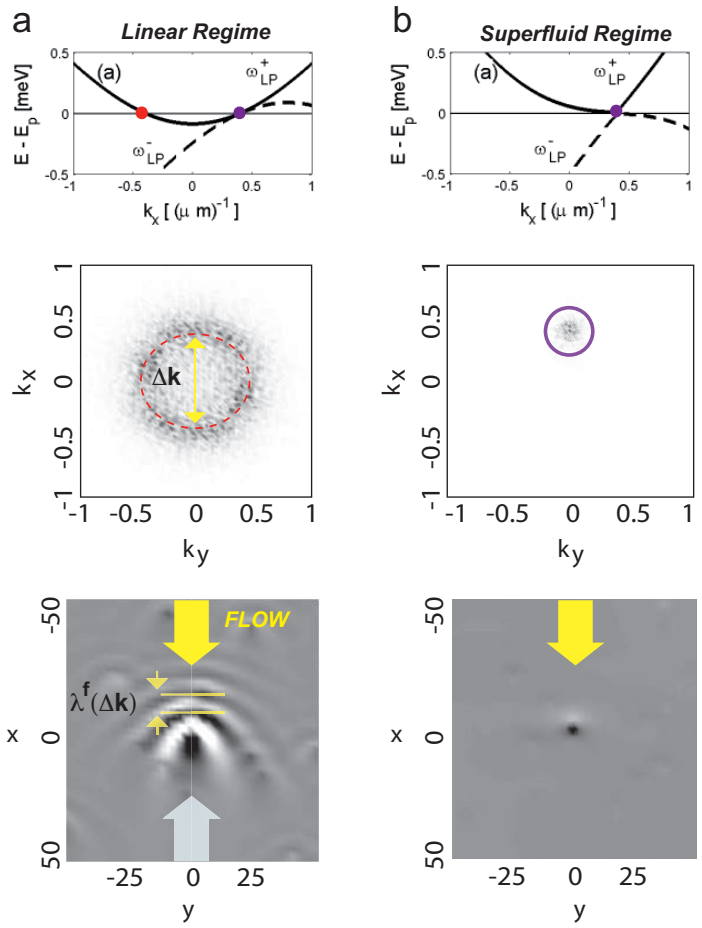

Figure 7.1: **Bogoliubov dispersions: linear and superfluid regimes** The exact calculations of the Bogoliubov dispersion are represented, together with the corresponding momentum space and real space densities. **a Linear regime** *Dispersions.* The pump (purple dot) is given a small wavevector $\mathbf{k_p} = 0.34\ \mu\mathrm{m}^{-1}$ and is at zero detuning $\omega_p - \omega_{LP}(\mathbf{k_p}) = 0$. The blueshift is extremely small (10^{-4} meV), so that the parabolic dispersions are unperturbed. The two dispersions ω^+_{LP} and ω^-_{LP} touch each-other at $\mathbf{k_x} = \mathbf{k_p}$. The dispersions are intersecting the 0 line (red dot) which corresponds to ω_p. *Momentum space.* In presence of a defect, polaritons will scatter to all the states that have the same energy of the laser $\omega_{LP}(\mathbf{k_p}) = \omega_p$ (see Eq. (7.12)). We obtain (red circle) the well known resonant Rayleigh scattering (RSS) ring . The speckles are due to the presence of many defects in the potential used for the calculation. *Real space.* The flow direction ($\mathbf{k_p}$) is indicated by the large yellow arrow. The scattering against a defect (center) is characterized by large parabolic fringes. This pattern results from the presence of counter-propagating waves (e.g. large grey arrow). The period of the fringes λ^f depends on the difference $\mathbf{\Delta k}$ between to interfering points of the momentum space. **b Superfluid regime** *Dispersions.* The dispersions are calculated for a large laser detuning compensated by the interactions. Here, the Landau criterion Eq. (7.13) is verified. A special situation occurs, where the Bogoliubov dispersions do not cross the 0 line. *Momentum space.* There is no solution for $\omega^{\pm}_{LP} = \omega_p$ and scattering is suppressed. The far-field emission collapses to the wavevector of the laser. *Real space.* The propagation is not perturbed by the defect. *From Ref. [Ciuti 05].*

7.1.3 Experiments on polariton superfluidity

Amo's experiments

Two important experiments on superfluidity have been carried out by Amo et al. The first one consisted in observing the time resolved dynamics of a polariton gas flowing against a defect without being scattered [Amo 09b]. In this experiment, the Landau criterion could not really be applied because of the non-equilibrium dynamics. The second experiment was closer to the proposal described above and clearly demonstrated the superfluid behavior of polaritons by direct application of the Landau criterion [Amo 09c].

Other indications

Other kinds of experiments also point out the superfluid behavior of polaritons. Let us mention the experiments on the Bogoliubov dispersion by the group of Yamamoto [Utsunomiya 08] and the experiments on full [Lagoudakis 08] and half [Lagoudakis 09] quantized vortices in a polariton condensate by Lagoudakis. Note that, this latter experiment not only constitutes the first observation of half-quantized vortices, but it is also a crucial experiment regarding the possibility of having decoupled fluid dynamics for spin-up and spin-down polaritons.

7.1.4 Other regimes

An exhaustive description of the different regimes that can be obtained apart from superfluidity is given in Ref. [Ciuti 05]. Among those, we highlight the sticking branches regimes and the Cerenkov regime where special scattering resonances produce peculiar propagation wavefronts. These regimes are illustrated in Figure 7.2, where we display the corresponding predicted near-field patterns.

Sticking branches

In Figure 7.2 a, the laser detuning is larger than the blueshift, so that $\Delta_p > 0$. Because of anti-hermitian coupling, the Bogoliubov branches stick together between their intersection points, yielding a linear region of the dispersion. The intensity of the corresponding region of the momentum space is enhanced. The real space pattern is characterized by large fringes and a shadow after the defect.

Narrow fringes

We consider the previous case of the sticking branches regime, but with a much larger Δ_p. In this case, the anti-hermitian coupling cannot overcome the separation between the two branches, so that they only stick in the vicinity of their intersection points (see Fig. 7.2 b). The pump is not touching the dispersions so it is immediately scattered. Two intense spots are visible in the Rayleigh ring. The corresponding propagating waves produce narrow interferences fringes all around the defect.

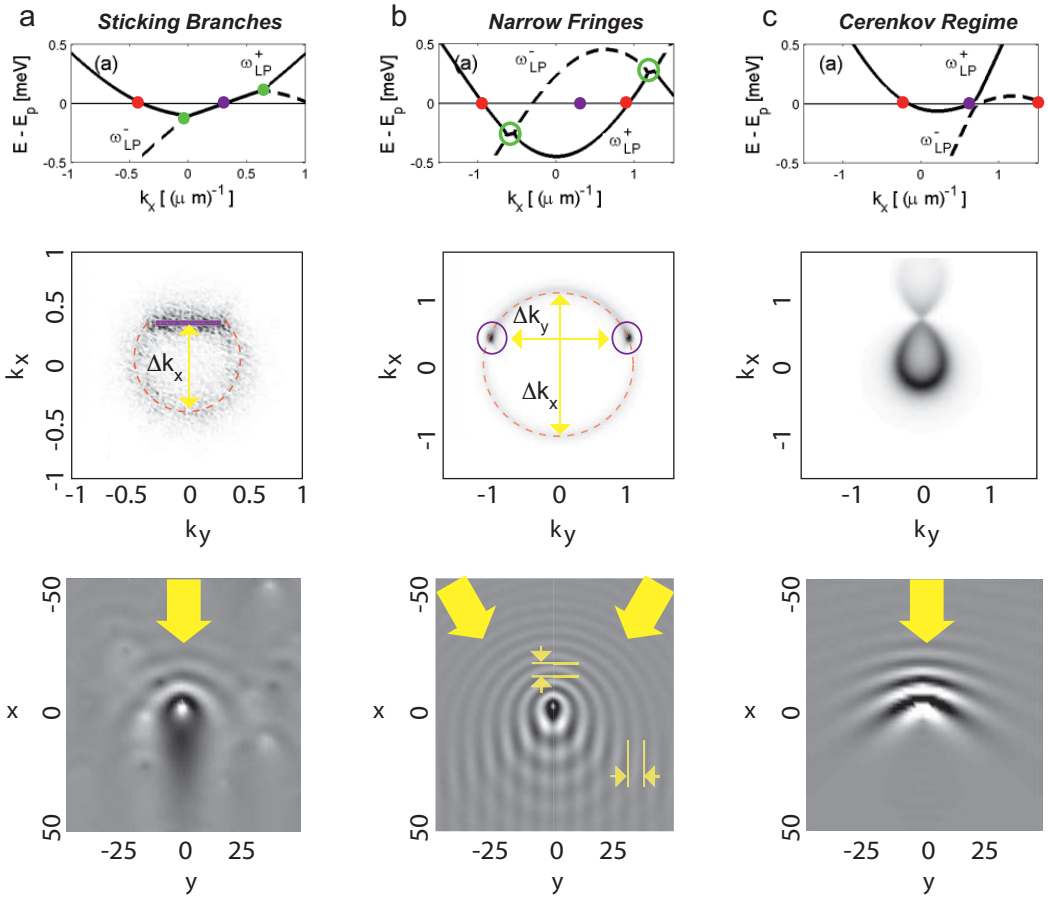

Figure 7.2: **Bogoliubov dispersions: other regimes** Different propagation regimes are calculated for a pump wavevector $\mathbf{k_p} = 0.34\ \mu\text{m}^{-1}$. **Sticking branches.** *Dispersions.* The laser detuning is small $\hbar(\omega_p - \omega_{LP}(\mathbf{k_p})) = 0.1\ meV$ and almost compensated by the blueshift $\alpha|\psi|^2 = 0.07$ meV. The two parabolic dispersion branches stick together between their intersection points (green dots) because of anti-hermitian coupling. This produces a linear modification of the dispersion. *Near field.* The intensity of the Rayleigh ring is increased in the region $\mathbf{k_x} \simeq \mathbf{k_p}$. *Real space.* The shadow after the defect is characteristic of this regime. **Narrow fringes.** *Dispersions.* The blueshift $\alpha|\psi|^2 = 0.075$ meV is small compared to the laser detuning $\hbar(\omega_p - \omega_{LP}(\mathbf{k_p})) = 0.47\ meV$. The ω^+_{LP} and ω^-_{LP} branches stick only close their intersection points (green circles), but in between, the anti-hermitian coupling is not large enough to compensate the spacing between them caused by the large laser detuning. *Momentum space.* The pump does not touch the Bogoliubov dispersions, so it scatters to the points of the RRS ring at $\mathbf{k_x} = \mathbf{k_p}$. *Real space.* The two bright spots in the momentum space give rise to two waves flowing with the same $\mathbf{k_x} = \mathbf{k_p}$ but opposite $\mathbf{k_y}$ (large yellow arrows). The interferences produces narrow fringes all around the defect, which period is related to the momentum difference: $\mathbf{\Delta k_{x,y}} \simeq 2\ \mu\text{m}^{-1}$. In the linear regime this difference was $\mathbf{\Delta k} \simeq 1\ \mu\text{m}^{-1}$, yielding a fringe period twice as large as in the present case. **Cerenkov-like regime.** In this regime, interactions compensate the laser detuning but the flow velocity is too large to satisfy the Landau criterion. The scattering waves are linear. One can retrieve the ratio between the sound and fluid velocities by measuring the aperture angle ϕ: $sin\phi = c_s/v_p$.

Cerenkov waves

We consider the superfluid regime, but with a much larger excitation wavevector $\mathbf{k_p}$. In this case, the Landau criterion is not fulfilled. One can think that $\mathbf{k_p}$ gives a tilt to the dispersions so that there is now a solution for Eq. 7.12 and scattering is possible. In this regime, called the Cerenkov regime (Fig. 7.2 c), the flow velocity is larger than the sound velocity in the polariton fluid. One observes linear scattering waves on top of the defect.

7.1.5 Spinor component

As suggested in Ref. [Solnyshkov 08], the polariton spin may have an influence on the Bogoliubov modes. Clearly, controlling polariton fluid dynamics by acting on polariton spins opens the way to very efficient spin-transport devices. We propose to explore the polariton flow dynamics of microcavity polaritons and its sensitivity to spinor effects.

7.2 Polariton fluid dynamics

In the following we describe *preliminary* studies of the polariton fluid dynamics. Although we do not demonstrate a clear superfluid transition, we have strong indications for a suppression of the scattering against the defect. This superfluid-like transition is in competition with the appearance of narrow fringes resembling the ones described in Fig. 7.2. However, in our case, the narrow fringes seem to originate from a coupling between 2D and 0D states. We also evidence a Cerenkov like regime. Finally we show that the dynamics of the polariton fluid is sensitive to the excitation polarization and also to the position of the defect.

7.2.1 Experimental procedure

We study the propagation of a polariton fluid created with a 30 μm diameter excitation spot. The fluid created with a given wavevector so that its flow is directed toward a 3 μm diameter mesa. The laser is initially positively detuned with respect to the polariton state. We use near field imaging in order to access the real space propagation pattern. In addition, we spectrally resolved far-field imaging to access the dynamics in the momentum space. A power study allows us to observe different propagation regimes. As the experimental results discussed here are preliminary, we discuss them only qualitatively. The observed dynamics did not significantly depend on the detuning.

7.2.2 First observations

In Figure 7.3, we show a first power dependent study of polaritons propagation against a mesa. We already can distinguish three phases.

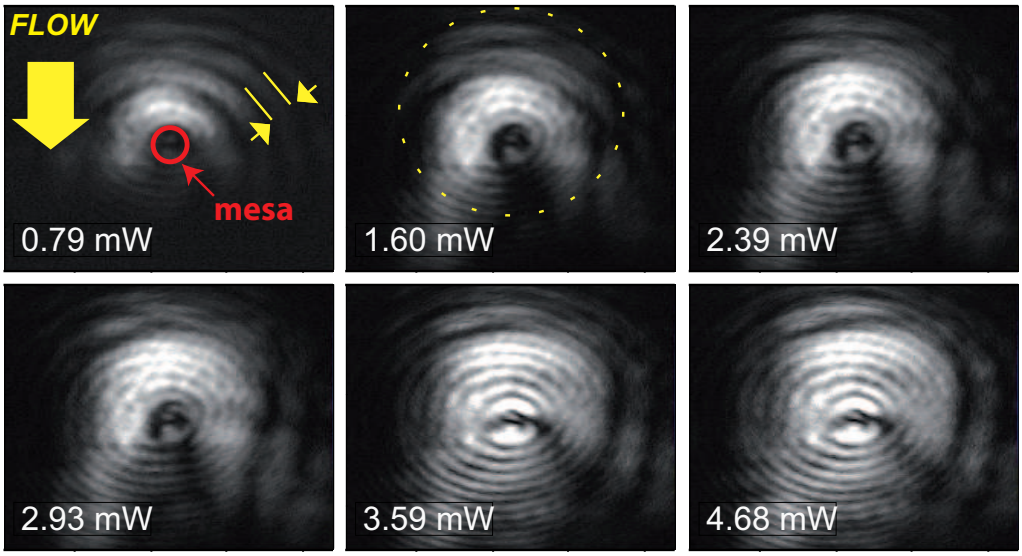

Figure 7.3: **Collective fluid dynamics: near-field** Polaritons are created by a 30 μm diameter excitation spot (dashed circle) and flow against a 3 μm diameter mesa. We record the near field pattern for 6 different powers. Two transitions can be observed: one to a regime where scattering is suppressed and another one to a 2D-0D coupling regime. **0.79 mW:** We distinguish large scattering waves. **1.60 mW:** The region around the mesa becomes smoother. A second, narrower wave pattern can be observed around the mesa. **2.39, 2.93 mW:** The scattering around the mesa is reduced. The large waves can be seen only at the edge of the polariton spot. **3.59, 4.68 mW:** At very high power, the polariton density becomes maximal at the mesa position. The narrow fringes pattern is also more visible. Horizontal axis: x, Vertical axis: y. *Parameters:* $\delta' \simeq -1.9$ *meV,* $\Delta \simeq 0.6$ *meV,* $k_{\text{laser}} \simeq 0.5\ \mu\text{m}^{-1}$.

Linear regime At low excitation power (0.79 mW), the system behaves as a non interacting gas and the flow is characterized by large scattering waves similarly to what is presented in Fig. 7.1.

Suppression of scattering fringes By increasing the excitation power (2.3, 2.4 mW), we reach a phase where the scattering intensity is reduced, reminding us the features of a collapsing RRS ring and could be related to the build-up of a superfluid phase. However, narrow fringes start to appear all around the mesa. In addition we observe a shadow after the mesa as in the sticking branches regime (see Fig. 7.2 a). The system is thus probably in competition between different regimes.

Narrow fringes At higher excitation power (>3 mW), the real-space pattern is similar to the prediction for the narrow fringes regime (see Fig. 7.2 b). Hence, we evidence two transitions dependent on the excitation power. However, there should not be any no power dependent transition between the regimes of Figs. 7.2 a and 7.2 b[1]. We propose to discuss the corresponding spectral information.

[1]Or, at least, the sticking branches regime of Fig. 7.2 a should occur at a higher excitation power than the narrow fringes regime of Fig. 7.2 b, contrary to what we observe.

7.2.3 Spectral information

Suppression of scattering fringes

We are first interested in the transition to the low scattering regime, characterized by a vanishing of the large scattering waves. The near-field is imaged on the slits of the spectrometer in order to obtain dispersion (E, k_y) images. Note that, here, we study the polariton fluid dynamics at a different detuning than shown previously. A similar two-transition dynamics is observed, the only difference being the values of the threshold powers. The planar polariton state is at zero detuning. The mesa acts as a 6 meV deep defect.

The first transition is characterized by a collapse of the far-field emission to the laser position. As shown in Figure 7.4 a to d, the backscattering peak suddenly disappears at the threshold power $P_1 \simeq 1.6$ mW. This indicates that the scattering is strongly reduced along this first transition. It is in agreement with the near-field images, where the suppression of the scattering waves around the mesa indicates a superfluid-like. However, the presence of a shadow after the mesa shows that the scattering on the mesa is not totally cancelled. This could be responsible for the halo around k_p observed in Fig. 7.4. In the following, we refer to this regime as the *low scattering intensity* regime.

Coupling to confined states

The second transition corresponds to the build-up of narrow fringes and of a strong emission from the region of the mesa. The spectral information shows that during this transition, the states of the mesa suddenly light-up. In addition, scattering lobes appear at large wavevectors and at the energy of the laser. This second transition is depicted in Figure 7.4 e to h.

Figure 7.4 e is the emission spectrum of Fig. 7.4 d, saturated at the laser energy to show that no emission is coming from the confined states. We observed a threshold power $1.6 < P_2 < 2.1$ mW at which the 0D polariton states start to emit (Fig. 7.4 f). Two lobes appear at $k = 1.9\ \mu\text{m}^{-1}$ and $k = -2.2\ \mu\text{m}^{-1}$. This kind of asymmetry is likely to appear in the case where the scattering to the ω_{LP}^{-} dispersion branch is important. The ground state being at very negative detuning, it has a very poor exciton content and therefore is only weakly populated by collisions.

At higher excitation power (Fig. 7.4 g and h), no significant change is observed in the intensity of the emission from the mesa.

Open question

The coupling to confined state regime coincides with a spatial pattern similar to the one predicted for the narrow fringes regime of Fig. 7.2. From our spectroscopic measurement (see Fig. 2.7), we know that at these detunings, there is an overlap in energy between the high-energy states of the mesa and the bottom of the planar polariton dispersion. Therefore we are not sure whether the appearance of the narrow fringes is due to the mesa states or to the scattering of planar polaritons. The fact that this regime appears at high excitation power (hence for a blueshift comparable to Δ_p) might be an indication in favor of a contribution from the mesa.

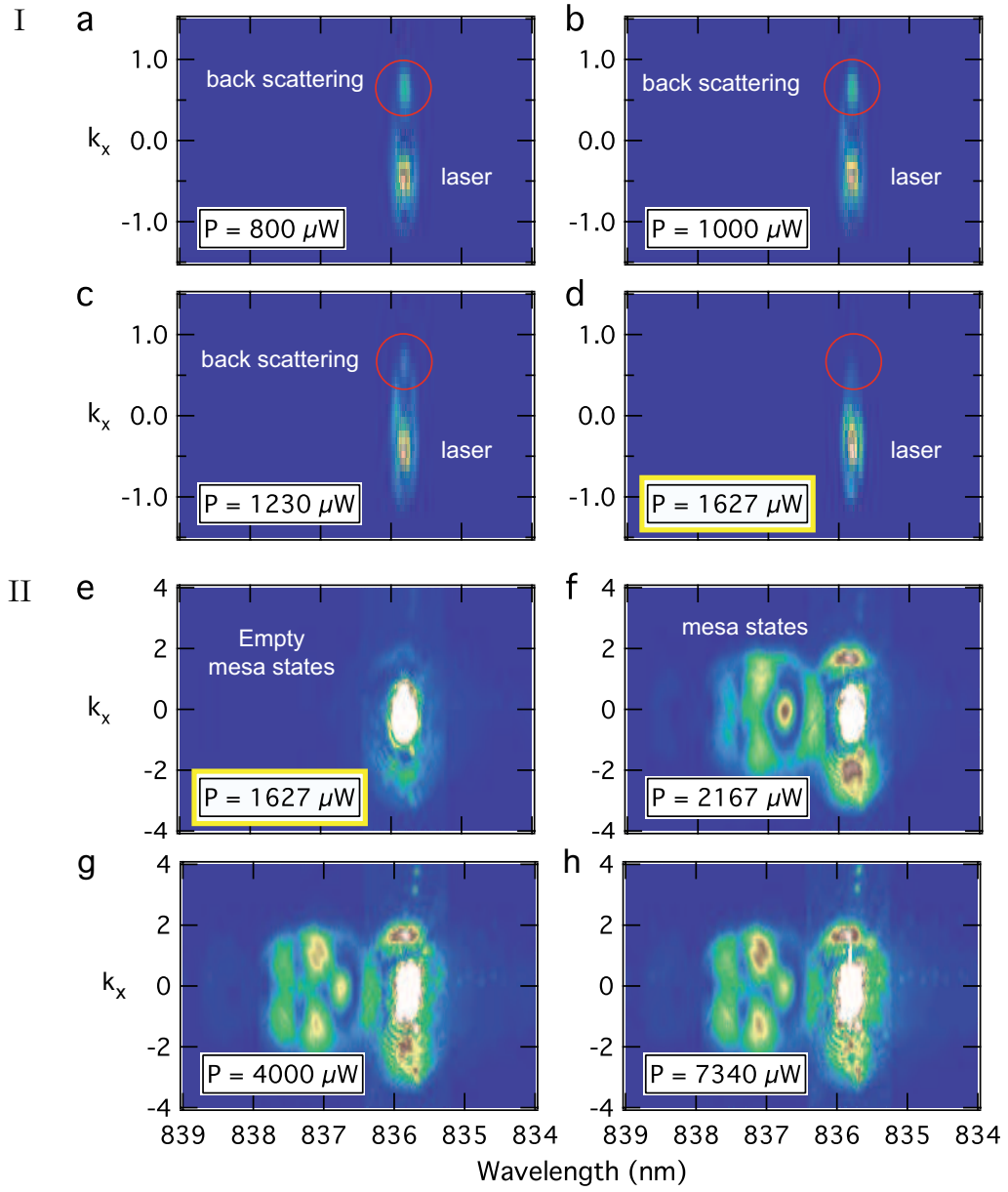

Figure 7.4: **Spectrally resolved far-field images a-d** Reduction of scattering intensity. **a** At 800 μW, the emission is characterized by a strong peak at the laser position $k_p = -0.6\ \mu\text{m}^{-1}$ spot and backscattering peak at -k_p. **b and c** When the power is increased, the backscattering peak becomes less important. **d** At 1.6 μW, at first transition occurs, where the backscattering peak disappears. This situation corresponds to the suppression of the large scattering waves observed in Fig. 7.3. **e,f** Coupling to confined states transition. **e** Shows the data of (d) with a saturated color scale to show that there is no emission coming from the mesa. **f** At 2167 μW, a new transition occurs and the confined state suddenly emit. In the near-field images, this corresponds to the appearance of a strong emission from the mesa and of the narrow scattering waves pattern. **g, h** At higher excitation power, there is no significant change in the intensity of the confined states. Note that the same color scale is used for (e) to (h). *Parameters:* $\delta' \simeq -1.57\ meV$, $\Delta \simeq 0.3\ meV$, $k_\text{p} \simeq 0.5\ \mu m^{-1}$.

This would indicate that the build-up of a superfluid phase is hindered by a coupling to the confined states in our system.

7.3 Spinor effects in the polariton fluid dynamics

7.3.1 Bistable transitions

We have evidenced transitions towards two scattering regimes for a polariton fluid flowing against a potential well. The first is characterized by a suppression of the scattering against the mesa and the second one to a coupling between the polariton fluid and the confined states. Because of the polariton spinor component, we evidenced different transitions under circularly or linearly polarized excitation.

In Figure 7.5, we plot the emission intensity with respect to the excitation power, integrated over the energy axis. In case of circularly polarized excitation (Fig. 7.5 a), we evidence two clear threshold powers at which the intensity jumps abruptly. The first one corresponds to the transition between the linear and the low scattering intensity regime. During this transition, the large scattering waves around the mesa disappear and the far-field emission collapses at k_p. The second transition rapidly follows as shown previously: it corresponds to the transition to the 2D-0D coupling regime. A clear bistability is observed for this transition. In some cases, we also observed a bistable behavior at the first transition. The two transitions are very close to each other, and this might be a reason why we don't observe a clear superfluid regime.

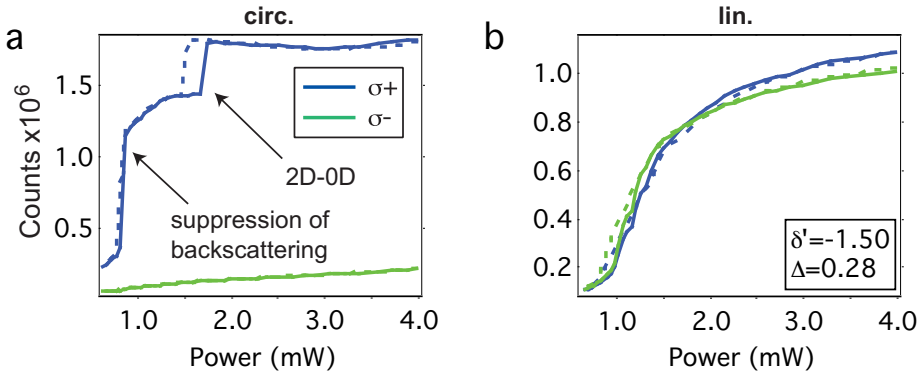

Figure 7.5: **Power study.** We plot the emission intensity as a function of the excitation power under circularly and linearly polarized excitation. The power is scanned from 0.6 to 4 mW and backward. We show the behavior of the polarization resolved emission in the ($\sigma+$,$\sigma-$) basis. **a** The excitation is $\sigma+$ polarized. The $\sigma-$ emission is negligible. We notice two sharp transitions in the evolution of the $\sigma+$ emission. The first one corresponds to the transition to a low scattering intensity regime and the second one to the coupling between 2D and 0D states. A hysteresis behavior can be observed or each transition. In the data shown here, the hysteresis is present for the second transition. **b** Under linearly polarized excitation, $\sigma+$ and $\sigma-$ emissions are equal. No sharp transition is observed any more. *Parameters:* $\delta' \simeq -1.50$ *meV*, $\Delta \simeq 0.3$ *meV*, $k_\mathrm{p} \simeq 0.5$ μm^{-1}.

In the case of linearly polarized excitation (Fig. 7.5 b), we observe a continuous transition. No peculiar threshold is identified. The near-field evolution is characterized by a very smooth transition between the different regimes.

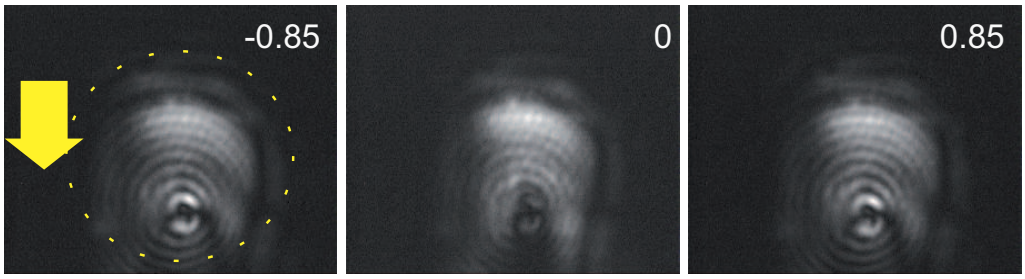

Figure 7.6: **Spinor effects** The fluid dynamics is controlled by the excitation polarization degree. Under nearly circularly polarized excitation, $\rho_p = \pm 0.85$, the system is in the 2D-0D coupling regime. Under linearly polarized excitation $\rho_p = 0$, the system is in the low scattering intensity regime.

7.3.2 Controlling parametric instabilities

By exploiting these differences, it is possible to tune the dynamics by simply changing the polarization degree of the excitation. That is, we prepared the system in the narrow fringes regime under left-circular excitation and then we continuously changed the excitation polarization to right-circular. At $\rho_p \simeq \pm 0.5$, we observed transitions between the low scattering intensity and narrow fringes regimes. We illustrate briefly this experiment in Fig. 7.6. At $\rho_p = \pm 0.85$, the polariton fluid is coupled to the mesa. Narrow fringes are observed around the mesa and the intensity is maximal at the mesa position. At $\rho_p = 0$, the scattering against the mesa is suppressed.

7.4 Position dependence

We finally discussed an interesting issue, which is the position of the mesa in the excitation spot. Since we use a gaussian spot of $30\,\mu$m diameter, the polariton density is strongly inhomogeneous. Depending on the position of the mesa, it is therefore possible to switch between the different regimes.

Figures 7.7 and 7.8 display experiments that illustrate this observation. In Fig. 7.7, the system is in the high density regime. The mesa position is changed and we observe successively a low scattering intensity regime, a narrow fringes regime and a Cerenkov-like regime when the mesa is at the bottom, the middle and the top of the spot, respectively. In Fig. 7.8, we show the power dependence study at two different positions of the mesa in the spot. When the mesa is at the bottom of the spot, we observe a transition to low scattering intensity regime. When the mesa is at the top of the spot, we observe the build-up of a Cerenkov-like linear waves pattern.

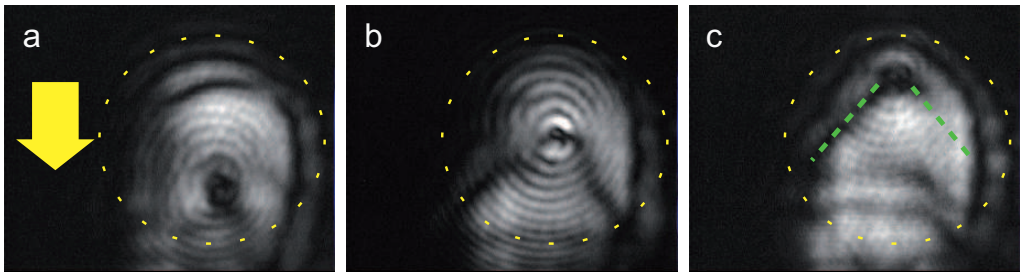

Figure 7.7: **Position dependence.** The dynamics regime of the polariton fluid strongly depends on the mesa position. **a** Low scattering intensity regime **b** 2D-0D coupling regime **c** Cerenkov-like regime.

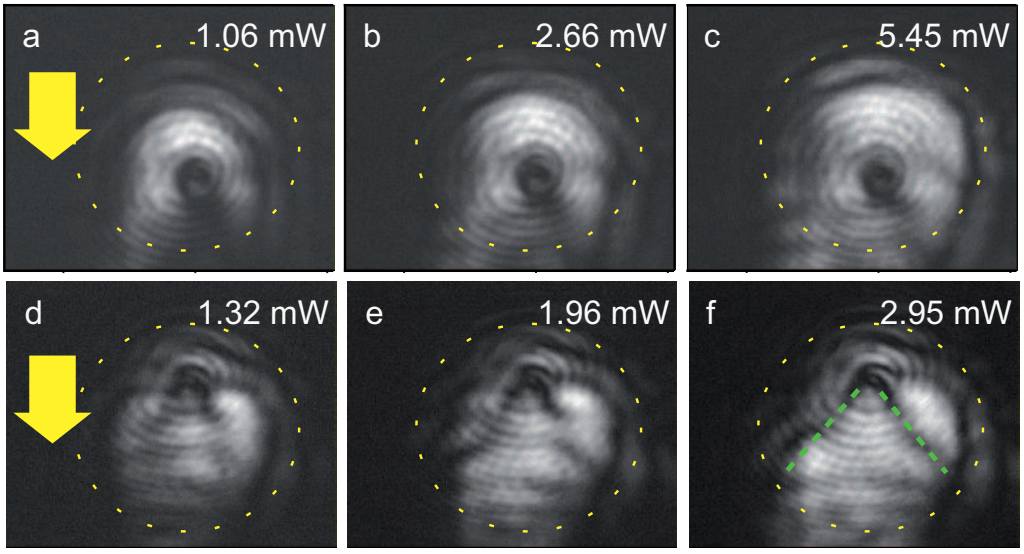

Figure 7.8: **Power study: position dependence** **a-c** Superfluid-like transition. **d-f** Cerenkov-like transition. Note that in both cases, the coupling to confined states is likely to be observed at even higher excitation powers.

7.5 Conclusion

In conclusion, we have presented preliminary experiments showing the great potential of the mesas structures to study polariton parametric instabilities and collective fluid dynamics.

In further studies, the role of various parameters such as the spot size, the spot shape, the relative depth of the mesa, the size of the mesa and the flow velocity (v_p) should be explored. The goal of this chapter is to show that it is possible to take advantage of spinor interactions to monitor the polariton fluid dynamics.

Our study points out a very rich phenomenology, with, in particular, a competition between the suppression of scattering and the coupling between 2D and 0D polaritons.

We observed striking differences in the dynamics under linearly or circularly polarized excitation and successfully controlled the fluid scattering regime with the excitation polarization.

Conclusion

The goal of this Ph.D. thesis was to study the dynamics of microcavity polaritons under lateral confinement. We analyzed different aspects of polariton interactions, some that had already been widely studied with planar microcavity polaritons, others that had not. As a general outcome, we showed that confining polaritons presents several advantages that lead us to explore a novel and very rich physics.

We design cylindrical extensions of the cavity spacer, called mesas, to trap polaritons by acting on their photonic component. Thanks to confinement, the polariton spectrum is discrete and the confined states present much narrower linewidths than planar polaritons. In addition, the significant energy spacing between the states allows us to work with single polariton levels. The system is thus easier to model and to manipulate.

Polariton interactions are dominated by scattering with phonons and free carriers in the low-density regime and by polariton-polariton scattering in the high-density regime. Moreover, collisions between polaritons are strongly influenced by the polariton spin. In this work, we characterize these interactions through appropriate examples and underline the peculiar physics of confined polaritons. We establish that the spinor nature of polaritons offers the possibility to achieve very efficient control of polariton interactions and to develop innovative polariton spintronic devices. We now review our main conclusions.

On the relaxation mechanisms of confined polaritons

We studied the way confined polaritons relax from the high-energy states to the low energy states and the ground state. By means of time-resolved spectroscopy and photoluminescence excitation experiments, we addressed this question both in the low and high-density regimes.

Enhancement of polariton thermalization

In the low-density regime, we performed experiments on polariton thermalization. It is well know that thermalization does not occur in planar microcavities unless the temperature is raised or an electron gas is injected in the system. We performed photoluminescence excitation experiments and studied the polariton energy distribution as a function of the mesa diameter. In addition, we were able to create

polaritons in a single energy levels of the upper or lower polariton multiplet and to measure the time needed for polaritons to relax to the ground energy level.

We demonstrated that **efficient polariton thermalization** takes place in the mesas of small (3 and 9 μm) diameters. In the large diameter mesas (20 μm), we showed that thermalization is inefficient, as in the case of planar microcavities. We could determine that scattering with phonons is favored by the relaxation of the momentum conservation rule in small mesas. In large mesas, we determined the role of states with large exciton content in slowing down the relaxation. In addition, we demonstrate that the coupling between planar and confined polaritons is weak so that no relaxation occurs between polaritons of different dimensionalities. We found a very good agreement between our experiment and a theoretical model. We developed a general picture for the mechanisms of polariton thermalization under lateral confinement.

Collisional relaxation

In the high-density regime, we studied the impact of polariton-polariton collisions on the spatial dynamics of microcavity polaritons. We performed two-dimensional time-resolved spectroscopy to observe the dynamics of the polariton density in the momentum space. We first created polaritons in a coherent superposition of the three lowest energy states of a 9 μm mesa. This resulted into a peculiar state, which dynamics was characterized by dipole oscillations of constant amplitude.

We compared the low and high-density regimes for mesas at negative and positive detuning. At negative detuning, we found that the amplitude of the oscillations decreases with the excitation power.

At positive detuning, where the larger exciton content increases the polariton-polariton scattering rate, we observed a continuous damping of the dipole oscillations during the polariton lifetime. We determined that this damping originates from multiple parametric scattering processes, which cause important energy redistribution to the benefit of the ground state.

The role of collisions was emphasized by polarization dependent excitation experiments in which we showed that the collisional damping is reduced under linearly polarized excitation compared to circularly polarized excitation.

Perspectives

Achieving Bose-Einstein condensation in a controlled environment is essential to deepen our knowledge of this peculiar state of matter. Obviously, the understanding of the relaxation mechanisms is important to develop new samples and original trapping structures. The research in determining new trapping techniques is fructuous and stimulating.

From a technological point of view, the spatial dynamics of polaritons in a trap is an important issue on the route to the development of polariton circuits. Our work shows that the polariton propagation is strongly influenced by the density and that it can be polarization controlled.

In the next years, a new generation of samples will be fabricated in our laboratory. Our findings may contribute to the design of smart and efficient structures.

Lasing and condensation

We showed that nonlinear effects under nonresonant excitation cannot take place in our sample because it contains only a single quantum well. Polariton lasing has been achieved by many groups now, and a similar sample as the one studied here with more quantum wells would certainly exhibit a kinetically driven transition towards a macroscopic coherent phase under nonresonant excitation.

From our results on thermalization, we expect the possibility to drive such a transition in the low density regime i.e. in the absence of collisions. This study should better be done in mesas of less than 10 μm diameter. Moreover, it would be interesting to address this problem in mesas of sub-micrometer diameters, in the presence of only one confined state.

Collisional relaxation

Collisional relaxation should be investigated with other combinations of states (higher energy, larger number of states, ...) and in mesas of different diameters, where the energy level spacings (hence the scattering conditions) are different.

In addition, while accidentally doing this experiment in the presence of line defects around the mesa, we observed strong polarization beats in the high density regime, but with very irregular periods. The study of collisional relaxation in strongly asymmetric mesas (large ellipticity, rectangles) should be a way to control this effect better.

On the spinor nature of polariton interactions

The collisional damping experiment was the start of deep investigations of the role of spin in polariton interactions. Optical bistability was the ideal subject to address this question since it originates essentially from polariton-polariton interactions. We performed polarization resolved bistability experiments and compared the cases of planar and confined polaritons.

Polarization control of optical instabilities

We observed that the optical bistability of planar polaritons is suppressed under linearly polarized excitation. Consequently, we showed that the transition between the different optical instability regimes (optical limiting, discrimination and bistability) could be monitored by the excitation polarization. We attributed these effects to the pairing of polaritons of opposite spins into biexcitons and reproduced the experiments with a simple phenomenological model.

Spin multistability

We then studied optical bistability of confined polaritons in 3 μm diameter mesas, where the energy difference between the ground state and the first excited state is large enough to do our experiments only with the ground state. We performed an extensive series of experiments to characterize spinor interactions and the role

of biexcitons. We determined a resonance for the polariton pairing and clearly defined the role of each control parameters (detunings, polarization, power). We were then able to achieve all-optical manipulation of a coherent spin ensemble in the solid state. We demonstrated high efficiency polarization conversion and modulation, polarization-controlled hysteresis, spin multistability and high contrast spin flip operations. This work opens many pathways to the spintronic applications of microcavity polaritons.

Collective fluid behavior

We finally did a preliminary study of the collective fluid behavior of planar polariton. In this case, we use the mesa structures as well-controlled defects. We investigated the polariton propagation against a 3 μm diameter mesa and compared the different regimes observed with theoretical predictions. We observed a competition between the build-up of a low viscosity regime and the coupling to confined states. In addition, we highlighted the role of the excitation polarization and of the position of the mesa in the excitation spot.

Perspectives

The spinor nature of polariton interactions is a subject that has been neglected for a long time. We show that, because of the strong anisotropy of spinor interactions, most polariton nonlinear phenomena can be controlled by the excitation polarization. We could determine the sign of the interaction constant for polaritons of opposite spin, which is opposite to what was generally assumed by theory. Note that this result is in agreement with independent studies of polariton superfluidity.

Interactions

Here again, we evidenced the advantages of polariton confinement. We could acquire a deep knowledge of spinor interactions and determine the conditions for observing multistability. The pairing of polaritons of opposite spins into non radiative states should be investigated theoretically in more details. In the case of confined polaritons, we could determine a resonance for this effect, which is determinant for achieving multistability in our system. In the case of planar polaritons, no sharp resonance could be observed. From our results, new samples could be designed to observe multistability with planar polaritons. For instance, with larger Rabi splittings and narrower linewidths, it could even be possible to study multistability far from the biexciton resonance and to obtain a multistable behavior similar to the original proposal.

Device

Future experiments in mesas will be oriented towards time resolved multi-valued spin switching. The coupling between bistable confined states and delocalized polariton states has been suggested by the collective fluid experiments and by the multistability with excited states experiment. This effect indicates the possibility

of coupling propagating information to a localized memory and should clearly be investigated in more details.

"Exotic" multistability

The multistability of excited states is an interesting issue. For instance one could imagine creating switches with optical vortices states. Multistability could also be used to generate half-vortices-like states.

Spinor superfluidity

Finally, the fundamental issues of polariton spinor fluid dynamics will also be explored. For instance, we have indications for the coexistence of superfluid and normal fluid phases depending on the polariton spins.

Certainly, many more interesting issues will come out of the study of polariton spin dynamics. Important connections can also be made with other fields.

Single photon generation, entanglement

The generation of on-demand single photon emitter is an important topic in the research with quantum dot. Bistability is strongly related to the photon blockade effect with quantum dots coupled to cavities, and one could imagine designing small diameter mesas to achieve this effect. Interestingly, a recent theoretical work proposed to take advantage of the biexciton resonance in microcavities to generate single photons. Regarding the importance of biexciton in our observations, this will probably be an important issue in further works. Finally, let us mention the possibility of observing spin squeezing and entanglement in polariton mesas. Indeed, since squeezing was observed in optical bistability experiments with planar cavities, we expect to see at least similar effects with confined polaritons by doing correlation measurements.

Curriculum Vitae

Taofiq K. Paraïso
ph.d. in physics, epfl
French, 30
Rue Schaub 10, 1202 Genève, Switzerland
taofiq.paraiso@a3.epfl.ch

UNIVERSITY DEGREES

- **PhD in Physics (06-2010)**
  Laboratory of Quantum Optoelectronics, Ecole Polytechnique Fédérale de Lausanne (EPFL), Switzerland
- **Diploma of Physics Engineer (04-2004)**
  Institute of Theoretical Physics (ITP), EPFL, Switzerland

PROFESSIONAL EXPERIENCE

Research

2006 - 2010: PhD in the Laboratory of Quantum Optoelectronics

- Study of the dynamics of microcavity polaritons under lateral confinement using ultrafast spectroscopy. Development of a general scheme for the energy redistribution of polaritons in a trap.
- Design of pioneering experiments in the spinor bistability and demonstration of the first realization of multivalued spin switching in the solid-state. Participation to the development of a generalized Gross-Pitaevskii model for polariton spinor interactions.

2005 – 2006: Research assistant at the Paul Scherrer Institute (PSI) Switzerland

- Development of a Geant4 Monte-Carlo simulation of a Low Energy Muon Spin Relaxation experiment for applications to the study of superconductivity.

09 - 12/2004: Invited in the Theoretical Biophysics group at NORDITA, Denmark

- Contribution to the development of a simulation of DNA denaturation 10/2003 - 04/2004: Diploma thesis in Statistical Biophysics, (EPFL)
- Development a Hamiltonian model for the description of DNA thermal denaturation.

Internships

05/2004 - 07/2004:

- Teacher assistant in Mathematical Physics, ITP EPFL

08/2003 - 04/2004:

- Internship in the LHCb Computing Collaboration, at CERN

08/2002 - 11/2002:

- Internship in Radiation-Therapy simulation at University Hospital, Québec, Canada

COMPETENCE AND SKILLS

- **Photonics:** ultrafast spectroscopy, pulse shaping, streak camera ,interferometry, polarimetry, spin manipulation, laser maintenance (pulsed, cw), general automation (Labview), cryogenics
- **Theory:** quantum and nonlinear optics, statistical physics, condensed-matter physics
- **Computing:** C++, Geant4, Igor Pro, Matlab, Python, Pascal
- **Clean room:** chemical etching, photolithography, waferbonding, PECVD
- **Teaching:** supervision of undergraduate students

LANGUAGES

French: mother tongue
English: fluent
Spanish: good
German: basic

SELECTED PUBLICATIONS

- Multistability of a coherent spin ensemble in a semiconductor microcavity
  T. K. Paraïso, M. Wouters, Y. Léger, F. Morier-Genoud and B. Deveaud-Plédran
  Accepted in Nature Materials (2010)
- Spatial dynamics of confined semiconductor microcavity polaritons
  R. Cerna, T. K. Paraïso, Y. Léger, M. Wouters, F. Morier-Genoud, M. T. Portella-Oberli, and B. Deveaud-Plédran
  Phys. Rev. B 81, 113306 (2010)
- Coherent optical control of the wave function of zero-dimensional exciton polaritons
  R. Cerna, D. Sarchi, T. K. Paraïso, G. Nardin, Y. Léger, M. Richard, B. Pietka, O. El Daïf, F. Morier-Genoud, V. Savona, M. T. Portella-Oberli, and B. Deveaud-Plédran
  Phys. Rev. B 80, 121309 (2009)
- Probability density optical tomography of confined quasiparticles in a semiconductor microcavity
  G. Nardin, T. K. Paraïso, R. Cerna, B. Pietka, Y. Léger, O. El Daïf, F. Morier-Genoud, and B. Deveaud-Plédran
  Appl. Phys. Lett. 94, 181103 (2009)
- Enhancement of microcavity polariton relaxation under confinement
  T. K. Paraïso, D. Sarchi, G. Nardin, R. Cerna, Y. Léger, B. Pietka, M. Richard, O. El Daïf, F. Morier-Genoud, V. Savona, and B. Deveaud-Plédran
  Phys. Rev. B 79, 045319 (2009)

HOBBIES

Reading, writing, jazz piano, running, hiking, swimming

Bibliography

[Abraham 82] E Abraham & S D Smith. *Optical bistability and related devices.* Reports on Progress in Physics, vol. 45, no. 8, pages 815–885, 1982.

[Agranovich 66] V. M. Agranovich & O. A. Dubovskii. *Effect of Retarded Interaction on the Exciton Spectrum in One-dimensional and Two-dimensional Crystals.* JETP Letters, pages 345–350, 1966.

[Alexandrou 01] A. Alexandrou, G. Bianchi, E. Péronne, B. Hallé, F. Boeuf, R. André, R. Romestain & Le Si Dang. *Stimulated scattering and its dynamics in semiconductor microcavities at 80 K under nonresonant excitation conditions.* Physical Review B, vol. 64, no. 23, 2001.

[Amo 09a] A. Amo, T. C. H. Liew, C. Adrados, E. Giacobino, A. V. Kavokin & A. Bramati. *Anisotropic optical spin Hall effect in semiconductor microcavities.* Physical Review B (Condensed Matter and Materials Physics), vol. 80, no. 16, page 165325, 2009.

[Amo 09b] A. Amo, D. Sanvitto, F. P. Laussy, D. Ballarini, E. del Valle, M. D. Martin, A. Lemaitre, J. Bloch, D. N. Krizhanovskii, M. S. Skolnick, C. Tejedor & L. Vina. *Collective fluid dynamics of a polariton condensate in a semiconductor microcavity.* Nature, vol. 457, no. 7227, pages 291–295, 2009.

[Amo 09c] Alberto Amo, Jerome Lefrere, Simon Pigeon, Claire Adrados, Cristiano Ciuti, Iacopo Carusotto, Romuald Houdre, Elisabeth Giacobino & Alberto Bramati. *Superfluidity of polaritons in semiconductor microcavities.* Nat Phys, vol. 5, no. 11, pages 805–810, 2009.

[Anderson 95] M. H. Anderson, J. R. Ensher, M. R. Matthews, C. E. Wieman & E. A. Cornell. *Observation of Bose-Einstein Condensation in a Dilute Atomic Vapor.* Science, vol. 269, no. 5221, pages 198–201, 1995.

[Andreani 91] Lucio Claudio Andreani, Francesco Tassone & Franco Bassani. *Radiative lifetime of free excitons in quantum wells.*

Solid State Communications, vol. 77, no. 9, pages 641–645, March 1991.

[Apfel 55] J. H. Apfel & L. N. Hadley. *Exciton Absorption in Cuprous Oxide*. Physical Review, vol. 100, no. 6, page 1689, December 1955.

[Apker 50] L. Apker & E. Taft. *Photoelectric Emission from F-Centers in KI*. Physical Review, vol. 79, no. 6, page 964, 1950.

[Baars 00] T. Baars, M. Bayer, A. Forchel, F. Schäfer & J. P. Reithmaier. *Polariton-polariton scattering in semiconductor microcavities: Experimental observation of thresholdlike density dependence*. Physical Review B, vol. 61, no. 4, page R2409, 2000.

[Baars 01] T. Baars, G. Dasbach, M. Bayer & A. Forchel. *Biexciton states in semiconductor microcavities*. Physical Review B, vol. 63, no. 16, page 165311, April 2001.

[Baas 04a] A. Baas, J. Ph. Karr, H. Eleuch & E. Giacobino. *Optical bistability in semiconductor microcavities*. Physical Review A, vol. 69, no. 2, page 023809, February 2004.

[Baas 04b] A. Baas, J.-Ph. Karr, M. Romanelli, A. Bramati & E. Giacobino. *Optical bistability in semiconductor microcavities in the nondegenerate parametric oscillation regime: Analogy with the optical parametric oscillator*. Physical Review B, vol. 70, no. 16, page 161307, October 2004.

[Baas 08] A. Baas, K. G. Lagoudakis, M. Richard, R. André, Le Si Dang & B. Deveaud-Plédran. *Synchronized and Desynchronized Phases of Exciton-Polariton Condensates in the Presence of Disorder*. Phys. Rev. Lett., vol. 100, no. 17, page 170401, 2008.

[Bajoni 07a] D. Bajoni, E. Peter, P. Senellart, J. L. Smirr, I. Sagnes, A. Lemaître & J. Bloch. *Polariton parametric luminescence in a single micropillar*. Appl. Phys. Lett., vol. 90, no. 5, page 051107, 2007.

[Bajoni 07b] D. Bajoni, P. Senellart, E. Peter, J. L. Smirr, I. Sagnes, A. Lemaître & J. Bloch. *Parametric polariton scattering in single micropillar microcavities*. AIP Conference Proceedings, vol. 893, no. 1, pages 1143–1144, 2007.

[Bajoni 08a] Daniele Bajoni, Elizaveta Semenova, Aristide Lemaître, Sophie Bouchoule, Esther Wertz, Pascale Senellart, Sylvain Barbay, Robert Kuszelewicz & Jacqueline Bloch. *Optical Bistability in a GaAs-Based Polariton Diode*. Physical Review Letters, vol. 101, no. 26, page 266402, 2008.

[Bajoni 08b] Daniele Bajoni, Pascale Senellart, Esther Wertz, Isabelle Sagnes, Audrey Miard, Aristide Lemaître & Jacqueline Bloch. *Polariton Laser Using Single Micropillar GaAs-GaAlAs Semiconductor Cavities*. Physical Review Letters, vol. 100, no. 4, page 047401, 2008.

[Balili 06] R. B. Balili, D. W. Snoke, L. Pfeiffer & K. West. *Actively tuned and spatially trapped polaritons*. Applied Physics Letters, vol. 88, no. 3, page 031110, 2006.

[Balili 07] R. Balili, V. Hartwell, D. Snoke, L. Pfeiffer & K. West. *Bose-Einstein Condensation of Microcavity Polaritons in a Trap*. Science, vol. 316, no. 5827, pages 1007–1010, 2007.

[Balili 09] R. Balili, B. Nelsen, D. W. Snoke, L. Pfeiffer & K. West. *Role of the stress trap in the polariton quasiequilibrium condensation in GaAs microcavities*. Phys. Rev. B, vol. 79, no. 7, page 075319, Feb 2009.

[Baumberg 08] J. J. Baumberg, A. V. Kavokin, S. Christopoulos, A. J. D. Grundy, R. Butté, G. Christmann, D. D. Solnyshkov, G. Malpuech, G. Baldassarri Höger von Högersthal, E. Feltin, J.-F. Carlin & N. Grandjean. *Spontaneous Polarization Buildup in a Room-Temperature Polariton Laser*. Physical Review Letters, vol. 101, no. 13, page 136409, 2008.

[Bezrukov 09] Sergey M. Bezrukov & Laszlo B. Kish. *Deterministic multivalued logic scheme for information processing and routing in the brain*. Physics Letters A, vol. 373, no. 27-28, pages 2338–2342, 2009.

[Bloch 98a] J. Bloch, F. Boeuf, J. M. Gérard, B. Legrand, J. Y. Marzin, R. Planel, V. Thierry-Mieg & E. Costard. *Strong and weak coupling regime in pillar semiconductor microcavities*. Physica E: Low-dimensional Systems and Nanostructures, vol. 2, no. 1-4, pages 915–919, 1998.

[Bloch 98b] J. Bloch, T. Freixanet, J. Y. Marzin, V. Thierry-Mieg & R. Planel. *Giant Rabi splitting in a microcavity containing distributed quantum wells*. Applied Physics Letters, vol. 73, no. 12, pages 1694–1696, 1998.

[Bloch 02] J. Bloch, B. Sermage, C. Jacquot, P. Senellart & V. Thierry-Mieg. *Time-Resolved Measurement of Stimulated Polariton Relaxation*. physica status solidi (a), vol. 190, no. 3, pages 827–831, 2002.

[Boeuf 00] F. Boeuf, R. André, R. Romestain, Le Si Dang, E. Péronne, J. F. Lampin, D. Hulin & A. Alexandrou. *Evidence of po-*

lariton stimulation in semiconductor microcavities. Physical Review B, vol. 62, no. 4, page R2279, 2000.

[Borri 99] P. Borri, W. Langbein, J. M. Hvam & F. Martelli. *Binding energy and dephasing of biexcitons in In0.18Ga0.82As/GaAs single quantum wells.* Physical Review B, vol. 60, no. 7, page 4505, 1999.

[Borri 00] P. Borri, W. Langbein, U. Woggon, J. R. Jensen & J. M. Hvam. *Biexcitons or bipolaritons in a semiconductor microcavity.* Physical Review B, vol. 62, no. 12, page R7763, 2000.

[Butté 02] R. Butté, G. Delalleau, A. I. Tartakovskii, M. S. Skolnick, V. N. Astratov, J. J. Baumberg, G. Malpuech, A. Di Carlo, A. V. Kavokin & J. S. Roberts. *Transition from strong to weak coupling and the onset of lasing in semiconductor microcavities.* Phys. Rev. B, vol. 65, no. 20, page 205310, 2002.

[Butté 02] R. Butté, G. Delalleau, A. I. Tartakovskii, M. S. Skolnick, V. N. Astratov, J. J. Baumberg, G. Malpuech, A. Di Carlo, A. V. Kavokin & J. S. Roberts. *Transition from strong to weak coupling and the onset of lasing in semiconductor microcavities.* Physical Review B, vol. 65, no. 20, page 205310, April 2002.

[Cao 97] H. Cao, S. Pau, J. M. Jacobson, G. Björk, Y. Yamamoto & A. Imamoglu. *Transition from a microcavity exciton polariton to a photon laser.* Physical Review A, vol. 55, no. 6, page 4632, 1997.

[Cao 04] Huy Thien Cao, T. D. Doan, D. B. Tran Thoai & H. Haug. *Condensation kinetics of cavity polaritons interacting with a thermal phonon bath.* Phys. Rev. B, vol. 69, no. 24, page 245325, Jun 2004.

[Carusotto 04] Iacopo Carusotto & Cristiano Ciuti. *Probing Microcavity Polariton Superfluidity through Resonant Rayleigh Scattering.* Physical Review Letters, vol. 93, no. 16, page 166401, October 2004.

[Carusotto 05] Iacopo Carusotto & Cristiano Ciuti. *Spontaneous microcavity-polariton coherence across the parametric threshold: Quantum Monte Carlo studies.* Physical Review B, vol. 72, no. 12, page 125335, 2005.

[Carusotto 10] Iacopo Carusotto. *Sorting superfluidity from Bose-Einstein condensation in atomic gases.* Physics, vol. 3, page 5, Jan 2010.

[Cavigli 05] Lucia Cavigli & Massimo Gurioli. *Optical bistability and laserlike emission in a semiconductor microcavity.* Physical Review B, vol. 71, no. 3, page 035317, 2005.

[Cecchi 82] S. Cecchi, G. Giusfredi, E. Petriella & P. Salieri. *Observation of optical tristability in sodium vapors.* Physical Review Letters, vol. 49, no. 26, pages 1928–1931, 1982.

[Cerna 10] R. Cerna, T. K. Paraïso, Y. Léger, M. Wouters, F. Morier-Genoud, M. T. Portella-Oberli & B. Deveaud-Plédran. *Spatial dynamics of confined semiconductor microcavity polaritons.* Physical Review B, vol. 81, no. 11, page 113306, March 2010.

[Chattopadhyay 09] Tanay Chattopadhyay, Jitendra Nath Roy & Ajoy Kumar Chakraborty. *Polarization encoded all-optical quaternary R-S flip-flop using binary latch.* Optics Communications, vol. 282, no. 7, pages 1287–1293, April 2009.

[Christmann 08] Gabriel Christmann, Raphaël Butté, Eric Feltin, Jean-François Carlin & Nicolas Grandjean. *Room temperature polariton lasing in a GaN/AlGaN multiple quantum well microcavity.* Applied Physics Letters, vol. 93, no. 5, page 051102, 2008.

[Christopoulos 07] S. Christopoulos, G. Baldassarri Höger von Högersthal, A. J. D. Grundy, P. G. Lagoudakis, A. V. Kavokin, J. J. Baumberg, G. Christmann, R. Butté, E. Feltin, J.-F. Carlin & N. Grandjean. *Room-Temperature Polariton Lasing in Semiconductor Microcavities.* Phys. Rev. Lett., vol. 98, no. 12, page 126405, Mar 2007.

[Ciuti 98] C. Ciuti, V. Savona, C. Piermarocchi, A. Quattropani & P. Schwendimann. *Threshold behavior in the collision broadening of microcavity polaritons.* Physical Review B, vol. 58, no. 16, page R10123, October 1998.

[Ciuti 00a] C. Ciuti, P. Schwendimann, B. Deveaud & A. Quattropani. *Giant Angle-Resonant Polariton Amplification.* physica status solidi (b), vol. 221, no. 1, pages 111–114, 2000.

[Ciuti 00b] C. Ciuti, P. Schwendimann, B. Deveaud & A. Quattropani. *Theory of the angle-resonant polariton amplifier.* Physical Review B, vol. 62, no. 8, page R4825, 2000.

[Ciuti 01] C. Ciuti. *Nonlinear dynamics of excitons and photons in semiconductor planar structures.* PhD thesis, Ecole polytechnique fédérale de Lausanne EPFL, June 2001.

[Ciuti 05] Cristiano Ciuti & Iacopo Carusotto. *Quantum fluid effects and parametric instabilities in microcavities*. physica status solidi (b), vol. 242, no. 11, pages 2224–2245, 2005.

[Cohen-Tanoudji 97] C. Cohen-Tanoudji. Mécanique quantique i. Hermann, October 1997.

[Combescot 09] M. Combescot & O. Betbeder-Matibet. *Biexciton oscillator strength*. Physical Review B, vol. 80, no. 20, page 205313, November 2009.

[Cooper 10] Nigel R. Cooper & Zoran Hadzibabic. *Measuring the Superfluid Fraction of an Ultracold Atomic Gas*. Phys. Rev. Lett., vol. 104, no. 3, page 030401, Jan 2010.

[Daif 06] O. El Daif, A. Baas, T. Guillet, J.-P. Brantut, R. Idrissi Kaitouni, J. L. Staehli, F. Morier-Genoud & B. Deveaud. *Polariton quantum boxes in semiconductor microcavities*. Applied Physics Letters, vol. 88, no. 6, page 061105, 2006.

[Dang 98] Le Si Dang, D. Heger, R. André, F. Boeuf & R. Romestain. *Stimulation of Polariton Photoluminescence in Semiconductor Microcavity*. Physical Review Letters, vol. 81, no. 18, page 3920, November 1998.

[Dasbach 01] G. Dasbach, M. Schwab, M. Bayer & A. Forchel. *Parametric polariton scattering in microresonators with three-dimensional optical confinement*. Physical Review B, vol. 64, no. 20, page 201309, October 2001.

[Dasbach 02] G. Dasbach, M. Schwab, M. Bayer, D.N. Krizhanovskii & A. Forchel. *Tailoring the polariton dispersion by optical confinement: Access to a manifold of elastic polariton pair scattering channels*. Physical Review B, vol. 66, no. 20, page 201201, November 2002.

[Davis 95] K. B. Davis, M. -O. Mewes, M. R. Andrews, N. J. van Druten, D. S. Durfee, D. M. Kurn & W. Ketterle. *Bose-Einstein Condensation in a Gas of Sodium Atoms*. Physical Review Letters, vol. 75, no. 22, page 3969, November 1995.

[del Valle 09] E. del Valle, D. Sanvitto, A. Amo, F. P. Laussy, R. André, C. Tejedor & L. Viña. *Dynamics of the Formation and Decay of Coherence in a Polariton Condensate*. Phys. Rev. Lett., vol. 103, no. 9, page 096404, Aug 2009.

[Deng 06] Hui Deng, David Press, Stephan Gotzinger, Glenn S. Solomon, Rudolf Hey, Klaus H. Ploog & Yoshihisa Yamamoto. *Quantum Degenerate Exciton-Polaritons in Thermal Equilibrium*. Phys. Rev. Lett., vol. 97, no. 14, page 146402, 2006.

[Deng 07] Hui Deng, Glenn S. Solomon, Rudolf Hey, Klaus H. Ploog & Yoshihisa Yamamoto. *Spatial Coherence of a Polariton Condensate*. Physical Review Letters, vol. 99, no. 12, page 126403, 2007.

[Deveaud 91] B. Deveaud, F. Clérot, N. Roy, K. Satzke, B. Sermage & D. S. Katzer. *Enhanced radiative recombination of free excitons in GaAs quantum wells*. Phys. Rev. Lett., vol. 67, no. 17, pages 2355–2358, Oct 1991.

[Dingle 74] R. Dingle, W. Wiegmann & C. H. Henry. *Quantum States of Confined Carriers in Very Thin AlxGa1-xAs-GaAs-AlxGa1-xAs Heterostructures*. Physical Review Letters, vol. 33, no. 14, page 827, 1974.

[El Daif 07] Ounsi El Daif. *0D microcavity polaritons : trapping light-matter quasiparticles*. PhD thesis, Ecole polytechnique fédérale de Lausanne EPFL, May 2007.

[El Daif 08] Ounsi El Daif, Gaël Nardin, Taofiq K. Paraïso, Augustin Baas, Maxime Richard, J.-P. Brantut, Thierry Guillet, Francois Morier-Genoud & Benoit Deveaud-Plédran. *Nonlinear relaxation of zero-dimension-trapped microcavity polaritons*. Applied Physics Letters, vol. 92, no. 8, page 081910, 2008.

[Erland 01] J. Erland, V. Mizeikis, W. Langbein, J. Jensen & J. Hvam. *Stimulated Secondary Emission from Semiconductor Microcavities*. Physical Review Letters, vol. 86, no. 25, pages 5791–5794, 2001.

[Fan 97] Xudong Fan, Hailin Wang, H. Q. Hou & B. E. Hammons. *Laser emission from semiconductor microcavities: The role of cavity polaritons*. Physical Review A, vol. 56, no. 4, page 3233, October 1997.

[Fano 56] U. Fano. *Atomic Theory of Electromagnetic Interactions in Dense Materials*. Physical Review, vol. 103, no. 5, page 1202, 1956.

[Frenkel 31] J. Frenkel. *On the Transformation of light into Heat in Solids. I.* Physical Review, vol. 37, no. 1, page 17, 1931.

[Giacobino 85] E. Giacobino. *Tristability and bifurcations in sodium vapor*. Optics Communications, vol. 56, no. 4, pages 249 – 254, 1985.

[Gibbs 85] H. M. Gibbs. Optical bistability: Controlling light with light. Academic, New York, 1985.

[Gippius 04] N. A. Gippius, S. G. Tikhodeev, V. D. Kulakovskii, D. N. Krizhanovskii & A. I. Tartakovskii. *Nonlinear dynamics of polariton scattering in semiconductor microcavity: Bistability vs. stimulated scattering.* EPL (Europhysics Letters), vol. 67, no. 6, pages 997–1003, 2004.

[Gippius 07] N. A. Gippius, I. A. Shelykh, D. D. Solnyshkov, S. S. Gavrilov, Yuri G. Rubo, A. V. Kavokin, S. G. Tikhodeev & G. Malpuech. *Polarization Multistability of Cavity Polaritons.* Physical Review Letters, vol. 98, no. 23, page 236401, 2007.

[Giusfredi 85] G. Giusfredi, P. Salieri, S. Cecchi & F. T. Arecchi. *Multistability in a sodium filled Fabry-Perot: D1 line, hyperfine and Zeeman pumping.* Optics Communications, vol. 54, no. 1, pages 39 – 46, 1985.

[Griffin 95] A. Griffin, D. W. Snoke & S. Stringari. Bose einstein condensation. Cambridge Univ. Press, Cambridge, 1995.

[Guillaume 70] C. Benoit a la Guillaume, A. Bonnot & J. M. Debever. *Luminescence from Polaritons.* Physical Review Letters, vol. 24, no. 22, page 1235, 1970.

[Gérard 96] J. M. Gérard, D. Barrier, J. Y. Marzin, R. Kuszelewicz, L. Manin, E. Costard, V. Thierry-Mieg & T. Rivera. *Quantum boxes as active probes for photonic microstructures: The pillar microcavity case.* Applied Physics Letters, vol. 69, no. 4, page 449, 1996.

[Gérard 98] J. M. Gérard, B. Sermage, B. Gayral, B. Legrand, E. Costard & V. Thierry-Mieg. *Enhanced Spontaneous Emission by Quantum Boxes in a Monolithic Optical Microcavity.* Physical Review Letters, vol. 81, no. 5, page 1110, 1998.

[Haelterman 94] M. Haelterman, S. Trillo & S. Wabnitz. *Polarization multistability and instability in a nonlinear dispersive ring cavity.* Journal of the Optical Society of America B, vol. 11, no. 3, pages 446–456, March 1994.

[Haug 85] H. Haug & S. Schmitt-Rink. *Basic mechanisms of the optical nonlinearities of semiconductors near the band edge.* J. Opt. Soc. Am. B, vol. 2, no. 7, pages 1135–1142, 1985.

[Hennessy 07] K. Hennessy, A. Badolato, M. Winger, D. Gerace, M. Atature, S. Gulde, S. Falt, E. L. Hu & A. Imamoglu. *Quantum nature of a strongly coupled single quantum dot-cavity system.* Nature, vol. 445, no. 7130, pages 896–899, February 2007.

[Hermann 85] C. Hermann, G. Lampel & V.I. Safarov. *Optical pumping in semiconductors*. Annales de Physique, vol. 10, no. 6, page 22 pages, 1985.

[Holland 96] M. Holland, K. Burnett, C. Gardiner, J. I. Cirac & P. Zoller. *Theory of an atom laser*. Physical Review A, vol. 54, no. 3, page R1757, 1996.

[Honold 89] A. Honold, L. Schultheis, J. Kuhl & C. W. Tu. *Collision broadening of two-dimensional excitons in a GaAs single quantum well*. Phys. Rev. B, vol. 40, no. 9, pages 6442–6445, Sep 1989.

[Hopfield 58] J. J. Hopfield. *Theory of the Contribution of Excitons to the Complex Dielectric Constant of Crystals*. Phys. Rev., vol. 112, no. 5, pages 1555–1567, Dec 1958.

[Houdré 94] R. Houdré, C. Weisbuch, R. P. Stanley, U. Oesterle, P. Pellandini & M. Ilegems. *Measurement of Cavity-Polariton Dispersion Curve from Angle-Resolved Photoluminescence Experiments*. Physical Review Letters, vol. 73, no. 15, page 2043, October 1994.

[Houdré 95] R. Houdré, J. L. Gibernon, P. Pellandini, R. P. Stanley, U. Oesterle, C. Weisbuch, J. O'Gorman, B. Roycroft & M. Ilegems. *Saturation of the strong-coupling regime in a semiconductor microcavity: Free-carrier bleaching of cavity polaritons*. Physical Review B, vol. 52, no. 11, page 7810, 1995.

[Houdré 00] R. Houdré, C. Weisbuch, R. P. Stanley, U. Oesterle & M. Ilegems. *Nonlinear Emission of Semiconductor Microcavities in the Strong Coupling Regime*. Physical Review Letters, vol. 85, no. 13, page 2793, 2000.

[Houdré 05] R. Houdré. *Early stages of continuous wave experiments on cavity-polaritons*. physica status solidi (b), vol. 242, no. 11, pages 2167–2196, 2005.

[Huang 90] Daming Huang, Jen-Inn Chyi & Hadis Morkoç. *Carrier effects on the excitonic absorption in GaAs quantum-well structures: Phase-space filling*. Phys. Rev. B, vol. 42, no. 8, pages 5147–5153, Sep 1990.

[Huang 00] R. Huang, F. Tassone & Y. Yamamoto. *Experimental evidence of stimulated scattering of excitons into microcavity polaritons*. Physical Review B, vol. 61, no. 12, page R7854, March 2000.

[Imamoglu 96a] A. Imamoglu & R. J. Ram. *Quantum dynamics of exciton lasers.* Physics Letters A, vol. 214, no. 3-4, pages 193–198, May 1996.

[Imamoglu 96b] A. Imamoglu, R. J. Ram, S. Pau & Y. Yamamoto. *Nonequilibrium condensates and lasers without inversion: Exciton-polariton lasers.* Physical Review A, vol. 53, no. 6, page 4250, 1996.

[Jaynes 62] E. T. Jaynes & F. W. Cummings. *Comparison of quantum and semiclassical radiation theories with application to the atom beam maser.* Proceedings of the IEEE, vol. 51, no. 89, 1962.

[Jensen 00] J. R. Jensen, P. Borri, W. Langbein & J. M. Hvam. *Ultranarrow polaritons in a semiconductor microcavity.* Applied Physics Letters, vol. 76, no. 22, pages 3262–3264, May 2000.

[Jonsson 99] Fredrik Jonsson & Christos Flytzanis. *Polarization State Controlled Multistability of a Nonlinear Magneto-optic Cavity.* Phys. Rev. Lett., vol. 82, no. 7, pages 1426–1429, Feb 1999.

[Kaitouni 06] R. Idrissi Kaitouni, O. El Daif, A. Baas, M. Richard, T. Paraiso, P. Lugan, T. Guillet, F. Morier-Genoud, J. D. Ganière, J. L. Staehli, V. Savona & B. Deveaud. *Engineering the spatial confinement of exciton polaritons in semiconductors.* Physical Review B (Condensed Matter and Materials Physics), vol. 74, no. 15, page 155311, 2006.

[Kappei 05] L. Kappei, J. Szczytko, F. Morier-Genoud & B. Deveaud. *Direct Observation of the Mott Transition in an Optically Excited Semiconductor Quantum Well.* Phys. Rev. Lett., vol. 94, no. 14, page 147403, Apr 2005.

[Karr 01] Jean-Philippe Karr. *Effets non linéaires et quantiques dans les microcavités semi-conductrices.* PhD thesis, Laboratoire Kastler Brossel (LKB (Jussieu)) CNRS : UMR8552 – Université Pierre et Marie Curie - Paris VI – Ecole Normale Supérieure de Paris - ENS Paris, December 2001.

[Karr 04] J. Ph. Karr, A. Baas, R. Houdré & E. Giacobino. *Squeezing in semiconductor microcavities in the strong-coupling regime.* Physical Review A, vol. 69, no. 3, page 031802, March 2004.

[Kasprzak 06] J. Kasprzak, M. Richard, S. Kundermann, A. Baas, P. Jeambrun, J. M. J. Keeling, F. M. Marchetti, M. H.

Szymanska, R. André, J. L. Staehli, V. Savona, P. B. Littlewood, B. Deveaud & Le Si Dang. *Bose-Einstein condensation of exciton polaritons*. Nature, vol. 443, pages 409–414, Sep 2006.

[Kasprzak 08] J. Kasprzak, D. D. Solnyshkov, R. André, Le Si Dang & G. Malpuech. *Formation of an Exciton Polariton Condensate: Thermodynamic versus Kinetic Regimes*. Phys. Rev. Lett., vol. 101, no. 14, page 146404, Oct 2008.

[Kavokin 03] A. Kavokin, P. G. Lagoudakis, G. Malpuech & J. J. Baumberg. *Polarization rotation in parametric scattering of polaritons in semiconductor microcavities*. Physical Review B, vol. 67, no. 19, page 195321, May 2003.

[Kavokin 05] Alexey Kavokin, Guillaume Malpuech & Mikhail Glazov. *Optical Spin Hall Effect*. Physical Review Letters, vol. 95, no. 13, page 136601, 2005.

[Keller 93] U. Keller, G. R. Jacobovitz-Veselka, J. E. Cunningham, W. Y. Jan, B. Tell, K. F. Brown-Goebeler & G. Livescu. *Microcavity enhanced vertical-cavity light-emitting diodes*. Applied Physics Letters, vol. 62, no. 24, pages 3085–3087, 1993.

[Khitrova 99] G. Khitrova, H. M. Gibbs, F. Jahnke, M. Kira & S. W. Koch. *Nonlinear optics of normal-mode-coupling semiconductor microcavities*. Reviews of Modern Physics, vol. 71, no. 5, page 1591, October 1999.

[Kira 97] M. Kira, F. Jahnke, S. W. Koch, J. D. Berger, D. V. Wick, T. R. Nelson, G. Khitrova & H. M. Gibbs. *Quantum Theory of Nonlinear Semiconductor Microcavity Luminescence Explaining "Boser" Experiments*. Physical Review Letters, vol. 79, no. 25, page 5170, December 1997.

[Kittel 04] Charles Kittel. Introduction to solid state physics. Wiley, 8 edition, November 2004.

[Kundermann 03] S. Kundermann, M. Saba, C. Ciuti, T. Guillet, U. Oesterle, J. L. Staehli & B. Deveaud. *Coherent Control of Polariton Parametric Scattering in Semiconductor Microcavities*. Phys. Rev. Lett., vol. 91, no. 10, page 107402, Sep 2003.

[Kuwata-Gonokami 97] Makoto Kuwata-Gonokami, Shin Inouye, Hidekatsu Suzuura, Masayuki Shirane, Ryo Shimano, Takao Someya & Hiroyuki Sakaki. *Parametric Scattering of Cavity Polaritons*. Physical Review Letters, vol. 79, no. 7, page 1341, 1997.

[Kwong 01] N. H. Kwong, R. Takayama, I. Rumyantsev, M. Kuwata-Gonokami & R. Binder. *Third-order exciton-correlation and nonlinear cavity-polariton effects in semiconductor microcavities.* Physical Review B (Condensed Matter and Materials Physics), vol. 64, no. 4, page 045316, 2001.

[Lagoudakis 02] P. G. Lagoudakis, P. G. Savvidis, J. J. Baumberg, D. M. Whittaker, P. R. Eastham, M. S. Skolnick & J. S. Roberts. *Stimulated spin dynamics of polaritons in semiconductor microcavities.* Physical Review B, vol. 65, no. 16, page 161310, April 2002.

[Lagoudakis 08] K. G. Lagoudakis, M. Wouters, M. Richard, A. Baas, I. Carusotto, R. Andre, Le Si Dang & B. Deveaud-Pledran. *Quantized vortices in an exciton-polariton condensate.* Nat Phys, vol. 4, no. 9, pages 706–710, 2008.

[Lagoudakis 09] K. G. Lagoudakis, T. Ostatnicky, A. V. Kavokin, Y. G. Rubo, R. Andre & B. Deveaud-Pledran. *Observation of Half-Quantum Vortices in an Exciton-Polariton Condensate.* Science, vol. 326, no. 5955, pages 974–976, 2009.

[Langbein 02] W. Langbein & J. M. Hvam. *Elastic Scattering Dynamics of Cavity Polaritons: Evidence for Time-Energy Uncertainty and Polariton Localization.* Phys. Rev. Lett., vol. 88, no. 4, page 047401, 2002.

[Langbein 04] Wolfgang Langbein. *Spontaneous parametric scattering of microcavity polaritons in momentum space.* Physical Review B, vol. 70, no. 20, page 205301, November 2004.

[Langbein 07] W. Langbein, I. Shelykh, D. Solnyshkov, G. Malpuech, Yu. Rubo & A. Kavokin. *Polarization beats in ballistic propagation of exciton-polaritons in microcavities.* Physical Review B, vol. 75, no. 7, page 075323, February 2007.

[Leyder 07a] C. Leyder, T. C. H. Liew, A. V. Kavokin, I. A. Shelykh, M. Romanelli, J. Ph. Karr, E. Giacobino & A. Bramati. *Interference of Coherent Polariton Beams in Microcavities: Polarization-Controlled Optical Gates.* Physical Review Letters, vol. 99, no. 19, page 196402, November 2007.

[Leyder 07b] C. Leyder, M. Romanelli, J. Ph. Karr, E. Giacobino, T. C. H. Liew, M. M. Glazov, A. V. Kavokin, G. Malpuech & A. Bramati. *Observation of the optical spin Hall effect.* Nat Phys, vol. 3, no. 9, pages 628–631, 2007.

[Leyronas 01] X. Leyronas & M. Combescot. *Quantum wells, wires and dots with finite barrier: analytical expressions for the bound*

states. Solid State Communications, vol. 119, no. 10-11, pages 631–635, August 2001.

[Liew 07] T. C. H. Liew, A. V. Kavokin & I. A. Shelykh. *Excitation of vortices in semiconductor microcavities*. Physical Review B, vol. 75, no. 24, page 241301, 2007.

[Liew 08a] T. C. H. Liew, A. V. Kavokin & I. A. Shelykh. *Optical Circuits Based on Polariton Neurons in Semiconductor Microcavities*. Physical Review Letters, vol. 101, no. 1, page 016402, 2008.

[Liew 08b] T. C. H. Liew, Yuri G. Rubo & A. V. Kavokin. *Generation and Dynamics of Vortex Lattices in Coherent Exciton-Polariton Fields*. Physical Review Letters, vol. 101, no. 18, page 187401, October 2008.

[Liew 09a] T. C. H. Liew, C. Leyder, A. V. Kavokin, A. Amo, J. Lefrère, E. Giacobino & A. Bramati. *Interplay between weak localization of exciton-polaritons and the optical spin Hall effect*. Physical Review B, vol. 79, no. 12, page 125314, March 2009.

[Liew 09b] T. C. H. Liew & I. A. Shelykh. *Polarization phenomena in resonantly pumped disordered semiconductor microcavities*. Physical Review B (Condensed Matter and Materials Physics), vol. 80, no. 16, page 161303, 2009.

[Love 08] A. P. D. Love, D. N. Krizhanovskii, D. M. Whittaker, R. Bouchekioua, D. Sanvitto, S. Al Rizeiqi, R. Bradley, M. S. Skolnick, P. R. Eastham, R. André & Le Si Dang. *Intrinsic Decoherence Mechanisms in the Microcavity Polariton Condensate*. Phys. Rev. Lett., vol. 101, no. 6, page 067404, Aug 2008.

[Lvovsky 09] Alexander I. Lvovsky, Barry C. Sanders & Wolfgang Tittel. *Optical quantum memory*. Nat Photon, vol. 3, no. 12, pages 706–714, December 2009.

[Maialle 93] M. Z. Maialle, E. A. de Andrada e Silva & L. J. Sham. *Exciton spin dynamics in quantum wells*. Physical Review B, vol. 47, no. 23, page 15776, 1993.

[Mannarini 06] G. Mannarini & R. Zimmermann. *Near-field spectra of quantum well excitons with non-Markovian phonon scattering*. Physical Review B, vol. 73, no. 11, page 115325, March 2006.

[Marchetti 08] F. M. Marchetti, M. H. Szymanska, J. M. J. Keeling, J. Kasprzak, R. Andre, P. B. Littlewood & Le Si Dang.

Phase diagram for condensation of microcavity polaritons: From theory to practice. Phys. Rev. B, vol. 77, no. 23, page 235313, 2008.

[Martín 02] M. D. Martín, G. Aichmayr, L. Viña & R. André. *Polarization Control of the Nonlinear Emission of Semiconductor Microcavities.* Physical Review Letters, vol. 89, no. 7, page 077402, 2002.

[Messin 01] G. Messin, J. Ph. Karr, A. Baas, G. Khitrova, R. Houdré, R. P. Stanley, U. Oesterle & E. Giacobino. *Parametric Polariton Amplification in Semiconductor Microcavities.* Physical Review Letters, vol. 87, no. 12, page 127403, 2001.

[Miller 84] D. A. B. Miller, D. S. Chemla, T. C. Damen, A. C. Gossard, W. Wiegmann, T. H. Wood & C. A. Burrus. *Novel hybrid optically bistable switch: The quantum well self-electro-optic effect device.* Applied Physics Letters, vol. 45, no. 1, pages 13–15, 1984.

[Nardin 09a] G. Nardin, K. G. Lagoudakis, M. Wouters, M. Richard, A. Baas, R. André, Le Si Dang, B. Pietka & B. Deveaud-Plédran. *Dynamics of Long-Range Ordering in an Exciton-Polariton Condensate.* Phys. Rev. Lett., vol. 103, no. 25, page 256402, Dec 2009.

[Nardin 09b] Gaël Nardin, Taofiq K. Paraïso, Roland Cerna, Barbara Pietka, Yoan Léger, Ounsi El Daif, François Morier-Genoud & Benoît Deveaud-Plédran. *Probability density optical tomography of confined quasiparticles in a semiconductor microcavity.* Applied Physics Letters, vol. 94, no. 18, page 181103, 2009.

[Nardin 10] Gaël Nardin, Roland Cerna, Taofiq K. Paraïso, Barbara Pietka, Yoan Léger, Ounsi El Daif, François Morier-Genoud & Benoît Deveaud-Plédran. *Probability density tomography of microcavity polaritons confined in cylindrical traps of various sizes.* Superlattices and Microstructures, vol. 47, no. 1, pages 207–212, 2010.

[Negoita 99] V. Negoita, D. W. Snoke & K. Eberl. *Stretching quantum wells: A method for trapping free carriers in GaAs heterostructures.* Applied Physics Letters, vol. 75, no. 14, page 2059, 1999.

[Nelsen 09] B. Nelsen, R. Balili, D. W. Snoke, L. Pfeiffer & K. West. *Lasing and polariton condensation: Two distinct transitions in GaAs microcavities with stress traps.* Journal of Applied Physics, vol. 105, no. 12, page 122414, 2009.

[Paraïso 09] T. K. Paraïso, D. Sarchi, G. Nardin, R. Cerna, Y. Leger, B. Pietka, M. Richard, O. El Daif, F. Morier-Genoud, V. Savona & B. Deveaud-Plédran. *Enhancement of microcavity polariton relaxation under confinement.* Phys. Rev. B, vol. 79, no. 4, page 045319, Jan 2009.

[Pau 96] Stanley Pau, Hui Cao, Joseph Jacobson, Gunnar Björk, Yoshihisa Yamamoto & Atac Imamoglu. *Observation of a laserlike transition in a microcavity exciton polariton system.* Physical Review A, vol. 54, no. 3, page R1789, 1996.

[Perrin 05] M. Perrin, P. Senellart, A. Lemaitre & J. Bloch. *Polariton relaxation in semiconductor microcavities: Efficiency of electron-polariton scattering.* Phys. Rev. B, vol. 72, no. 7, page 075340, 2005.

[Porras 02a] D. Porras, C. Ciuti, J. J. Baumberg & C. Tejedor. *Polariton dynamics and Bose-Einstein condensation in semiconductor microcavities.* Phys. Rev. B, vol. 66, no. 8, page 085304, Aug 2002.

[Porras 02b] D. Porras, C. Ciuti, J. J. Baumberg & C. Tejedor. *Polariton dynamics and Bose-Einstein condensation in semiconductor microcavities.* Physical Review B, vol. 66, no. 8, page 085304, 2002.

[Raizen 89] M. G. Raizen, R. J. Thompson, R. J. Brecha, H. J. Kimble & H. J. Carmichael. *Normal-mode splitting and linewidth averaging for two-state atoms in an optical cavity.* Physical Review Letters, vol. 63, no. 3, page 240, 1989.

[Reithmaier 04] J. P. Reithmaier, G. Sek, A. Loffler, C. Hofmann, S. Kuhn, S. Reitzenstein, L. V. Keldysh, V. D. Kulakovskii, T. L. Reinecke & A. Forchel. *Strong coupling in a single quantum dot-semiconductor microcavity system.* Nature, vol. 432, no. 7014, pages 197–200, November 2004.

[Renucci 05] P. Renucci, T. Amand, X. Marie, P. Senellart, J. Bloch, B. Sermage & K.V. Kavokin. *Microcavity polariton spin quantum beat without a magnetic field: A manifestation of Coulomb exchange in dense and polarized polariton systems.* Physical Review B (Condensed Matter and Materials Physics), vol. 72, no. 7, page 075317, 2005.

[Richard 04] M. Richard. *Quasi-condensation de polaritons sous excitation incohérente dans les microcavités II-VI à base de CdTe.* PhD thesis, Laboratoire de Spectrométrie Physique – CNRS UMR 5588 – Université Joseph Fourier – Grenoble 1, November 2004.

[Richard 05] Maxime Richard, Jacek Kasprzak, Robert Romestain, Régis André & Le Si Dang. *Spontaneous Coherent Phase Transition of Polaritons in CdTe Microcavities*. Physical Review Letters, vol. 94, no. 18, page 187401, May 2005.

[Romanelli 07] M. Romanelli, C. Leyder, J. Ph. Karr, E. Giacobino & A. Bramati. *Four Wave Mixing Oscillation in a Semiconductor Microcavity: Generation of Two Correlated Polariton Populations*. Physical Review Letters, vol. 98, no. 10, page 106401, March 2007.

[Rubo 07] Yuri G. Rubo. *Half Vortices in Exciton Polariton Condensates*. Physical Review Letters, vol. 99, no. 10, page 106401, 2007.

[Saba 00] M. Saba, F. Quochi, C. Ciuti, U. Oesterle, J. L. Staehli, B. Deveaud, G. Bongiovanni & A. Mura. *Crossover from Exciton to Biexciton Polaritons in Semiconductor Microcavities*. Physical Review Letters, vol. 85, no. 2, page 385, 2000.

[Saba 01] M. Saba, C. Ciuti, J. Bloch, V. Thierry-Mieg, R. Andre, Le Si Dang, S. Kundermann, A. Mura, G. Bongiovanni, J. L. Staehli & B. Deveaud. *High-temperature ultrafast polariton parametric amplification in semiconductor microcavities*. Nature, vol. 414, no. 6865, pages 731–735, December 2001.

[Saleh 91] Bahaa E.A. Saleh & Malvin Carl Teich. Fundamentals of photonics. John Wiley & Sons Inc, September 1991.

[Sanvitto 09] D. Sanvitto, A. Amo, L. Viña, R. André, D. Solnyshkov & G. Malpuech. *Exciton-polariton condensation in a natural two-dimensional trap*. Phys. Rev. B, vol. 80, no. 4, page 045301, Jul 2009.

[Sarchi 07] D. Sarchi & V. Savona. *Long-range order in the Bose-Einstein condensation of polaritons*. Phys. Rev. B, vol. 75, no. 11, page 115326, 2007.

[Sarchi 08a] D. Sarchi & V. Savona. *Spectrum and thermal fluctuations of a microcavity polariton Bose-Einstein condensate*. Phys. Rev. B, vol. 77, no. 4, page 045304, 2008.

[Sarchi 08b] Davide Sarchi, Iacopo Carusotto, Michiel Wouters & Vincenzo Savona. *Coherent dynamics and parametric instabilities of microcavity polaritons in double-well systems*. Physical Review B, vol. 77, no. 12, page 125324, March 2008.

[Savona 99] Vincenzo Savona, Carlo Piermarocchi, Antonio Quattropani, Paolo Schwendimann & Francesco Tassone. *Optical properties of microcavity polaritons*. Phase Transitions: A Multinational Journal, vol. 68, no. 1, page 169, 1999.

[Savona 07] Vincenzo Savona. *Effect of interface disorder on quantum well excitons and microcavity polaritons*. Journal of Physics: Condensed Matter, vol. 19, no. 29, page 295208 (23pp), 2007.

[Savvidis 00a] P. G. Savvidis, J. J. Baumberg, R. M. Stevenson, M. S. Skolnick, D. M. Whittaker & J. S. Roberts. *Angle-Resonant Stimulated Polariton Amplifier*. Physical Review Letters, vol. 84, no. 7, page 1547, February 2000.

[Savvidis 00b] P. G. Savvidis, J. J. Baumberg, R. M. Stevenson, M. S. Skolnick, D. M. Whittaker & J. S. Roberts. *Asymmetric angular emission in semiconductor microcavities*. Physical Review B, vol. 62, no. 20, page R13278, November 2000.

[Schafer 02] Wilfried Schafer & Martin Wegener. Semiconductor optics and transport phenomena. Springer-Verlag Berlin and Heidelberg GmbH & Co. K, March 2002.

[Sell 71] D. D. Sell, R. Dingle, S. E. Stokowski & J. V. DiLorenzo. *Observation of Polaritons in GaAs: A New Interpretation of the Free-Exciton Reflectance and Luminescence*. Physical Review Letters, vol. 27, no. 24, page 1644, December 1971.

[Senellart 99] P. Senellart & J. Bloch. *Nonlinear Emission of Microcavity Polaritons in the Low Density Regime*. Physical Review Letters, vol. 82, no. 6, page 1233, February 1999.

[Senellart 03] P. Senellart. *Polaritons de microcavité : relaxation spontanée et stimulée*. Annales de Physique, vol. 28, no. 4, page 180 pages, 2003.

[Sermage 79] Bernard Sermage & Guy Fishman. *Resonant Brillouin Scattering of Polaritons in ZnSe: Heavy and Light Excitons*. Physical Review Letters, vol. 43, no. 14, page 1043, October 1979.

[Shelykh 04] I. Shelykh, G. Malpuech, K. V. Kavokin, A. V. Kavokin & P. Bigenwald. *Spin dynamics of interacting exciton polaritons in microcavities*. Physical Review B, vol. 70, no. 11, page 115301, 2004.

[Shelykh 05] I. A. Shelykh, A.V. Kavokin & G. Malpuech. *Spin dynamics of exciton polaritons in microcavities*. physica status solidi (b), vol. 242, no. 11, pages 2271–2289, 2005.

[Shelykh 08] I. A. Shelykh, T. C. H. Liew & A. V. Kavokin. *Spin Rings in Semiconductor Microcavities*. Physical Review Letters, vol. 100, no. 11, page 116401, 2008.

[Singh 03] Jasprit Singh. Electronic and optoelectronic properties of semiconductor structures. Cambridge University Press, 2003.

[Smalyukh 10] Ivan I. Smalyukh, Yves Lansac, Noel A. Clark & Rahul P. Trivedi. *Three-dimensional structure and multistable optical switching of triple-twisted particle-like excitations in anisotropic fluids*. Nat Mater, vol. 9, no. 2, pages 139–145, February 2010.

[Solnyshkov 08] D. D. Solnyshkov, I. A. Shelykh, N. A. Gippius, A. V. Kavokin & G. Malpuech. *Dispersion of interacting spinor cavity polaritons out of thermal equilibrium*. Physical Review B (Condensed Matter and Materials Physics), vol. 77, no. 4, page 045314, 2008.

[Stanley 96] R. P. Stanley, R. Houdré, C. Weisbuch, U. Oesterle & M. Ilegems. *Cavity-polariton photoluminescence in semiconductor microcavities: Experimental evidence*. Phys. Rev. B, vol. 53, no. 16, pages 10995–11007, Apr 1996.

[Stanley 97] R. P. Stanley, S. Pau, U. Oesterle, R. Houdré & M. Ilegems. *Resonant photoluminescence of semiconductor microcavities: The role of acoustic phonons in polariton relaxation*. Physical Review B, vol. 55, no. 8, page R4867, February 1997.

[Steiglitz 01] Ken Steiglitz. *Multistable collision cycles of Manakov spatial solitons*. Physical Review E, vol. 63, no. 4, page 046607, March 2001.

[Stevenson 00] R. M. Stevenson, V. N. Astratov, M. S. Skolnick, D. M. Whittaker, M. Emam-Ismail, A. I. Tartakovskii, P. G. Savvidis, J. J. Baumberg & J. S. Roberts. *Continuous Wave Observation of Massive Polariton Redistribution by Stimulated Scattering in Semiconductor Microcavities*. Physical Review Letters, vol. 85, no. 17, page 3680, October 2000.

[Szymanska 06] M. H. Szymanska, J. Keeling & P. B. Littlewood. *Nonequilibrium Quantum Condensation in an Incoherently Pumped Dissipative System*. Phys. Rev. Lett., vol. 96, no. 23, page 230602, Jun 2006.

[Tartakovskii 99] A. I. Tartakovskii, V. D. Kulakovskii, D. N. Krizhanovskii, M. S. Skolnick, V. N. Astratov, A. Armitage & J. S. Roberts.

Nonlinearities in emission from the lower polariton branch of semiconductor microcavities. Physical Review B, vol. 60, no. 16, page R11293, October 1999.

[Tartakovskii 00] A. I. Tartakovskii, M. Emam-Ismail, R. M. Stevenson, M. S. Skolnick, V. N. Astratov, D. M. Whittaker, J. J. Baumberg & J. S. Roberts. *Relaxation bottleneck and its suppression in semiconductor microcavities*. Physical Review B, vol. 62, no. 4, page R2283, 2000.

[Tassone 90] F. Tassone, F. Bassani & L.C. Andreani. *Resonant and surface polaritons in quantum wells*. Il Nuovo Cimento D, vol. 12, no. 12, pages 1673–1687, December 1990.

[Tassone 97] F. Tassone, C. Piermarocchi, V. Savona, A. Quattropani & P. Schwendimann. *Bottleneck effects in the relaxation and photoluminescence of microcavity polaritons*. Physical Review B, vol. 56, no. 12, page 7554, 1997.

[Tredicucci 96] Alessandro Tredicucci, Yong Chen, Vittorio Pellegrini, Marco Börger & Franco Bassani. *Optical bistability of semiconductor microcavities in the strong-coupling regime*. Physical Review A, vol. 54, no. 4, page 3493, October 1996.

[Ulbrich 77] Rainer G. Ulbrich & Claude Weisbuch. *Resonant Brillouin Scattering of Excitonic Polaritons in Gallium Arsenide*. Physical Review Letters, vol. 38, no. 15, page 865, April 1977.

[Utsunomiya 08] S. Utsunomiya, L. Tian, G. Roumpos, C. W. Lai, N. Kumada, T. Fujisawa, M. Kuwata-Gonokami, A. Loffler, S. Hofling, A. Forchel & Y. Yamamoto. *Observation of Bogoliubov excitations in exciton-polariton condensates*. Nat Phys, vol. 4, no. 9, pages 700–705, 2008.

[Wannier 37] Gregory H. Wannier. *The Structure of Electronic Excitation Levels in Insulating Crystals*. Physical Review, vol. 52, no. 3, page 191, 1937.

[Weisbuch 77a] Claude Weisbuch. *Contribution à l'étude du pompage optique dans les semiconducteurs III-V*. PhD thesis, Université de Paris VII, Université de Paris VII, 1977.

[Weisbuch 77b] Claude Weisbuch & Rainer G. Ulbrich. *Resonant Polariton Fluorescence in Gallium Arsenide*. Physical Review Letters, vol. 39, no. 10, page 654, 1977.

[Weisbuch 92] C. Weisbuch, M. Nishioka, A. Ishikawa & Y. Arakawa. *Observation of the coupled exciton-photon mode splitting in a semiconductor quantum microcavity*. Physical Review Letters, vol. 69, no. 23, page 3314, December 1992.

[Winterling 77a] G. Winterling & E. Koteles. *Resonant Brillouin scattering near the a exciton in CdS.* Solid State Communications, vol. 23, no. 2, pages 95–98, 1977.

[Winterling 77b] G. Winterling, E. S. Koteles & M. Cardona. *Observation of Forbidden Brillouin Scattering near an Exciton Resonance.* Physical Review Letters, vol. 39, no. 20, page 1286, November 1977.

[Wouters 10] Michiel Wouters & Iacopo Carusotto. *Are non-equilibrium Bose-Einstein condensates superfluid?*, 2010.

[Yoshie 04] T. Yoshie, A. Scherer, J. Hendrickson, G. Khitrova, H. M. Gibbs, G. Rupper, C. Ell, O. B. Shchekin & D. G. Deppe. *Vacuum Rabi splitting with a single quantum dot in a photonic crystal nanocavity.* Nature, vol. 432, no. 7014, pages 200–203, November 2004.

[Yu 05] Peter Y. Yu & Manuel Cardona. Fundamentals of semiconductors. Springer, May 2005.